Arrayed Microfluidic Actuation for Active Sorting of Fluid Bed Particulates

by

Antimony L. Gerhardt

S.B., Electrical Science and Engineering
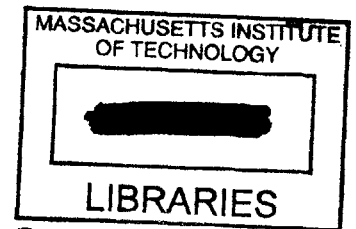Massachusetts Institute of Technology, 2003

Submitted to the Department of Electrical Engineering and Computer Science
in Partial Fulfillment of the Requirements for the Degree of

Master of Engineering in Electrical Engineering and Computer Science

at the
Massachusetts Institute of Technology
December 2003
[February 2004]

Signature of Author _____
Department of Electrical Engineering and Computer Science
December 3, 2003

Certified by _____
Martin A. Schmidt
Professor of Electrical Engineering and Computer Science
Thesis Supervisor

Certified by _____
Martha L. Gray
Edward Hood Taplan Professor of Electrical Engineering
Thesis Supervisor

Certified by _____
Mehmet Toner
Professor of Biomedical Engineering, Harvard Medical School, and Massachusetts General Hospital
Thesis Supervisor

Accepted by _____
Arthur C. Smith
Chairman, Department Committee on Graduate Theses
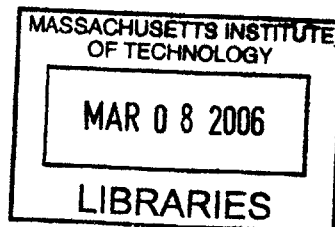
2

Arrayed Microfluidic Actuation for Active Sorting of Fluid Bed Particulates

by

Antimony L. Gerhardt

Submitted to the Department of Electrical Engineering and Computer Science
December 3, 2003, in Partial Fulfillment of the Requirements for the Degree of
Master of Engineering in Electrical Engineering and Computer Science

Abstract

Fluidic actuation offers a facile method to move large quantities of small solids, often referred to as fluid-bed movement. Applications for fluid bed processing are integral to many fields including petrochemical, petroleum, chemical, pharmaceutical, biochemical, environmental, defense, and medical. Thermal vapor microbubbles have been shown to be a low power input with high work output fluidic actuation technique with demonstrated commercial applications in ink jet printing and optical switching.

This thesis further develops microbubble actuation (μBA) as an arrayed particulate actuation technology for active sorting in particulate fluid beds. Numerical and analytical models of flows, forces, and fields affecting a μBA-based system are presented. The design and fabrication of an arrayed μBA-powered device are delineated with notation of specifications that may focus future design iterations. Performance testing and characterization of μBA technology, including over a hundred in-plane and out-of-plane nucleation site geometries, serve as the impetus for the technical guidelines that are presented, which include a detailed comparison of in-plane and out-of-plane nucleation site geometry performance.

Thesis Supervisor: Martin A. Schmidt
Title: Professor of Electrical Engineering and Computer Science

Thesis Supervisor: Martha L. Gray
Title: Edward Hood Taplan Professor of Electrical Engineering

Thesis Supervisor: Mehmet Toner
Title: Professor of Biomedical Engineering, Massachusetts General Hospital, and Harvard Medical School

Acknowledgements

Contents

List of Figures

13

14

List of Tables

Nomenclature

a	semi-major axis, m
A	constant; area, m^2
b	semi-minor axis, m
B	magnetic field, T
$\mathbf{B}$	magnetic field vector, T
C_{nb}	constant in nucleate boiling correlation
c	centricity ratio
d	diameter, m; distance, m
e	eccentricity ratio
D	diameter, m
E	cardinal direction
f_Δ	pulse frequency, Hz
F	force, N
G	conductance, Siemens
$\mathbf{G}$	conductance matrix, Siemens
G_n	conductance between nodes in the n directions, Siemens
h_{fg}	enthalpy of vaporization, J/kg
H	height, m; thickness, m
i	node; current, A
I	current, A
K	pressure gradient, Pa·m
N	cardinal direction
m	coordinate; slope
n	coordinate
L	sampling length; length, m; characteristic length, m
P	power, W
P	pressure, Pa
$\boldsymbol{P}$	power matrix, W

$\widetilde{P}$	power density, W/m^3
q	heat flux, W/m^2
Q	volumetric flow rate, m^3/s
$\dot{Q}$	rate of heat transfer into system, rate of heat flow, W
$\dot{Q}_v$	internal heat source, W
$\widetilde{Q}_v$	volumetric heat source per unit volume, W/m^3
r	radius, m
$\mathbf{r}$	radius vector, m
R	electrical resistance, Ω; thermal resistance, K/W
R_a	average roughness, m
R_n	thermal resistance between nodes in the n directions, K/W
R_x	thermal resistance between nodes in the x direction, K/W
R_y	thermal resistance between nodes in the y direction, K/W
R_{Pois}	fluidic resistance, Pa·s/m^3
Re	Reynolds number
s	length, m
$\mathbf{s}$	length vector, m
S	cardinal direction
t	time, s
t_q	time of q termination, s
T	temperature, K
$\boldsymbol{T}$	temperature matrix, K
$\overline{U}$	mean flow velocity, m/s
V	volume, m^3; voltage, V
W	cardinal direction; width, m
x	rectangular coordinate, m

y rectangular coordinate, m; elevation, m

z rectangular coordinate, m; elevation, m

Greek Symbols

α thermal diffusivity, m²/s

δ pulse width, s

δ_t temperature penetration depth, m

Δ finite increment; thermal boundary layer thickness, m; time between pulse wavefronts, s

ΔT_x excess temperature, K

θ angle, rad; contact angle, °

κ thermal conductivity, W/m·K

μ viscosity, Pa·s

μ^* kinematic viscosity, m³/s

μ_o permeability constant, H/m

ξ variable of integration

ρ_e electrical resistivity, Ω·m

ρ_m mass density, kg/m³

ρ_v saturated vapor density, kg/m³

σ_{st} surface tension of liquid-vapor interface, N/m

ψ_{min} angle between sidewall of cavity and heating surface, °

Subscripts

c cavity, constant

ch channel

d development, dissipation

D hydraulic diameter

DI deionized header

CS cross section

e ellipsoid

eq equivalent

$eject$ ejection

g gravity

h hydraulic

i node

I interface

IM input medium

in inlet

j jet

L linear

ns nucleation site

o initial

out outlet

p particle; particular solution

P point of observation

Pt platinum

pl power lead

Q quartz

r resistor

S serpentine

SA surface area

sat saturated

Ti titanium

w surface; solid wall

W water

Diacritics

—   average

Acronyms

AfCS	Alliance for Cellular Signaling
AOE	advanced oxide etcher
BioMEMS	biological microelectromechanical systems
MEMS	microelectromechanical systems
MTL	Microsystems Technology Laboratories
DC	direct current
DEP	dielectrophoresis
DI	deionized
DNA	deoxyribonucleic acid
dpi	dots per inch
EML	Exploratory Materials Laboratory
HMDS	hexamethyldisilazane
IC	integrated circuit
ICL	Integrated Circuits Laboratory
IM	input medium
IP	in-plane
IR	infrared
LPCVD	low pressure chemical vapor deposition
MMI	macro-to-micro interface
NIH	National Institutes of Health
OP	out-of-plane
PDMS	polydimethylsiloxane
PHE	platinum heating electrode
RF	radio frequency
SEM	scanning electron microscope, scanning electron micrograph
TRL	Technology Research Laboratory
TSC	test structure chip
UIM	user interface module
μBA	microbubble actuation
μDAC	microfabrication-based dynamic array cytometer

Chapter 1   Introduction

1.1 Background

Macro fluidic actuation is the use of mechanical devices to move or control fluids. Fluidic actuation yields a mechanical advantage in hydraulic systems utilizing pistons and serves as a facile method to move large quantities of small solids, often referred to as fluid bed movement. Integrating fluidic actuators, then, with sensors and distribution channels offers the ability to process significant amounts of solid materials entrained in a fluid flow. Mass production processing such as sorting, aerating, moving, drying, cooling, granulation, and coating of thermally sensitive and insensitive particulates can be accomplished at a commercial level using this fluid bed movement. Applications are integral to many fields including petrochemical, petroleum, chemical, pharmaceutical, biochemical, environmental, defense, and medical [1, 2].

1.1.1 Microfluidics

An extension of macro fluidics was made possible by the microelectromechanical systems (MEMS) revolution. Miniaturized macro fluidics, microfluidics, has applications for many small-particulate handling and processing systems as liquids and entrained particles can be handled more precisely [3-5]. A completely integrated micro fluid handler inherently has faster response times, smaller dead volumes, reduced sample sizes, and higher throughputs. Flow can be sensed and controlled on the order of 1 μl/min, and devices can be paired with microsensors to enable feedback control [6]. Higher precision sensing and control will allow greater reliability and repeatability. Additionally, miniaturized flow devices can be batch processed at a lower cost than the macro counterparts and are inherently more portable.

The benefits of moving from the macro to micro fluid bed regimes have inspired research in microflow components — actuators [7-9], valves [9-14], pumps [15-18], ducts [19], mixers [20-22], switches [23, 24], sensors [25-29], and others such as heat-exchangers, reactors, motors, and flow controllers. These building block components then are integrated

to produce more complex systems such as microflow devices. Commercial applications of microflow technology include industrial gas and liquid control systems, chemical analysis, whole blood preparation systems, drug targeting, gene therapy, bioreactors, particle counting and sorting, and inkjet printers [10, 22, 30-32].

Commercially successful, inkjet printing is based on the concept of using a resistor to heat approximately 0.3% of the ink in a chamber [33, 34]. The heated ink vaporizes. The expansion displaces surrounding ink, and some of the displaced ink is ejected out of the printer nozzle. The ejected ink prints on a sheet of paper. As the vapor bubble collapses, a vacuum is created that pulls the remaining ink back into the cartridge. The dots per inch (dpi) resolution of a printer is determined by the size of the ejected droplet and the spacing between nozzles in the array. Because the thermally formed bubble ejects the ink, inkjet printers are often called bubble jet or thermal printers. Figure 1-1 illustrates ink ejecting from a nozzle of an inkjet printer head.
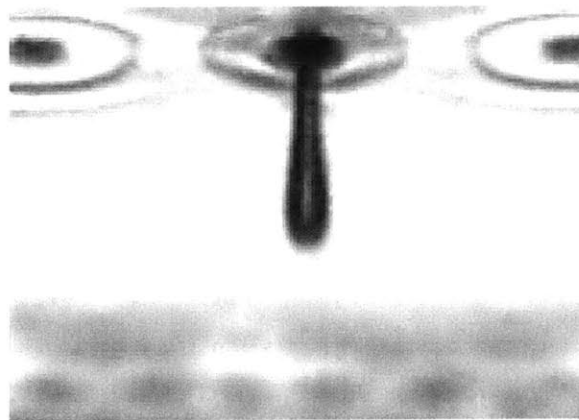
Figure 1-1. *Inkjet Printing.* (Copyright of Hewlett-Packard Company; used with permission.)

The mechanism behind inkjet printing can be assorted as thermal actuation, microbubble actuation (μBA), or the phenomenon of boiling. Compared with other actuation technologies such as electromagnetic, electrostatic, thermal bimetallic, and piezoelectric, μBA can be accomplished with a design that requires no mechanical moving parts and relatively simple electronics [35]. μBA is not prone to mechanical failure resulting from

fatigue and fabrication defects like other actuation techniques, and relatively low power inputs generate large forces. Microbubbles can be nucleated in open or controlled environments [3]. Further, as inkjet printing demonstrates, the µBA technology is scalable, robust, and can be cost effective enough to be commercialized.

The same bubble mechanism used in inkjet printing was shown to be commercially viable as an optical switch [36, 37]. Using the high-reflectivity bubble as a pseudo-mirror, Agilent Technologies developed a printed circuit where multiple wave guides intersect at critical cross points. The cross points contain fluids with the same optical characteristics as the waveguide. A bubble nucleated at a cross point redirects the light along a new path, switching information in a fast and reliable manner with no mechanical parts. Figure 1-2 depicts this optical bubble technology device, which was dubbed Champagne because of the similarity between a thermally formed microbubble and the minute bubbles in a glass of champagne. At the center of the image is the cross point, where light currently is being redirected by a microbubble.
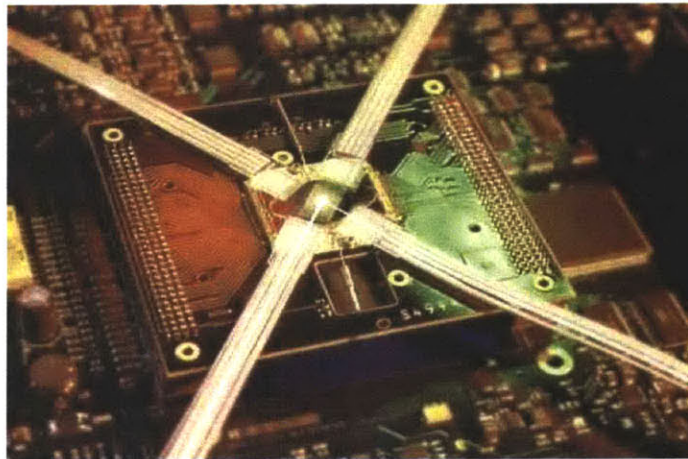
Figure 1-2. *Optical Switching [36].*

The development of integrated circuit (IC) technology led to the advent of extremely smooth surfaces. With glabrous microscale geometries, research of boiling phenomena moved from the more traditional mediums of meta saturated and meta cool liquid. Local

bubble nucleation has been found to be a much more powerful process in the microdimensions, as the potential to do work is greater. A large effort has been invested in the study of the microscale mechanism of boiling phenomena — formation, dissipation, and applications of thermally formed microbubbles [3, 34, 35, 38-53].

In addition to the largest commercial application of inkjet printing and the ongoing research to improve the process, a µBA DNA ejection device, an extension of current inkjet printing technologies, expels DNA creating a microarray for biological screening [54]. Other potential applications for µBA-powered systems include fluid mixing for chemical analysis, prime movers in micro steam engines, and integrated cooling for ICs. Additionally improvements in bubble jet printing such as eliminating satellite ink drops [30, 31] and increasing resolution by decreasing fluidic ejection volumes are current areas of focus in µBA research.

µBA-based components such as micropumps, microdrop valves, flow controllers, mixers, microinjectors, check-valves, filters, and diffusers are in the research and development stages [44, 55, 56].

(a)   (b)   (c)
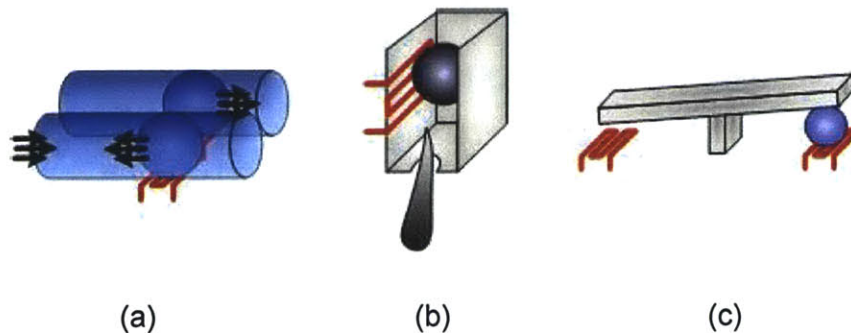
Figure 1-3. *µBA-Based Components.*

Figure 1-3 illustrates a portion of one µBA-based device and two µBA-based components. The image in column (a) is a pair of microchannels. The forefront microchannel contains a bubble that has been formed to temporarily stop the flow of fluid. A bubble in the background microchannel initiates fluid flow by means of fluidic displacement. The

component in (b) is a caricature of an inkjet printer nozzle, and a bubble-powered mixer is shown in (c).

1.1.2 BioMEMS

Microfluidics and other subdivisions of MEMS research have resulted in commercial applications ranging from bubble jet printers and later high-resolution inkjet-based color printers to accelerometers for air bags in the automotive industry [57]. In tandem, a field of MEMS coined Biological MEMS (BioMEMS) has emerged. BioMEMS devices have an enormous global market and the potential to dramatically alter current health care practice and research by serving as a supplement to current macro technologies.

The advantages of using MEMS in biology and medicine are vast [58]. MEMS mean the ability to maintain small device size, allowing the use of microscale phenomenon such as μBA. High surface-area-to-volume ratios enhance surface physical effects, such as heat dissipation. Thus, greater temperatures can be obtained without the adverse heating effects often encountered in the macro regime. Electronic integration can abate the overall device size, increase electromagnetic compatibility, improve reliability between interconnections, and potentially decrease production costs [57].

The "velocity" in units of cells or samples per second, throughput, is often the rate-limiting factor in biological research. The number of samples that can be read on a spectrophotometer or the number of cells that can be analyzed and sorted in a flow cytometer in a given time determines, to a great extent, the amount of time required to perform an assay. The high throughput potential of MEMS, processing samples in massive parallelization on a micro scale, promises drastically faster analysis.

Small sample volumes increase the usability of each histological sample, decrease the size requirement for medical diagnostics in which the sample material is scarce, reduce costs per assay especially when expensive reagents are involved, and can be used to deliver more precise dosages for chemotherapy and other treatments. Batch processing permits multitudes of devices to be created as simply as one. Thus, batch processing is cost effective and reduces device-to-device inconsistencies present in most macro construction. Geometrical

control also allows interaction between tissues, cell, or other biological components to be carefully regulated.

Small device size, high surface-area-to-volume ratio, electronic integration, high throughput, small sample volume, batch processing, and geometrical control are some of the advantages MEMS technology can offer biomedicine. Researchers predict that the medical applications resulting from BioMEMS devices are a multi-billion dollar market [59]. Until recently, however, the focus of MEMS research was toward industrial rather than medical applications.

MEMS applications in biomedicine include sample handling using microdroplet generators [60]. Microdroplet generators for biomedical and chemical sample handling for mass spectrometry have been demonstrated by [61] and [62]. The objective of the devices is to output liquid samples such as DNA or proteins in a controlled fashion that increases the performance of the mass spectrometry system. A variation of microdroplet dispensers, conceptually similar to the inkjet printing method, have been used by [63]. High-density gene arrays were printed with 300 dpi resolution onto hybridization membranes and hybridized with specific genes or total cDNA as probes. More complex microarrays could be created to facilitate hybridization of larger quantities of genes.

Another application of microsystems in medicine is using biosensors in functional assays ranging from receptor and ligand interaction characterization, toxicology, and chemotherapeutic agent evaluation [64, 65]. Biosensors are also used for blood-gas monitoring and in electrolyte sensing [66]. Information about physiological changes in cultured cells can be obtained using microphysiometry, and cell flow characteristics have been studied using microdevices. Drug targeting and gene therapy [32] as well as implantable devices [59] are other uses of BioMEMS devices and systems. Implantable devices, consisting of sensors and integrated processing electronics, could be used for biotelemetry, providing medical practitioners additional information for diagnostics and treatment.

Most biological applications of MEMS depend heavily on microfluidics. The microdroplet ejectors spray sample volumes on the order of microliters. Biosensors to detect

28

receptor ligand interaction are submerged in a fluidic medium. Blood-gas monitoring systems draw microliters of blood, analyze the volume for gas content, and return the fluid to the patient.

Because BioMEMS involves mircofluids, refining current microfluidic technology is crucial to the advancement of BioMEMS devices and systems. To achieve higher precision sensing and control micosystem devices, the fluid-bed movement of fluids and particles can be studied and current methods of actuation and control can be developed further. With fluidic components created with greater accuracy, higher levels of control and predictability can be achieved, yielding results, devices, and systems that are more reliable, repeatable, and robust.

1.2 Motivation

Thermal vapor microbubbles have been shown to be a low power input with high work output fluidic actuation technique with applications in thermal bubble printing, as prime movers in micro steam engines, and in other devices as components. While microbubbles or μBA have been shown to do useful work, a method to control the nucleation site of thermal bubbles, limit the number of nucleations on a resistor, and ensure bubble dissipation in short time scales was still needed. In [67-70], such a method was presented. The research objectives were controlled nucleation sites and short dissipation times. A proof-of-concept device demonstrated that individual particulate sorting on a non-arrayed basis was an additional process that could be performed in particulate fluid beds.

1.2.1 Microfabrication-based Dynamic Array Cytometer

While μBA has the potential for use in a variety of industries as well as in biomedicine and medicine, a medical application offered an immediate challenge for which controlled μBA might serve as a means of solution. This application of the individual particulate sorting capability of microfluid beds corresponds to the long-term goal of the microfabrication-based dynamic array cytometer (μDAC) project. The goal of the μDAC

project is to create an arrayed dynamic cell analysis system that combines the concepts of microscopy and flow cytometry [71].

Through microscopy, researchers can collect time responses of a small quantity of cells. Sorting is time intensive and must be done on a cell-by-cell basis. Current flow cytometry technology, a method for quantizing structural features of cells, allows researchers to gather instantaneous responses of a large quantity of cells [72-74]. Cells in a monodisperse suspension serially flow past a laser beam. Several parameters, such as quantity of scattered light and emitted fluorescent light, are measured simultaneously for each cell. Based on the instantaneous response, each cell then can be sorted via microfluidic tubing into vials for assays. Figure 1-4 conceptually illustrates the cell analysis techniques of microscopy and flow cytometry. In (a), the cells have been patterned in a microarray, formed by creating hydrophobic and hydrophilic surfaces. In (b), a series of cells are being processed in a flow cytometer. A photo detector shown at the bottom of the figure collects the scattering and emission data from the analyzed cell.

(a)   (b)
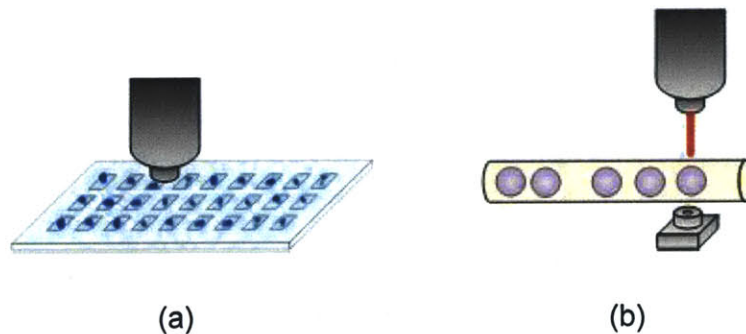
Figure 1-4. *Microscopy and Flow Cytometry.*

A method of laser capture microdissection allows specified cell populations to be selected rapidly from heterogeneous tissue [75]. Variations of the laser capture microdissection method now are commercially available, giving researchers the ability to sort cells from tissues or groups of cells. However, cells are destroyed in the process. Thus, although the cell-by-cell analysis concept is well acknowledged in the literature, no reliable

method of sorting live cells from a group of cells without causing cell damage or death exists.

Melding microscopy, flow cytometry, and laser capture microdissection will enable researchers to work with both large and small quantities of cells. Time responses can be gathered instantaneously and over the course of minutes, hours, or days. Sorting can be performed based on time and instantaneous responses, and throughput can be adjusted depending on the amount of information the researcher wishes to gather per cell. Additionally, the μDAC yields a greater signal-to-noise ratio than bulk assays that will enable more detailed characterization. Thus, μDAC will allow researchers to gather fluorescence data at a single cell level while tracking many cells over time and sorting the cells based upon dynamic responses. Table 1-1 provides a summary comparison of microscopy, flow cytometry, laser microdissection, and μDAC properties.

Table 1-1. *Attribute Comparison of Microscopy, Flow Cytometry, and μDAC.*

Property	Cell Analysis Method			
	Microscopy	Flow Cytometry	Laser Microdissection	μDAC
Quantity of cells	Small	Large	Large	Both
Response	Over time	Instantaneous	Over time	Both
Sorting	Difficult	Basic	Advanced	Advanced
Throughput	Low	High	High	High
Cell damage/death	Yes	Yes	Yes	No

1.2.2 Conceptual μDAC System

The μDAC design combines aspects of microscopy and flow cytometry to yield a novel, useful cell analysis tool for researchers and scientists. Figure 1-5 illustrates the conceptual μDAC system. The critical components include a: (1) fluidic system consisting of input and output headers for bioparticulate and reagent injection and bioparticulate collection; (2) microfabricated capture sites array that simultaneously handles on the order of 10^5 particulates; (3) computerized optical system that enables fluorescence data to be acquired on an individual particle basis; and (4) computerized control system programmed

to respond to optical data acquired and selectively eject particulates displaying a given intensity. Thus, this system will enable large particulate populations to be electronically and physically sorted by intensity response in a manner currently not feasible with existing technologies.
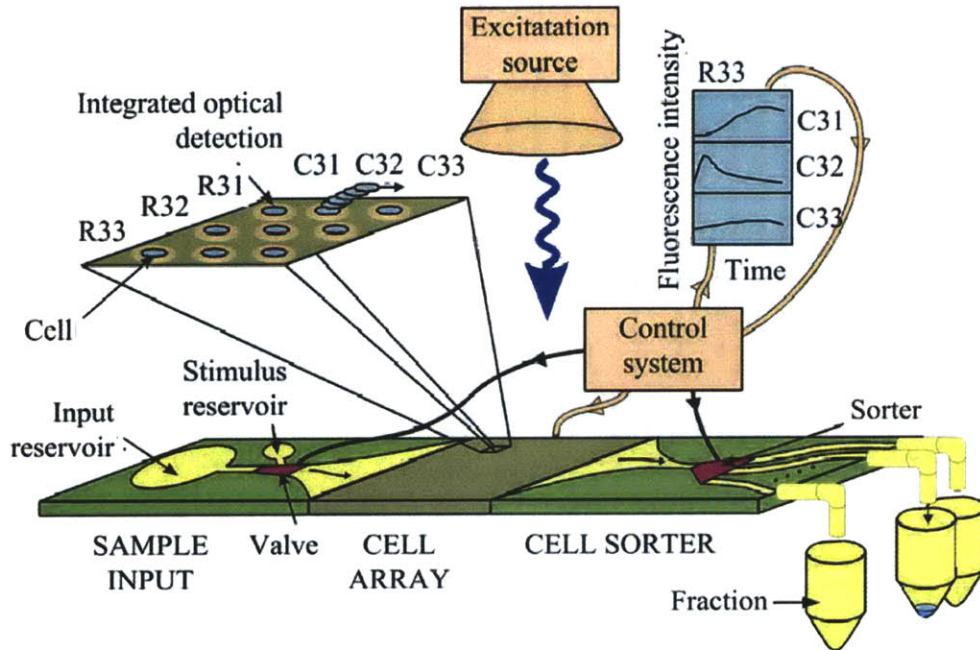
Figure 1-5. *Conceptual µDAC System [76].*

1.2.3 µDAC Progress

Efforts toward a µDAC system were initiated using dielectrophoresis (DEP) to trap and release cells. In [20, 21, 58, 71, 76-82], a method of particle position control using DEP traps was demonstrated. Using DEP, the particle was captured in a potential well and actively held during analysis by a high frequency alternating current (AC) field to minimize the effects of potential difference across the cell membrane. Figure 1-6 contains two scanning electron microscope (SEM) images of a DEP array. Image (a) is a zoom of a single capture site. The cell would flow to the middle of the four gold posts. Trapped by the potential well, the cell would remain until the AC field was turned off. SEM image (b) is an

aerial capture of a single row array of DEP capture sites. A particle is shown captured in the right, four-post potential well.

(a)   (b)
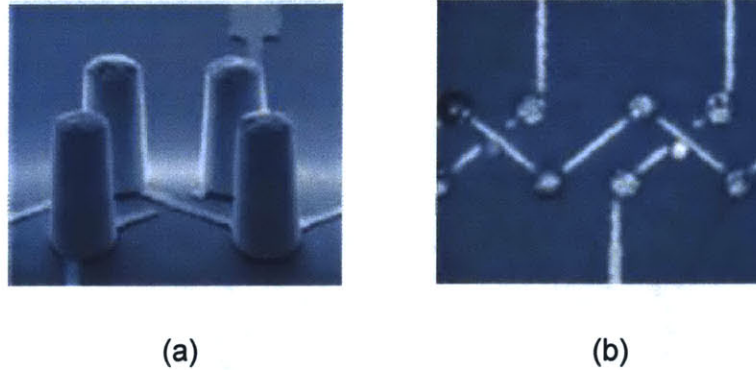
Figure 1-6. *Early DEP-Powered µDAC Efforts [77].*

Early progress in the DEP concept inspired research in a second method of particle position control, a method employing µBA. In µBA, the particle is captured in a capture site or well by a pressure gradient. The particle then is actively released by a jet of fluid displaced from the bubble chamber with the formation of a microbubble. The mechanism is similar to that of inkjet printing. In [67-70, 83], we illustrated the proof-of-concept design of a non-arrayed, µBA-driven realization of the µDAC project. The µBA proof-of-concept device demonstrated that a particulate could be captured in a predetermined location, held against the bulk fluid flow, and then actively sorted by µBA release into a specific fraction reservoir.

1.2.4 µBA Device Concept

The µBA device concept is similar to other bubble-powered devices in that the electronics are simple, and the power needed to operate the device is relatively low. A single capture and release site is schematically depicted in Figure 1-7. In this illustration, the *particulate* is a 10 µm bead. The particulate is captured with a pressure differential between the bubble chamber and the input header in which the particles flow (illustrated as the surface of the device). The *backflow channel* is utilized to ensure that the needed pressure gradient

for successful capture is present. For the first generation of the device, the backflow port was left open to atmosphere, providing a pressure base (atmospheric) in the bubble chamber.

The particle is captured in the *capture well* and held against the flow via the pressure gradient and the geometry of the well. For scaling purposes, the particle depicted is 10 μm in diameter. The capture well is 15 μm in width. The bubble jet channel is 5 μm in width. The bubble chamber is 250 μm in width, and the platinum resistor is 100 μm in width.
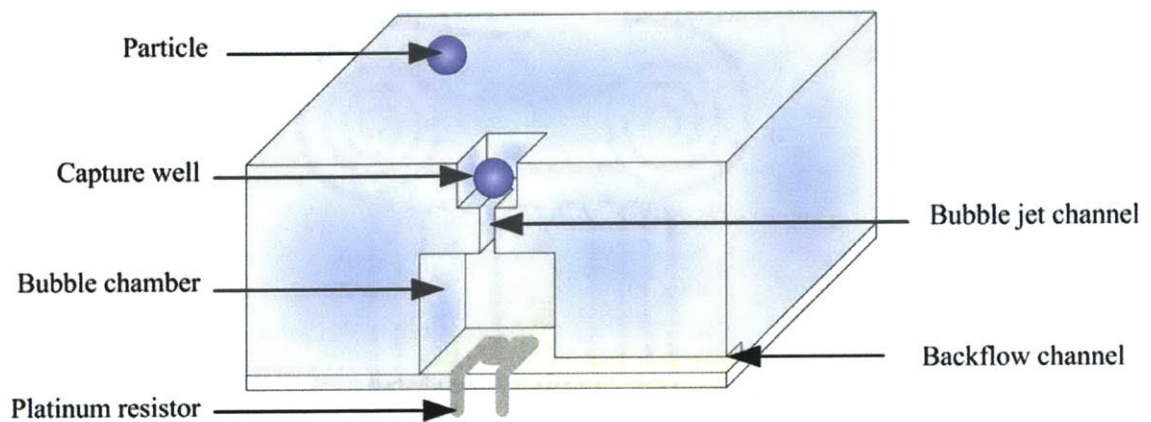
Figure 1-7. *Early μBA Capture Site.*

While captured, the particle could be analyzed for fluorescence data, optically inspected for deformations or differentiation, and maintained for a length of time consistent with the in-progress assay. After the needed data have been collected, a pulse of voltage is applied across the *platinum resistor* in the *bubble chamber* which generates a current through the resistor. The heat generated by the resistor creates a temperature field in the surrounding water. At an etched cavity on the platinum resistor, a bubble nucleates. The bubble grows rapidly within the bubble chamber. The bubble formation then displaces a jet of fluid that jets through the *bubble jet channel* ejecting the captured particulate. The ejected particle is entrained in the flow of the fluid, ready to be recaptured or, as a sorted particle, directed to an awaiting reservoir. See Figure 1-8.
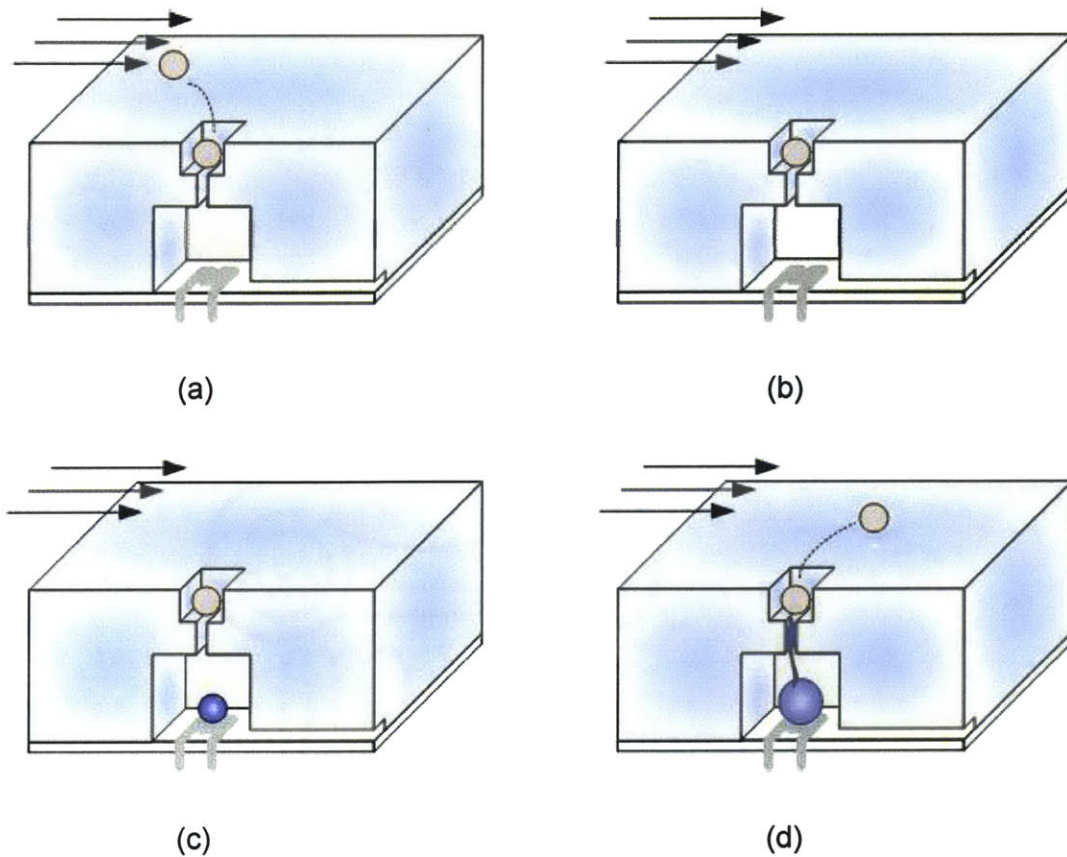
Figure 1-8. *Early μBA Capture and Release Schematic.*

The first and second chip designs had a geometry consisting of two rows of resistive heating elements. In the first, the resistors were line resistors. In the second, the resistors were folded. Both designs used an out-of-plane etched cavity as the nucleation site. Each row of resistors in both generations spans a width of approximately 8 cm. Each resistive element could be utilized as a capture site. The upper layer silicon chip containing the etched bubble chamber and capture well was bonded to the quartz resistor chip shown in Figure 1-9. Each pair of platinum lines perpendicular to the long dimension of the chip represents the pair of leads for a resistive heating element. The pictured chip contains resistors of different geometries ranging in width from about 100 to 1000 μm. The package used to test the μBA application is shown in Figure 1-10. Assembled, the first-generation package was approximately 15 mm long by 8 mm wide and 12 mm high.
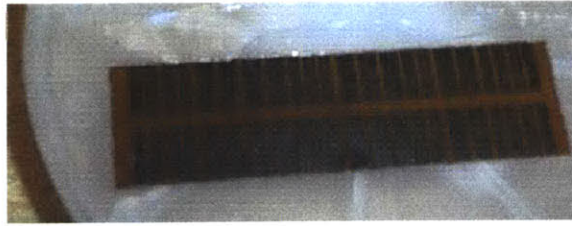
Figure 1-9. *Early μBA Fabricated Chip.*
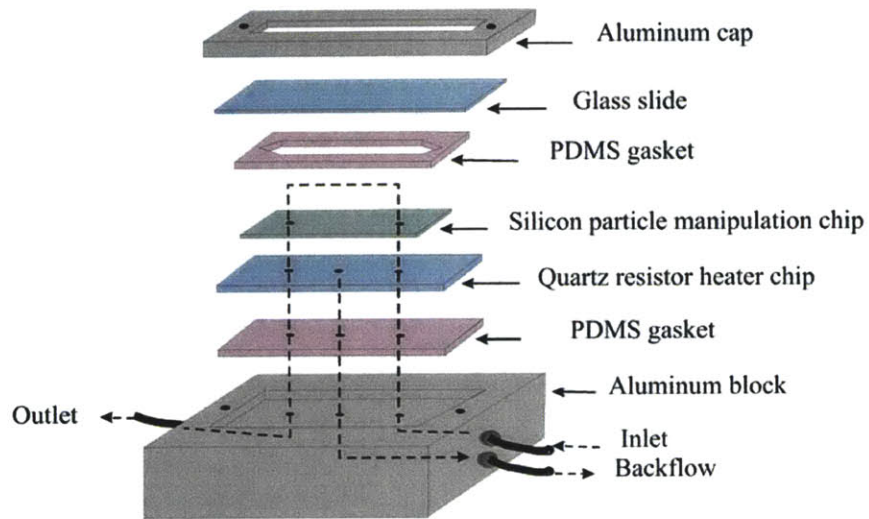
Figure 1-10. *First-Generation Package [68].*

1.3 Objective

In previous work [67-70, 83], the μBA technique was shown to be capable of nucleating a thermally formed microbubble at a specified location and dissipating that bubble on a time scale of the order of seconds. Additionally, a proof-of-concept μBA-driven device was shown to be capable of capturing a particle at a predetermined location, holding the particle against the bulk flow, and releasing the particle at a chosen time. The next step in the development of the μBA technology is to use the information gained from characterizing

the microbubble formation properties and the first-generation μBA-driven device to design arrayed μBA-driven actuation technology. This can be accomplished in conjunction with the goals of the μDAC project.

The main objective of this thesis is to demonstrate the feasibility of microbubble actuation as an arrayed particulate actuation technology for active sorting in particulate fluid beds. To accomplish this objective, (1) an arrayed μBA-driven device was designed and fabricated, (2) the μBA technology was tested and characterized in detail including over a hundred in-plane and out-of-plane nucleation site geometries, and (3) technical guidelines for μBA-based devices and systems are presented. Therefore, in the course of research, the first-generation μBA for sorting technique was improved upon and further characterized while developing an application device that has the potential to serve as a tool for the researcher and scientist in the laboratory.

1.4 Scope

Chapter 1 provides an introductory background in the areas of microfluidics, μBA, BioMEMS, and the μDAC project. In Chapter 2, some of the theory relevant to a μBA-based device in industrial contexts is presented. Chapter 3 elucidates numerical and analytical models of flows, forces, and fields affecting a μBA-based system. Chapter 4 describes fundamental parameters that influence design of a μBA device and the resulting device design for the μDAC application. Other applications of the μBA-powered technology that can be extrapolated from the μDAC design are discussed in the concluding sections. The focus of Chapter 5 is to discuss experimental hypotheses, protocols, and results of chip performance testing. The final chapter is dedicated to a discussion of the μBA chip performance including a detailed comparison of in-plane and out-of-plane nucleation site geometries, remaining problems and potential resolution for those problems, and suggestions for the focus of future work and potential μBA applications.

1.5 References

[1] R. B. White and A. Zakhari, "Internal Structures in Fluid Beds of Different Scales: An Application of Electrical Capacitance Tomography," In *Proc. 1st World Congress on Industrial Process Tomography*, Burdon, Greater Manchester, England, 1999, pp. 39-46.

[2] L. J. Shadle, E. R. Monazam, and J. S. Mei, "Circulating Fluid Bed Operating Regimes," In *Proc. 7th International CFB Conference*, Niagara Falls, New York, 2001, pp. 255-262.

[3] J. Tsai and L. Lin, "Transient Thermal Bubble Formation on Polysilicon Micro-Resistors," *Journal of Heat Transfer.*, vol. 124, Apr., pp. 375-382, 2002.

[4] A. Hatch, A. E. Kamholz, G. Holman, P. Yager, and K. F. Böhringer, "A Ferrofluidic Magnetic Micropump," *Journal of Microelectromechanical Systems*, vol. 10, no. 2, Jun., pp. 215-221, 2001.

[5] P. Dutta, A. Beskok, and T. C. Warburton, "Electroosmotic Flow Control in Complex Microgeometries," *Journal of Microelectromechanical Systems*, vol. 11, no. 1, Feb., pp. 36-44, 2002.

[6] S. Shoji and M. Esashi, "Microflow Devices and Systems," *Journal of Micromechanics and Microengineering*, vol. 4, pp. 157-171, 1994.

[7] Y. Su, L. Lin, and A. P. Pisano, "A Water-Powered Osmotic Actuator," *Journal of Microelectromechanical Systems*, vol. 11, no. 6, Dec., pp. 736-742, 2002.

[8] T. Stanczyk, B. Ilic, P. J. Hesketh, and J. G. B. IV, "A Microfabricated Electrochemical Actuator for Large Displacements," *Journal of Microelectromechanical Systems*, vol. 9, no. 3, pp. 314-320, 2000.

[9] R. H. Liu, Q. Yu, and D. J. Beebe, "Fabrication and Characterization of Hydrogel - Based Microvalves," *Journal of Microelectromechanical Systems*, vol. 11, no. 1, Feb., pp. 45-53, 2002.

[10] A. K. Henning, "Microfluidic MEMS," In *Proc. IEEE Aerospace Conference*, vol. / paper 4.906, Piscataway, New Jersey: IEEE Press, 1998.

[11] H. Jerman, "Electrically-activated, normally closed diaphragm valves," *Journal of Micromechanics and Microengineering*, vol. 4, pp. 210-216, 1994.

[12]   H. Jerman, "Electrically-activated micromachined diaphragm valves," In *Proc. IEEE Solid State Sensors, Actuators, and Microsystems Workshop*, Hilton Head, South Carolina, 1990, pp. 65-69.

[13]   J. S. Fitch, A. K. Henning, E. B. Arkilic, and J. M. Harris, "Pressure-based mass-flow control using thermopneumatically-actuated microvalves," In *Proc. IEEE Solid-State Sensor, Actuator, and Microsystems Workshop*, Cleveland, Ohio: Transducers Research Foundation, 1998, pp. 162-165.

[14]   N. Vandelli, D. Wroblewski, M. Velonis, and T.Bifano, "Development of a MEMS Microvalve Array for Fluid Flow Control," *Journal of Microelectromechanical Systems*, vol. 7, no. 4, Dec., pp. 395-403, 1998.

[15]   M. Koch, N. Harris, A. G. R. Evans, N. M. White, and A. Brunnschweiler, "A novel micromachined pump based on thick-film piezoelectric actuation.," *Sensors and Actuators A: Physical*, vol. 70, pp. 98-103, 1998.

[16]   A. Manz, C. S. Effenhauser, N. Burggraf, D. J. Harrison, K. Seiler, and K. Fluri, "Electroosmotic pumping and electrophoretic separations for miniaturized chemical analysis systems," *Journal of Micromechanics and Microengineering*, vol. 4, pp. 257-265, 1994.

[17]   R. Zengerle, J. Ulrich, S. Kluge, M. Richter, and A. Richter, "A bidirectional silicon micropump," *Sensors and Actuators A: Physical*, vol. 50, no. 1-2, pp. 81-86, 1995.

[18]   R. Zengerle, M. Richter, F. Brosinger, A. Richter, and H. Sandmaier, "Performance simulation of microminiaturized membrane pumps," In *Proc. 7th International Conference of Solid-State Sensors, Actuators, and Microsystems (Transducers '93)*, Yokohama, Japan, 1993, pp. 106-109.

[19]   D. Armani and C. Liu, "Re-configurable Fluid Circuits By PDMS Elastomer Micromachining," In *Proc. 12th International Conference on MEMS (MEMS '99)*, Orlando, Florida, 1999, pp. 222-227.

[20]   J. Voldman, M. L. Gray, and M. A. Schmidt, "An integrated liquid mixer/valve," *Journal of Microelectromechanical Systems*, vol. 9, pp. 295-302, 2000.

[21]   J. Voldman, M. L. Gray, and M. A. Schmidt, "Liquid mixing studies using an integrated mixer/valve," In *Proc. Micro Total Analysis Systems (μTAS '98)*, Netherlands: Kluwer Academic Publishers, 1998, pp. 181-184.

[22]   M. Elwenspoek, T. S. J. Lammerink, R. Miyake, and J. H. J. Fluitman, "Towards integrated microliquid handling systems," *Journal of Micromechanics and Microengineering*, vol. 4, pp. 227-245, 1994.

[23]   D. C. Duffy, O. J. A. Schueller, S. T. Brittain, and G. M. Whitesides, "Rapid Prototyping of Microfluidic Switches in Poly(dimethyl siloxane) and their Actuation by Electro-osmotic Flow," *Journal of Micromechanics and Microengineering*, vol. 9, no. 3, pp. 211-217, 1999.

[24]   L. Latorre, J. Kim, J. Lee, P.-P. de Guzman, H. J. Lee, P. Nouet, and C.-J. Kim, "Electrostatic Actuation of Microscale Liquid-Metal Droplets," *Journal of Microelectromechanical Systems*, vol. 11, no. 4, Aug., pp. 302-308, 2002.

[25]   L. L. Chu, K. Takahata, P. Selvaganapathy, J. L. Shohet, and Y. B. Gianchandani, "A Micromachined Kelvin Probe for Surface Potential Measurements in Microfluidic Channels and Solid-State Applications," In *Proc. 12th International Conference on Solid State Sensors, Actuators, and Microsystems (Transducers '03)*, vol. 1, Boston, Massachusetts, 2003, pp. 384-387.

[26]   J. Shih, J. Xie, and Y. C. Tai, "Surface Micromachined and Integrated Capacitive Sensors for Microfluidic Applications," In *Proc. 12th International Conference on Solid State Sensors, Actuators, and Microsystems (Transducers '03)*, vol. 1, Boston, Massachusetts, 2003, pp. 388-395.

[27]   E. Meng and Y.-C. Tai, "A Parylene MEMS Flow Sensing Array," In *Proc. 12th International Conference on Solid State Sensors, Actuators, and Microsystems (Transducers '03)*, vol. 1, Boston, United States, 2003, pp. 686-689.

[28]   G. Hong, A. S. Holmes, M. E. Heaton, and K. R. Pullen, "Design, Fabrication, Characterization of an Axial-Flow Turbine for Flow Sensing," In *Proc. 12th International Conference on Solid State Sensors, Actuators, and Microsystems (Transducers '03)*, vol. 1, Boston, Massachusetts, 2003, pp. 702-705.

[29]   C.-J. Lin and F.-G. Tseng, "A Novel Micro Faby-Perot Sensor Utilizing Refractive Index Matched Medium for High Sensitive Shear Stress Sensing," In *Proc. 12th International Conference on Solid State Sensors, Actuators, and Microsystems (Transducers '03)*, vol. 1, Boston, Massachusetts, 2003, pp. 710-713.

[30]   F. Tseng, C. Kim, and C. Ho, "A High-Resolution High-Frequency Monolithic Top-Shooting Microinjector Free of Satellite Drops - Part I: Concept, Design, and Model," *Journal of Microelectromechanical Systems*, vol. 11, no. 5, Oct., pp. 427-436, 2002.

[31]   F. Tseng, C. Kim, and C. Ho, "A High-Resolution High-Frequency Monolithic Top-Shooting Microinjector Free of Satellite Drops - Part II: Fabrication, Implementation, and Characterization," *Journal of Microelectromechanical Systems*, vol. 11, no. 5, pp. 437-447, 2002.

[32]   S. S. Davis, "Biomedical applications of nanotechnology - implications for drug targeting and gene therapy," *Trends in Biotechnology*, vol. 15, Jun., pp. 217-224, 1997.

[33]   Hewlett-Packard Company, "Myths About Thermal Inkjet Printings," [Online document], 1994, [cited 2003 July 21], Available HTTP: http://www.hp.com.

[34]   R. R. Allen, J. D. Meyer, and W. R. Knight, "Thermodynamics and Hydrodynamics of Thermal Ink Jets," *Hewlett-Packard Journal*, vol. 36, May, pp. 21-27, 1985.

[35]   B. Choi, M. Ma, C. White, and C. Liu, "Electrolytic and thermal bubble generation using AC inductive powering," In *Proc. 10th International Conference of Solid-State Sensors, Actuators, and Microsystems (Transducers '99)*, Sendai, Japan, 1999.

[36]   Agilent Technologies, "Building Australian businesses based on frontier technologies," [Online document], 2003, [cited 2003 October 26], Available HTTP: http://www.agilent.com.

[37]   Agilent Technologies, "Tiny bubbles - the secret to tomorrow's broadband networks," [Online document], 2000, [cited 2003 October 26], Available HTTP: http://www.agilent.com.

[38]   A. Asai, "Application of the Nucleation Theory to the Design of Bubble Jet Printers," *Japanese Journal of Applied Physics*, vol. 28, pp. 909-915, 1989.

[39]   C. C. Beatty, "A chronology of thermal ink-jet structures," In *Proc. IEEE Solid-State Sensor, Actuator, and Microsystems Workshop*, Hilton Head, South Carolina, 1996, pp. 200-204.

[40]   R. Cole, "Boiling Nucleation," in *Advances in Heat Transfer*, J. P. Hartnett and T. F. Irvine, Eds. Chicago, Illinois: Academic Press, 1974.

[41]   R. Cole and S. V. Stralen., *Boiling Phenomena*. vol. 1, Washington, D.C.: Hemisphere Publishing Corporation, 1979.

[42]   J. D. Evans and D. Liepmann, "The Bubble Spring and Channel (BSaC) Valve: An Actuated, Bi-stable Mechanical Valve for In-Plane Fluid Control," In *Proc. 10th International Conference on Solid-State Sensors, Actuators, and Microsystems (Transducers '99)*, Sendai, Japan, 1999, pp. 1122-1125.

[43]   X. Geng, H. Yuan, H. N. Oguz, and A. Prosperetti, "Bubble-Based Micropump for Electrically Conducting Liquids," *Journal of Micromechanics and Microengineering*, vol. 11, no. 3, pp. 270-276, 2001.

[44]   L. Lin and A. P. Pisano, "Bubble Forming on a Micro Line Heater," In *Proc. DSC ASME Micromechanical Sensors, Actuators, and Systems - Winter Annual Meeting*, vol. 32, 1991, pp. 147-163.

[45]   L. Lin and A. P. Pisano, "Thermal Bubble Powered Microactuators," *Microsystem Technologies Journal*, vol. 1, no. 1, pp. 51-58, 1994.

[46]   L. Lin, A. P. Pisano, and A. P. Lee, "Microbubble Powered Actuator," In *Proc. 6th International Conference on Solid-State Sensors, Actuators, and Microsystems (Transducers '91)*, San Francisco, California, 1991, pp. 1041-1044.

[47]   L. Lin, K. S. Udell, and A. P. Pisano, "Phase Change Phenomena on a Heated Polysilicon Micro Heater in Confined and Unconfined Micro Channels," *Thermal Sciences and Engineering*, vol. 2, pp. 52-59, 1994.

[48]   L. S. Tong and Y. S. Tang, *Boiling Heat Transfer and Two-Phase Flow*. 2nd ed., Washington, D.C.: Taylor and Francis, Incorporated, 1997.

[49]   J. Tsai and L. Lin, "A Thermal-Bubble-Actuated Micronozzle-Diffuser Pump," *Journal of Microelectromechanical Systems*, vol. 11, no. 6, Dec., pp. 665-671, 2002.

[50]   J. Tsai and L. Lin, "Nozzle-Diffuser Based Micro Bubble Pump," In *Proc. Late News Poster Session Supplemental Digest of IEEE Solid-State Sensors, Actuators, and Microsystems Workshop*, Hilton Head, South Carolina, 2000, pp. 13-14.

[51]   J. Tsai and L. Lin, "Transient Bubble Formation On A Polysilicon Micro Resister," In *Proc. 2000 ASME International Mechanical Engineering Congress and Exposition, ASME Heat Transfer Division*, vol. 2, Orlando, Florida, 2000, pp. 251-258.

[52]   J. Tsai and L. Lin, "Active Microfluidic Mixer and Gas Bubble Filter Driven by Thermal Bubble Micropump," *Sensors and Actuators A: Physical*, vol. 97-98, pp. 665-671, 2002.

[53]   B. B. Mikic and W. M. Rohsenow, "Bubble Growth Rates in Non-uniform Temperature Field," in *Progress in Heat and Mass Transfer*, vol. 2, T. F. Irvine, W. E. Ibele, J. P. Hartnett, and R. J. Goldstein, Eds. Oxford, England: Pergamon Press, 1969, pp. 283-294.

[54]   T. Okamoto, T. Suzuki, and N. Yamamoto, "Microarray Fabrication with Covalent Attachment of DNA Using Bubble Jet Technology," *Nature Biotechnology*, vol. 18, Apr., pp. 438-441, 2000.

[55]   M. Yang, C. Li, and J. Yang, "Cell Docking and On-Chip Monitoring of Cellular Reactions with a Controlled Concentration Gradient on a Microfluidic Device," *Analytical Chemistry*, vol. 74, pp. 3991-4001, 2002.

[56]   J. Evans, D. Liepmann, and A. P. Pisano, "Planar Laminar Mixer," In *Proc. 10th International Conference of Solid-State Sensors, Actuators, and Microsystems (Transducers '99)*, Sendai, Japan, 1999, pp. 96-101.

[57]   S. D. Senturia, *Microsystem Design*. Norwell, Massachusetts: Kluwer Academic Publishers, 2001.

[58]   J. Voldman, M. L. Gray, and M. A. Schmidt, "Microfabrication in Biology and Medicine," *Annual Review of Biomedical Engineering*, vol. 1, pp. 401-425, 1999.

[59]   G. Kotzar, M. Freas, P. Abel, A. Fleischman, S. Roy, C. Zorman, J. M. Moran, and J. Melzak, "Evaluation of MEMS materials of construction for implantable medical devices," *Biomaterials*, vol. 23, pp. 2737-2750, 2002.

[60]   M. Gad-el-Hak, Ed., *The MEMS Handbook*. Boca Raton, Florida: CRC Press, 2001.

[61]   P. Luginbuhl, P.-F. Indermuhle, M.-A. Grétillat, F. Willemin, N. F. de Rooij, D. Gerber, G. Gervasio, J.-L. Vuilleumier, D. Twerenbold, M. Düggelin, D. Mathys, and R. Guggenheim, "Femtoliter injector for DNA mass spectrometry," *Sensors and Actuators B: Chemical*, vol. 63, pp. 167-177, 2000.

[62]   X.-Q. Wang, A. Desai, Y.-C. Tai, and T. D. Lee, "Polymer-based electrospray chips for mass spectrometry," In *Proc. 12th International Conference on Microelectromechanical Systems (MEMS '99)*, Orlando, Florida, 1999.

[63]   T. Goldmann and J. S. Gonzalez, "DNA-printing: utilization of a standard inkjet printer for the transfer of nucleic acids to solid supports," *Journal of Biochemical and Biophysical Methods*, vol. 42, no. 3, pp. 105-110, 2000.

[64]   L. Bousse and W. Parce, "Applying Silicon Micromachining to Cellular Metabolism," *IEEE Engineering in Medicine and Biology*, vol. 13, no. 3, pp. 396-401, 1994.

[65]   L. Bousse, "Whole Cell Biosensors," *Sensors and Actuators B: Chemical*, vol. 34, no. 1-3, pp. 270-275, 1996.

[66]   C.-C. Liu and Z. Jin, "Applications of microfabrication and micromachining techniques in biotechnology," *Trends in Biotechnology*, vol. 15, Jun., pp. 213-216, 1997.

[67]   R. A. Braff, "Microbubble Cell Actuator," S.M. Thesis, Cambridge, Massachusetts: Massachusetts Institute of Technology (MIT), 1999.

[68]   R. A. Braff, A. L. Gerhardt, M. Toner, M. L. Gray, and M. A. Schmidt, "A Microbubble Bioparticle Actuator," In *Proc. IEEE Conference on Solid State Sensor, Actuator, and Microsystems Workshop*, Hilton Head, South Carolina, 2002, pp. 138-141.

[69]   R. B. Maxwell, A. L. Gerhardt, M. Toner, M. L. Gray, and M. A. Schmidt, "A Microbubble-Powered Bioparticle Actuator," *Journal of Microelectromechanical Systems*, vol. 12, no. 5, pp. 630-640, 2003.

[70]   R. A. Braff, A. L. Gerhardt, M. Toner, M. L. Gray, and M. A. Schmidt, "Controllable Vapor Microbubbles," *Journal of Microelectromechanical Systems*, Submitted for publication, 2003.

[71]   J. Voldman, M. L. Gray, M. Toner, and M. A. Schmidt, "A Microfabrication-Based Dynamic Array Cytometer," *Analytical Chemistry*, vol. 74, no. 16, pp. 3984-3990, 2002.

[72]   Z. Darzynkiewicz, E. Bedner, X. Li, W. Gorczyca, and M. R. Melamed, "Laser-Scanning Cytometry: A New Instrumentation with Many Applications," *Experimental Cell Research*, vol. 249, no. 1, pp. 1-12, 1999.

[73]   L. A. Kamentsky and M. R. Melamed, "Spectrophotometric Cell Sorter," *Science*, vol. 156, pp. 1364-1365, 1967.

[74]   D. J. Beebe, G. A. Mensing, and G. M. Walker, "Physics and Applications of Microfluidics in Biology," *Annual Review of Biomedical Engineering*, vol. 4, no. 1, pp. 261-286, 2002.

[75]   M. R. Emmert-Buck, R. F. Bonner, P. D. Smith, R. Chuaqui, F., Z. Zhuang, S. R. Goldstein, R. A. Weiss, and L. A. Liotta, "Laser Capture Microdissection," *Science*, vol. 274, pp. 998-1001, 1996.

[76]   M. L. Gray, M. A. Schmidt, M. Toner, J. Voldman, and R. A. Braff, "Microfabrication-based Dynamic Array Cytometer (μDAC)," Alliance for Cellular Signaling (AfCS), Bridging Project Proposal, 1999.

[77]   J. Voldman, "A Microfabricated dielectrophoretic trapping array for cell-based biological assays," PhD Dissertation, Cambridge, Massachusetts: Massachusetts Institute of Technology (MIT), 2001.

[78]   J. Voldman, R. A. Braff, M. Toner, M. L. Gray, and M. A. Schmidt, "Holding Forces of Single-Particle Dielectrophoretic Traps," *Biophysical Journal*, vol. 80, no. 1, pp. 531-541, 2001.

[79]   J. Voldman, R. A. Braff, M. Toner, M. L. Gray, and M. A. Schmidt, "Quantitative design and analysis of single-particle dielectrophoretic traps," In *Proc. Micro Total Analysis Systems (μTAS '00)*, Twente, Netherlands: Kluwer Academic Publishers, 2000, pp. 431-434.

[80]   J. Voldman, M. Toner, M. L. Gray, and M. A. Schmidt, "Design and analysis of extruded quadrupolar dielectrophoretic traps," *Journal of Electrostatics*, vol. 57, pp. 69-90, 2003.

[81]   J. Voldman, M. Toner, M. L. Gray, and M. A. Schmidt, "A dielectrophoresis-based array cytometer," In *Proc. 11th International Conference of Solid-State Sensors, Actuators, and Microsystems (Transducers '01)*, Munich, Germany, 2001, pp. 322-325.

[82]   J. Voldman, M. Toner, M. L. Gray, and M. A. Schmidt, "A Microfabrication-Based Dynamic Array Cytometer," *Analytical Chemistry*, vol. 74, pp. 3984-3990, 2002.

[83]   M. L. Gray, M. A. Schmidt, M. Toner, R. A. Braff, J. Voldman, and A. L. Gerhardt, "Microfabrication-based Dynamic Array Cytometer (μDAC)," Presented at *Proc. Alliance for Cellular Signaling (AfCS) 2nd Annual Meeting*, Dallas, Texas, 2002.

Chapter 2   Theoretical Properties of Microbubbles

The underlying mechanism of μBA-based devices and systems, the thermal vapor microbubble, can be examined with bubble nucleation theory. Understanding the nucleation, growth, and dissipation cycle of a bubble enables the system parameters affecting the cycle to be determined. In turn, the system parameters can be chosen specifically to facilitate preferred nucleation and dissipation characteristics for μBA-based devices and systems.

2.1 Vapor Bubbles

2.1.1 Pool Boiling

For μBA-based devices and systems, a thermal vapor microbubble is formed on a wire, which serves as a heating surface. Referred to as boiling in heat and mass transfer literature, this process of forming a bubble on a heated surface is primarily a convectional process involving heat transfer from liquid to vapor [1, 2]. Industrial applications of boilers form bubbles in at least two distinct contexts — pool boiling and forced-convection boiling. Pool boiling is considered the simpler of the two processes and is the employed method for μBA.

In pool boiling, the plate or wire serving as the heating surface is submerged in stagnant liquid at saturation temperature T_{sat}. Natural convection transfers heat from the heating surface at temperature T_w to the adjacent liquid as long as

$$T_w > T_{sat} \tag{2-1}$$

and the difference between temperatures ΔT is within a few degrees. For μBA-based devices and systems, the liquid is often distilled water or, in the case of optical applications such as Champagne, a fluid with specifically chosen optical characteristics. The wire is present in the liquid at T_{sat}. A voltage is applied to the wire, which acts as resistor, and the wire heats to the temperature T_w.

Figure 2-1 illustrates a typical boiling curve for a horizontal wire heated electrically in a pool of distilled water at atmospheric pressure with a corresponding saturation

temperature of *373.1 K*. The heat flux q is plotted against the excess temperature ΔT. The boiling curve has been divided into five regimes — pure convection, individual bubble, slugs and columns, transition boiling, and stable film boiling.
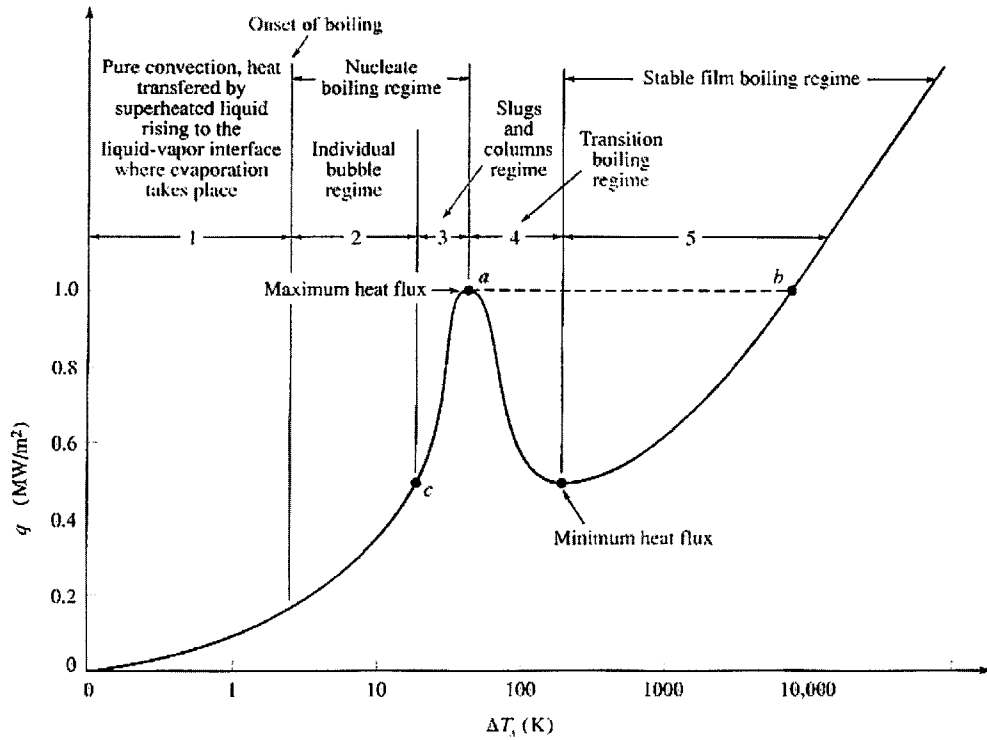
Figure 2-1. *Boiling Regimes [2].*

In [3, 4], we demonstrated operation of a μBA-powered device in the second regime. In the individual bubble regime, q increases rapidly with an increase in surface temperature and formation of bubbles at nucleation sites, nucleate boiling, occurs.

2.1.2 Heterogeneous Nucleation

The bubble formation process either can be homogeneous, occurring in the liquid, or heterogeneous, occurring at the liquid-solid interface. The μBA-devices employ

heterogeneous nucleation where bubbles form at suitable nucleation sites when T_w is greater than T_{sat}. Nucleation occurs in the superheated liquid at defects in the heating surface such as pits, grooves, crevices, and other imperfections created during surface manufacture. Too small to admit liquid because of surface tension, the defects trap small amounts of gas and serve as vapor bubble nucleation sites.

2.1.3   Growth and Dissipation Mechanisms

Liquid adjacent to the newly formed bubble provides thermal energy to vaporize more liquid at the liquid-vapor interface, stimulating bubble growth. The bubble grows rapidly, displacing equivalent volumes of liquid upward. The growth rate decreases dramatically when the top of the bubble extends beyond the layer of superheated liquid, where the thermal energy per unit volume is less. At the point that the bubble extends far into the cooler fluid, more heat is lost by evaporation and convection than is provided by conduction. With the inertial forces depleted, the bubble collapses, and cooler liquid flows into the newly vacated volumes. The microconvection currents flow over the defect effectively resetting the site for another nucleation.
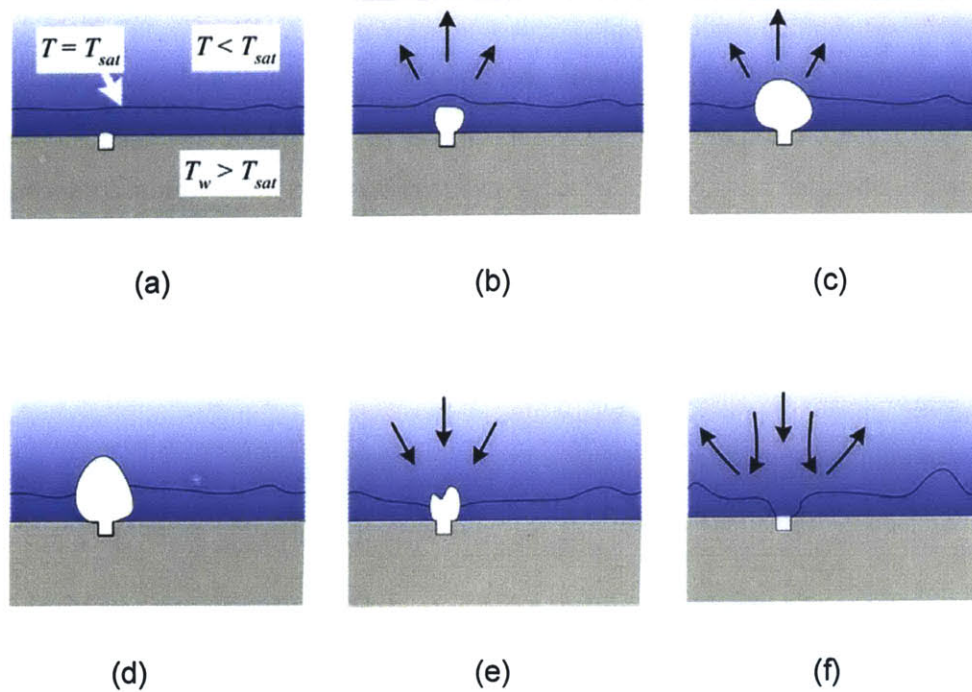
Figure 2-2. *Bubble Cycle and Induced Flow Patterns [2].*

Figure 2-2 illustrates the individual bubble cycle and the microflow patterns induced by the bubble formation, growth, and dissipation in a subcooled boiling liquid. In (a), the heating surface temperature T_w and the temperature of the liquid shrouding the heating surface are greater than T_{sat}. The temperature of the interface between the liquid shrouding the heating surface and the ambient liquid is equal to T_{sat}, and the ambient liquid is at a temperature less than T_{sat}. A small quantity of vapor can be seen trapped at the nucleation site. The bubble grows and is seen in (b) moving the heating liquid and ambient liquid interface upward, as denoted with arrows illustrating the direction of higher temperature liquid motion. The top of the bubble has broken into ambient temperature liquid in (c). After the inertial forces have dissipated (d), bubble collapse begins as cooler liquid flows into the vacated bubble volume. Cool water floods the nucleation site, reinitiating the process [1, 2, 5-7].

2.2 System Parameters Affecting Vapor Bubble Formation

The vapor bubble formation process can be affected by system parameters. By specifically choosing the parameters to employ in μBA-based technology, preferred nucleation and dissipation characteristics can be facilitated. For example, the excess temperature ΔT_x at which vapor bubbles nucleate, depicted on the boiling curve as the interface between the convection and individual boiling regimes, depends on the system. This system variation, often described in the literature with the empirical constant C_{nb}, depends on the combined nature of a heating surface and pool of liquid. Surface texture, wettability, contamination, heater geometry, system pressure, and heat flux application are some of the system parameters that effectively can shift the boiling curve left or right [2, 8]. The shift in the boiling curve corresponds to a physical decrease or increase in the needed ΔT_x, where

$$\Delta T_x \propto C_{nb} \tag{2-2}$$

2.2.1 Surface Properties

According to [9], surface texture is the pattern of a surface that deviates from the nominal surface by structural deviations. Deviations may include repetitive or random roughness, which includes irregularities from the surface production process; waviness, lay, which is the direction of the predominant surface pattern; and flaws, which are unwanted interruptions in the typical topography. The real surface consists of the surface area, or peripheral skin of the surface, that serves as the boundary between the surface and surrounding medium. The standard parameter of real surface roughness is the arithmetic mean roughness value R_a defined as

$$R_a = \frac{1}{L} \int_0^L |Z(y)| dz \tag{2-3}$$

where L is the sampling length. A large R_a corresponds to a large number of nucleation sites at a given temperature, which effectively shifts the boiling curve left. Thus,

$$C_{nb} \propto \frac{1}{R_a}$$ (2-4)

For surfaces with very small R_a values such as virgin MEMS substrates, boiling literature suggests machining cavities to serve as active nucleation sites [10, 11]. A small range of cavity sizes and geometries can form suitable sites. The cavity must have sharp enough edges to trap gases and a radius r_c that corresponds to an active nucleation site radius for the superheat temperature. The surface superheat for a given r_c can be calculated with

$$\Delta T = \frac{2\sigma_{st}T_{sat}}{h_{fg}\rho_v r_c}$$ (2-5)

where σ_{st} is the surface tension of the liquid-vapor interface, h_{fg} is the latent heat of vaporization, and ρ_v is the saturated vapor density. Equation 2-5 has been shown to have reasonable agreement with experimental data for small cavity radii on the order of 10-100 μm [10, 11]. Additionally, cavity depth is a relevant factor, where deeper cavities provide greater seeds for nucleation and are more effective [3, 4].

(a)   (b)   (c)
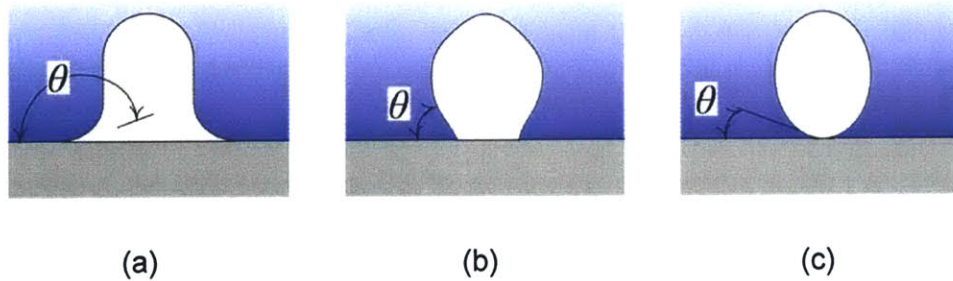
Figure 2-3. *Effect of Surface Wettability on Contact Angle [2].*

Surface wettability is a measure of the contact angle θ between the heating surface and bubble. Figure 2-3 demonstrates this relationship. A non-wetted surface (a) has a very large contact angle. As the surface becomes partially wetted (b), the contact angle decreases. A totally wetted surface (c) has the smallest contact angle.

The heat transfer between the heated surface and the bubble is most efficient when the minimum surface area between the real surface and the bubble is in contact. Thus, a totally wetted surface is the most favorable condition for effective heat transfer, where

$$C_{nb} \propto \frac{1}{\theta} \qquad (2\text{-}6)$$

However, [12] have shown that increasing the wettability of a surface decreases the number of effective nucleation sites. Further, [13] developed a gas-vapor entrapment criterion for cavities present by defect or machined on a surface. A cavity will successfully trap gas and vapor if

$$\theta > \psi_{min} \qquad (2\text{-}7)$$

where ψ_{min} is the angle between the side wall of the cavity and the heating surface as depicted in Figure 2-4.
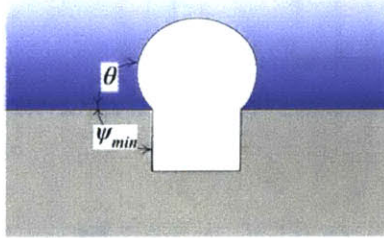
Figure 2-4. *Gas Entrapment Criterion.*

Surface contamination changes the properties of the boiling surface. Slow chemical reactions between the heating surface and dissolved gases or electrolytes in the liquid can lead to corrosion. Deposition of foreign matter from the liquid can deactivate existing nucleation sites, while activating new ones. Further, matter can change the wettability of the surface, often shifting the boiling curve right.

2.2.2 System Properties

Heater geometries can be numerous combinations and permutations of linear and serpentine resistors on horizontal, vertical, or sloped surfaces. Differences between horizontal and vertical heater geometries have been shown to have an effect on heat transfer [8]. However, in plane, the geometric shape of the heating surface is reported to have no appreciable effect on the nucleate boiling mechanism [2].

The pressure P under which the vapor bubble nucleates is related to the incipient superheat [8]. A system at a higher pressure has a lower superheat. Hence,

$$C_{nb} \propto \frac{1}{P} \tag{2-8}$$

The boiling curve can also be affected by the heat flux application. For metal resistors submerged in liquid, an electrical current can be applied in a steady state or transient manner. For exponential times less than one second, [14] have shown that heat flux increases as exponential time decreases.

2.3 References

[1]   A. F. Mills, *Basic Heat and Mass Transfer*. Concord, Massachusetts: Irwin, 1995.

[2]   F. Kreith and M. S. Bohn, *Principles of Heat Transfer*. 5th ed., Saint Paul, Minnesota: West Publishing Company, 1993.

[3]   R. B. Maxwell, A. L. Gerhardt, M. Toner, M. L. Gray, and M. A. Schmidt, "A Microbubble Bioparticle Actuator," *Journal of Microelectromechanical Systems*, Accepted for publication, 2003.

[4]   R. A. Braff, A. L. Gerhardt, M. Toner, M. L. Gray, and M. A. Schmidt, "Controllable Vapor Microbubbles," *Journal of Microelectromechanical Systems*, Submitted for publication, 2003.

[5]   A. F. Mills, *Heat and Mass Transfer*. Concord, Massachusetts: Irwin, 1995.

[6]   A. F. Mills, *Heat Transfer*. Concord, Massachusetts: Irwin, 1992.

[7]   R. Rammig and R. Weiss, "Growth of vapor bubbles from artificial nucleation sites," *Cryogenics*, vol. 31, Jan., pp. 64-69, 1991.

[8]   S. G. Kandlikar, M. Shoji, and V. K. Dhir, Eds., *Handbook of Phase Change: Boiling and Condensation*. Philadelphia, Pennsylvania: Taylor & Francis, 1999.

[9]   M. S. Lou, J. C. Chen, and C. M. Li, "Surface Roughness Prediction Technique for CNC End-Milling," *Journal of Industrial Technology*, vol. 15, no. 1, Nov. - Jan., pp. 2-6, 1998.

[10]   Y. Y. Hsu, "On the Size Range of Active Nucleation Cavities on a Heating Surface," *Journal of Heat Transfer*, Aug., pp. 207-216, 1962.

[11]   S.-S. Hsieh, C.-J. Weng, and J.-J. Chiou, "Nucleate Pool Boiling on Ribbed Surfaces at Low and Moderate Heat Flux," *Journal of Heat Transfer*, vol. 121, May, pp. 376-385, 1999.

[12]   C. H. Wang and V. K. Dhir, "Effect of Surface Wettability on Active Nucleation Site Density During Pool Boiling of Water on a Vertical Surface," *Journal of Heat Transfer*, vol. 115, Aug., pp. 659-669, 1993.

[13]   C. H. Wang and V. K. Dhir, "On the Gas Entrapment and Nucleation Site Density During Pool Boiling of Saturated Water," *Journal of Heat Transfer*, vol. 115, Aug., pp. 670-679, 1993.

[14]   A. Sakurai and M. Shiotsu, "Transient Pool Boiling Heat Transfer, Part 1: Incipience Boiling Superheat," *Journal of Heat Transfer.*, vol. 99, no. 547-553, 1997.

Chapter 3   Flows, Forces, and Fields

For sensitive particulates in fluid beds, numerical and analytical models can be developed to examine the flows, forces, and fields of the system. Critical heat flow issues include heat transfer from the nucleation site at the boundary between substrate and fluid to the fluid containing the particulates. The ejection force on a particulate given a range of realizable geometries, and the electromagnetic field generated from the pulse of current through the resistor will also be examined.

3.1 In-Plane Heat Flow

Two resistor geometries have been shown to effectively nucleate individual thermal vapor microbubbles — linear and serpentine [1-6]. The linear resistor has an in-plane nucleation site formed by narrowing the resistor at its midpoint. The serpentine resistor utilizes an out-of-plane machined cavity nucleation site. Finite difference models of both geometries without nucleation sites were developed to predict the steady state in-plane temperature distribution along the heating elements [5, 6]. Figure 3-1 illustrates top view diagrams of the linear (a) and serpentine (b) geometries. The linear resistor is 100 µm long by 10 µm wide, and the serpentine resistor is 650 µm long by 10 µm wide.

(a)   (b)
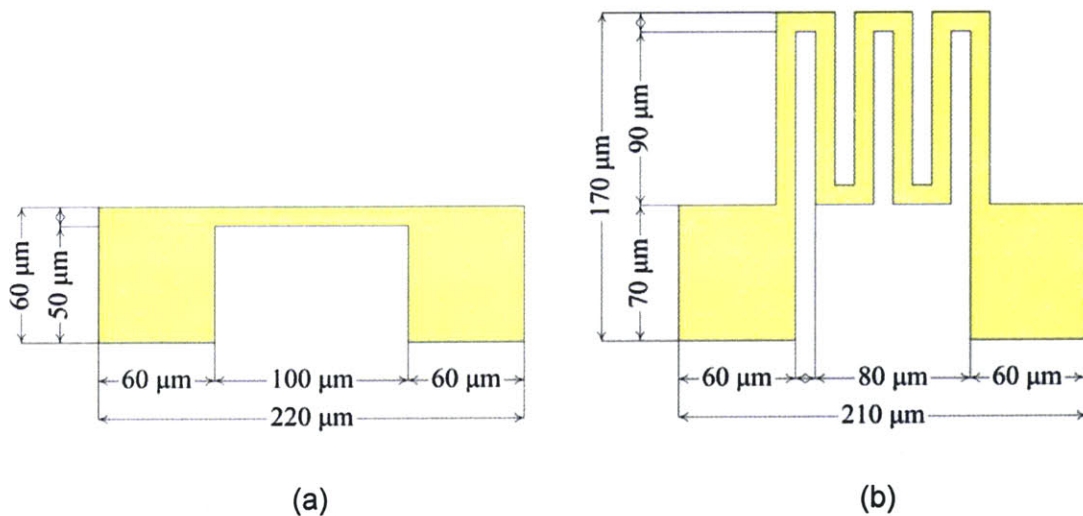
Figure 3-1. *µBA-Based Components.*

3.1.1 Finite-Difference Model of Steady Conduction

To model the temperature distribution across the plane of the resistor, the in-plane temperature distribution, an in-plane steady state conduction model of the geometries shown in Figure 3-1 with a finite control volume Δx by Δy by height Δz is constructed. The finite control volume is illustrated in Figure 3-2 [7]. A coordinate pair (m, n) describes the node, and compass directions designate element faces.
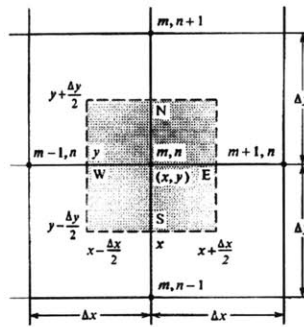
Figure 3-2. *Finite Control Volume [7].*

A rate form of the first law of thermodynamics

$$\rho_m V \frac{dT}{dt} = \dot{Q} + \dot{Q}_v \tag{3-1}$$

applied to the finite control volume reduces to

$$0 = \dot{Q} + \dot{Q}_v \tag{3-2}$$

where ρ_m is the mass density, V is the volume of the system, T is temperature, $\dot{Q}$ is the rate of heat transfer into the system, and $\dot{Q}_v$ is the rate of heat generated within the system. The heat transfer into the system can be separated into the conduction across the four faces — denoted by the cardinal directions N, E, S, and W — of the control volume, where

$$0 = -\dot{Q}_y\big|_N - \dot{Q}_x\big|_E + \dot{Q}_y\big|_S + \dot{Q}_x\big|_W + \Delta \dot{Q}_v \tag{3-3}$$

Following the standard positive sign convention of heat transfer into the system, the heat transfer for each face is

$$\dot{Q}_y\big|_N = -\kappa \frac{\partial T}{\partial y}\bigg|_N \Delta x \Delta z \tag{3-4}$$

$$\dot{Q}_x\big|_E = -\kappa \frac{\partial T}{\partial x}\bigg|_E \Delta y \Delta z \tag{3-5}$$

$$\dot{Q}_y\big|_S = -\kappa \frac{\partial T}{\partial y}\bigg|_S \Delta x \Delta z \tag{3-6}$$

$$\dot{Q}_x\big|_W = -\kappa \frac{\partial T}{\partial x}\bigg|_W \Delta y \Delta z \tag{3-7}$$

If a linear temperature gradient between nodes (m-1, n) and (m,n) is assumed,

$$\frac{\partial T}{\partial y}\bigg|_N \Rightarrow \frac{T_{m,n+1} - T_{m,n}}{\Delta y} \tag{3-8}$$

$$\frac{\partial T}{\partial x}\bigg|_E \Rightarrow \frac{T_{m+1,n} - T_{m,n}}{\Delta x} \tag{3-9}$$

$$\frac{\partial T}{\partial y}\bigg|_S \Rightarrow \frac{T_{m,n} - T_{m,n-1}}{\Delta y} \tag{3-10}$$

$$\frac{\partial T}{\partial x}\bigg|_W \Rightarrow \frac{T_{m,n} - T_{m-1,n}}{\Delta x} \tag{3-11}$$

The heater transfer at each face becomes

$$\dot{Q}_y\big|_N = -\kappa \frac{T_{m,n+1} - T_{m,n}}{\Delta y} \Delta x \Delta z \tag{3-12}$$

$$\dot{Q}_x\big|_E = -\kappa \frac{T_{m+1,n} - T_{m,n}}{\Delta x} \Delta y \Delta z \tag{3-13}$$

$$\dot{Q}_y\big|_S = -\kappa \frac{T_{m,n} - T_{m,n-1}}{\Delta y} \Delta x \Delta z \tag{3-14}$$

$$\dot{Q}_x\big|_W = -\kappa \frac{T_{m,n} - T_{m-1,n}}{\Delta x} \Delta y \Delta z \tag{3-15}$$

where T is the temperature at a node designated with indices denoting x and y locations. κ is the thermal conductivity of the material through which the heat conducts.

The internally generated heat $\Delta \dot{Q}_v$ can be written as

$$\Delta \dot{Q}_v = \tilde{\dot{Q}}_v \Delta x \Delta y \Delta z \qquad (3\text{-}16)$$

where $\tilde{\dot{Q}}_v$ is the volumetric heat source. A boundary condition was determined using the characteristic time equation

$$\delta_t = \sqrt{\alpha_Q t} \qquad (3\text{-}17)$$

where δ_t is the temperature penetration depth, α_Q is the thermal diffusivity of quartz, and t is the characteristic time or duration of heat application. Using the values $\alpha_Q = 5.3 \times 10^{-6}$ m^2/s and $t = 10$ ms yields a δ_t of approximately 230 µm. The boundary condition calculated in Equation 3-17 was one of prescribed temperature, where the temperature at δ_t is 295 K.

Discretizing into 5 µm by 5 µm control areas and letting $\delta_t = 230$ µm, nodal meshes were constructed for both resistor geometries. Figure 3-3 shows the meshes for linear (a) and serpentine (b) resistor geometries, employing intrinsic adiabatic lines of symmetry.

(a) (b)
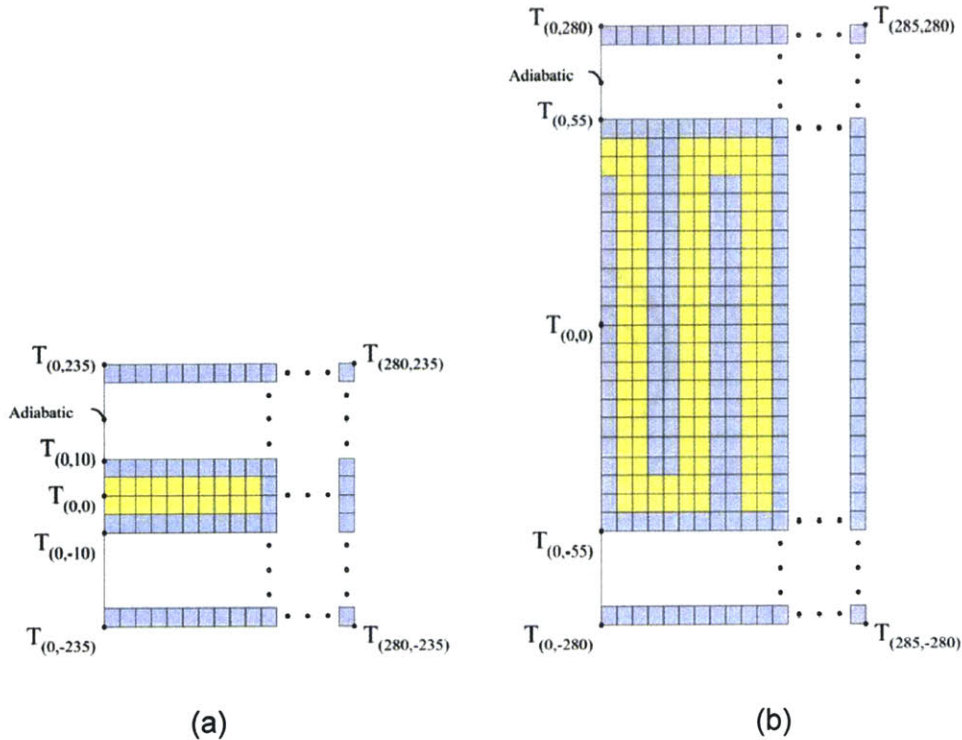
Figure 3-3. *Nodal Meshes for Steady Conduction in Resistor Geometries.*

3.1.2 Numerically Simulated Temperature Distributions

To numerically solve the Poisson equation, a MATLAB® script was written using the equation

$$G \cdot T = P \qquad (3\text{-}18)$$

in vector-matrix notation where G is a diagonally dominant pentdiagonal conductance matrix, T is a temperature matrix, and P is a power matrix [8]. When expanded, the equation becomes

$$
G \cdot
\begin{bmatrix}
T_1 \\
T_2 \\
\vdots \\
T_{n-1} \\
T_n \\
\vdots \\
T_{N-1} \\
T_N
\end{bmatrix}
= \Delta y \Delta x \Delta t \widetilde{P}
\begin{bmatrix}
0 \\
0 \\
\vdots \\
1 \\
1 \\
\vdots \\
0 \\
0
\end{bmatrix}
\qquad (3\text{-}19)
$$

where **G** is of the form

$$
G =
\begin{bmatrix}
1 & 0 & 0 & \cdots & & & 0 \\
-G_{n_Q} & 4G_{n_Q} & -G_{n_Q} & \cdots & 0 & -G_{n_Q} & 0 \\
\vdots & \ddots & \ddots & \ddots & & & \vdots \\
0 & & \ddots & 4G_{n_{P_t}} & -G_{n_{P_t}} & & 0 \\
0 & & & -G_{n_{P_t}} & 4G_{n_{P_t}} & & 0 \\
\vdots & & & & \ddots & \ddots & \ddots & \vdots \\
0 & & -G_{n_Q} & 0 & \cdots & -G_{n_Q} & 4G_{n_Q} & -G_{n_Q} \\
0 & & & & \cdots & 0 & 0 & 1
\end{bmatrix}
\qquad (3\text{-}20)
$$

and $G_{n_{P_t}}$ and G_{n_Q} are thermal conductances of platinum and quartz, respectively, between nodes in direction n : $n = x, y$; T_i is the temperature at node i : $i = 1,2,...,N-1, N$; Δx, Δy, and Δz are the mesh spacings; and $\widetilde{P}$ is the power density.

$G_{n_{P_t}}$ is defined as

$$G_{n_{P_t}} = \frac{1}{R_{n_{P_t}}}$$

(3-21)

where $R_{n_{P_t}}$ is the thermal resistance of platinum between nodes in the n directions and has the values

$$R_{x_{P_t}} = \frac{\Delta x}{\kappa_{P_t} \Delta y \Delta z}$$

(3-22)

$$R_{y_{P_t}} = \frac{\Delta y}{\kappa_{P_t} \Delta x \Delta z}$$

(3-23)

with κ_{P_t} representing the thermal conductivity of platinum. With identical mesh spacing in the n directions, Equation 3-22 and Equation 3-23 become

$$R_{x_{P_t}} = R_{y_{P_t}} = R_{n_{P_t}} = \frac{1}{\kappa_{P_t} \Delta z}$$

(3-24)

With $\Delta z = 1$ kÅ and the $\kappa_{P_t} = 71.6$ W/m·K at 295 K, $G_{n_{P_t}} = 7.2 \times 10^{-6}$ Siemens.

During device fabrication, a thin titanium layer is deposited beneath the thicker layer of platinum for adhesion reasons. The effect of the titanium on the thermal resistance of the metal layer can be calculated. With equal mesh spacing in the n directions, $G_{n_{T_i}}$ is defined as

$$G_{n_{T_i}} = \frac{1}{R_{n_{T_i}}} = \kappa_{T_i} \Delta z$$

(3-25)

where $R_{n_{T_i}}$ is the thermal resistance of titanium between nodes in the n directions and κ_{T_i} is the thermal conductivity of titanium. Using the values $\Delta z = 0.1$ kÅ and $\kappa_{T_i} = 8.4$ W/m·K at 295 K, $G_{n_{T_i}} = 8.4 \times 10^{-8}$ Siemens.

Top View (a)

Cross Section A-A' (b)

Electrical Circuit Analogy (c)
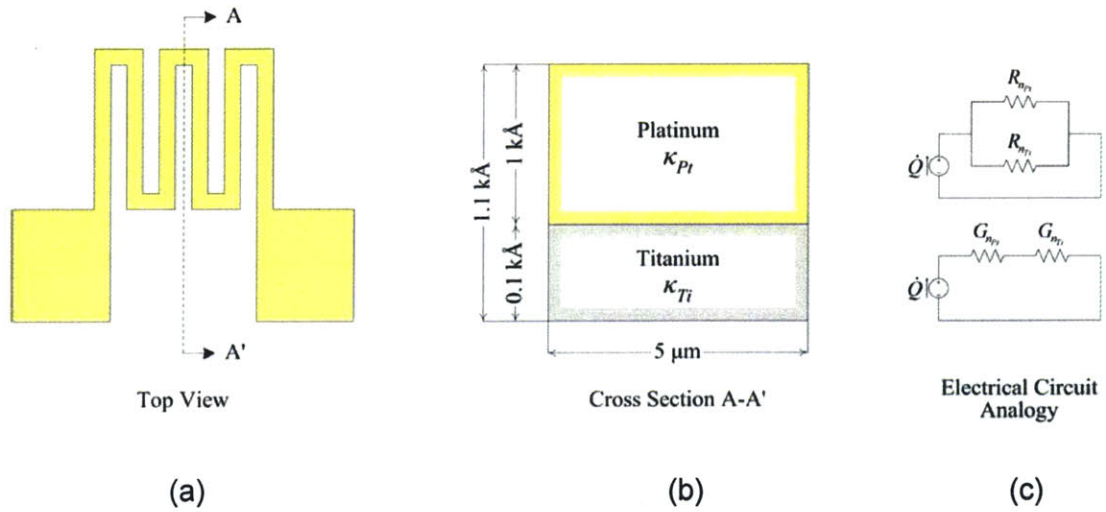
Figure 3-4. *Composite Conduction in Resistor Geometries.*

Figure 3-4 shows the serpentine resistor (a) composed of an upper layer of platinum and a lower layer of titanium. This composite becomes apparent when examining cross section A-A' (b). The parallel thermal paths can be converted to thermal or electrical circuits (c) with resistances or conductances. Summing the individual conductances between nodes in the n directions simplifies the conductance circuit. As

$$G_{n_{Pt}} + G_{n_{Ti}} \cong G_{n_{Pt}} \qquad (3\text{-}26)$$

the effect of the titanium layer can be disregarded for first-order modeling purposes.

Similarly, G_{n_Q} is defined as

$$G_{n_Q} = \frac{1}{R_{n_Q}} = \kappa_Q \Delta z \qquad (3\text{-}27)$$

where R_{n_Q} is the thermal resistance of quartz between nodes in the n directions. κ_Q is the thermal conductivity of quartz. With $\Delta z = 1$ kÅ and $\kappa_Q = 10.4$ W/m·K at 295 K, $G_{n_Q} = 1.04 \times 10^{-6}$ Siemens.

Figure 3-5 illustrates the theoretically calculated steady conduction temperature profile for a linear resistor. For this temperature distribution, the surface is considered to be composed entirely of quartz as per [4, 5]. Meaning, the value of $G_{n_{Pt}}$ in Equation 3-20 is set equal to the value of G_{n_Q}. The temperature profile is symmetric about the resistor and has a maximum value of < 490 K. As 295 K is set as ground — room temperature — for the system, the change in temperature at the resistor is about 200 K.
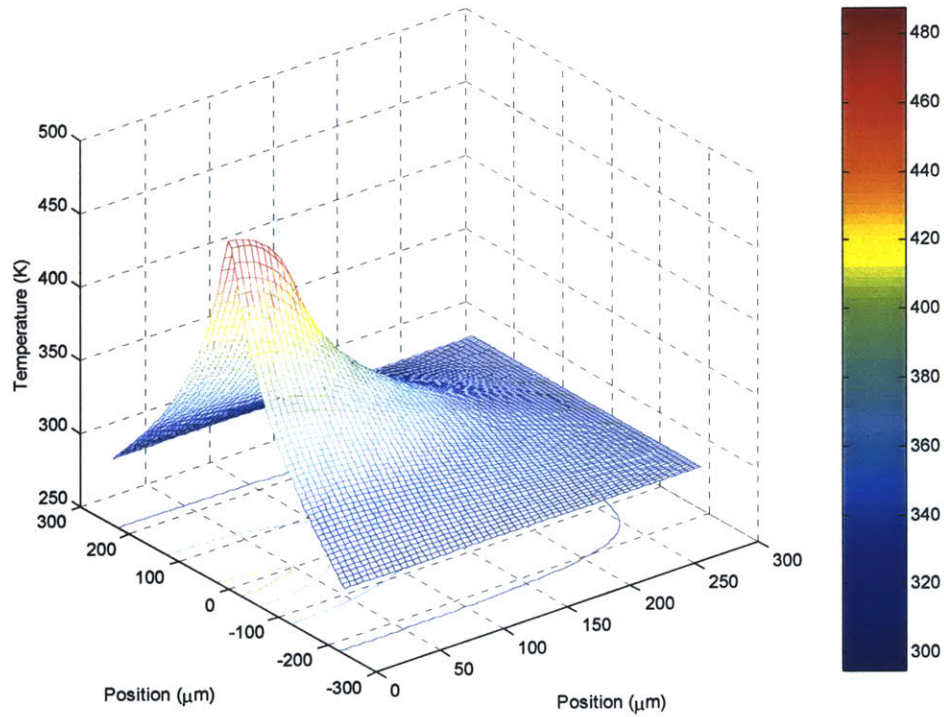
Figure 3-5. *Temperature Distribution in Linear Resistor with $G_{Pt} = G_Q$.*

The results of Figure 3-5 are based on the assumption that $G_{n_{Pt}} = G_{n_Q}$. As

$$G_{n_{Pt}} > G_{n_Q} \gg G_{n_{Ti}} \tag{3-28}$$

a more accurate model can be determined by taking into account $G_{n_{Pt}}$ and G_{n_Q}. The resulting temperature distribution in the linear resistor with $G_{n_{Pt}} \neq G_{n_Q}$ is shown in Figure 3-6. In kind

to Figure 3-5, the temperature profile is symmetric about the resistor. The maximum temperature is less than 470 K, which is about 20 K cooler than the results illustrated in Figure 3-5. The cooler maximum temperature in the model is due to the higher conductivity of platinum. With 295 K set as ground for the system, the change in temperature at the resistor is about 180 K.
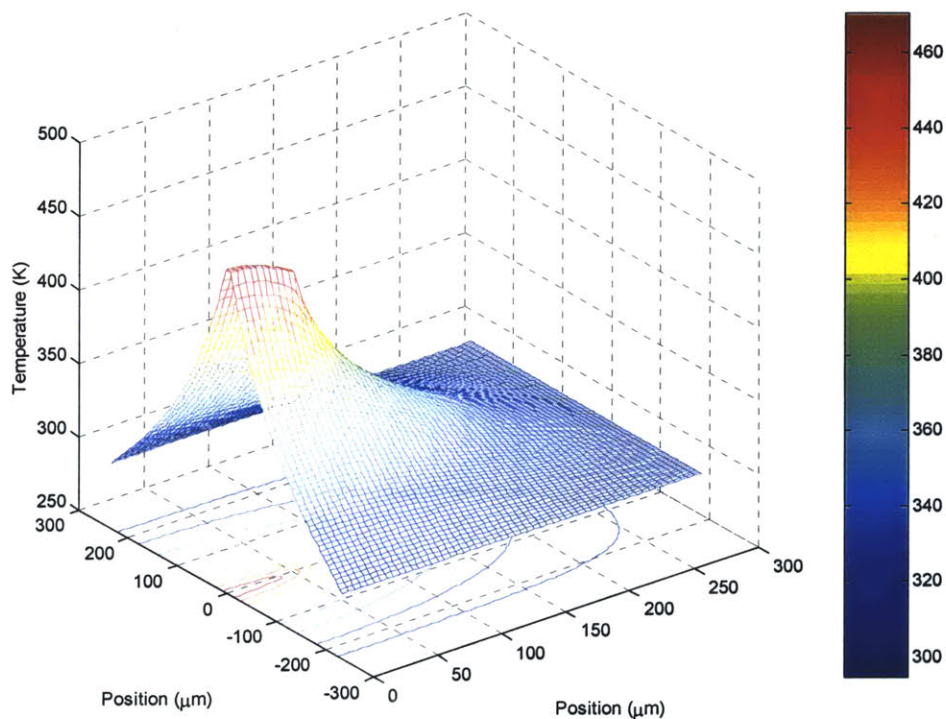
Figure 3-6. *Temperature Distribution in Linear Resistor with $G_{Pt} \neq G_Q$.*

Figure 3-7 depicts the simulated in-plane temperature distribution for a serpentine resistor with a surface modeled to be entirely quartz in composition. Meaning, the value of $G_{n_{Pt}}$ in Equation 3-20 was set equal to the value of G_{n_Q}. The temperature profile is symmetric about the serpentine resistor and has a maximum value of < 1,250 K. As 295 K is set as ground, the change in temperature at the resistor is < 1,000 K.
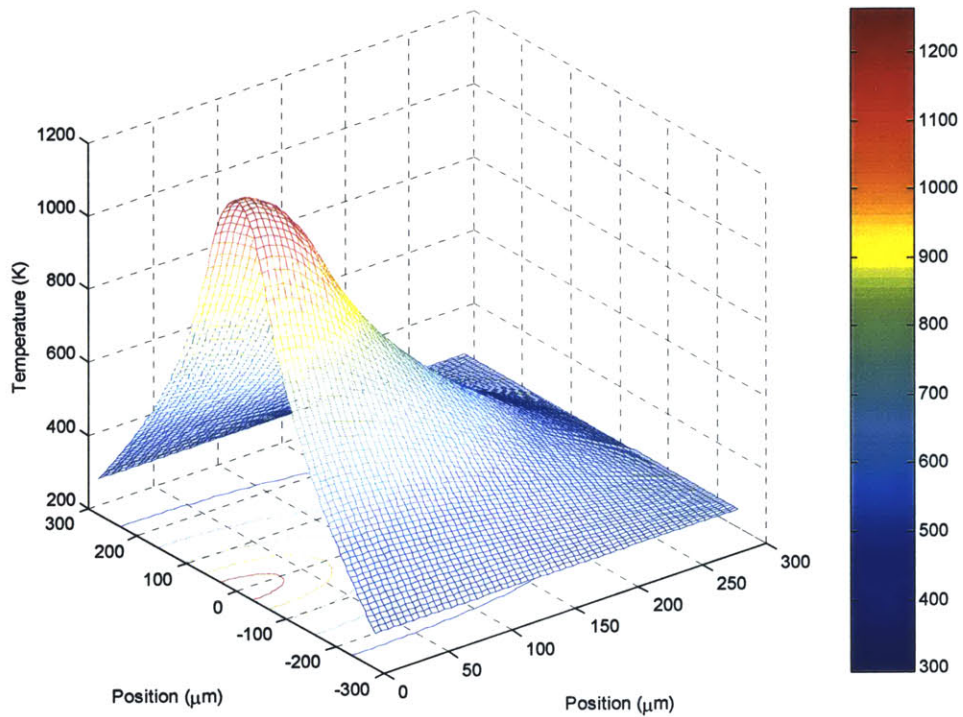
Figure 3-7. *Temperature Distribution in Serpentine Resistor with $G_{Pt} = G_Q$.*

The resulting temperature distribution in the serpentine resistor also is calculated for $G_{n_{Pt}} \neq G_{n_Q}$ and is shown in Figure 3-8. In kind to Figure 3-7, the temperature profile is symmetric about the serpentine resistor. The maximum temperature is less than 1,150 K, which is about 100 K cooler than the results in Figure 3-7. Again, the cooler maximum temperature in the model is due to the higher conductivity of platinum. As 295 K is set as ground for the system, the change in temperature at the resistor is less than 1,000 K.
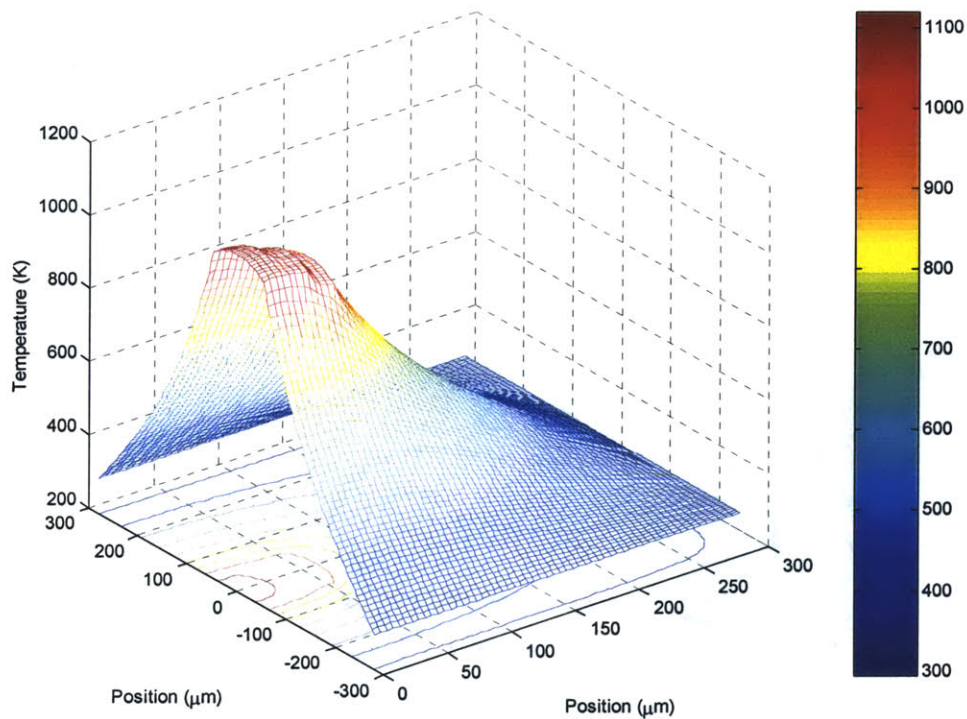
Figure 3-8. *Temperature Distribution in Serpentine Resistor with $G_{Pt} \neq G_Q$.*

Steady conduction, in-plane modeling has demonstrated a variation in temperature distribution according to the resistor geometry, surface area, and resistance of the resistor. The geometrically influenced temperature distribution is most evident in Figure 3-8 where the broader overall shape of the serpentine resistor can be seen in the contour plot. Similarly, the linear resistor is evident in the contour plot in Figure 3-6. The effect of total resistor surface area and resistance is manifest when comparing the maximum temperatures in Figure 3-5 with Figure 3-7 and comparing the maximum temperatures in Figure 3-6 with Figure 3-8. The greater surface area and greater resistance serpentine resistor has a higher temperature peak than the lower-resistance linear resistor due to a constant distribution in power density for each node of the resistor in Equation 3-19.

The results of the in-plane heat flow modeling support the conclusion that both $G_{n_{P_t}}$ and G_{n_Q} are crucial. Including both conductances yields more accurate temperature profiles, as shown in Figure 3-6 and Figure 3-8. However, the in-plane modeling does not take into account heat transfer down into the quartz substrate or up into the body of fluid covering the resistor. Including heat loss to the quartz and fluid would reduce the temperatures in the in-plane profiles for all four figures.

3.2 Out-of-Plane Heat Flow

For heat sensitive particulates in fluid beds, a second critical issue is the heat transfer from the nucleation site to the height of the fluid where the particulates are detained. The out-of-plane heating effect of the thermal microbubble actuation technique on the surrounding fluid and particulates in the fluid bed can be modeled using analytical techniques. Assuming thermal properties are independent of position and temperature and isothermal surfaces be planes parallel to $y = 0$, analytical solutions to the equation of linear conduction of heat can be developed to model the early transient response of the device to the temperature change at the quartz-fluid interface. The derivation and resultant solutions are similar to those presented in [9, 10].

The equation of linear flow of heat is

$$\frac{\partial^2 T}{\partial y^2} - \frac{1}{\alpha}\frac{\partial T}{\partial t} = 0 \tag{3-29}$$

where T is temperature, α is thermal diffusivity of the body, and t is time. First order solutions to Equation 3-29 for the linear and serpentine resistors may be one-dimensional as

$$L >> W \tag{3-30}$$

for both resistors, where L is the length of the resistor and W is the width of the resistor.

Figure 3-9 illustrates top view diagrams of the linear (a) and serpentine (b) geometries and the compound solid (c) to be modeled consisting of the quartz, quartz-fluid interface, and the water (H_2O). The quartz substrate height H_Q is 650 µm. The interface

height H_I is on the order of 1 kÅ. And, the maximum water height H_W, determined by device design, is 300 μm. As

$$H_Q > H_W >> H_I \tag{3-31}$$

the height of the interface can be neglected for first order modeling.
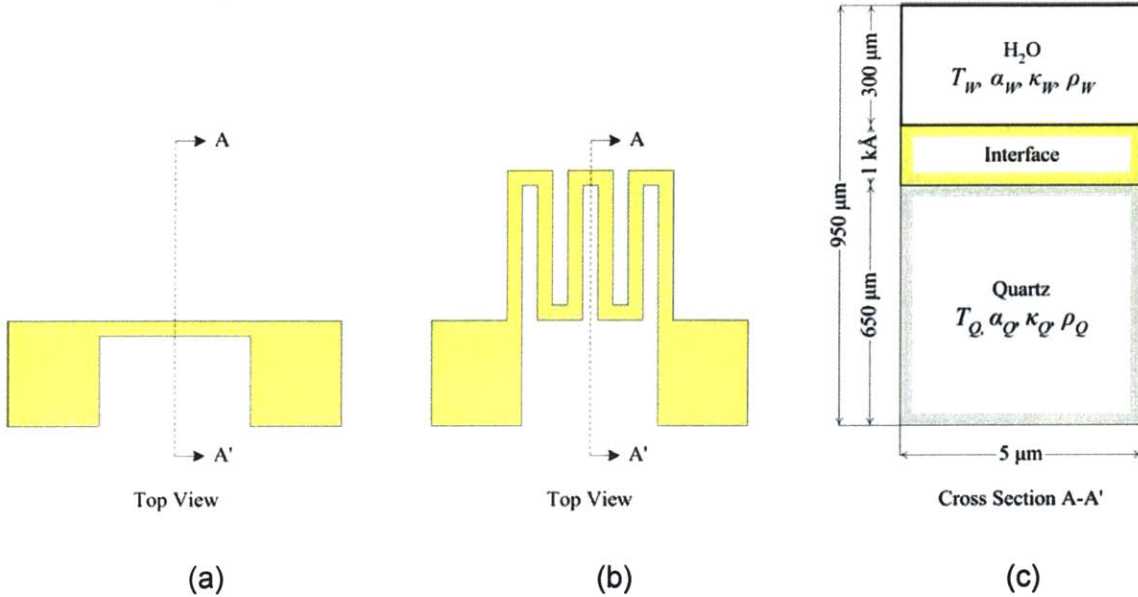
Figure 3-9. *Schematic Diagram for Transient Out-of-Plane Conduction.*

3.2.1 Analytical Model of Transient Conduction

In the infinite region $-\infty < y < \infty$ with the initial condition that

$$T = f(y) : t = 0 \tag{3-32}$$

a particular integral $T_p(y,t)$ which satisfies Equation 3-29 is

$$T_p(y,t) = \frac{1}{\sqrt{\pi \alpha t}} e^{-(y-y')^2/4\alpha t} \tag{3-33}$$

Meaning, when $T_p(y,t)$ is substituted into Equation 3-29 and simplified with

$$\frac{\partial T_p(y,t)}{\partial y} = -\frac{(y-y')}{4\alpha t \sqrt{\pi \alpha t}} e^{-(y-y')^2/4\alpha t} \tag{3-34}$$

$$\frac{\partial^2 T_p(y,t)}{\partial y^2} = -\frac{2\alpha t - y^2 + 2yy' - (y')^2}{8\alpha^2 t^2 \sqrt{\pi \alpha t}} e^{-(y-y')^2/4\alpha t}$$

(3-35)

$$\frac{\partial T_p(y,t)}{\partial t} = -\frac{2\alpha t - y^2 + 2yy' - (y')^2}{8\alpha t^2 \sqrt{\pi \alpha t}} e^{-(y-y')^2/4\alpha t}$$

(3-36)

the result is

$$0 = 0$$

(3-37)

which shows that $T_p(y,t)$ is a particular integral of the equation of linear flow of heat.

The linear combination of any number of integrals is an integral of the linear combination of the functions. Thus, T can be written as a sum of any number of particular integrals, where

$$T = \frac{1}{2\sqrt{\pi \alpha t}} \int_{-\infty}^{\infty} f(y') e^{-(y-y')^2/4\alpha t} dy'$$

(3-38)

If the integral is convergent, T satisfies the equation of linear flow of heat. Setting

$$y' = y + 2\xi\sqrt{\alpha t}$$

(3-39)

Equation 3-39 becomes

$$T = \frac{1}{\sqrt{\pi}} \int_{-\infty}^{\infty} f\{y + 2\xi\sqrt{\alpha t}\} e^{-\xi^2} d\xi$$

(3-40)

Taking the limit as $t \to 0$,

$$f\{y + 2\xi\sqrt{\alpha t}\} = f(y)$$

(3-41)

as long as the function is continuous. The limiting value of the integral then is

$$\frac{1}{\sqrt{\pi}} \int_{-\infty}^{\infty} f(y) e^{-\xi^2} d\xi = f(y)$$

(3-42)

Therefore, the temperature in the infinite solid due to the initial condition is

$$T = \frac{1}{2\sqrt{\pi \alpha t}} \int_{-\infty}^{\infty} f(y') e^{-(y-y')^2/4\alpha t} dy'$$

(3-43)

With the initial condition of Equation 3-29, the solution in the semi-infinite regime where $0 \leq y < \infty$, $y = 0$ may be deduced from that of the infinite solid. For the infinite solid, the assumption was that the solid continued on the negative side of the plane $y = 0$, with initial temperatures for $y' > 0$ of $f(y')$ at y' and $-f(y')$ at $-y'$. Thus, the temperature at the plane $y = 0$ will remain at zero. Therefore,

$$T = \frac{1}{2\sqrt{\pi\alpha t}}\left\{\int_0^\infty f(y')e^{-(y-y')^2/4\alpha t}dy' + \int_{-\infty}^0 \{-f(-y')\}e^{-(y-y')^2/4\alpha t}dy'\right\} \qquad (3\text{-}44)$$

which simplifies to

$$T = \frac{1}{2\sqrt{\pi\alpha t}}\int_0^\infty f(y')\left\{e^{-(y-y')^2/4\alpha t} - e^{-(y-y')^2/4\alpha t}\right\}dy' \qquad (3\text{-}45)$$

Assuming a constant initial temperature T_o and setting

$$y' = y + 2\xi\sqrt{\alpha t} \qquad (3\text{-}46)$$

in the first part of the integral and

$$y' = -y + 2\xi\sqrt{\alpha t} \qquad (3\text{-}47)$$

in the second, Equation 3-44 becomes

$$T = \frac{T_o}{\sqrt{\pi}}\int_{-y/2\sqrt{\alpha t}}^{y/2\sqrt{\alpha t}} e^{-\xi^2} d\xi = \frac{2T_o}{\sqrt{\pi}}\int_0^{y/2\sqrt{\alpha t}} e^{-\xi^2} d\xi \qquad (3\text{-}48)$$

The error function is defined as

$$erf(x) = \frac{2}{\sqrt{\pi}}\int_0^x e^{-\xi^2} d\xi \qquad (3\text{-}49)$$

Letting $x = y/2\sqrt{\alpha t}$

$$T = T_o erf\left\{\frac{y}{2\sqrt{\alpha t}}\right\} \qquad (3\text{-}50)$$

The resulting temperature then depends on the dimensionless parameter

$$\frac{y}{2\sqrt{\alpha t}} \qquad (3\text{-}51)$$

These results can be used to determine temperatures at different times and locations in the semi-infinite solid. Further, the rate of cooling at point y is

$$-\frac{\partial T}{\partial t} = \frac{T_o y}{2\sqrt{\pi \alpha t^3}} e^{-y^2/4\alpha t} \tag{3-52}$$

and the temperature gradient at y is

$$\frac{\partial T}{\partial y} = \frac{T_o y}{\sqrt{\pi \alpha t}} e^{-y^2/4\alpha t} \tag{3-53}$$

For an initial temperature of zero and a boundary $y = 0$ at constant temperature T_o, the solution becomes

$$T = T_o \left\{ 1 - erf \frac{y}{2\sqrt{\alpha t}} \right\} = T_o erfc \frac{y}{2\sqrt{\alpha t}} \tag{3-54}$$

For a situation of constant flux q_c applied to the system per unit time per unit area at $y = 0$, the flux q is defined as

$$q = -\kappa \frac{\partial T}{\partial y} \tag{3-55}$$

where κ is the thermal conductivity of the body. The flux must satisfy a similar differential equation as T where

$$\frac{\partial^2 q}{\partial y^2} - \frac{1}{\kappa} \frac{\partial q}{\partial t} = 0 \tag{3-56}$$

for $y > 0$ and $t > 0$. From Equation 3-54, a solution that satisfies the differential equation is for constant flux of heat q_c at $y = 0$ is

$$q = q_c erfc \frac{y}{2\sqrt{\alpha t}} \tag{3-57}$$

A property of the error function is that

$$i^n erfc(x) = \int_0^\infty i^{n-1} erfc(\xi) \, d\xi \tag{3-58}$$

where

$$i^0 erfc(x) = erfc(x) \tag{3-59}$$

Writing *ierfc(y)* instead of $i^I erfc(y)$ for brevity and integrating by parts yields

$$ierfc(x) = \frac{1}{\sqrt{\pi}} e^{-x^2} - x \cdot erfc(x) \tag{3-60}$$

From Equation 3-57 and by the properties of error functions,

$$T = \frac{q_c}{\kappa} \int_y^\infty erfc \frac{y}{2\sqrt{\alpha t}} dy \tag{3-61}$$

By Equation 3-58, Equation 3-61 becomes

$$T = \frac{2q_c \sqrt{\alpha t}}{\kappa} ierfc \frac{y}{2\sqrt{\alpha t}} \tag{3-62}$$

The solution for the infinite composite solid where the region $y > 0$ is of one substance with properties κ_1 and α_1, $y < 0$ is of another substance with properties κ_2 and α_2, and the plane of separation is $y = 0$ may be deduced from that of the semi-infinite solid. The boundary conditions are that the flux applied to the system must equal the fluxes into the two regions where

$$\kappa_1 \frac{\partial T_1}{\partial y} + \kappa_2 \frac{\partial T_2}{\partial y} = q_c \tag{3-63}$$

and that

$$T_1 = T_2 : y = 0, t > 0 \tag{3-64}$$

where T_I is the temperature in the region $y > 0$ and T_2 is the temperature in the region $y < 0$.

From Equation 3-62,

$$T_1 = \frac{2q_1 \sqrt{\alpha_1 t}}{\kappa_1} ierfc \frac{y}{2\sqrt{\alpha_1 t}} : y > 0 \tag{3-65}$$

$$T_2 = \frac{2q_2 \sqrt{\alpha_2 t}}{\kappa_2} ierfc \frac{y}{2\sqrt{\alpha_2 t}} : y < 0 \tag{3-66}$$

where q_I and q_2 are unknown constants that can be determined by evaluating the boundary conditions at $y = 0$. From the boundary condition in Equation 3-64,

$$T_1\big|_{y=0} = T_2\big|_{y=0} \tag{3-67}$$

Therefore,

$$\frac{q_1\sqrt{\alpha_1}}{\kappa_1} = \frac{q_2\sqrt{\alpha_2}}{\kappa_2} \tag{3-68}$$

Additionally, from the boundary condition in 3-63,

$$q_1 + q_2 = q_c \tag{3-69}$$

Solving for q_1 and q_2 yields the equations

$$q_1 = \frac{q_c\kappa_1\sqrt{\alpha_2}}{\kappa_1\sqrt{\alpha_2} + \kappa_2\sqrt{\alpha_1}} \tag{3-70}$$

$$q_2 = \frac{q_c\kappa_2\sqrt{\alpha_1}}{\kappa_1\sqrt{\alpha_2} + \kappa_2\sqrt{\alpha_1}} \tag{3-71}$$

Substituting into Equation 3-65 and Equation 3-66 results in

$$T_1 = \frac{2q_c\sqrt{\alpha_1\alpha_2 t}}{\kappa_1\sqrt{\alpha_2} + \kappa_2\sqrt{\alpha_1}} ierfc\frac{y}{2\sqrt{\alpha_1 t}} : y > 0 \tag{3-72}$$

$$T_2 = \frac{2q_c\sqrt{\alpha_1\alpha_2 t}}{\kappa_1\sqrt{\alpha_2} + \kappa_2\sqrt{\alpha_1}} ierfc\frac{|y|}{2\sqrt{\alpha_2 t}} : y > 0 \tag{3-73}$$

which solves the equation of linear flow of heat for a compound semi-infinite solid for $y > 0$ and $y < 0$ with an initial temperature of zero and constant heat application q_c at the $y = 0$ plane for $t > 0$. The solutions can be modified to model the regions after the heat flux ceased at time t_q. Given that the heat flux is terminated at t_q, the solutions for $t > t_q$ are

$$T_1 = \frac{2q_c\sqrt{\alpha_1\alpha_2}}{\kappa_1\sqrt{\alpha_2} + \kappa_2\sqrt{\alpha_1}}\left[\sqrt{t} \cdot ierfc\frac{y}{2\sqrt{\alpha_1 t}} - \sqrt{t - t_q} \cdot ierfc\frac{y}{2\sqrt{\alpha_1(t - t_q)}}\right] : y > 0 \tag{3-74}$$

$$T_2 = \frac{2q_c\sqrt{\alpha_1\alpha_2}}{\kappa_1\sqrt{\alpha_2} + \kappa_2\sqrt{\alpha_1}}\left[\sqrt{t} \cdot ierfc\frac{|y|}{2\sqrt{\alpha_2 t}} - \sqrt{t - t_q} \cdot ierfc\frac{|y|}{2\sqrt{\alpha_2(t - t_q)}}\right] : y < 0 \tag{3-75}$$

3.2.2 Analytically Simulated Temperature Distributions

Let the quartz-water interface be at $y = 0$ with quartz at $y < 0$ and water at $y > 0$. The temperature in the quartz is T_Q for $y < 0$, and the temperature of the water is T_W for $y > 0$. At the quartz-water boundary, the temperatures must be the same in both materials, meaning

$$T_Q = T_W : y = 0, t > 0 \tag{3-76}$$

Additionally, the heat flux applied to the system at constant rate q_c per unit time per unit area must equal the sum of the heat fluxes into the quartz and water. Thus,

$$\kappa_Q \frac{\partial T_Q}{\partial y} + \kappa_W \frac{\partial T_W}{\partial y} = q_c \tag{3-77}$$

where κ_Q and κ_W are the thermal conductivities of quartz and water.

The temperature distribution in the quartz-water composite solid may be solved using linear semi-infinite solid theory as long as the conditions of the problem are such that the compound semi-infinite solid assumption is valid. For the quartz to be suitably modeled as a semi-infinite solid,

$$\delta_{t_Q} < H_Q \tag{3-78}$$

where δ_{t_Q} is the penetration depth into the quartz substrate. Similarly, for the water to be accurately modeled in the semi-infinite solid domain,

$$\delta_{t_W} < H_W \tag{3-79}$$

where δ_{t_W} is the temperature penetration depth into water.

According to Equation 3-72 and Equation 3-73, the solutions to the linear conduction of heat in a compound semi-infinite solid for the prescribed boundary conditions are

$$T_Q = \frac{2q_c\sqrt{\alpha_Q\alpha_W t}}{\kappa_Q\sqrt{\alpha_W} + \kappa_W\sqrt{\alpha_Q}} ierfc\frac{|y|}{2\sqrt{\alpha_Q t}} : y < 0 \tag{3-80}$$

$$T_W = \frac{2q_c\sqrt{\alpha_Q\alpha_W t}}{\kappa_Q\sqrt{\alpha_W} + \kappa_W\sqrt{\alpha_Q}} ierfc\frac{y}{2\sqrt{\alpha_W t}} : y > 0 \tag{3-81}$$

The modified solutions to model the quartz-water system at a time after the heat flux ceased at t_q are, per Equation 3-74 and Equation 3-75,

$$T_Q = \frac{2q_c \sqrt{\alpha_Q \alpha_W}}{\kappa_Q \sqrt{\alpha_W} + \kappa_W \sqrt{\alpha_Q}} \left[\sqrt{t} \cdot ierfc \frac{|y|}{2\sqrt{\alpha_Q t}} - \sqrt{t - t_q} \cdot ierfc \frac{|y|}{2\sqrt{\alpha_Q (t - t_q)}} \right] : y < 0 \qquad (3\text{-}82)$$

$$T_W = \frac{2q_c \sqrt{\alpha_Q \alpha_W}}{\kappa_Q \sqrt{\alpha_W} + \kappa_W \sqrt{\alpha_Q}} \left[\sqrt{t} \cdot ierfc \frac{y}{2\sqrt{\alpha_W t}} - \sqrt{t - t_q} \cdot ierfc \frac{y}{2\sqrt{\alpha_W (t - t_q)}} \right] : y > 0 \qquad (3\text{-}83)$$

A MATLAB® script was written to graphically plot the temperature profiles as functions of the distance y from the interface at $y = 0$. The heat flux q_c is defined as

$$q_c = \frac{P}{A_{SA}} \qquad (3\text{-}84)$$

where A_{SA} is the surface area of the resistor. P, the power of the resistor, is defined as

$$P = I^2 R = \frac{V^2}{R} \qquad (3\text{-}85)$$

In Equation 3-85, I is current, V represents the voltage applied to the resistor, and R is the resistance of the resistor. Using typical serpentine resistor values from [2, 4, 6] of $R = 93.63 \ \Omega$, $A_{SA} = 8.53 \times 10^{-9} \, m^2$, and $V = 5$ V, $q_c = 3.13 \times 10^7$ W/m^2.

Figure 3-10 illustrates the calculated analytical solutions to the linear conduction of heat equations. The solutions depict temperature as a function of distance from the interface at $y = 0$ into the quartz for $y < 0$ and into the water for $y > 0$. The solutions were plotted in 1 ms steps to facilitate inspection of the heating of the quartz, water, and interface as a function of time. At 5 ms, the heat application was stopped. Thus, $t_q = 5$ ms.
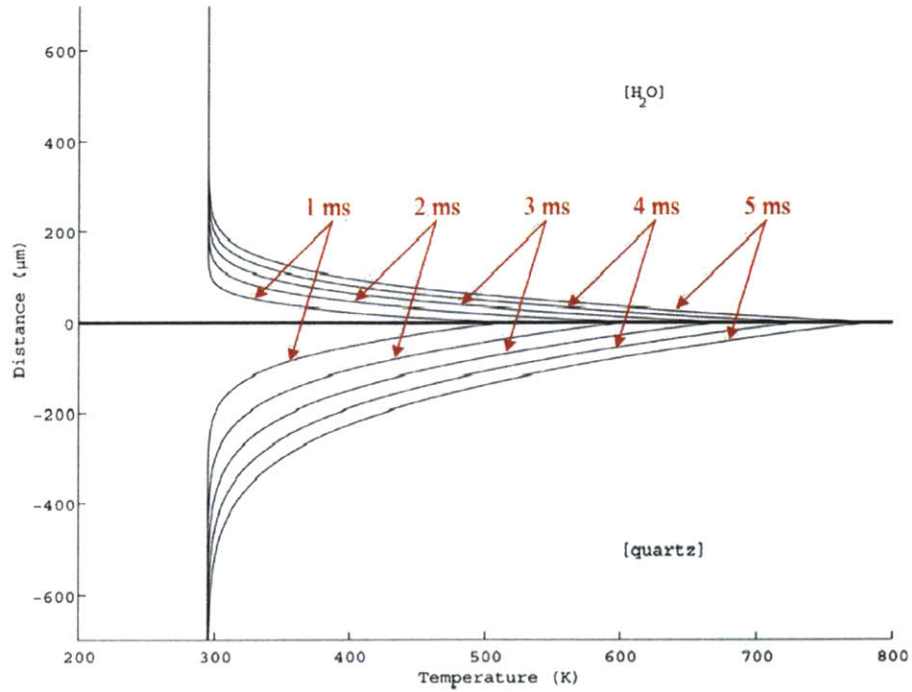
Figure 3-10. *Heating Out-of-Plane Temperature Profile for Fixed q_c.*

Figure 3-11 depicts the cooling of the quartz, water, and interface from the time of cessation of the heat application at 5 ms. The solid line is the temperature profile at 5 ms, as seen in Figure 3-10. The dashed lines represent the cooling temperature profiles in 10 ms steps beginning with $t = 10$ ms. The dotted line represents the temperature profile at 1 s, after the system has cooled for 995 ms.
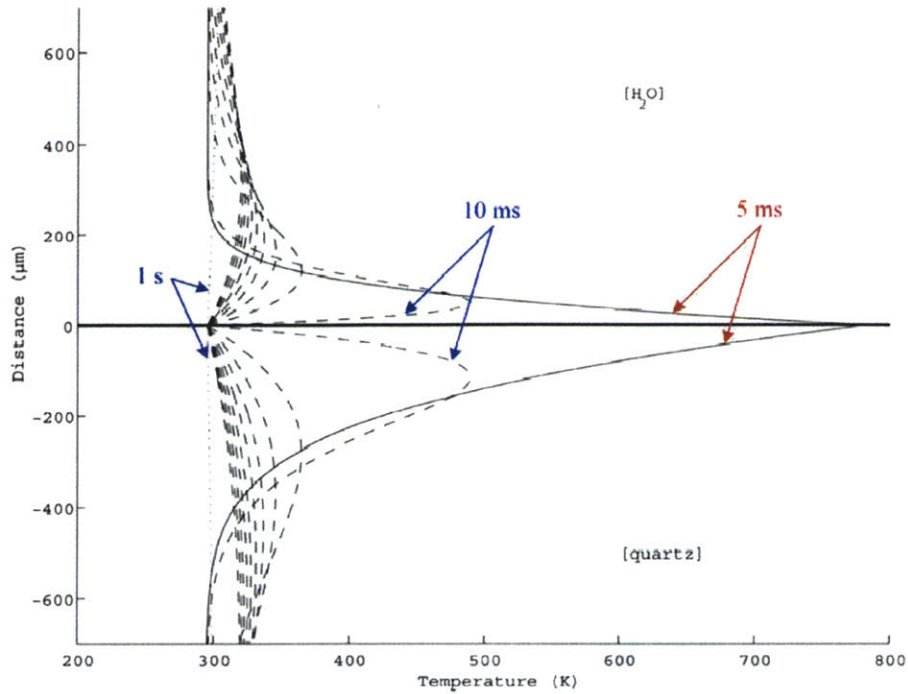
Figure 3-11. *Cooling Out-of-Plane Temperature Profile for Fixed q_c.*

To simulate resistors of varying length, q_c is calculated for resistors of $R = 10 - 100 \, \Omega$ where R is defined as

$$R = \frac{L}{WH} \rho_{e_{Pt}} \tag{3-86}$$

and where $\rho_{e_{Pt}}$ is the electrical resistivity of platinum. Using values $L = 30 - 900 \, \mu m$, $W = 10 \, \mu m$, $H = 1 \, k\text{Å}$, and $\rho_{e_{Pt}} = 10.6 \times 10^8 \, \Omega \cdot m$, resultant values of q_c are $q_c = 3 \times 10^7 - 4 \times 10^9 \, W/m^2$. Table 3-1 contains the calculated analytical solutions to the linear conduction of heat equations for varying q_c. The displayed data corresponds to the change in temperature ΔT at a distance of $y = 300 \, \mu m$, which corresponds to a point in the water $300 \, \mu m$ from the heat source.

Table 3-1. *Change in Temperature at y = 300 μm for Variable q_c.*

Heat Flux (W/m²)	Change in Temperature (ΔT) at 300 μm from Heat Source (K)					
	$t_q = 5$ ms	$t_q = 10$ ms	$t_q = 20$ ms	$t_q = 30$ ms	$t_q = 40$ ms	$t_q = 50$ ms
1 x 10⁷	0.13	3.07	21.68	48.98	79.20	110.14
5 x 10⁷	0.63	15.35	108.42	244.88	396.01	550.69
1 x 10⁸	1.30	30.70	216.80	489.80	792.00	1101.40
5 x 10⁸	6.30	153.50	1084.20	2448.80	3960.10	5509.60
1 x 10⁹	13.00	307.00	2168.00	4898.00	7920.00	11014.00
5 x 10⁹	63.00	1535.00	10842.00	24488.00	39601.00	55096.00

The results of the out-of-plane heat flow modeling demonstrate that the resistor geometry and heat flux application largely affect the temperature change at the particulate. However, in kind to the in-plane modeling, the out-of-plane modeling does not take into account some heat transfers. The heat transfer across the plane of the heat source and along the quartz substrate is neglected. Including this heat loss through the quartz and limiting the length of the resistor would reduce the temperatures in the in-plane profiles for all illustrated pictures and temperature calculations depicted in Table 3-1.

3.3 Ejection Force

Stokes flow, creeping flow, is used to generate a first order calculation of the ejection force applied to the particle and is compared with the force of gravity on the particle [3, 8, 11]. For the presumed Stokes flow to be valid, the regime must be characterized by a Reynolds number $Re < 1$, with

$$Re = \frac{\rho_f \overline{U}}{\mu} = \frac{L\overline{U}}{\mu^*} \tag{3-87}$$

where ρ_m is the mass density of the fluid, L is the characteristic length for the problem, $\overline{U}$ is the mean flow velocity, μ is the viscosity of the fluid, and μ^* is the kinematic viscosity of the fluid. In MEMS devices, $Re < 1$ which means that viscous, rather than inertial, forces tend to dominate. The modeling can be initiated by assuming $Re < 1$, and the validity of the a priori decision can be verified later in the calculation.
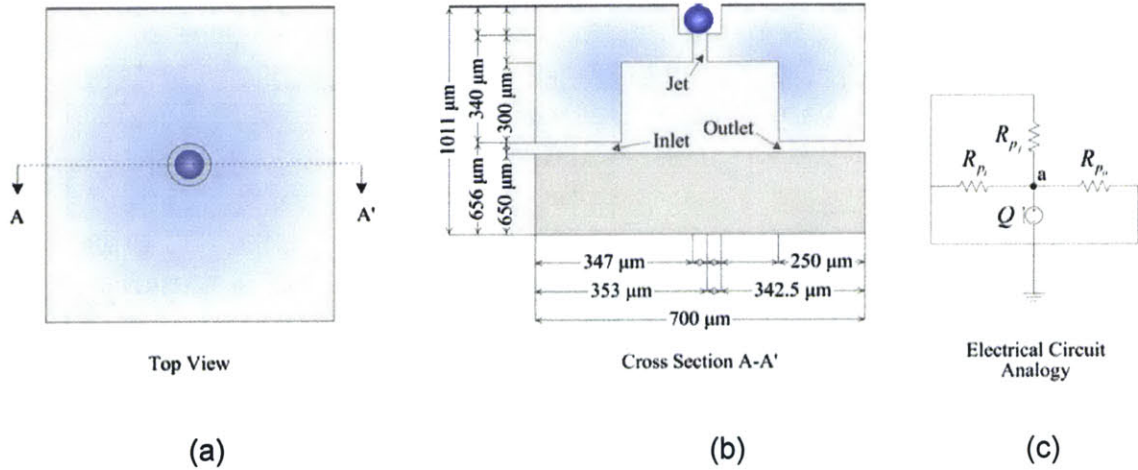
Figure 3-12. *Schematic Diagram for Particle Ejection Force.*

Figure 3-12 illustrates the top view of a cylindrical 15 μm capture well holding a 10 μm particle against the bulk fluid flow (a), the A-A' cross section of the capture well (b), and a simplified electrical circuit analogy of the mechanical effect of the formation of a vapor microbubble assuming no bulk or inlet flow (c). R_{Pois} is a lumped element model of Poiseuille flow and is defined as

$$R_{Pois} = \frac{\Delta P}{L} \tag{3-88}$$

where ΔP is a pressure drop between two points along a pipe of length L. The pressure drop is related to the flow Q by

$$\Delta P = \frac{12\mu L}{WH^3} Q \tag{3-89}$$

where W is the width of the channel and H is the height of the channel. For a circular cross section, the flow rate Q is

$$Q = \frac{\pi \cdot r_{ch}^4}{32\mu} K \tag{3-90}$$

where r_{ch} is the channel radius, and K is the pressure gradient defined as

$$K = \frac{\Delta P}{L} \qquad (3\text{-}91)$$

Solving for R_{Pois} yields

$$R_{Pois} = \frac{32\mu L}{\pi \cdot r_{ch}^{4}} \qquad (3\text{-}92)$$

In Figure 3-12, R_{Pois_j} is the lumped element model of Poiseuille fluidic through the fluidic *jet*. Similarly, $R_{P_{in}}$ and $R_{P_{out}}$ are the lumped models of the fluidic *inlet* and *outlet*, respectively. Inserting the values for the viscosity of water $\mu = 1 \times 10^{-3}$ kg/m·s, the pipe lengths $L_j = 40$ μm and $L_{in} = L_{out} = 250$ μm, and the radii of the pipes $r_i = 3$ μm into Equation 3-92 yields $R_{Pois_j} = 5.0 \times 10^{15}\,\Omega$ and $R_{Pois_{in}} = R_{Pois_{out}} = 3.1 \times 10^{16}\,\Omega$.

As previously discussed in Section 2.1.3, a forming bubble grows rapidly and displaces an equivalent volume of liquid. Thus, for first order modeling purposes, the bubble formation process can be assumed to be a volume displacement process, and the flow rate can be calculated according to

$$Q = \frac{V}{t} \qquad (3\text{-}93)$$

where t is the time required for the bubble to nucleate and grow to volume V.

A serpentine resistor with an etched nucleation site is used to estimate the time in which a given volume of fluid is displaced by the bubble formation. Figure 3-13 contains three frames from a video capture of microbubble formation on a 10 μm wide resistor with an etched cavity.

| $t = 0.16$ s | $t = 0.17$ s | $t = 0.18$ s |
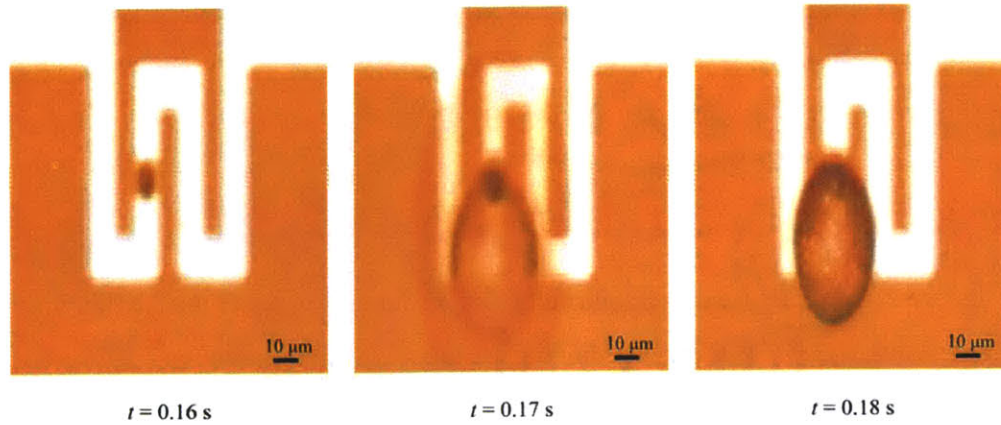
Figure 3-13. *Bubble Formation on Serpentine Resistor with Etched Cavity.*

From the frames, the time required for a microbubble to nucleate and grow to a height of 65 µm and a width of 30 µm is < 0.02 s, where the estimate is limited by the frame rate of the video capture device. Using the volume formula for an ellipsoid,

$$V_e = \frac{4}{3}\pi \frac{LWH}{2} \tag{3-94}$$

the volume of the microbubble V_e, where $L \approx W \approx 30$ µm and $H \approx 65$ µm, is 1.2×10^{-13} m³. Thus, $Q \approx 6 \times 10^{-12}$ m³/s.

The amount of Q moving through the fluidic jet Q_j can be calculated using the circuit diagram (c) in Figure 3-12. By Kirchoff's current law (KCL) at node a, the algebraic sum of currents entering node a is zero.

$$-Q + Q_{in} + Q_{out} + Q_j = 0 \tag{3-95}$$

where Q_{in} and Q_{out} are the amounts of Q moving through the inlet and outlet, respectively. As resistors in parallel have the same voltage drop V across them and $R_{Pois_{in}} = R_{Pois_{out}}$,

$$Q_{in} = Q_{out} \tag{3-96}$$

and

$$V = Q_{in}R_{Pois_{in}} = Q_{out}R_{Pois_{out}} = Q_j R_{Pois_j} \tag{3-97}$$

Combining equations and solving for Q_j gives

$$Q_j = Q \frac{R_{Pois_{in}}}{R_{Pois_{in}} + 2R_{Pois_j}} = Q \frac{R_{Pois_{out}}}{R_{Pois_{out}} + 2R_{Pois_j}} \tag{3-98}$$

Thus, $Q_j = 4.5 \times 10^{-12}$ m³/s.

Using Q_j, the mean flow velocity through the fluidic jet $\overline{U}_j$ can be determined.

$$\overline{U} = \frac{Q}{A_{CS}} \tag{3-99}$$

The cross sectional area A_{CS} calculated using the radius of the fluid jet r_j is

$$A_{CS} = \pi \cdot r^2 \tag{3-100}$$

and has a value of 2.8×10^{-11} m² for $r = 3$ μm. Thus, $\overline{U}_j = 16$ cm/s. The lumped element model of Poiseuille flow is valid as long as the flow has reached a steady-state profile within L. The length required for flow to reach a steady-state profile is the development length L_d and is defined roughly as

$$L_d \approx \frac{D_h}{16} Re_D \tag{3-101}$$

where the hydraulic diameter D_h is the diameter d for a circular tube, and

$$D_h \approx \frac{4 \times area}{perimeter} \tag{3-102}$$

The Reynolds number based on the hydraulic diameter Re_D is

$$Re_D = \frac{2\rho \overline{U} r}{\mu} \tag{3-103}$$

for a circular tube. With the density of water $\rho_W = 1 \times 10^3$ kg/m³, Re_D for the fluidic jet is $0.96 < 1$; thus, the a priori assumption of Stokes flow is valid. Further, L_d is 0.36 μm $< L$, which validates the Poiseuille lumped modeling.

In the Stokes flow regime, the ejection force on the particle F_e is

$$F_{eject} = 6\pi\mu\overline{U} r_p \tag{3-104}$$

Assuming a 5 μm particle radius, the ejection force from the fluidic jet F_{eject_j} = 15 nN. Similarly, the force due to gravity on the particle F_{g_j} is

$$F_g = (\rho_p - \rho_f)g\frac{4\pi r_p^3}{3} \tag{3-105}$$

where the density of the particle ρ_p = 1.062 × 10³ kg/m³ for fluorescent polymer beads (Bangs Laboratories, Inc., Fishers, IN) and acceleration due to gravity g = 9.8 m/s². Thus, F_{g_j} = 0.3 pN.

3.4 Electromagnetic Field

Particle ejection in the thermal microbubble system is accomplished using a resistor of linear or serpentine geometry to nucleate a microbubble. A voltage is applied across the resistor, which generates a current through the resistor. In turn, the current through the resistor produces a magnetic field. A first-order calculation of the induced magnetic field can be modeled with the Biot-Savart law [12, 13] assuming that the resistor is a long straight wire.

In vector form, the law of Biot and Savart is

$$d\mathbf{B} = \frac{\mu_o}{4\pi}\frac{i\,d\mathbf{s}\times\mathbf{r_P}}{r_P^3} \tag{3-106}$$

where $\mathbf{B}$ is the magnetic field vector, μ_o is the permeability constant, i is the current, $d\mathbf{s}$ is a differential vector representing a segment of the resistor, $\mathbf{r_P}$ is a vector that points from the current element to the point of observation P, and r_P is the distance from a current element in the wire to P. The magnitude of the Bio-Savart law is expressed as

$$dB = \frac{\mu_o}{4\pi}\frac{i\,ds\,\sin\theta}{r_P^2} \tag{3-107}$$

where θ is the angle between the vectors $d\mathbf{s}$ and $\mathbf{r}$. θ is related to s, r_P, and r, the radial distance between the wire and P, by

$$\sin\theta = \sin(\pi - \theta) = \frac{r}{\sqrt{s^2 + r^2}} \tag{3-108}$$

and

84

$$r_p = \sqrt{s^2 + r^2} \tag{3-109}$$

The total magnetic field can be found by integrating Equation 3-107 from $-\infty$ to ∞ or by taking twice the integral from 0 to ∞. Choosing z to be the variable of integration that runs along the wire,

$$B = \int dB = \frac{\mu_o i}{4\pi} \int_{-\infty}^{\infty} \frac{\sin\theta}{r_p^2} dz = \frac{\mu_o i}{2\pi} \int_0^{\infty} \frac{\sin\theta}{r_p^2} dz \tag{3-110}$$

With substitutions from Equation 3-108 and Equation 3-109, the integrand becomes

$$B = \frac{\mu_o i}{2\pi} \int_0^{\infty} \frac{r}{\left(z^2 + r^2\right)^{3/2}} dz = \frac{\mu_o i}{2\pi r} \left. \frac{z}{\left(z^2 + r^2\right)^{1/2}} \right|_0^{\infty} = \frac{\mu_o i}{2\pi r} \tag{3-111}$$

Using the value $\mu_o = 1.26 \times 10^{-6}$ H/m, a MATLAB® script was written to graphically plot the B as a function of r. The current i is defined as

$$i = \frac{V}{R} \tag{3-112}$$

where V is the voltage applied to the resistor and R is the resistance of the resistor. With $V = 5$ V and resistor values of $R_L = 10\ \Omega$ for a linear resistor and $R_S = 100\ \Omega$ for a serpentine resistor, $i_L = 500$ mA and $i_S = 50$ mA.
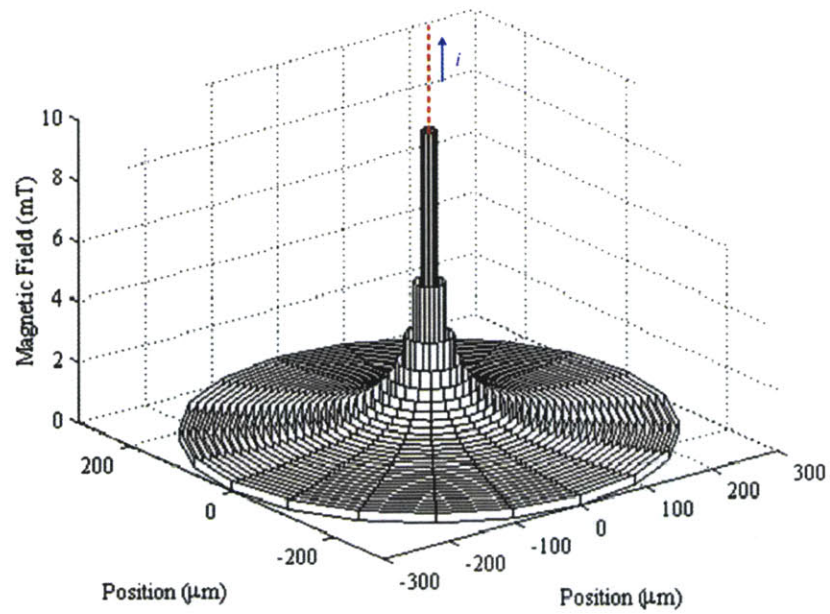
Figure 3-14. *Magnetic Field Lines and Amplitudes for R = 10 Ω.*
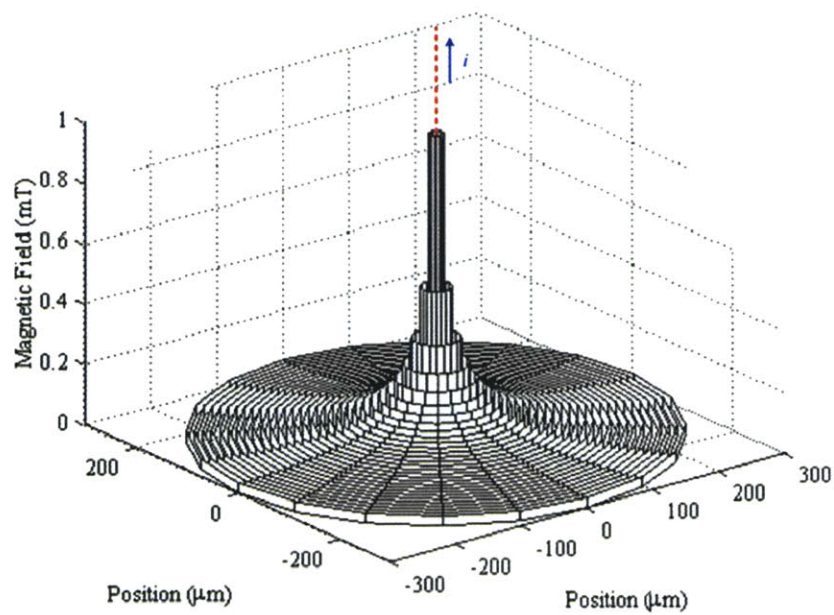
Figure 3-15. *Magnetic Field Lines and Amplitudes for R = 100 Ω.*

Figure 3-14 and Figure 3-15 illustrate the magnetic field lines and amplitudes induced by current through a 10 Ω and 100 Ω resistor, respectively. The resistor, modeled as a wire and represented as a dotted line in the diagram, is situated at (0,0) and runs in the z direction. Current moving in the $-z$ to $+z$ direction induces counter-clockwise magnetic field lines. At 300 μm, the magnitude of B for the 10 Ω resistor is 334.2 μT, and the magnitude of B for the 100 Ω resistor is 33.4 μT.

3.5 Discussion

Critical system issues, especially for sensitive fluid bed particulates, are examines with numerical and analytical models for flows, forces, and fields. The numerically modeled in-plane temperature distributions across the resistor demonstrate temperature profile variation according to resistor geometry, surface area, and total resistance. With constant heat flux per finite control volume, greater surface area resistors result in higher peak temperatures. As the thickness of the resistor is constant between the linear and serpentine geometries, a greater surface area also corresponds to a greater resistor resistance. Changes in temperature due to an input heat flux for the linear resistor are about 100 K, while the temperature change for the serpentine resistor is about 1,000 K.

As the in-plane temperature profiles are two-dimensional, the analytical one-dimensional out-of-plane model completes the sketch of the three-dimensional temperature distribution profiles. Out-of-plane models further support the result that temperature profile at the resistor and at the location where the particulate is held are affected by resistor geometry. Heat flux application also is shown to affect the temperature profile.

In-plane heat flow modeling examines two-dimensions, and out-of-plane modeling investigates the third dimension. The two models yield temperature distributions of the same order of magnitude. Combining the two models into a single three-dimensional model would reduce the illustrated temperature profiles, as heat loss in all dimensions would be included. A three-dimensional model further would enable more precise boundary conditions, such as the bottom of the quartz substrate, and the possibility of including heat loss through the leads.

The ejection force on a particle with 5 μm radius due to a microbubble that displaces 120 pL of fluid is three orders of magnitude greater than the force due to gravity. The ejection force can be modified by affecting the size of the bubble formed in the system, a process that is explained in Chapter 5 and Chapter 6. This modeling suggests that the actuation technique is suitable for ejecting a range of particle sizes with forces that are appropriate for the sensitivity of a particle in a specific application. A model examining the forces for a varying range of fluidic volumes could help determine specific volumes needed for particular ejection applications.

Magnetic force calculations show that the magnetic field due to a constant current applied to a 10 Ω and 100 Ω resistor has strength of about 300 μT and 30 μT, respectively. Including the pulse duration in the calculations would decrease the time-dependent strength of the magnetic field, as no magnetic field is induced when current flow is zero. For reference, the strength of the Earth's magnetic field is about 40 μT [13]. Thus, the strengths of the magnetic fields due to the ejection mechanism are similar to the strength of the magnetic field of the Earth. Future models also could examine the strength of electric fields induced in the ejection process.

3.6 References

[1]   P. Deng, Y.-K. Lee, and P. Cheng, "Design and Characterization of a Micro Single Bubble Actuator," In *Proc. 12th International Conference on Solid State Sensors, Acutuators, and Microsystems (Transducers '03)*, vol. 1, Boston, Massachusetts, 2003, pp. 647-650.

[2]   R. A. Braff, A. L. Gerhardt, M. Toner, M. L. Gray, and M. A. Schmidt, "A Microbubble Bioparticle Actuator," In *Proc. IEEE Conference on Solid State Sensor, Actuator, and Microsystems Workshop*, Hilton Head, South Carolina, 2002, pp. 138-141.

[3]   R. A. Braff, "Microbubble Cell Actuator," S.M. Thesis, Cambridge, Massachusetts: Massachusetts Institute of Technology (MIT), 1999.

[4]   R. A. Braff, A. L. Gerhardt, M. Toner, M. L. Gray, and M. A. Schmidt, "Controllable Vapor Microbubbles," *Journal of Microelectromechanical Systems*, Submitted for publication, 2003.

[5]   R. B. Maxwell, "Controllable Vapor Microbubble for Use in Bioparticle Actuation," PhD Dissertation, Cambridge, Massachusetts: Massachusetts Institute of Technology (MIT), 2003.

[6]   R. B. Maxwell, A. L. Gerhardt, M. Toner, M. L. Gray, and M. A. Schmidt, "A Microbubble Bioparticle Actuator," *Journal of Microelectromechanical Systems*, Accepted for publication, 2003.

[7]   A. F. Mills, *Basic Heat and Mass Transfer*. Concord, Massachusetts: Irwin, 1995.

[8]   S. D. Senturia, *Microsystem Design*. Norwell, Massachusetts: Kluwer Academic Publishers, 2001.

[9]   H. S. Carslaw and J. C. Jaeger, *Conduction of Heat in Solids*. 2nd ed., Amen House, London: Oxford University Press, 1959.

[10]   F. Kreith and M. S. Bohn, *Principles of Heat Transfer*. 5th ed., Saint Paul, Minnesota: West Publishing Company, 1993.

[11]   J. A. Fay, *Introduction to Fluid Mechanics*. Cambridge, Massachusetts: MIT Press, 1994.

[12]   D. Halliday, R. Resnick, and J. Walker, *Fundamentals of Physics*. New York, New York: John Wiley & Sons, Inc., 1993.

[13]   D. Halliday, R. Resnick, and K. S. Krane, *Physics: Part Two*. New York, New York: John Wiley & Sons, Inc., 1992.

Chapter 4   Design and Manufacture

The goal of an actuator is to move or control an element such as a shutter for droplet dispensing, a tunable infrared (IR) filter, or a particulate in a fluid bed. While the overarching mechanism of the devices can be classified as actuation, the execution of device design and manufacture can vary dramatically depending on the application. Limning device specifications for the μDAC project and incorporating more general μBA-based specifications enable the design of system architecture and corresponding fabrication procedures.

4.1 Specifications

The μBA-based device is engineered to yield information for further design iterations and to initiate movement of the device concept from the realms of academia toward industry applications and products. In the process of matching market opportunities with μBA technology development, fundamental parameters of device design and operation for the μDAC project and other industry applications can be delineated. Critical design parameters can be incorporated in the design. After understanding the ranges of device performance, a more market-driven design can be tailored to meet the specific needs of a given industry application [1].

4.1.1 Processing Time

Many industries require high throughput or minimal processing time of large populations of particulates. The rate at which particles are passively filtered or actively sorted can affect the cost of the process, with longer time periods corresponding to greater cost. In addition to cost, the processing time can largely determine the development rate of a new product. For example, screening applications of compounds for drug therapies are pushing the maximum high-throughput rate in an effort to speed the process between research of a compound and a new drug therapy. High throughput is crucial to signaling assays [2]. Many assays must be completed in entirety within the first fifteen minutes. At

times greater than fifteen minutes, cells can enter the transcription domain, at which point the quantitative data is no longer relevant to the desired experiment.

In the μBA-driven realization of the μDAC project, the device functions as a microfabrication-based dynamic array cytometer. Thus, for an industry setting, the μBA-driven device will need to function with a throughput similar to or greater than current flow cytometers to be a viable solution. According to [2], laboratories today have 20-50 ms delays between measurements of individual cells in a population on the order of 10,000 cells. The current sorting rate is about 2,000 cells/min. Thus, a crucial design parameter for the device is a processing time on the order of 20 ms per particle in an electrically addressed μBA-driven array that handles on the order of 10,000 cells in approximately 5 minutes.

4.1.2 Optical Interface

Whether run data is acquired automatically or manually, the optical interface of the device determines the type of data that can be collected. Previous iterations of the μBA- and DEP-driven devices allowed for optical observation from the positive vertical axis, facilitating the collection of magnitude information in cellular applications. Adding the second vertical axis as a valid viewing port additionally would enable phase data to be collected.

For large scale arrays on the order of 10,000 sites, the optical interface also affects the number of sites that can be viewed at a time. Thus, a cycle of data would be collected by viewing, in series or parallel, a set of sites until all of the sites have been viewed. Thus, the number of cycles required to collect the data over the array is one of the factors affecting the processing time.

4.1.3 Reliability and Robustness

Inherent in the μBA-based device is a non-mechanical mechanism for capturing and sorting particulates. A non-mechanical actuation mechanism is not prone to fatigue and failure like its mechanical counterpart. The non-mechanical composition of the device means that robustness is inherent in the bubble-based technology. Further, previous iterations have shown that bubble nucleation is a robust process, yielding for a given power input a microbubble as the output. With careful material selection, a novel design, and several iterations to determine the optimum configurations, devices have the potential to be manufactured to achieve industry-level reliability and robustness application specifications.

4.1.4 Ease of Operation

An electrically addressed array or sites can be controlled with a physical interface box for manual optical viewing and control or by a computer program such as LabVIEW (National Instruments, Austin, TX) with automated capture and sort routines. The addressable array allows 200 inputs to control 10,000 sites individually. Minimizing the number of components a user must interface while maximizing the data and information available will yield a product that is user-friendly and straightforward considering the quantity of information available. Further, to make the devices more appropriate to industry applications, different user interfaces can be designed to meet the needs, jargon, and expectations of the industry. Thus, the design specification is for an intrinsically adaptable user interface. The ease of operation for the current iteration will involve meeting the needs of the researcher to gather information about the technology and how to adapt the technology in an effort to build an industry-applicable device.

4.1.5 Cost Effectiveness

To maximize cost effectiveness, the device can be designed to have components constructed in parallel methods and with system partitioning, separating components that would need to be replaced more frequently from those that may survive the usefulness of the device. The system partitioning can be made by creating a chip that is able to be cleaned or

replaced between uses and a set of separate control electronics. For non-biological industry applications, the chip on which the sorting takes place could be cleaned between uses with a neutral medium. After a series of uses, the chip then would be replaced. For biological applications, in general, the chip would be replaced between each assay to ensure no cross-contamination of particles.

4.1.6 Compatibility

Tight application compatibility constraints exist for fragile or biological particulates. For a μBA-driven device, first-order models of in-plane and out-of-plane thermal radiation, particle ejection forces, and electromagnetic fields are examined in Chapter 3. In addition to ensuring the operation of the device does not negatively affect the particles, the device itself must be constructed with materials that are biocompatible if the device is to be utilized in biological applications.

4.2 System Architecture

With design challenges and considerations delineated, a system architecture construction focus is to maximize the usage of commercially available components without sacrificing the desired performance of the μBA-driven device. The resultant architecture consists of microfabricated components, custom electronics, electronics, and packaging. The whole system is shown in Figure 4-1.
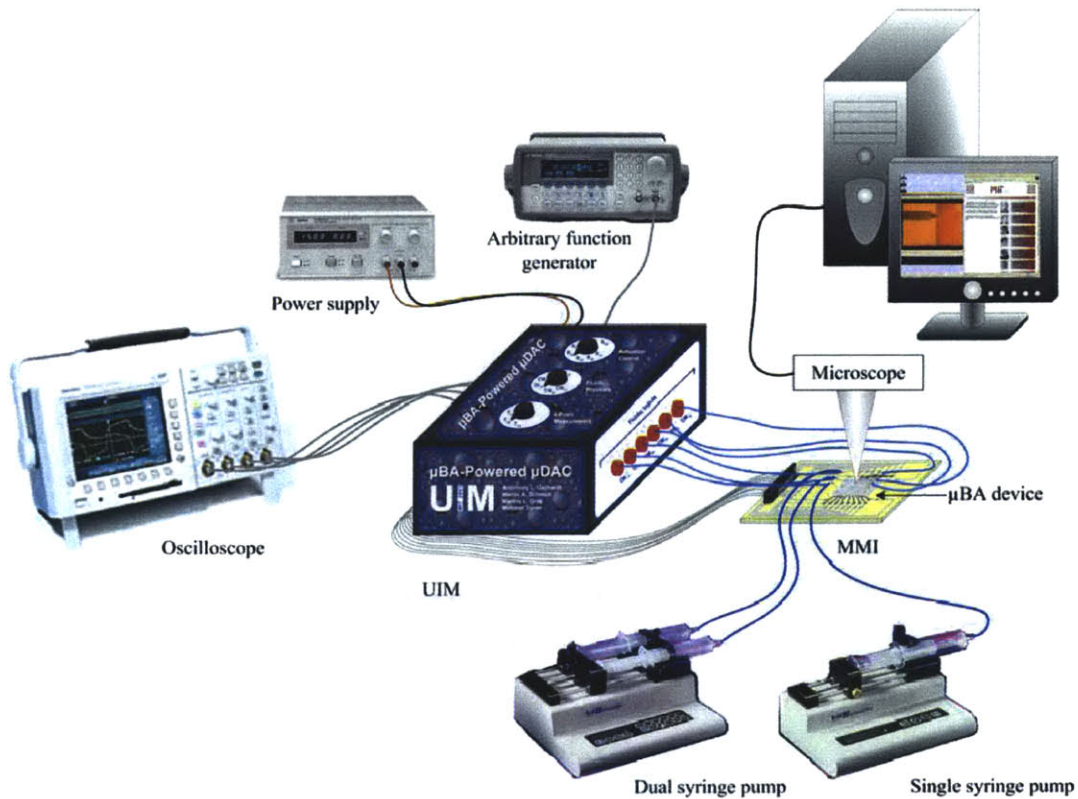
Figure 4-1. *System Architecture.*

The heart of the system is the assembled µBA-based device, which consists of several components including a platinum heating electrode (PHE) chip or test structure chip (TSC) and a fluidic system. The µBA-based device has electrical and fluidic inputs and outputs and an optical output. The electrical outputs are soldered to the macro-to-micro interface (MMI), which has a twenty-five pin female D-Sub mount output (3M, Maplewood, MN). A male-female D-Sub cable (3M, Maplewood, MN) connects the MMI to the user interface module (UIM). The UIM is powered by a direct current (DC) power supply (E3610A, Agilent Technologies, Englewood, CO) and has a signal input from an arbitrary function generator (33220A, Agilent Technologies, Englewood, CO). An oscilloscope (TDS 210, Tektronix, Beaverton, OR) is used to monitor the signal input to the system and various outputs of the UIM.

A single (KDS101, KD Scientific, New Hope, PA) and a dual (KDS210, KD Scientific, New Hope, PA) syringe pump serve as flow sources for the μBA-based device. Fluidic connections from the device to the UIM allow for pressure monitoring, and connections from the device to one or multiple vials (not shown) fluidically ground the system. The optical interface is a Microzoom microscope (Wentworth Labs, Brooksfield, CT) on a semiconductor probe station outfitted with digital video camera (Panasonic 5000, Panasonic, Bridgeport, NJ).

4.2.1 Platinum Heating Electrode Chip

Based on previous iterations of the non-arrayed form of the device, the PHE chip design purpose is to facilitate bubble nucleation. Each chip is 3 cm by 2 cm. The design consists of two columns of serpentine resistors spaced such that two rows, four resistors, can be seen under the microscope objective at any given time. Figure 3.2 depicts an illustration of a PHE chip (a), a zoomed screen shot of the mask where controlled nucleation occurs at the individual resistors (b), and an individual nucleation site on the mask (c). A 6 μm by 6 μm square nucleation cavity is located at the vertical line of symmetry at the vertical midpoint for each resistor. Cavity dimension and location are based on previous research iterations of a single-site nucleation device [3-5].

(a)   (b)   (c)
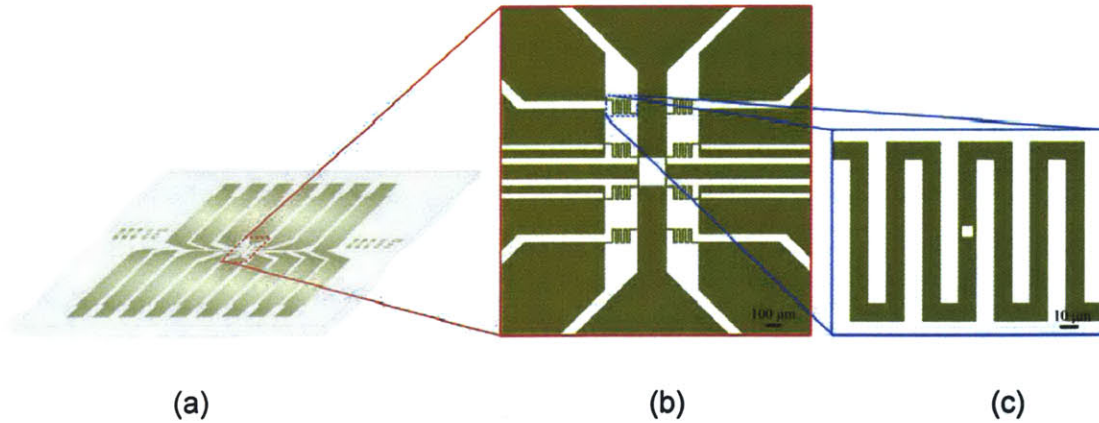
Figure 4-2. *PHE Chip.*

The designations for the pads of the PHE chip are depicted in the mask screen shot (a) and the electrical schematic (b) of Figure 4-3. See Appendix C for the full PHE chip electrical schematic diagram.

(a)   (b)
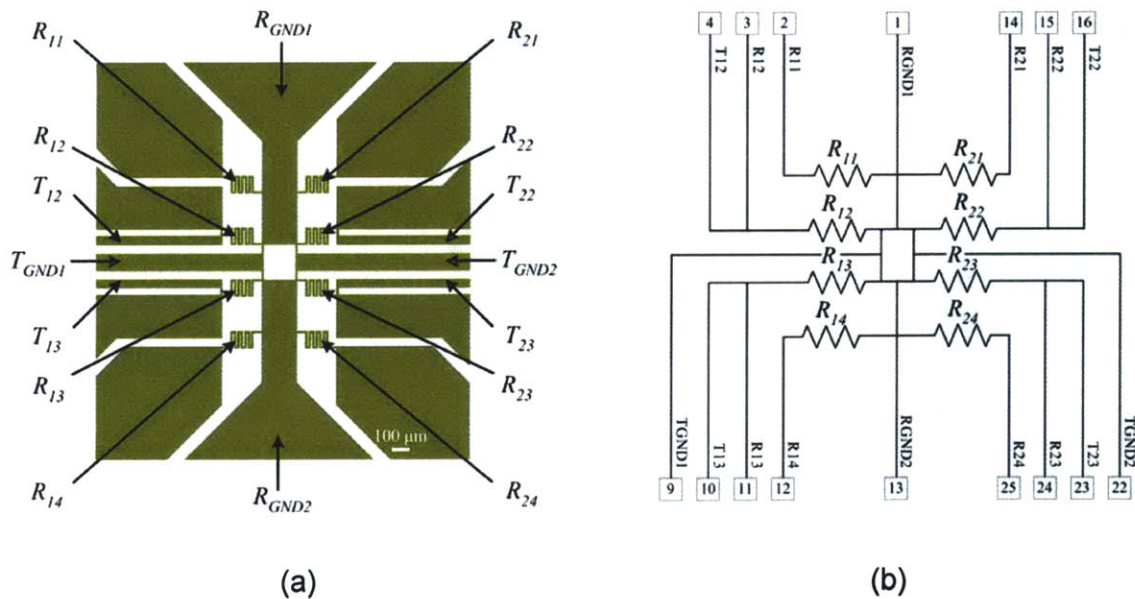
Figure 4-3. *PHE Chip Pad Designations.*

The common ground is the middle pad on both the near and far sides of the chip. The common ground is labeled R_{GND1} and R_{GND2}, respectively. The two pads to the left and right of the common ground on the near side of the chip are the power leads for the lower four resistors, denoted in (*column, row*) notation as R_{13}, R_{14}, R_{23}, and R_{24}. Similarly, the two pads to the left and right of the common ground on the far side of the chip are the power leads for the upper four resistors R_{11}, R_{12}, R_{21}, and R_{22}. The inner four resistors — R_{12}, R_{13}, R_{22}, and R_{23} — each have an additional power and ground lead to enable four-point measurements when the device is in operation. The four-point power and ground lead for R_{12} is T_{12} and T_{GND1}. The same notation is used for the other three, four-point resistors.

Each resistor is 10 μm wide by 860 μm long by 1.1 kÅ thick. Given the thickness of the resistor, composed of a 0.1 kÅ titanium adhesion layer beneath the 1 kÅ platinum layer, the resistance R of the resistor due to a layer of given resistivity can be calculated by

$$R = \left(\frac{L}{WH}\right)\rho_e \qquad (4\text{-}1)$$

where L, W, and H are the length, width, and height of the resistor. ρ_e is the electrical resistivity. The two layers act in parallel; thus, the equivalent resistance R_{eq} is

$$\frac{1}{R_{eq}} = \frac{1}{R_{Pt}} + \frac{1}{R_{Ti}} \Rightarrow R_{eq} = \frac{R_{Pt}R_{Ti}}{R_{Pt} + R_{Ti}} \qquad (4\text{-}2)$$

Using the value $\rho_{e_{Pt}} = 10.6 \times 10^{-8}\,\Omega\text{·m}$, $R_{Pt} \approx 83\,\Omega$. Similarly, with $\rho_{e_{Ti}} = 40.0 \times 10^{-8}\,\Omega\text{·m}$, $R_{Ti} \approx 3440\,\Omega$. Thus, $R_{eq} \approx 81\,\Omega$. The titanium adhesion layer of thickness 0.1 kÅ theoretically changes the resistance by approximately 2 Ω, a minimal effect considering the resistance variations inherent in the fabrication process.

The resistance of the power lead for each resistor was designed to be a factor of ten less resistive than the resistor. As seen in (a) of Figure 4-2, two lead lengths comprise the chip. R_{11}, R_{14}, R_{21}, and R_{24} are of one length, and R_{12}, R_{13}, R_{23}, and R_{24} are of a second length. All of the leads on the chip have the same H and ρ_e as those variables are dependent on the metal reposition rather than the mask design. Thus, the effect of lead length on the resistance of the lead can be examined by comparing L/W ratios for each resistor length. The R_{11} length resistors have $L/W = 4.67$, and the R_{12} length resistors have a L/W ratio of 5.22.

Using Equation 4-1 with the resistivity of platinum, the resistance of the lead $R_{pl} \approx 5\ \Omega$, and the variation in resistance between leads is $< 1\ \Omega$. Thus, the resistance of each lead is less than $0.1 \cdot R_{Pt}$.

4.2.2 Test Structure Chip

Previous iterations of the device demonstrate a method of controllable bubble formation with out-of-plane nucleation cavities and serve as a basis for the current PHE chip designs. However, the question of controllable bubble formation without cavities remains to be investigated. A TSC and subsequent TSC iterations investigate the possibility of controlled nucleation with in-plane nucleation sites rather than out-of-plane nucleation cavities. An in-plane nucleation site is a narrowing in the resistor, which creates an area of higher resistivity and, hopefully, promotes nucleation at the specified site. Figure 4-4 contains three TSC iterations.

TSCv3.0   TSCv3.1   TSCv3.2
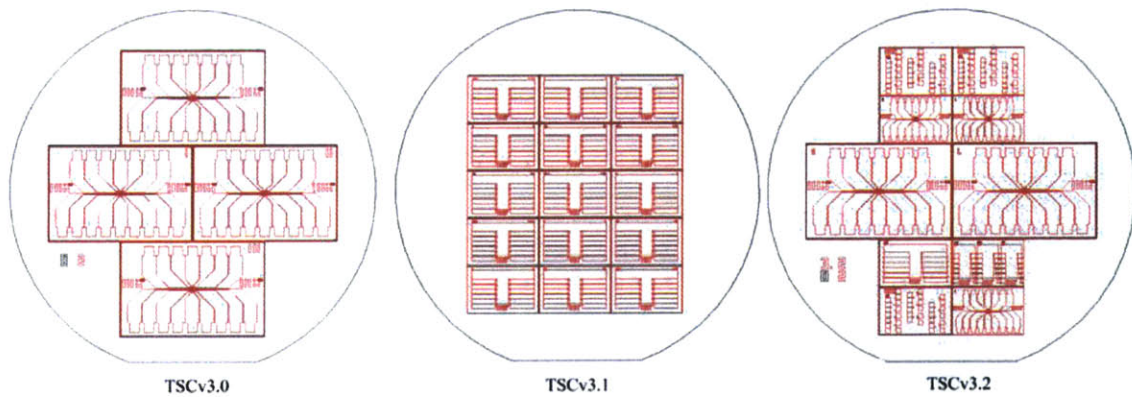
Figure 4-4. *TSC Iterations.*

Test Structure Chip v3.0

The first TSC design, TSCv3.0, is a modified, twice magnified (2×) PHE chip. The chip size is 6 cm by 4 cm, and each chip contains two columns of nucleation sites. Each resistor in the two columns is 1,720 µm long by 20 µm wide. Four geometrical variations of

the PHE Chip are shown in Figure 4-5. An in-plane nucleation site is located at the vertical line of symmetry at the horizontal midpoint for each resistor. The chip-to-chip variations are no nucleation site (a), a 10 μm by 10 μm nucleation site (b), a 20 μm by 10 μm nucleation site (c), and a 30 μm by 10 μm nucleation site (d).

(a)   (b)   (c)   (d)
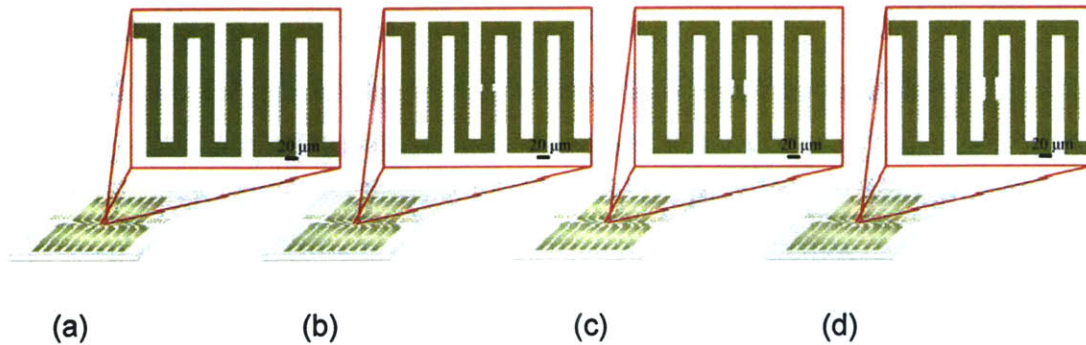
Figure 4-5. *TSCv3.0 Geometrical Variations.*

The pad designations for the TSCv3.0 are the same as the PHE Chip pad designations depicted in Figure 4-3. For the no nucleation site geometry, the *L/W* ratio is identical to that of the PHE chip. Thus, the resistance of the resistors using the conductivity of platinum in Equation 4-1 remains $R_r \approx 83 \ \Omega$. The resistance of the nucleation sites R_{ns} for geometries (b), (c), and (d) can be similarly calculated and are approximately 1, 2, and 3 Ω, respectively. Thus, $R_{ns} < 1/20 \ R_r$.

Test Structure Chip v3.1

The second TSC design, TSCv3.1, has a chip size of 3 cm by 2 cm. Each resistor in the two columns of six resistors each is 2,580 μm long by 30 μm wide. Figure 4-6 depicts an illustration of one of the three TSCv3.1 chip variations (a), a zoomed screen shot of the mask where controlled nucleation occurs at the individual resistors (b), and an individual nucleation site on the mask (c). Each resistor has a separate power lead and connects to the common ground, which is located at the center of the chip. A nucleation site is located at the vertical line of symmetry at the vertical midpoint for each resistor.

(a)   (b)   (c)
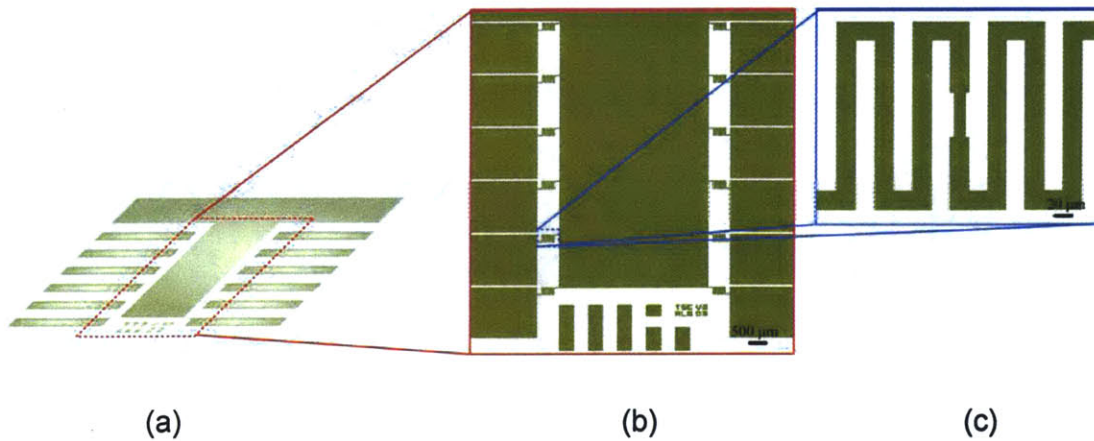
Figure 4-6. *TSCv3.1.*

Three different chip geometries are part of the TSCv3.1 design. Within a chip geometry, the nucleation site width remains constant, while the nucleation site length varies. Six different nucleation site lengths compose a column, and the second column is identical to the first. Figure 4-7 illustrates the eighteen geometrical variations that were designed for the TSCv3.1. Each column represents the three chip geometries at a single site on a chip. Each row comprises all of the variations present on a given chip geometry.

For example, the first geometry consists of 6 μm wide nucleation sites that are 0, 18, 36, 54, 72, and 90 μm long. The 0 μm long nucleation site is located in the first column and is schematically shown as the first resistor in the first column. Similarly, the 18 μm long nucleation site is located in the second column and is schematically shown as the second resistor in the first column. The second geometry consists of 12 μm wide nucleation sites that are 0, 18, 36, 54, 72, and 90 μm long, as shown in the second row. And, the third geometry consists of 18 μm wide nucleation sites that are 0, 18, 36, 54, 72, and 90 μm long, which is depicted in the third row.
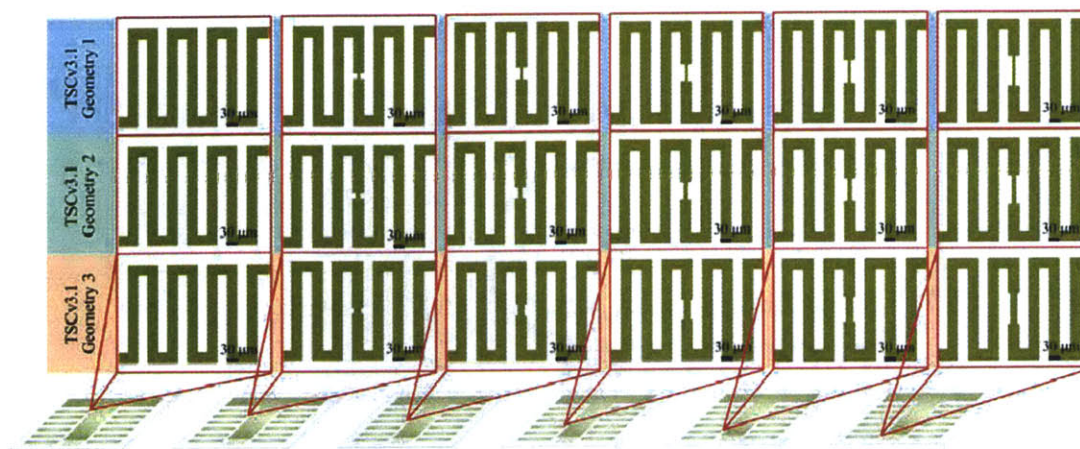
Figure 4-7. *TSCv3.1 Geometrical Variations.*

Test Structure Chip v3.2

The third TSC, TSCv3.2, is comprised of seven 3 cm by 2 cm chip designs and two 6 cm by 4 cm chip designs for a total of nine different chip geometries. Figure 4-8 illustrates the chip designs, for which two geometrical variations exist for both (a) and (b), and three geometrical variations exist for (d). Chips (a) and (b) are modified forms of the PHE chip in linear and serpentine resistor form. A modified TSCv3.1 composes the geometries of (c) and (e). Chip (d) is a series of test structures comprising a total of three chip geometries.

(a)   (b)   (c)   (d)   (e)
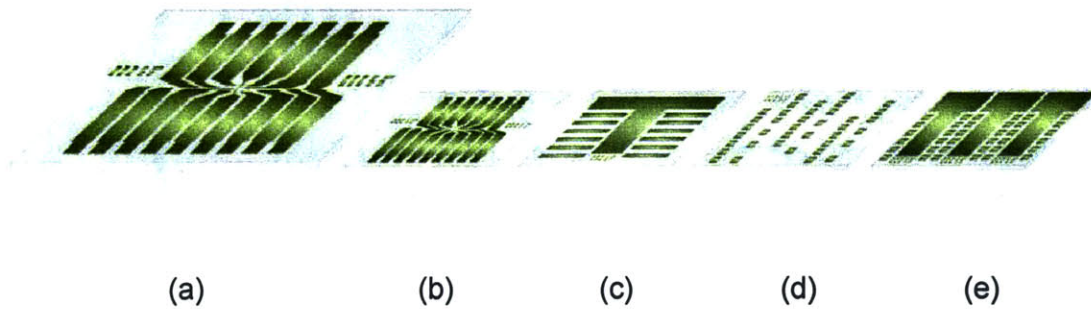
Figure 4-8. *TSCv3.2 Chips.*

The first TSCv3.2 geometry is a modified, twice magnified (2×) PHE Chip. The 6 cm by 4 cm chip contains two columns of nucleation sites. Each serpentine resistor is 1720 μm long by 10 μm wide with 10 μm long and 3 μm wide nucleation sites. The chip and resistor geometry are depicted in Figure 4-9. Similarly, the second TSCv3.2 geometry is an altered, twice magnified (2×) PHE chip. The 6 cm by 4 cm chip contains two columns of nucleation sites comprised of linear resistors. Each linear resistor is 640 μm long by 10 μm wide with 10 μm long by 3 μm wide nucleation sites. The chip and resistor geometry are depicted in Figure 4-9.

A 3 cm by 2 cm refashioned PHE chip comprises the third TSCv3.2 geometry. The chip contains two columns of nucleation sites with serpentine resistors. Each resistor is 850 μm long by 10 μm wide with 10 μm long by 3 μm wide nucleation sites. In kind, the fourth geometry is a PHE chip mutation with a chip size of 3 cm by 2 cm. Linear resistors comprise the two columns of nucleation sites. Each linear resistor is 3,200 μm long by 10 μm wide with 10 μm long by 3 μm wide nucleation sites, as shown in Figure 4-9.
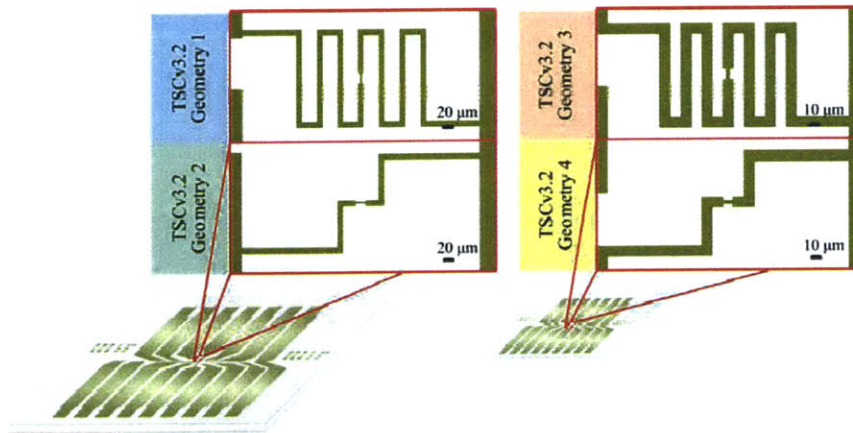
Figure 4-9. *TSCv3.2 Geometries 1-4.*

The fifth TSCv3.2 geometry is a 3 cm by 2 cm modified TSCv3.1. Six different resistor lengths compose a column, and the second column is a continuation of the first with greater resistor length variation between rows. Figure 4-7 illustrates the twelve geometrical variations that were designed. The first column consists of 10 μm wide by 30, 50, 70, 90, 110, and 130 μm long resistors with 10 μm long by 3 μm nucleation sites. The second column consists of 10 μm wide by 210, 410, 610, 810, 1,010, and 1,210 μm long resistors with 10 μm long by 3 μm nucleation sites.
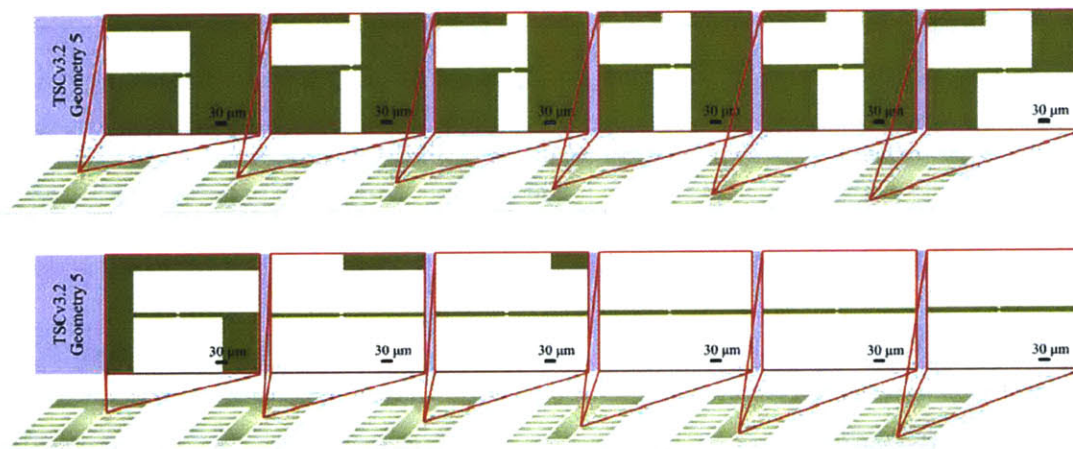
Figure 4-10. *TSCv3.2 Geometry 5.*

A series of test structures constitute the sixth, seventh, and eighth chip geometries. For the three chip geometries, the nucleation site width remains a constant 3 μm; the nucleation site length is 10, 20, and 30 μm, respectively, for the sixth, seventh, and eighth geometries. Figure 4-11 and Figure 4-12 illustrate the seventy-two geometries. The first two columns on each chip consist of resistors that share grounds, as depicted in Figure 4-11. The third and fourth columns consist of resistors with independent ground pads, as shown in Figure 4-12.
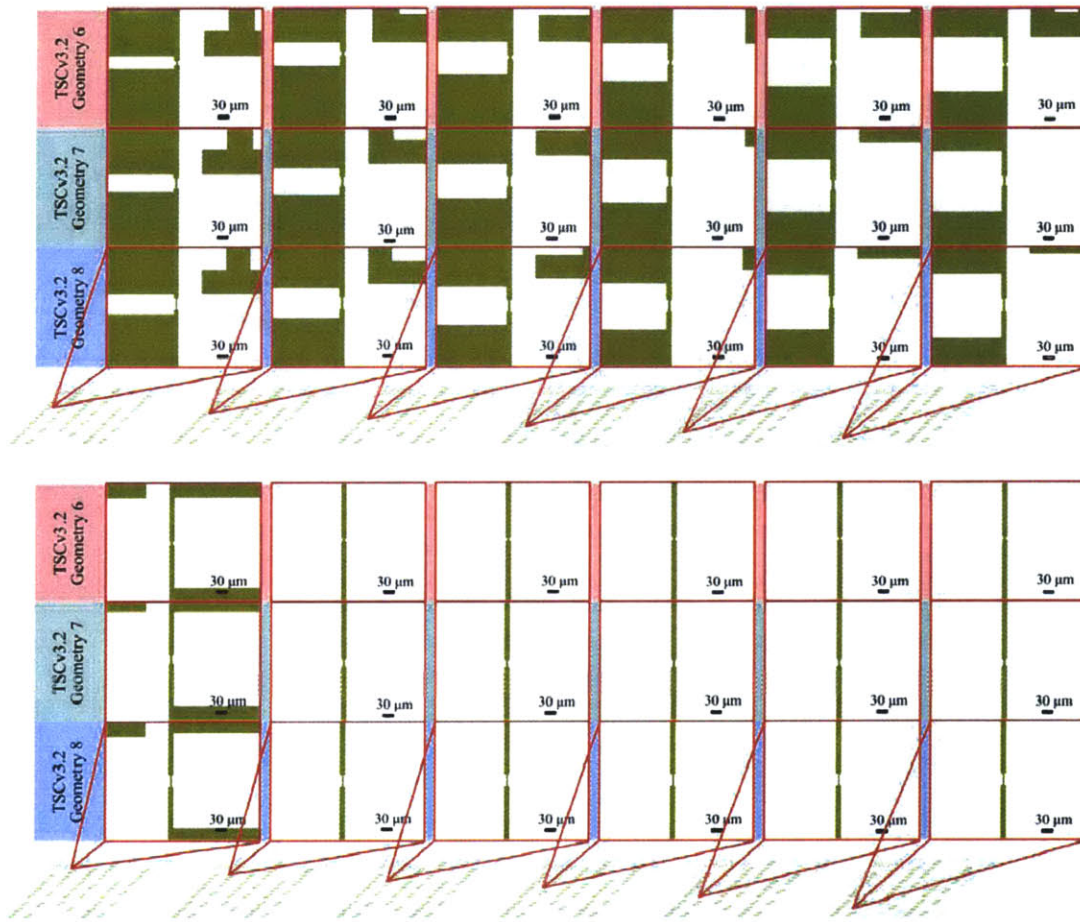
Figure 4-11. *TSCv3.2 Geometries 6-8 with Shared Ground.*

For the sixth geometry, resistor lengths are 30, 50, 70, 90, 110, 130, 210, 410, 610, 810, 1,010, and 1,210 µm. The seventh geometry has resistor lengths of 40, 60, 80, 100, 120, 140, 220, 420, 620, 820, 1,020, and 1,220 µm. The eighth geometry resistors have lengths of 50, 70, 90, 110, 130, 150, 230, 430, 630, 830, 1,030, and 1,230 µm.

Figure 4-12. *TSCv3.2 Geometries 6-8 with Independent Ground.*

The final TSCv3.2 geometry, the ninth, is also a 3 cm by 2 cm modified TSCv3.1. Each pair of columns is similar to a TSCv3.1 structure. Six different resistor lengths compose a column, and the second column is a continuation of the first with greater resistor length variation between rows. Figure 4-13 illustrates the thirty-six geometrical variations that were designed.

The first two columns compose the first TSCv3.1 structure. The first column of the structure consists of 10 μm wide by 30, 50, 70, 90, 110, and 130 μm long resistors with 10 μm long by 3 μm nucleation sites. The second column consists of 10 μm wide by 210, 410, 610, 810, 1,010, and 1,210 μm long resistors with 10 μm long by 3 μm nucleation sites.

The second TSCv3.1 structure corresponds to the third and fourth columns. The third column is comprised of 10 μm wide by 40, 60, 80, 100, 120, and 140 μm long resistors with 20 μm long by 3 μm nucleation sites. The fourth column consists of 10 μm wide by 220, 420, 620, 820, 1,020, and 1,220 μm long resistors with 10 μm long by 3 μm nucleation sites.

The final TSCv3.1 modified geometry is represented in the fifth and sixth columns. The fifth column has resistors of length 50, 70, 90, 110, 130, and 150 μm long resistors with 30 μm long by 3 μm nucleation sites. The sixth columns contains resistors of length 230, 430, 630, 830, 1,030, and 1,230 μm also with 30 μm long by 3 μm nucleation sites.
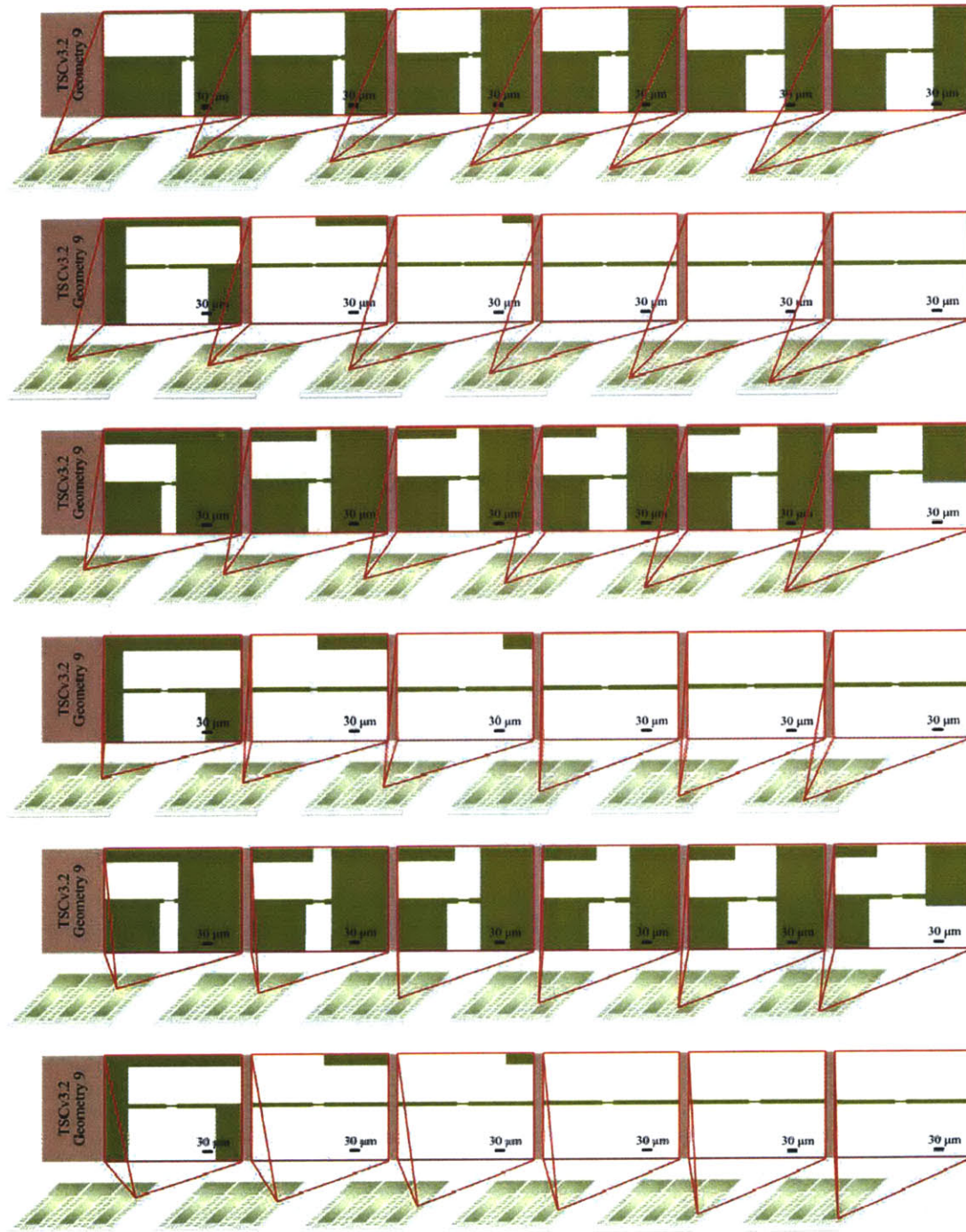
Figure 4-13. *TSCv3.2 Geometry 9.*

4.2.3 Fluidic System

The fluidic system is designed to capture a *particulate* with a pressure differential between the *nucleation chamber* and the input medium (IM) header in which the particles flow (illustrated as the surface of the device). The *fluidic inlet* and *fluidic outlet* are part of the dionized water (DI) header. By engineering the fluidic resistance in the *jet channel* and controlling the flow rates in the IM and DI headers, a pressure drop between the headers will ensure particulate capture at the *capture site*. The particulate is held in the site against the flow via the pressure gradient and the geometry of the well. In the design, the capture site is a cylinder with a diameter of 30 µm and a height of 15 µm (shown rectangular in Figure 4-14). The nucleation chamber is a rectangular solid with dimensions of 400 µm in length and 300 µm in width and height. Figure 4-14 illustrates the particulate-level fluidic system (a) and designations for the lumped model resistance elements (b).
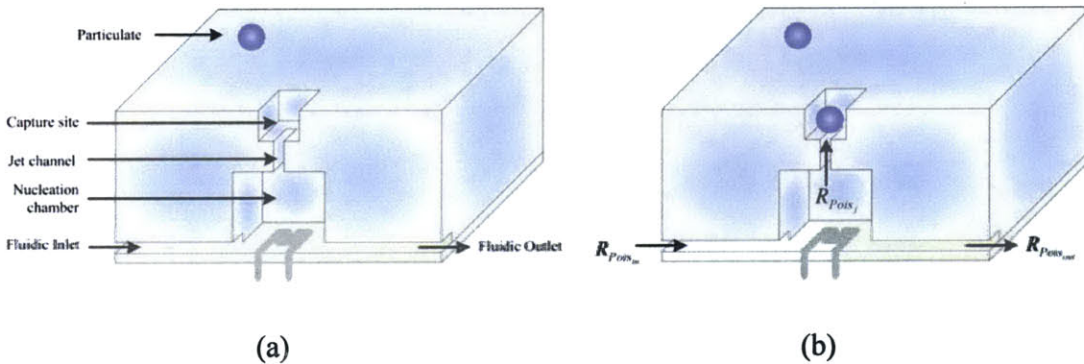
Figure 4-14. *Particulate-Level Fluidic System.*

Ejection force modeling in Chapter 5 demonstrates that $Re < 1$ and that a steady state profile was reached within the jet channel during the bubble nucleation and particle ejection process. By maintaining typical MEMS fluid flow input rates to the device, $Re < 1$ and steady state profiles can be maintained throughout the fluidic system. Thus, a Poiseuille lumped element resistance model is a valid method of system analysis. Figure 4-15 depicts a lumped element model in three dimensions for the system. The upper horizontal fluidic plane is the IM header with input source indices of (*input number, 1*) where the one denotes

input and output indices of (*input number, 2*) where the two denotes output. The dual input allows two mediums to be input into the system simultaneously. For applications where the same input is desired in both IM headers, a Y-connector could be used at the macro level. The lower horizontal fluidic plane is the DI header with input and output labeled with the same system of indices. Variable resistors are micro needling valves (UpChurch Scientific, Oak Harbor, WA). Vertical fluid channels connect the two horizontal fluidic planes.
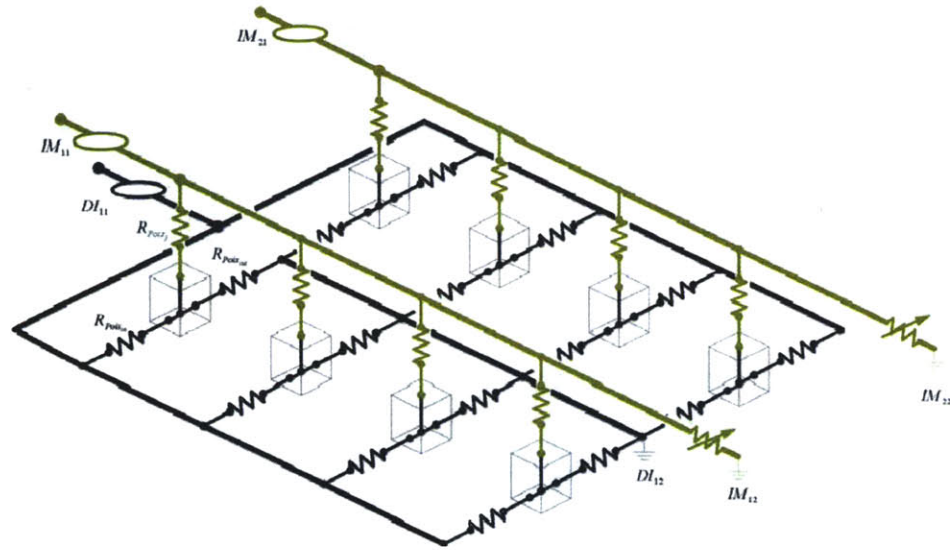
Figure 4-15. *Lumped Element Model of Fluidic System.*

In Chapter 5, the lumped element model of Poiseuille flow R_{Pois} was defined as

$$R_{Pois} = \frac{32\mu L}{\pi \cdot r_{ch}^4} \tag{4-3}$$

where μ is the viscosity of the fluid and r_{ch} is the channel radius for a channel of length L. For square channels, the hydraulic radius is used as r_{ch} where the hydraulic diameter D_h is

$$D_h \approx \frac{4 \times area}{perimeter} \tag{4-4}$$

Table 4-1 summaries the fluidic dimensions and corresponding Poiseuille lumped element values that were chosen to ensure that $R_{Pois_j} \ll R_{Pois_{in}} = R_{Pois_{out}} \ll R_{Pois_{DI}} = R_{Pois_{IM}}$

Table 4-1. *Fluidic Dimensions and Calculated Poiseuille Lumped Element Values.*

Channel	Dimension (μm)				Poiseuille Lumped Element	
	Length	Width	Height	Diameter	D_h (μm)	R_{pois} (Ω)
DI Header	31600	1000	306		469	1.34×10^{10}
IM Header	31600	1000	300		462	1.42×10^{10}
Inlet	250	6	6		6	3.93×10^{15}
Jet	15			6	6	2.36×10^{14}
Outlet	250	6	6		6	3.93×10^{15}

4.2.4 Electronic Interface

The MMI serves to connect a PHE chip or TSC to the macro electrical interface via a twenty-five pin female D-Sub mount output. Figure 4-16 depicts an illustration of the circuit board (a) and an electrical diagram of the MMI (b). Appendix C contains the full electrical schematic diagram of the MMI. Designed in Visio Professional 2002 (Microsoft Corporation, Waltham, MA), the MMI works with 2 cm by 3 cm and 4 cm by 6 cm chips. A through-hole located at the center of the pads allows microscope viewing from both vertical positions.
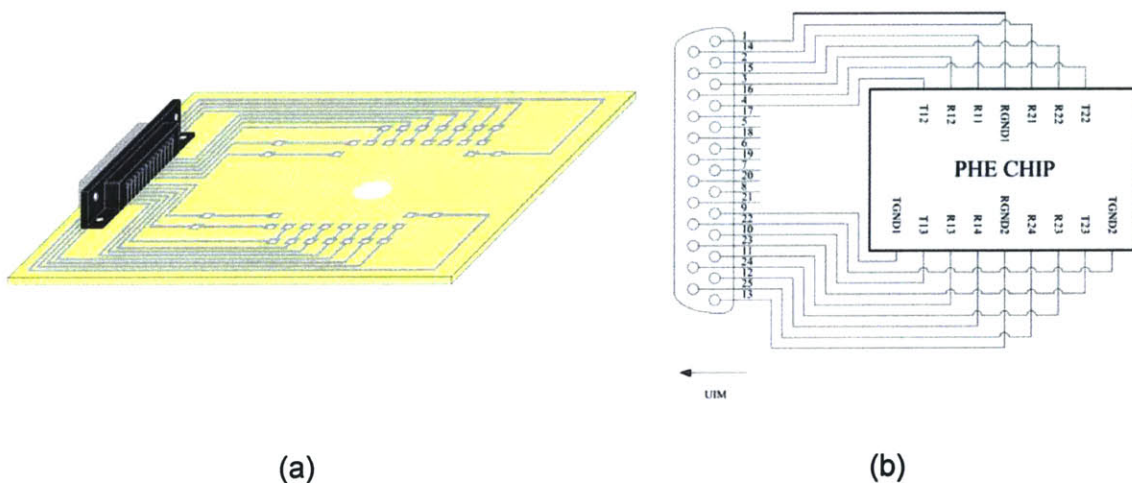
(a)   (b)

Figure 4-16. *MMI Design.*

The 12.5 cm by 10 cm circuit board layout is printed by a prototype circuit board company (ExpressPCB™, Santa Barbara, CA). The board is made of FR-4 epoxy glass laminate with a copper thickness of 43 μm. Final finish is tin-lead reflow. The maximum operating temperature specification is 398 K. Figure 4-17 is a photograph of a manufactured MMI.
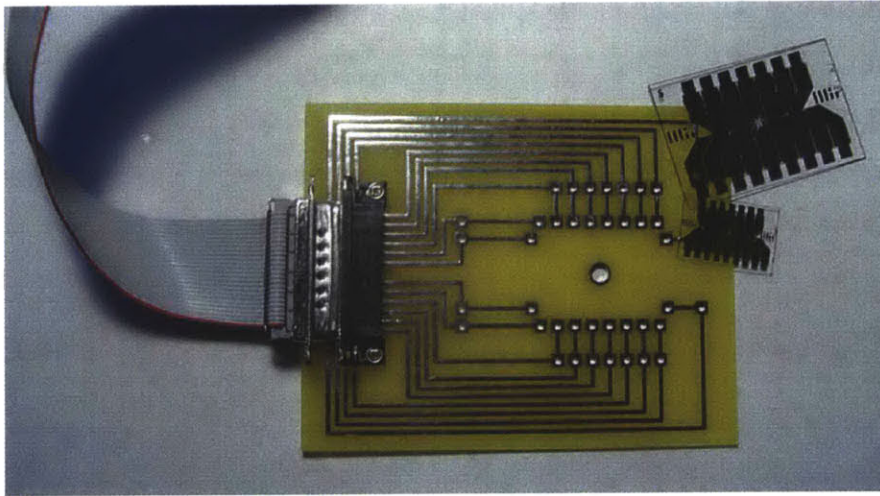
Figure 4-17. *Manufactured MMI.*

Designed in Visio Professional 2002, the UIM features single site actuation control, fluidic pressure monitoring such that the fluidic circuit presented in Figure 4-15 can be solved, and four-point measurement control. Figure 4-18 depicts an illustration of the UIM (a) and an electrical diagram of the UIM (b). Appendix C contains a full electrical schematic diagram of the UIM.
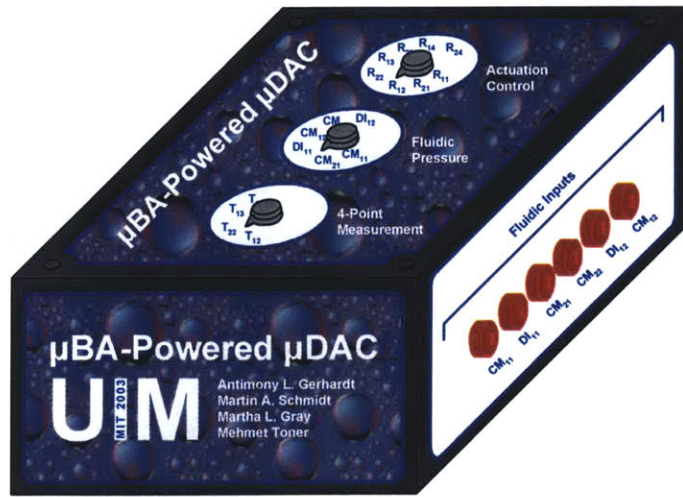
(a)
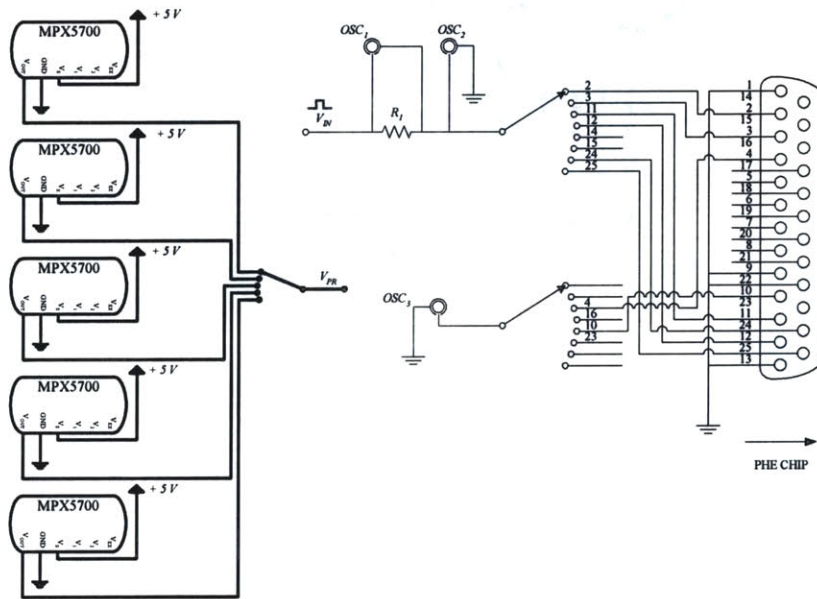
(b)

Figure 4-18. *UIM Design.*

Major electrical components include gauge compensated pressure sensors (MPX5700, Motorola, Schaumburg, IL); a 10 Ω, 5 W, 1% tolerance resistor (Huntington Electronic, Inc., Huntington, IN); and single pole, twelve position rotary switches (Electroswitch, Raleigh, NC). A male solder cup D-Sub connector (3M, Maplewood, MN) serves as the connector between the UIM and MMI. Crucial fluidic components include unions, ferrules, nuts, adapters, and 1.59 mm PEEK^{TM} and 6.35 mm Teflon tubing (UpChurch Scientific, Oak Harbor, WA). Figure 4-19 is a photograph of the assembled UIM.

Figure 4-19. *Assembled UIM.*

4.3 Microfabrication

4.3.1 Platinum Heating Electrode Chip

The PHE chip is fabricated on 150 mm diameter quartz wafers. Other optically transparent substrates such as glass wafers (Pyrex 7740, Mark Optics, Inc., Santa Ana, CA; Borofloat, Mark Optics, Inc., Santa Ana, CA) can be used. However, substitute substrate viability is limited by available etching technologies, as the fabrication requires etching of a 5-6 μm diameter cavity of 10-20 μm depth. An illustration of the process flow is in Figure

4-20. Appendix A contains a more delineated description of the process flow, and Appendix B illustrates the masks for the fabrication process.

The fabrication procedure is initiated with an RCA clean of the quartz substrates. RCA clean is a procedure that was developed by RCA Laboratories in 1970. The cleaning process involves three main steps: (1) removal of insoluble organic contaminants, (2) removal of metallic contaminants, and (3) removal of ionic and heavy metal atomic contaminants. In the first step, the wafers are submerged in a 348.15-353.15 K bath of 5:1:1 $H_2O:H_2O_2:NH_4$ for ten minutes and then cascade rinsed. Next, wafers are submerged in a diluted 50:1 $H_2O:HF$ bath for fifteen seconds followed by a cascade rinse. Lastly, the wafers are submerged in a a 348.15-353.15 K bath of 6:1:1 $H_2O:H_2O_2:HCl$ for fifteen minutes, cascade rinsed, and spun dry.

A SVG Thermco low pressure chemical vapor deposition (LPCVD) reactor (SVG Thermco, Santa Clara, California) is used to deposit 2 μm of polysilicon by a prolysis of silane (SiH_4). The polysilicon layer serves as an etch mask later in the process. Nucleation sites are patterned in the polysilicon using standard positive photolithography techniques. The wafers are hexamethyldisilazane (HMDS) primed in a vapor prime oven (YES-3, Yield Engineering Systems, San Jose, CA) with a recipe created to achieve a 72° contact angle. HMDS improves photoresist adhesion by creating a bond between the silicon with silizanes and the resist with methyls. A photoresist coater (5110, Solitec, Milpitas, CA) is used to spin on 1 μm of positive photoresist (OCG 825 20CS, Arch Chemicals, Inc., Norwalk, CT). The wafers are prebaked at 363.15 K for 30 minutes, exposed on a mask aligner (EV620, Electronic Visions, Inc., Phoenix, AZ) using mask 1, and postbaked at 393.15 K for 30 minutes. The resist is developed (OCG 934 1:1, Arch Chemicals, Inc., Norwalk, CT).
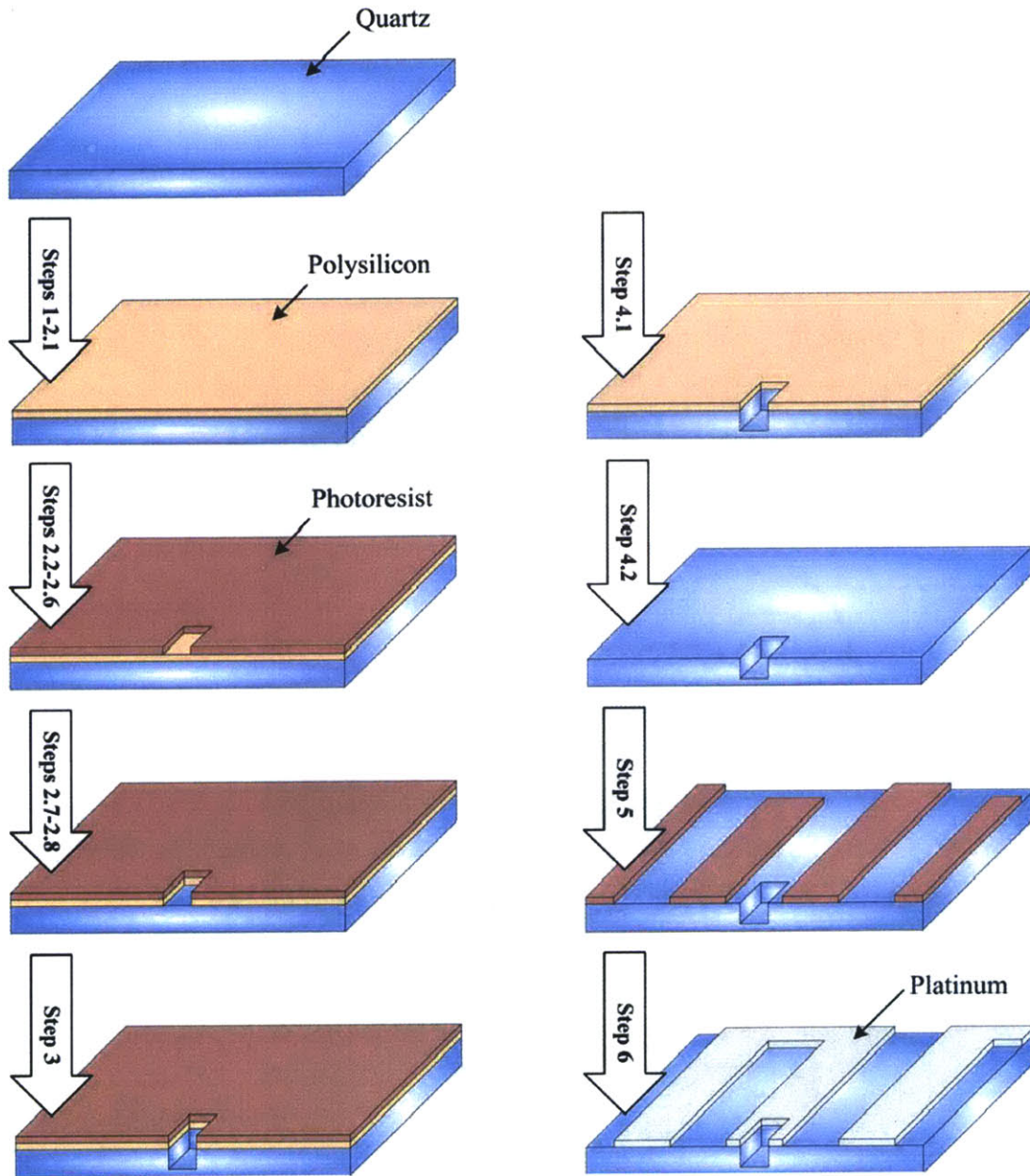
Figure 4-20. *PHE Chip Pictorial Process Flow.*

The polysilicon mask is made by etching through the 2 μm of polysilicon in a deep trench etcher system (Multiplex System, Surface Technology Systems, Portsmouth, NH) using a recipe created to achieve nearly vertical sidewalls. The mask then is used to etch the 6 μm diameter by 16 μm deep cavities in the quartz.

Surface Technology Systems (STS) performed the quartz wafer etching in this process. After removing the resist which might burn in a aggressive etch, an advanced oxide etcher (AOE) medium etch and a proprietary process with etch rate of 481 nm/minute was used to achieve nearly vertical sidewalls, uniformity, and the desired depth of 16 μm. Figure 4-21 contains scanning electron micrographs (SEMs) taken using a Jeol 800 SEM (Peabody, MA) after the first wafer had been etched. The SEMs show a process selectivity of 18:1, an etch profile angle of 88.8°, and an etch depth of 14 μm. The dirt in the features is due to the handling and cleaving required for the SEMs of small features. The profiles, shown in the background of the images, are relatively clear. The etch time was increased for the remaining wafers in the lot to achieve the desired 16 um etch depth.

(a)   (b)
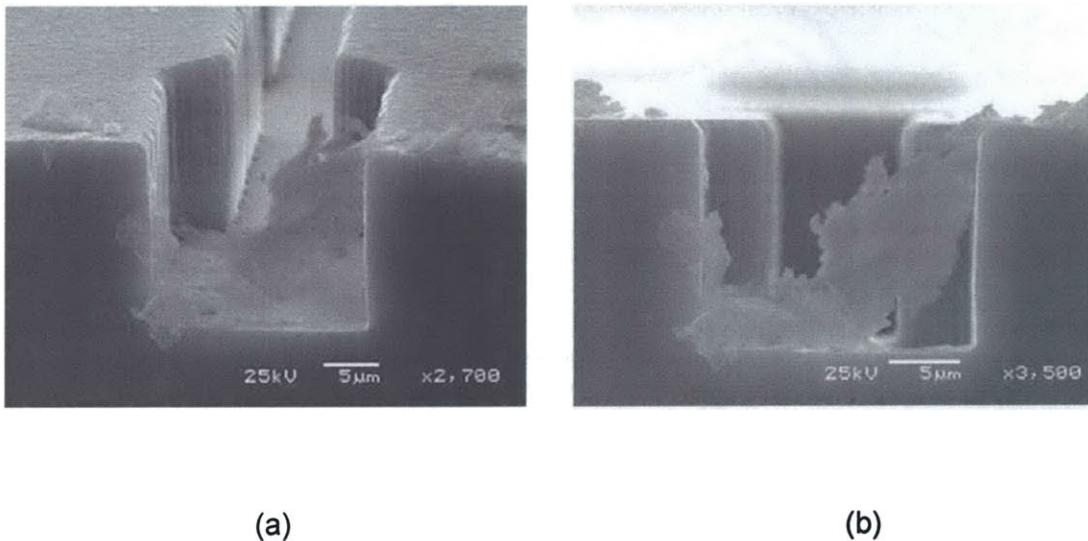
Figure 4-21. *SEMs of Nucleation Site.* (Courtesy of STS.)

The wafers are piranha cleaned in a bath of 1:4 H_2O_2: H_2SO_4 for 10 minutes, cascade rinsed, and spun dry. The polysilicon mask is removed by etching in a polysilicon etcher (LAM 490, LAM Research, Fremont, CA). The metal is patterned using standard image reverse photolithography techniques. The wafers are HMDS primed in a vapor prime oven with a 72° contact angle recipe. A photoresist coater is used to spin on 2 μm of negative resist. The wafers are prebaked at 363.15 K for 30 minutes, exposed on a mask aligner using

mask 2, and hardbaked at 378.15 K for 30 minutes. The photoresist is flood exposed on the mask aligner for 60 s and developed.

An evaporative deposition system (VES-2550, Temescal, Boxford, MA) is used to deposit a 100 Å Titanium adhesion layer and 1,000 Å Platinum. After metallization, excess metal is lifted off in a bath of acetone. To enable device reliability comparison, a portion of the wafer lot was annealed in an atmospheric diffusion tube (MRL Industries, Sonora CA) at 873.15 K for an hour with Nitrogen flowing through the tube at a rate of 5 L/min. The wafers are cut into chips with the diesaw (DAD-2H/6T, Disco, Santa Clara, CA). After diesawing, some chip surfaces are modified using silane (tridecafluoro-1,1,2,2-tetrahydrooctyl-1-triethoxysilane, United Chemical Technologies, Bristol, PA), which makes the surfaces more hydrophobic. A chip is silanized by pumping a 2% solution of silane in ethanol through the packaged μBA device. The solution is allowed to remain stagnant in the channels for about a minute before the system is flushed with ethanol.

4.3.2 Test Structure Chip

The TSC substrate is fabricated on 150 mm diameter fused silica, quartz, wafers (Fused Quartz, Mark Optics, Inc., Santa Ana, CA). An illustration of the process flow is in Figure 4-4. Appendix A contains a more delineated description of the process flow, and Appendix B depicts the masks for the process. After a piranha clean for 10 minutes, the metal mask is patterned using standard image reverse photolithography techniques. The wafers are HMDS primed in a vapor prime oven with a 72° contact angle recipe. A photoresist coater is used to spin on 2 μm of image reversal resist (AZ® 5124-E, Clariant Corporation, Somerville, NJ). The wafers are prebaked at 363.15 K for 30 minutes, exposed on a mask aligner, and hardbaked at 378.15 K for 30 minutes. The resist is flood exposed on the mask aligner and developed (AZ® 422, Clariant Corporation, Somerville, NJ).

Quartz

Steps 1-2

Photoresist

Step 3
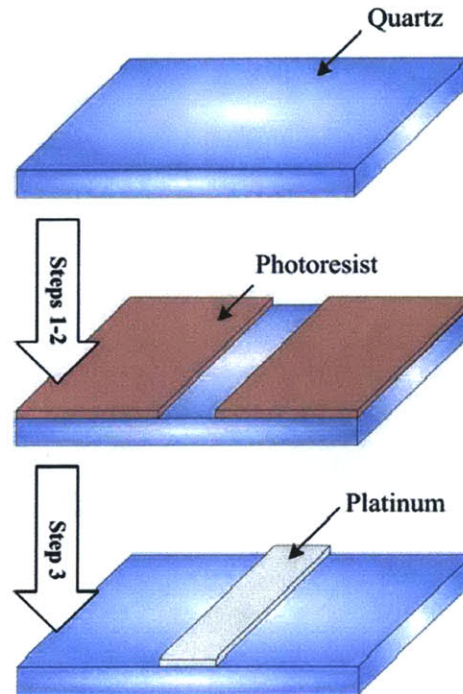
Platinum

Figure 4-22. *TSC Pictorial Process Flow.*

An evaporative deposition system is used to deposit a 100 Å Titanium adhesion layer and a 1,000 Å Platinum layer. After metallization, excess metal is lifted off in an acetone bath. The wafers are cut into chips with the diesaw. To enable device reliability comparisions, a portion of the wafer lot is annealed in an atmospheric diffusion tube at 873.15 K for an hour with Nitrogen flowing through the tube at a rate of 5 L/min. Figure 4-23, Figure 4-24, and Figure 4-25 are photographs of completed TSC wafers.
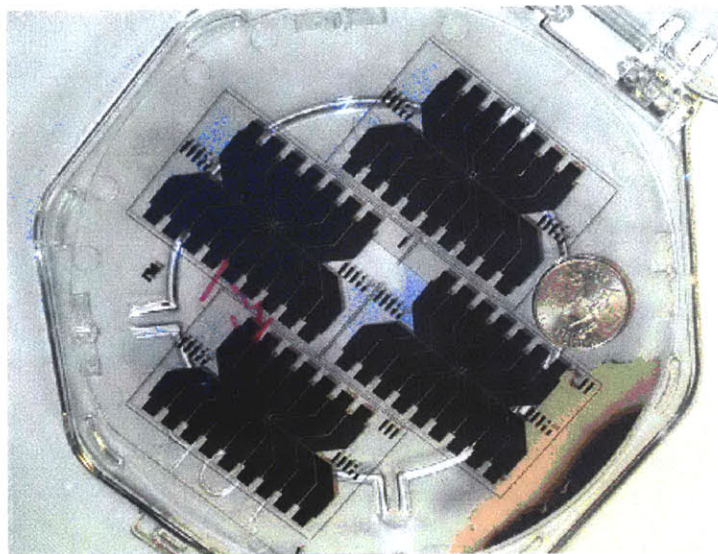
Figure 4-23. *Fabricated TSCv3.0 Wafer.*
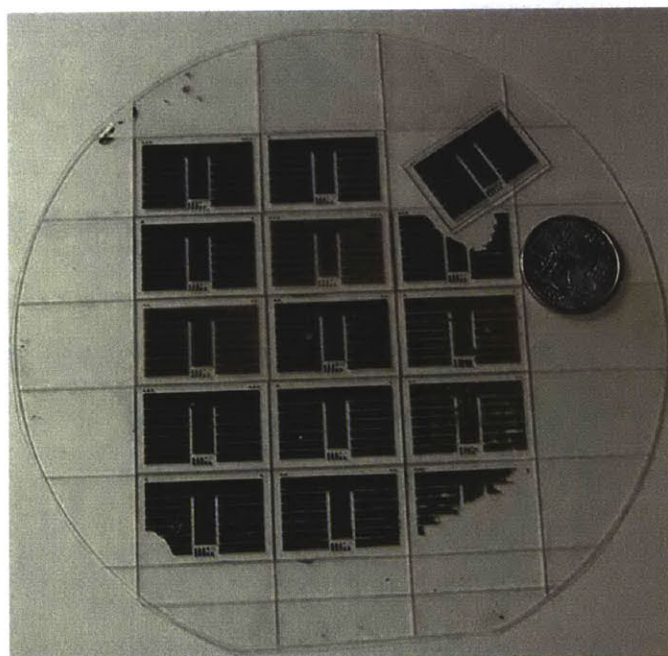
Figure 4-24. *Fabricated TSCv3.1 Wafer.*
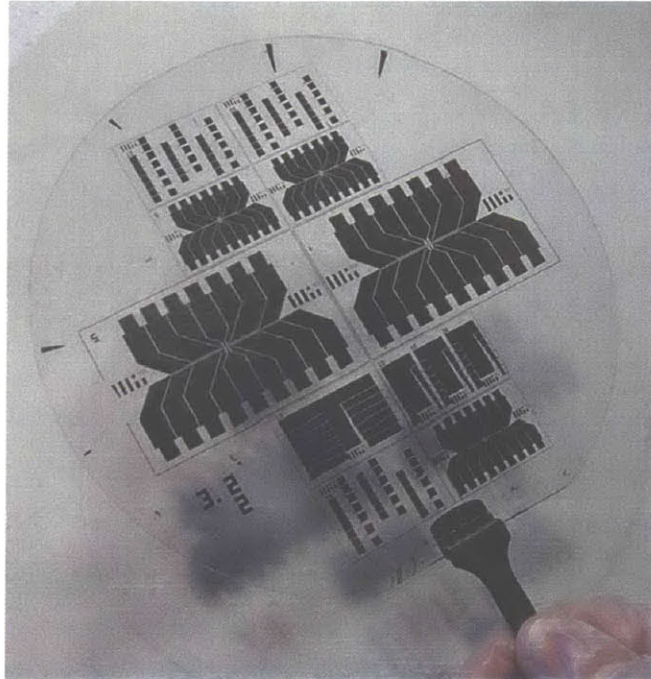
Figure 4-25. *Fabricated TSCv3.2 Wafer.*

4.3.3 Deionized Header Mold

The DI header mold forms the lower fluidic layer of the µBA device and is fabricated on 150 mm diameter silicon wafers (6706P P – Jeida Prime, Wafernet, Inc., San Jose, CA). An illustration of the process flow is in Figure 4-26. Appendix A contains a more delineated description of the process flow, and Appendix B details the masks for the process.
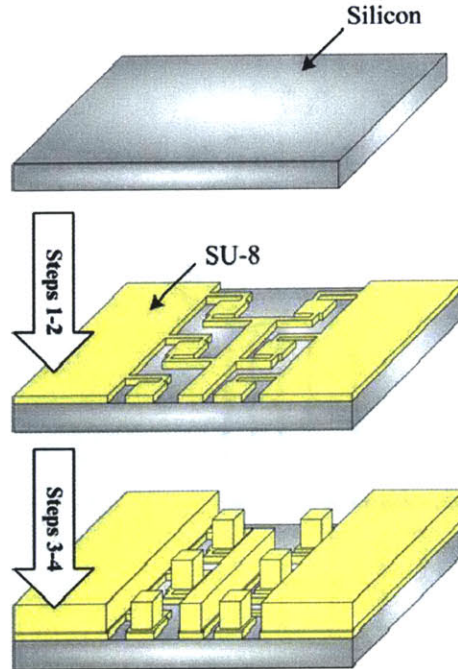
Figure 4-26. *DI Header Mold Pictorial Process Flow.*

After a piranha clean, custom alignment marks optimized for viewing through thick layers of photoresist are patterned using standard positive photolithography techniques. The wafers are HMDS primed in a vapor prime oven with a 72° contact angle recipe. A photoresist coater is used to spin on 1 μm of positive photoresist. The photoresist is prebaked at 363.15 K for 30 minutes, exposed on a mask aligner using mask 8, postbaked at 393.15 K for 30 minutes, and then developed. The alignment marks are etched in a deep trench etcher system to a depth of 3 μm.

Figure 4-27 contains two screenshots of the alignment mark patterns. The physically machined features are the arrows and filled cross feature (not shown). The square and inscribed, unfilled cross feature compose the upper alignment features located on the fluidic masks. The four inscribed squares within the large square and the four circumscribing squares that compose the larger square (not shown) serve as viewing areas to facilitate alignment. The machined arrows direct alignment between the mask and wafer from (a) to (b).

(a)   (b)
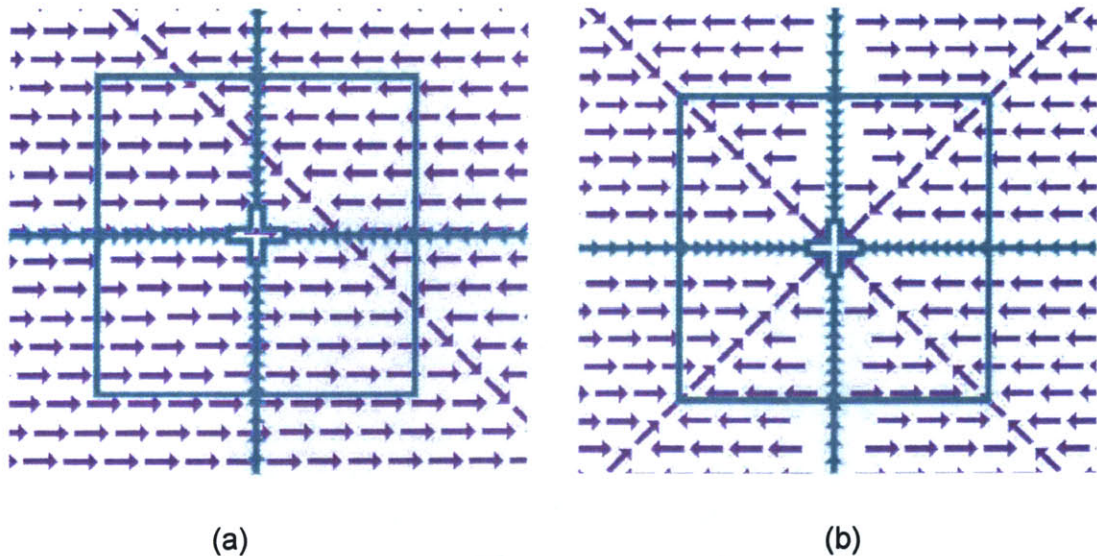
Figure 4-27. *Thick Photoresist Alignment Marks.*

After a second piranha clean, the wafers are dehydrated serially on a hot plate at 473.15 K for 5 minutes or in parallel in a convection oven at 473.15 K for 30 minutes. A polyimide coater (CB15, Headway Research, Inc., Garland, TX) is used to spin on 6 μm of negative resist (SU-8 2005, MicroChem Corporation, Newton, MA). The resist is soft baked at 338.15 K and 463.15 K for 1 and 2 minutes, respectively; exposed on a mask aligner using mask 3; and postbaked at 338.15 K and 463.15 K for 1 minute at each temperature.

Next, a three-layer process is used to deposit a total of 300 μm of negative resist (SU-8 50, MicroChem Corporation, Newton, MA; SU-8 2075, MicroChem Corporation, Newton, MA). The coater is used to spin on 100 μm of resist, which is then soft baked at 338.15 K and 463.15 K for 10 and 30 minutes or 5 and 20 minutes, respectively. This two step process is repeated thrice at which point the 300 μm of photoresist is air dried for 72 hours and then baked in a convection oven on a metal plate until hard. Bake time is humidity dependent but is generally 1-3 hours. The photoresist is then exposed on a mask aligner using mask 4, postbaked at 338.15 K and 463.15 K for 1 and 20 minutes, developed (SU-8 Developer, MicroChem Corporation, Newton, MA). Developing time is dependent on the additive bake time. Typical develop times range from 4-6 hours. An isopropanol rinse and nitrogen dry

complete the DI mold fabrication process. A finished wafer is shown in Figure 4-28.
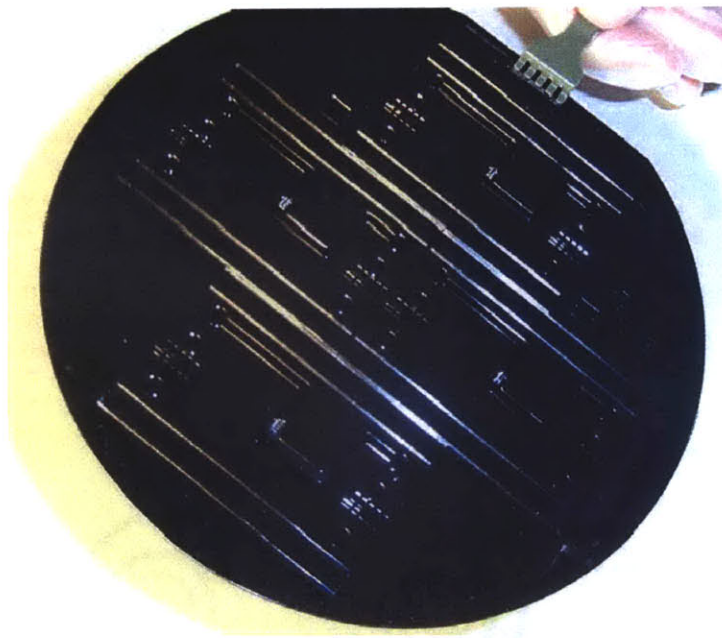
Figure 4-28. *Fabricated DI Header Mold.*

4.3.4 Input Medium Header Mold

The IM header mold is fabricated on 150 mm diameter silicon wafers as illustrated in Figure 4-29. Appendix A contains a more delineated description of the process flow, and Appendix B depicts the masks for the process. After a piranha clean, custom alignment marks optimized for viewing through thick layers of resist are patterned using standard positive photolithography techniques. The alignment marks are shown in Figure 4-27.

Silicon

SU-8

Steps 1-2

Step 3

Steps 4-5
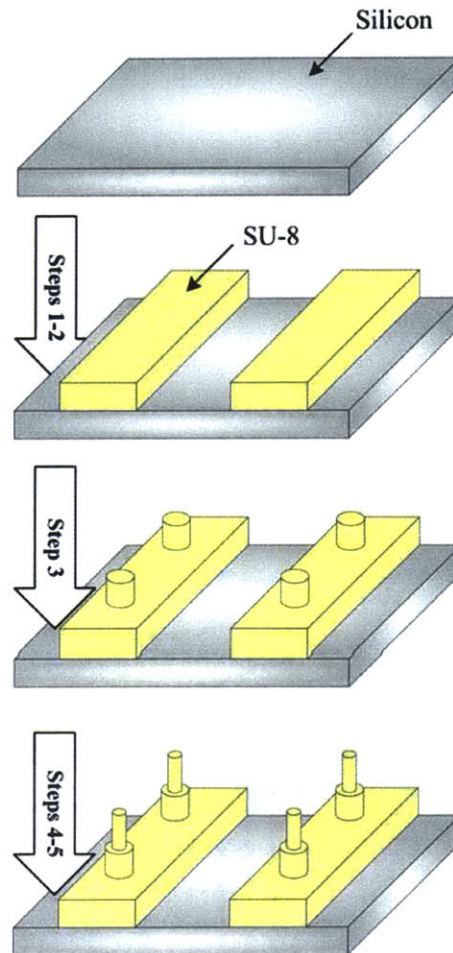
Figure 4-29. *IM Header Mold Pictorial Process Flow.*

To pattern the alignment marks, the wafers are HMDS primed in a vapor prime oven with a 72° contact angle recipe. A photoresist coater is used to spin on 1 μm of positive photoresist. The photoresist is prebaked at 363.15 K for 30 minutes, exposed on a mask aligner using mask 8, postbaked at 393.15 K for 30 minutes, and then developed. The alignment marks are etched in a deep trench etcher system to a depth of 3 μm.

After another piranha clean, the wafers are dehydrated serially on a hot plate at 473.15 K for 5 minutes or in parallel in a convection oven at 473.15 K for 30 minutes. A three-layer process, identical to that of the DI Process, is used to deposit 300 μm of photoresist (SU-8 50, MicroChem Corporation, Newton, MA; SU-8 2075, MicroChem

Corporation, Newton, MA). The coater is used to spin on 100 μm of resist, which is then soft baked at 338.15 K and 463.15 K for 10 and 30 minutes or 5 and 20 minutes, respectively. This two step process is repeated thrice at which point the 300 μm of photoresist is air dried for 72 hours and then baked in a convection oven on a metal plate until hard. Bake time is humidity dependent but is generally 1-3 hours. The resist is then exposed on a mask aligner using mask 7; postbaked at 338.15 K and 463.15 K for 1 and 20 minutes, respectively.

The coater is used to spin on 15 μm of negative resist (SU-8 2010, MicroChem Corporation, Newton, MA). The resist is soft baked at 338.15 K and 463.15 K for 1 and 2 minutes, respectively; exposed on a mask aligner using mask 6; and postbaked at 338.15 K and 463.15 K for 1 minute and 2 minutes, respectively.

After a convection oven bake on a metal plate until hard, the coater is used to spin on 50 μm of negative resist (SU-8 50, MicroChem Corporation, Newton, MA). The resist is soft baked at 338.15 K and 463.15 K for 6 and 20 minutes, respectively; exposed on a mask aligner using mask 5; and postbaked at 338.15 K and 463.15 K for 1 minute and 5 minutes, respectively. The photoresist is then developed. Developing time is dependent on the additive bake time. Typical develop times range from 4-6 hours. An isopropanol rinse and nitrogen dry complete the IM mold fabrication process.
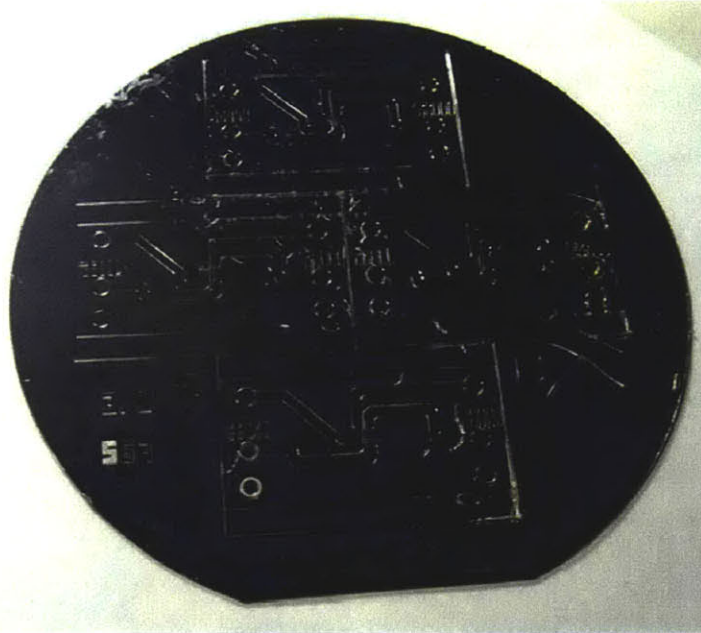
Figure 4-30. *Fabricated IM Header Mold.*

4.3.5 Microfabrication Challenges

During the course of processing, two main fabrication challenges arose. One challenge was the image reverse resist process necessary for lift-off metallization. The image reverse process has a reputation for being finicky, depending heavily on humidity conditions and bake times. The first TSC iteration, with relatively broad nucleation site features, was not affected. However, subsequent TSC iterations became increasingly sensitive to bake and exposure times as the width of the in-plane nucleation site narrowed with each new design.

With bake times held constant between days of processing, exposure times were determined daily by varying exposure time 0.4 – 1.3 s in 0.1 s increments across a single wafer. Suggested exposure for quartz wafers was 1.3 s. After developing, the patterns were inspected under a microscope. Tolerance to exposure time was shown to be less than 0.1 s. On August 26, 2003, for example, exposing a wafer for 0.6 s yielded a good pattern. Exposure for times from 0.7 - 1.3 s resulted in the nucleation site feature being partially or completely covered with resist. Partial coverage would result in a poorly metallized

nucleation site, and complete resist coverage would result in an open circuit instead of a nucleation site. Exposures less than 0.6 s also yielded poorly defined features.

A second processing challenge was the multi-layer SU-8 structures. After learning the art of a good SU-8 pour and spin, no challenges were experienced with single SU-8 layer of thickness less than 50-100 μm. However, thicker layers did not harden adequately after recommended soft baking times. The lack of hardening corresponds to solvent still within the photoresist. Continued processing to exposure resulted in masks adhering to substrates, regardless of aligner contact mode and separation distances, so firmly that prolonged piranha cleans would not separate them. The silicon wafers had to be chipped off to save the masks.

Process development showed that the soft bake time was a crucial factor. Increasing hot plate soft bake time up to 8 hours resulted in adherent wafers. Similarly, adding an additional air dry for up to 72 hours succeeding the soft bake did not improve the situation. A method was developed in which the wafers were placed on an aluminum foil covered metal plate within a convection oven immediately following the soft bake. If a time lag occurs between soft bake and oven bake, the wafers were ramped on a hot plate first. The times and temperatures used to successfully create the multi-layer SU-8 molds are included in Appendix A. However, the length of time needed for the solvent to evaporate depends on humidity and rate of heat transfer and ventilation in the convection oven used.

4.4 Assembly and Packaging

4.4.1 Assembly and Packaging Process

The μBA device assembly is completed at the chip level. First, the DI and IM molds are silanized to facilitate separating the mold from the cast. Then, polydimethylsiloxane (PDMS) (Sylgard 184® Silicone Elastomer, Dow Corning Corporation, Midland, MI) castings are made. The casting process begins by pouring a by-weight mixture of the two pre-polymer components over the mold in a plastic Petri dish. The PDMS is degassed under vacuum and then cured at 338.15 K for about two hours. The mold is peeled from the cast. The mold designs include chip separators to enable each chip to be removed in series.

Figure 4-31 illustrates the individual chips that are to be assembled. From bottom to top, the chips are the PHE chip, DI header cast, IM header cast, and a blank PDMS chip, which serves to close the fluidic channels.
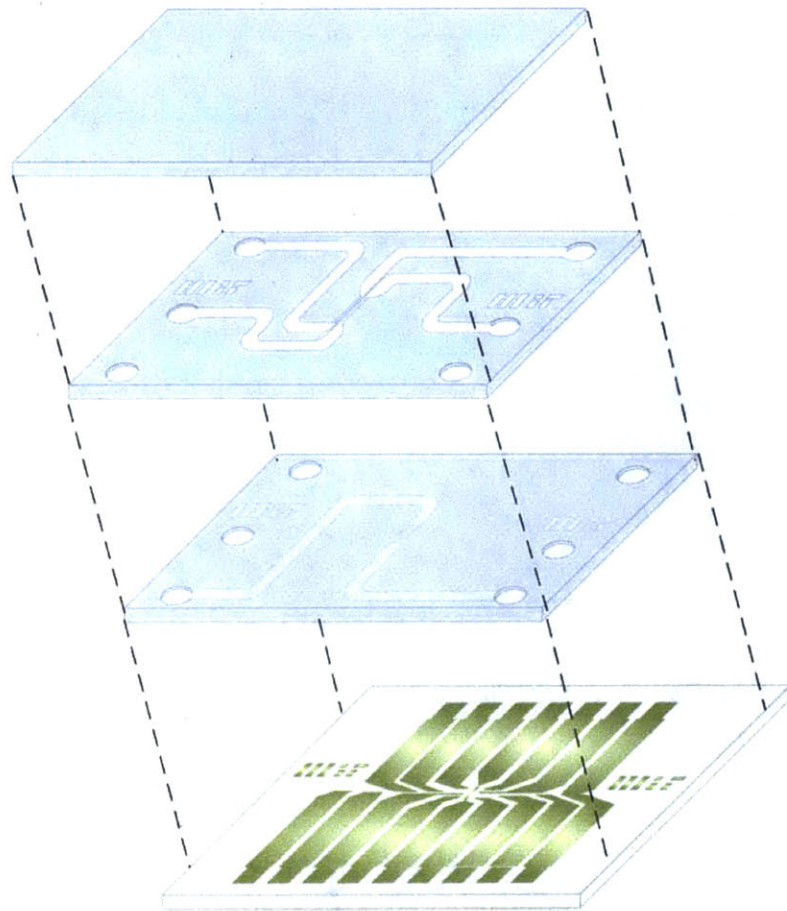
Figure 4-31. *μBA Device Assembly.*

First, the DI header cast is loosely aligned to a glass slide, with the side to be aligned to PHE chip away from the slide. Then, the surfaces of the PHE chip and DI header cast are activated in an RF plasma cleaner/sterilizer unit for 1 minute after the oxygen plasma has turned pink.
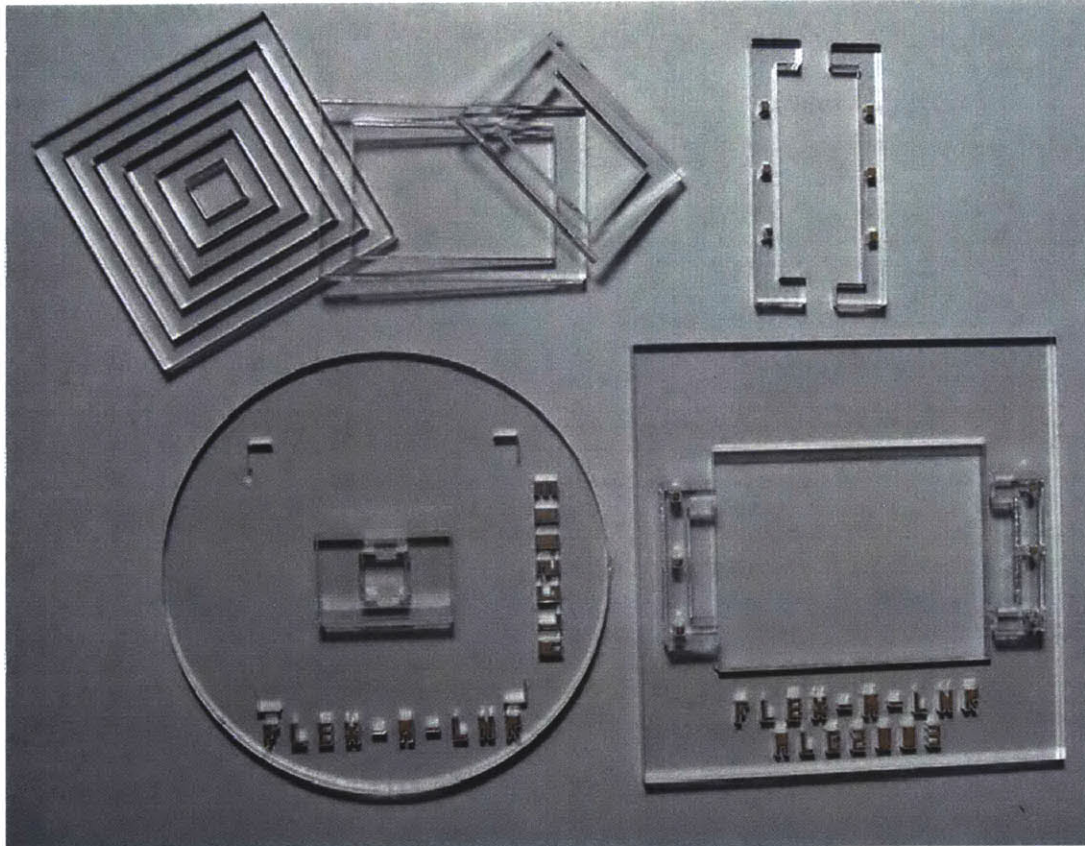
Figure 4-32. *PDMS Alignment Jig.*

Then, the pieces are aligned and brought into contact using the Flex-A-Lnr shown in Figure 4-32. The Flex-A-Lnr is a custom alignment jig that was cut in 0.5 cm clear acrylic using a laser engraving, cutting, and marking system (Legend 24TT, Epilog, Golden, CO). The alignment jig works with standard 100 mm mask aligners. The pseudo-wafer, bottom left in Figure 4-32, is placed in the stead of the wafer. The PHE chip is placed on the platform located at its center, which can be modified in size from 10 - 60 mm square in 10 mm increments by placing the rectangular or square outlines shown at top left over the fixed 10 mm square platform. The pseudo-wafer, bottom right in Figure 4-32, is placed in the stead of the mask. The pseudo-wafer in outfitted with a set of pegs onto which slide brackets, shown on and in the top right of Figure 4-32, can be placed to hold either 75 mm by 25 mm sliders or 75 mm by 50 mm slides. The glass slide is placed into the brackets with the

PDMS layer facing down. The separation of the mask and substrate is reduced, while adjustments are made in the x, y, and θ directions to assure alignment with error on the order of 5 μm [6]. The activation and alignment procedures then are repeated between the IM header and newly bound PHE chip and DI header and finally between the blank PDMS chip and the newly bound PHE chip and headers

Next, the device is fluidically packaged. Macro fluidic connections are made with a 16-gauge syringe tip. PEEK™ tubing (UpChurch Scientific, Oak Harbor, WA) outfitted with a PEEK™ nut and ferrule on one end are inserted into the macro fluid connection holes, nut and ferrule end out. Quick setting epoxy (Radio Shack™, Fort Worth, TX) is used to create a seal between the tubing and PDMS. Figure 4-33 depicts the fluidically packaged device.
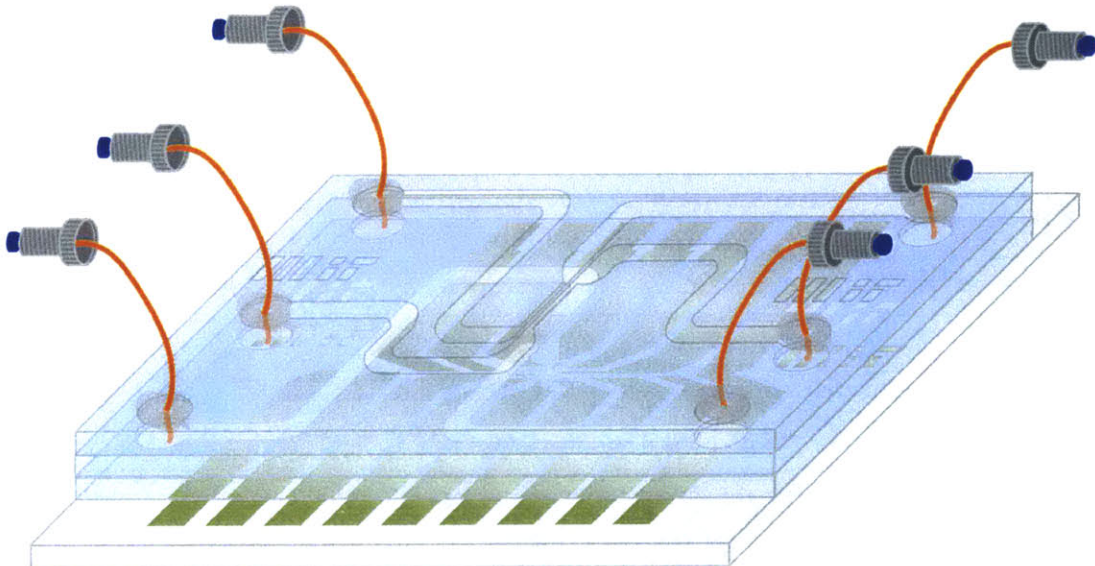
Figure 4-33. *Fluidically Packaged μBA-Based Device.*

The μBA-based device is then soldered to a MMI from which macro connections to the rest of the system architecture can be rapidly made. This packaging scheme allows quick device exchange between testing and characterization runs.
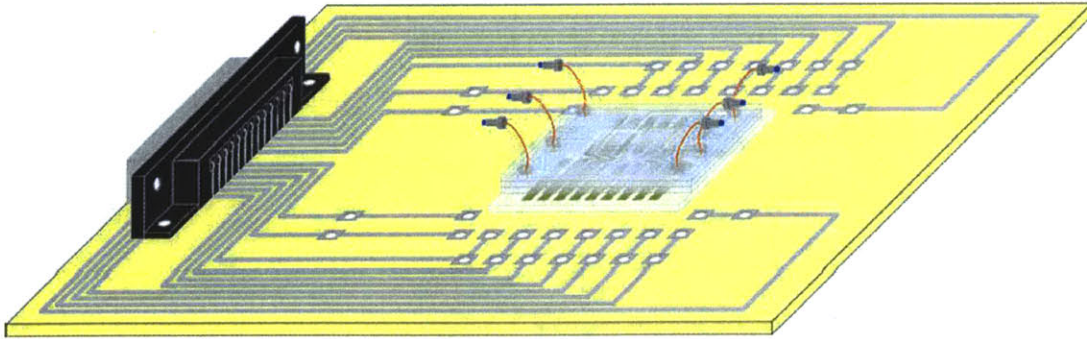
Figure 4-34. *Fluidically Packaged µBA-Based Device.*

4.4.2 Assembly and Packaging Challenges

During the course of assembly and packaging, one main challenge arose —
fabricating the IM and DI casts. The IM cast includes the jet channels, which are
approximately 15 µm in height. Through the jet channels, the IM and DI are fluidically
connected. Thus, the IM and DI casts must be made such that the top of the 50 µm fluidic jet
mold is not covered with PDMS. Similarly, the top of the nucleation chamber mold must not
be covered with PDMS.

In the case of the DI mold, the DI headers and the nucleation chamber are of the same
300 µm height. With practice and exactness, the PDMS can be cast such that the nucleation
chamber is left uncovered. However, a very flat surface must be used for the casting process,
and the PDMS cannot be moved until it is completely cured. In general, leaving the PDMS
covered and left to dry overnight assured a level, low particle count cast.

The IM mold proved a much more challenging casting process, as the 50 µm fluidic
jet could not be optically inspected without a microscope. Additionally, thicker SU-8
depositions on the order of hundreds of micrometers result in a measured 20 - 50 µm height
variation across a wafer. Thus, PDMS casting was completed under a microscope and was
only successful in cases where the height variation across the wafer permitted a careful
selection of which jets were to be covered and which were to be left uncovered. General
results were about half of the jets uncoated and half of the jets coated with PDMS.

4.5   References

[1]   S. D. Senturia, *Microsystem Design*. Norwell, Massachusetts: Kluwer Academic Publishers, 2001.

[2]   E. Ross, Private communication. Alliance for Cellular Signaling (AfCS) 3rd Annual Meeting, Pasadena, CA, 2003.

[3]   R. A. Braff, A. L. Gerhardt, M. Toner, M. L. Gray, and M. A. Schmidt, "Controllable Vapor Microbubbles," *Journal of Microelectromechanical Systems*, Submitted for publication, 2003.

[4]   R. A. Braff, A. L. Gerhardt, M. Toner, M. L. Gray, and M. A. Schmidt, "A Microbubble Bioparticle Actuator," In *Proc. IEEE Conference on Solid State Sensor, Actuator, and Microsystems Workshop*, Hilton Head, South Carolina, 2002, pp. 138-141.

[5]   R. A. Braff, "Microbubble Cell Actuator," S.M. Thesis, Cambridge, Massachusetts: Massachusetts Institute of Technology (MIT), 1999.

[6]   D. J. Bedard, A. L. Gerhardt, T. M. Montalbo, P. R. Russo, M. Shusteff, and L. Theogarajan, "Integration of Microfluidics and Microelectronics: Enabling High Speed Sample Switching and pH Detection," Massachusetts Institute of Technology (MIT), Cambridge, Massachusetts 6.151 Report, May 2002.

Chapter 5   Performance

Testing chip performance involves evaluating the operation of individual resistor geometries and finding trends in the behaviors of individual resistors or in a summation of geometries. The results of such an evaluation can be used to validate the in-plane geometry as a dependable mechanism for microbubble formation. Further, by testing the performance of the fabricated in-plane resistors, a set of guidelines can be presented that serve to forward geometries that offer more repeatable, favorable, or robust results. An overarching performance evaluation adduces out-of-plane geometries in order to present a more complete reference for future microbubble resistor design.

5.1 Hypotheses

5.1.1 Control of Microbubble Shape and Location

In the growth stage of a nucleated microbubble, adjacent liquid provides energy to vaporize more liquid at the liquid-vapor interface. This process stimulates microbubble growth. Modifying the location of the hot adjacent liquid potentially could be used to affect the resultant shape of a microbubble, if heat were applied in a non-symmetric manner. To alter the location of the hot adjacent liquid, the geometry of the resistor is refashioned. By creating a symmetric resistor geometry, the microbubble should be symmetric in shape, namely spherical. Similarly, a non-symmetric resistor geometry should result in asymmetrical microbubbles.

The in-plane heat transfer modeling in Chapter 3 illustrated that for a symmetric resistor, the hottest point on the resistor is at the intersection of the horizontal and vertical lines of symmetry. Thus, for any symmetric geometry with a valid nucleation site, the microbubble should nucleate at the intersection of the horizontal and vertical lines of symmetry. From a collaboration of theory and modeling, the shape and location hypothesis is: bubble shape and location can be controlled by microfabrication.

5.1.2 Regulation of Microbubble Size

Liquid adjacent to the nucleated bubble serves as a growth factor by providing thermal energy to vaporize more liquid at the liquid-vapor interface. By affecting the regional amount of thermal energy available, the maximum size of the microbubble should be able to be affected. Thermal energy is input into the system by means of voltage applied across the resistor for a specified amount of time. By changing the length of time over which voltage is applied, the total energy input into the system is modified.

More energy input into the system should result in more thermal energy available at the liquid-vapor interface. The regulation of microbubble size hypothesis is: Bubble size is a function of energy input, which can be modified by pulse length, resistor resistance, and geometry.

5.1.3 Regulation of Microbubble Dissipation

According to microbubble theory, microbubble dissipation occurs when the bubble has extended beyond the layer of superheated liquid. At this point, thermal energy at the liquid vapor interface is no longer acting as a growth factor, and the bubble dissipates through evaporation and convection losses. The larger a microbubble is, the more vaporized liquid it contains within its volume. And, the larger a microbubble is, the more time the microbubble should require to dissipate. Thus, the microbubble dissipation hypothesis is: bubble dissipation is a function of maximum bubble size.

5.2 Methods

5.2.1 Experimental Apparatus

The chips are tested using the relevant portions of the system architecture presented in Chapter 4. For convenience, Figure 5-1 redepicts this architecture.
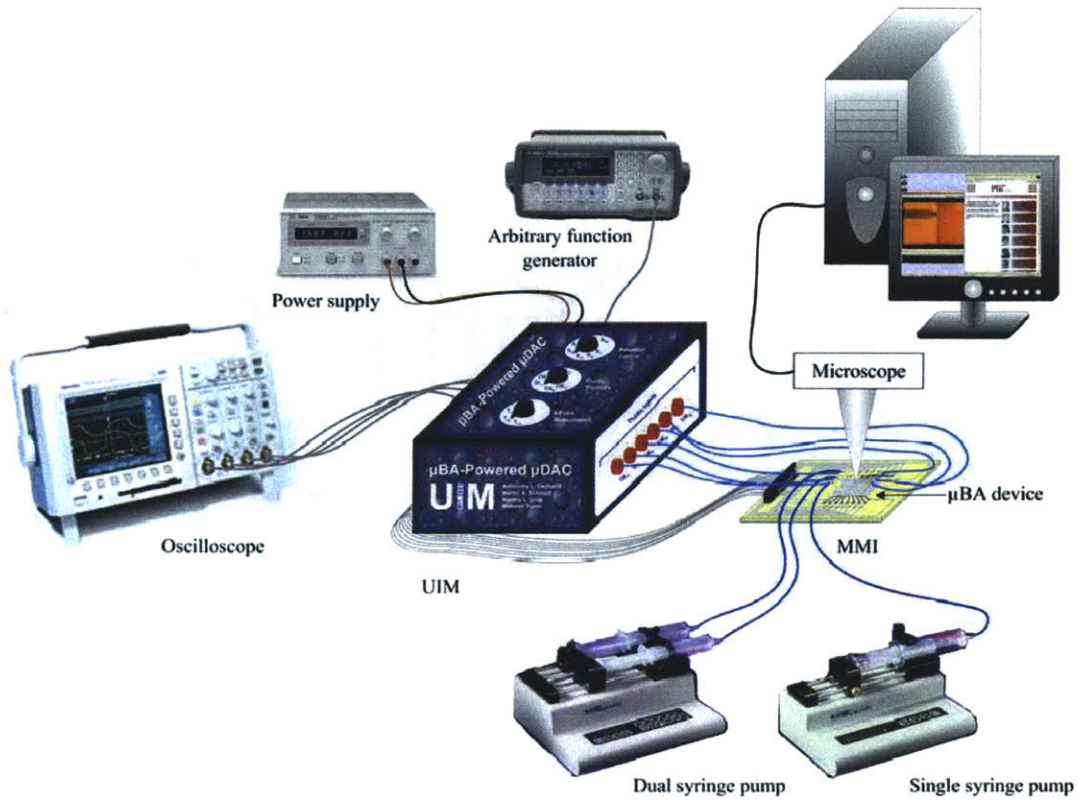
Figure 5-1. *System Architecture.*

Each PHE chip is soldered to an MMI, which is then connected to the UIM via a male-female D-Sub cable. The arbitrary function generator is used to input pulses of varying length, and the microbubbles are observed under the probe station microscope outfitted with a digital video camera. An oscilloscope is used to monitor the signal input for the system and various outputs of the UIM. The TSCs are tested in a similar manner. However, the TSCs are designed to maximize the number of geometries on an individual chip rather than to be compatible with the MMI. Thus, probe tips are used to make the electrical connection with the individual resistor pads. Figure 5-2 illustrates the standard electrical contacts for a TSC.
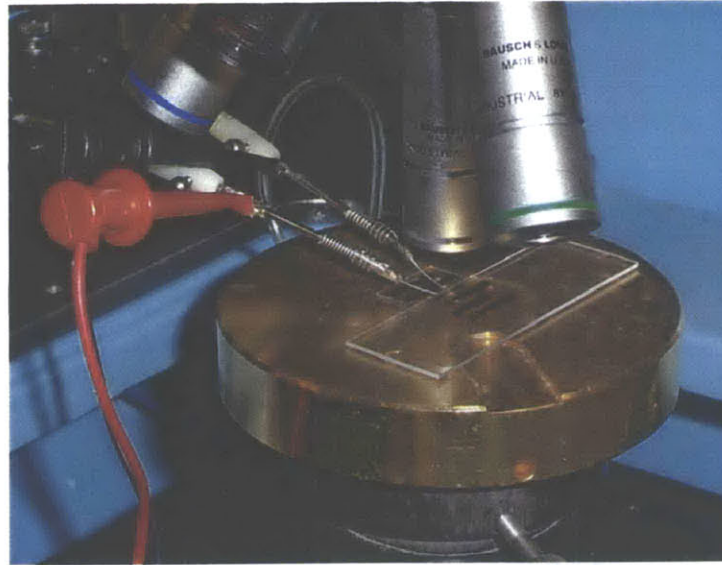
Figure 5-2. *TSC Electrical Contact Scheme.*

Previous research [1-5] using tap DI water as the medium for bubble nucleation reported a problem with residual air bubbles that remained in the system for more than an hour. To diminish this problem, a method of decreasing the dissolved air content of the water was implemented. Boiling the DI water before use decreased the water solubility, which improved microbubble dissipation times. A similar protocol is used for the purposes of the performance testing. Before use, tap DI water is boiled in a beaker on a hotplate. Only after the DI reaches a rapid boil is the water pipetted from the beaker. Pipetted DI water age is recorded during all experiments.

In early testing after the electrical connections were made, boiled DI water was immediately pipetted onto the chip over the resistors of interest, and a glass slide was placed on top. This is also shown in Figure 5-2. To maintain a consistent amount of DI water over the resistors of interest and to more closely simulate the system conditions of a packaged device, later testing uses PDMS gaskets that were manufactured in similar manner to the fluidic channel PDMS fabrication process described in Chapter 4. To enable rapid gasket exchange, the PDMS is not activated in oxygen plasma. Instead, the inherent adhesiveness of the PDMS is used to create a seal. After aligning a fresh PDMS gasket, the gasket is filled

with boiled DI, and a cover slip is placed on top. Figure 5-3 illustrates a schematic of a PDMS gasket aligned over a series of resistors on a TSC, and Figure 5-4 is the corresponding photograph.
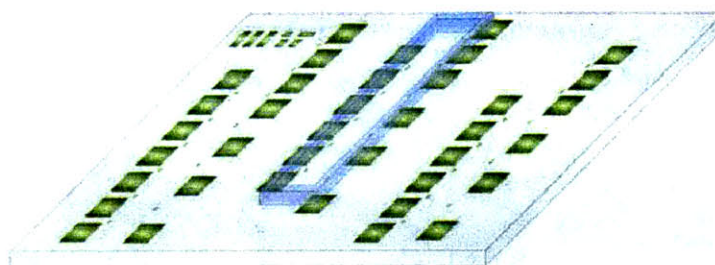
Figure 5-3. *Illustration of PDMS Gasket on TSC.*
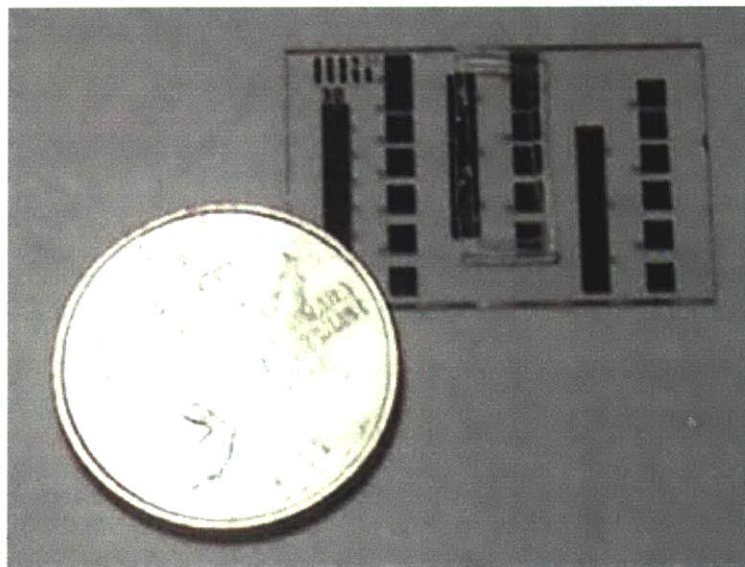
Figure 5-4. *Photograph of PDMS Gasket on TSC.*

Because the PDMS gaskets could not be resealed to a chip after one or two uses, new PDMS gaskets are used throughout the experiments.

5.2.2 Microscope-to-Video Measurement Calibration

The video captures from the capture software outputting the microscope view are used to measure the microbubble at its various stages of growth and decay. To calibrate the measurements, 14.69 μm microspheres (FS07F/5838, Bangs Laboratories, Fishers, IN) are injected into the boiled DI solution contained in a gasket on a TSC. Several video captured microspheres are measured at the crucial objective powers.

5.2.3 Resistor Element Values

To determine resistances of the fabricated resistors, probe tips are used to make electrical contact. A multimeter (TEK DMM254, Tektronix, Inc., Beaverton, OR) then is connected to the probe tips and used to take a resistance reading both before and after resistor operation. The resistance readings are used to validate theoretical calculations made using Equation 4-1. Given the resistance readings do validate the theoretical calculations for larger resistance resistors, theoretical values are used for smaller resistors, where heating due to the multimeter current causes variable resistance readings.

5.2.4 System Inputs

Two distinct input patterns were used in the performance testing of the chips — standard input and chirped input. The standard input is depicted in Figure 5-5. In the standard input, the pulse has height 5 V and width δ and is repeated with a frequency f_Δ of $1/\Delta$. For the testing, $\delta = 0.125 - 50$ ms, and $\Delta = 1$ s, 2 min, and 15 min.

140
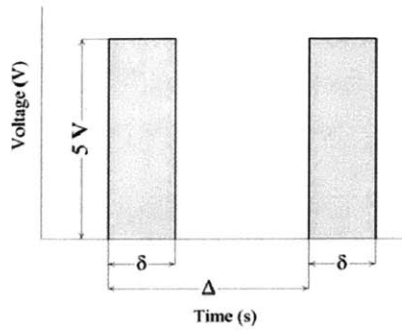
Figure 5-5. *Standard Input.*

The chirped input is depicted in Figure 5-6. For the chirped input, the pulse has height 5 V and width δ and is repeated with a frequency f_Δ of $1/\Delta$. For the testing, the most common pulse widths are δ = 5, 10, 20, 30, 40, 50 ms, which can be written as 5, 10:10:50 ms. Other pulse widths include: δ = 5:5:50 ms, δ = 1:1:10 ms, δ = 1:1:40 ms, and δ = 1, 2:2:10 ms. For all δs, Δ = 1 s, 2 min, 15 min, or ∞.
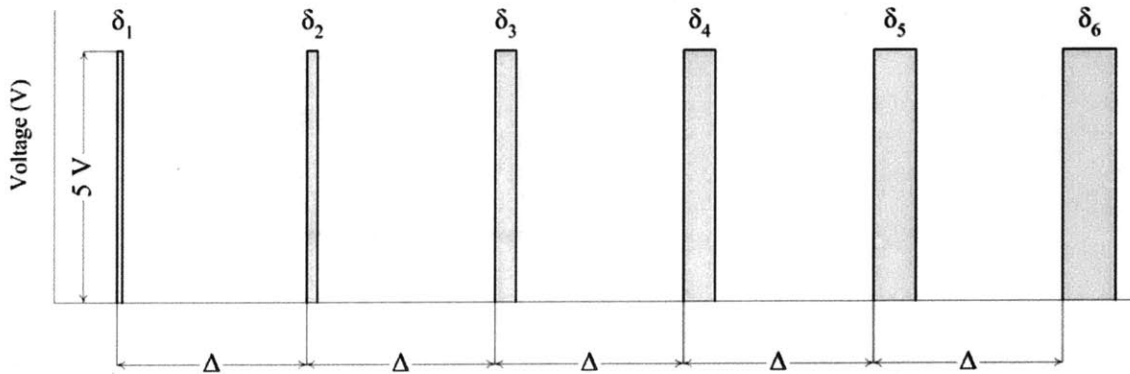
Figure 5-6. *Chirped Input.*

5.2.5 Eccentricity

Eccentricity e is a parameter often used in mathematics and astronomy to measure the deviation of a conic section from circularity or the ellipticity of an object. This parameter quantifies the shape of an object. The eccentricity is defined as

$$e = \sqrt{1 - \frac{b^2}{a^2}} \qquad (5\text{-}1)$$

where a is the length of the semi-major axis, and b is the length of the semi-minor axis. As a point of reference, a perfect circle would have $e = 0$. An ellipse would have $0 < e < 1$. For a microbubble, an eccentricity measurement is taken as shown in Figure 5-7.
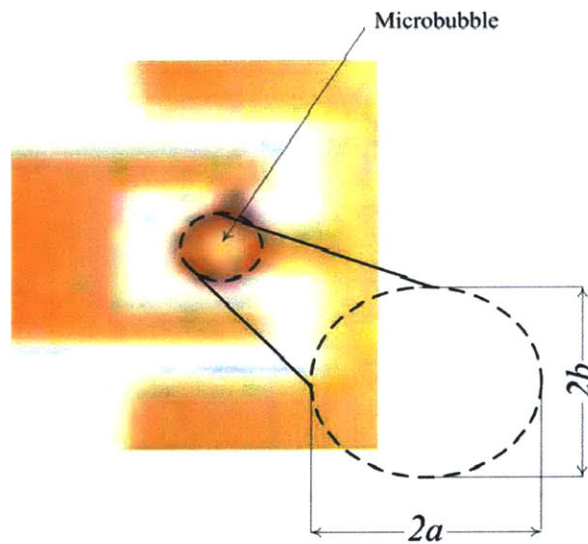
Figure 5-7. *Eccentricity.*

5.2.6 Centricity

Centricity c is a constant used to quantify the deviation of the center of a circle or ellipse from a designated point. The centricity is defined as

$$c_x = \frac{d_x}{r_x} \tag{5-2}$$

$$c_y = \frac{d_y}{r_y} \tag{5-3}$$

where d is the distance from the center of the nucleation site to the center of the microbubble in the x- or y-direction, and r is the radius of the microbubble. As a point of reference, a perfectly centered microbubble would have $c_x = c_y = 0$. A microbubble whose left edge was at the nucleation site and was centered in the y-direction would have $c_x = 1$ and $c_y = 0$. For a microbubble, an centricity measurement would be taken as shown in Figure 5-7.
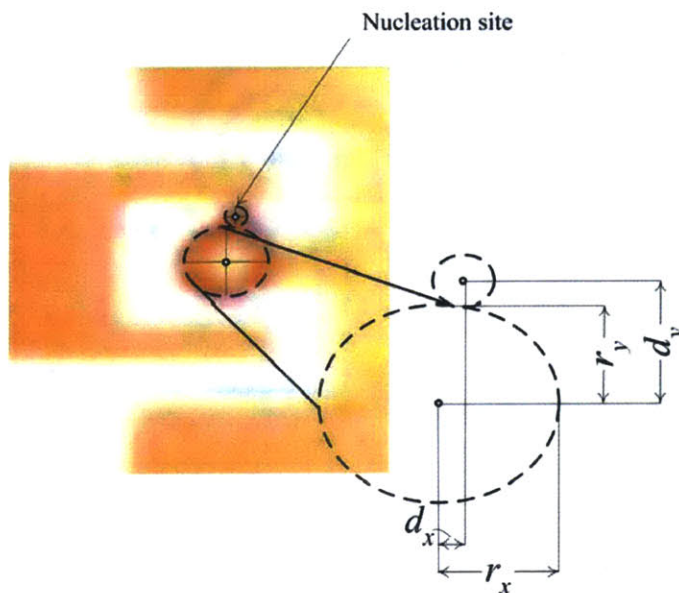
Figure 5-8. *Centricity.*

5.2.7 Transient Diameters

A typical complete system response to a standard pulse input of width δ = 30 ms with micrographs of the system at critical points along the dissipation curve is shown in Figure 5-9. For this example, a standard input pulse with δ = 30 ms is applied to a resistor with a 30 µm long by 3 µm wide nucleation site. The total resistance of the resistor is approximately 35 Ω. The complete system response consists of a fast transient response and a slow transient response. For each transient response, the average diameter $\overline{D}$ is measured along the major and minor axes of the microbubble at different times in the dissipation process.
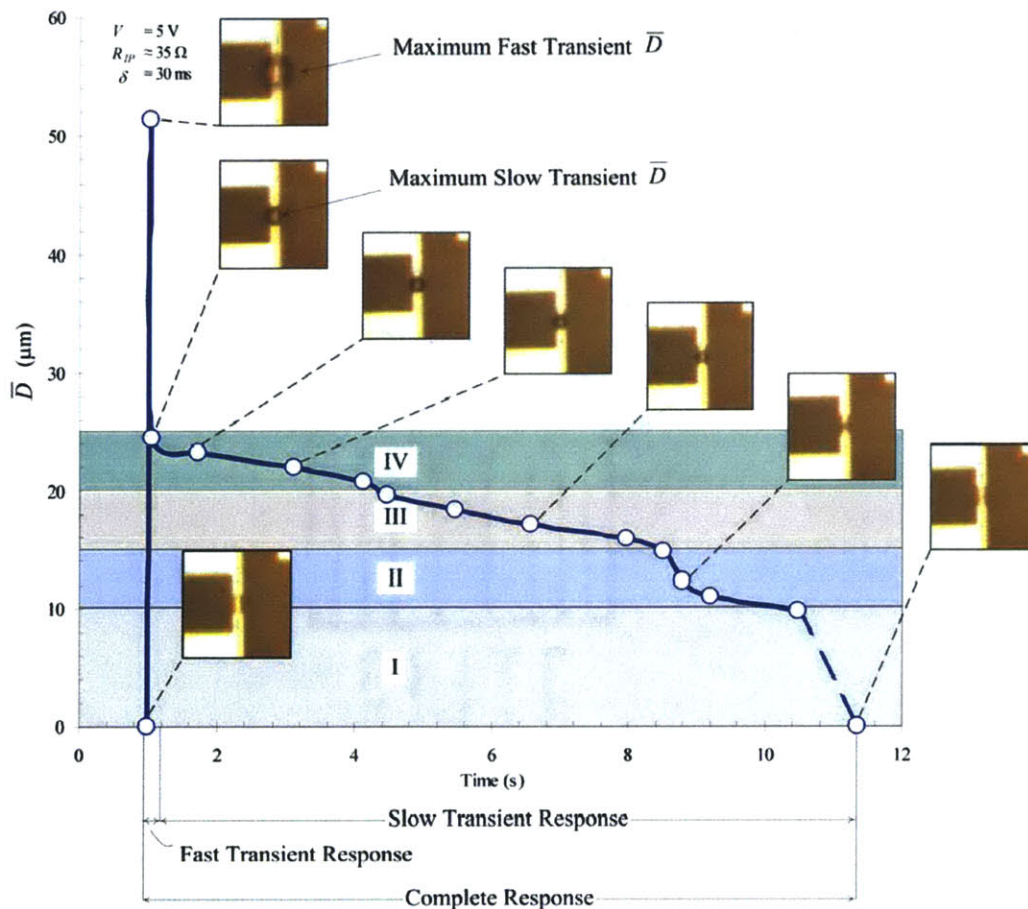
Figure 5-9. *Transient Diameters.*

The $\overline{D}$ is defined as

$$\overline{D} = \frac{2a + 2b}{2}$$

(5-4)

where a is the length of the semi-major axis, and b is the length of the semi-minor axis. The maximum $\overline{D}$ is defined as the largest measured transient $\overline{D}$ for a given response. Thus, each complete response has two maximum $\overline{D}$ values.

The confidence interval in $\overline{D}$ measurements mainly is due to the limitation of the resolution of the video capture device and the power of the objective. A 25× objective was used throughout the data acquisition process. The confidence interval increases as the microbubble diameter decreases as smaller microbubbles consist of fewer pixels, which makes it challenging to clearly define the outline of the microbubble.

For example, Figure 5-10 contains three micrographs of a microbubble dissipating with time. In the first frame at $t = 1.034$ s, the fast transient is visible. In the second frame at $t = 1.068$ s, the slow transient is visible, which dissipates to the frame at $t = 10.611$ s. In the final micrograph, the microbubble clearly is visible at the center of the nucleation site. However, measuring the first fast transient microbubble is a visually simpler task than measuring the nearly dissipated microbubble in the third frame. Endpoints of the D measurements for $2a$ and $2b$ are indicated on the lower row of micrographs.

t = 1.034 s   *t* = 1.068 s   *t* = 10.611 s
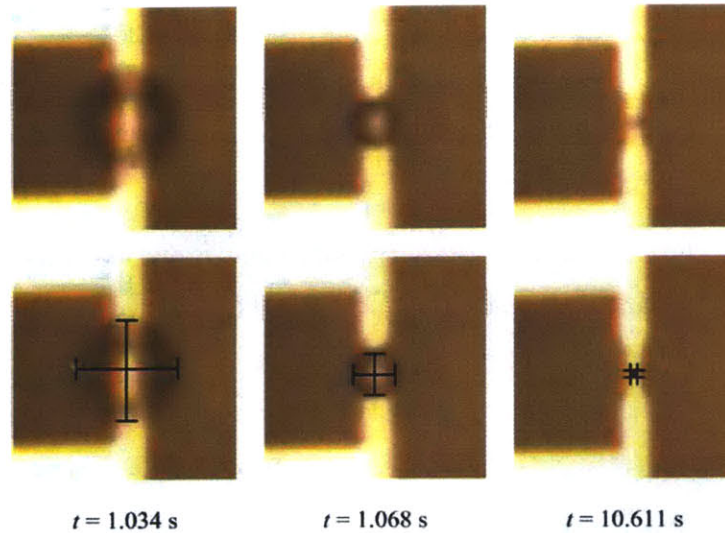
Figure 5-10. *Transient Diameter Micrographs.*

To quantify the confidence interval in $\overline{D}$ measurements, the maximum reading and minimum reading for each axis was recorded for several microbubble for varying diameter. The confidence interval was determined to be ± 1.5 μm for microbubbles in region V, ± 2 μm for microbubbles in region IV, ± 2.5 μm for microbubbles in region III, ± 3.5 μm for microbubbles in region II, and data for microbubbles in region I will be omitted or denoted with dashed lines as depicted in Figure 5-9.

The maximum $\overline{D}$ confidence interval for the slow transient follows the same confidence interval increase with diameter decrease progression as the standard $\overline{D}$ measurements. However, the maximum $\overline{D}$ confidence interval for the fast transient mainly is due to the limitation of frame rate on the video camera, as the fast transient is only visible in one or two frames. Thus, the fast transient most likely does not peak in dimension in one of the frames captured for further analysis.

5.2.8 Transient Dissipation Times

A typical complete system response to a pulse input of width δ is shown in Figure 5-11. Micrographs depict the system at critical points along the dissipation curve. For this example, a standard input pulse with $\delta = 30$ ms is applied to a resistor with a 30 μm long by 3 μm wide nucleation site. The total resistance of the resistor is approximately 35 Ω.
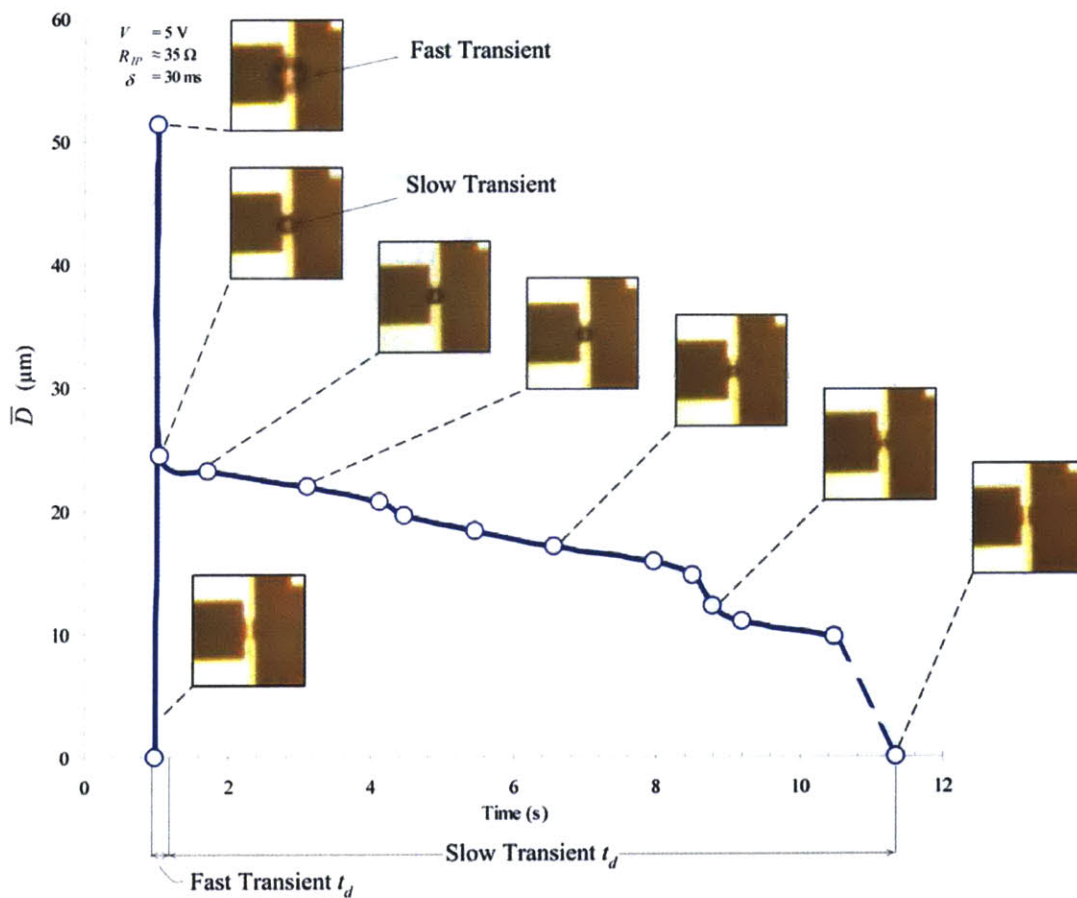
Figure 5-11. *Transient Dissipation Times.*

The complete system response consists of a fast transient response and a slow transient response. For each transient response, the dissipation time t_d is measured.

The fast transient dissipation time is denoted in Figure 5-11 and illustrated in Figure 5-12. The fast transient t_d is measured from the frame before the transient is evident to the

frame after the transient is no longer evident. For example, Figure 5-12 illustrates dissipation micrographs. The captures are shown at the limit of the frame rate of the video camera. In the first frame at $t = 1.001$ s, no microbubble is visible. In the second frame at $t = 1.034$ s, the fast transient response is visible and has ended before the time of the third micrograph at $t = 1.068$ s where the slow transient response is evident. Thus, the fast transient response is reported as $t_d = 6.7$ ms. During testing, the longest fast transient response is visible in two micrographs, meaning $t_d = 10$ ms.

| $t = 1.001$ s | $t = 1.034$ s | $t = 1.068$ s | $t = 1.101$ s |
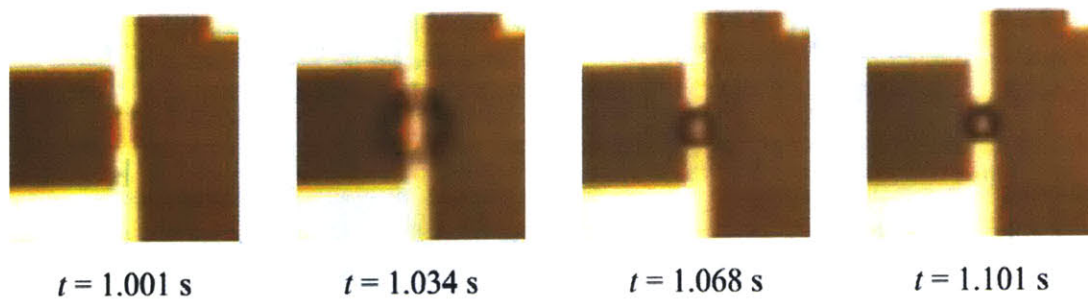
Figure 5-12. *Fast Transient Dissipation Micrographs.*

The size of the confidence interval in the fast transient t_d measurement mainly is due to the limitation of the frame rate of the video capture device. The camera captures at a rate of 30 frames/sec. When the fast transient is visible in one micrograph, the confidence interval is ± 0.032 ms, as the transient was not visible 33 ms before or 33 ms after the frame. However, the data is not available for the time between the frames displaying the event. The same confidence interval applies when the fast transient is visible in two micrographs as the data is not available to determine if the fast transient appeared at 20 ms before the micrograph displaying the transient or only 1 ms before the micrograph.

The slow transient dissipation time is denoted in Figure 5-11 and illustrated in Figure 5-13. The slow transient t_d is measured from the frame where the slow transient first is evident to the frame after the transient is no longer evident. For example Figure 5-12 illustrates dissipation micrographs. In the first frame at $t = 1.034$ s, the fast transient response is visible and has ended before the time of the third micrograph at $t = 1.068$ s where

the slow transient response first is evident. The slow transient response continues through hundreds of frames, diminishing in diameter with time. In the frame at $t = 11.311$ s, the slow transient barely is visible. When viewing frame-by-frame at higher resolution, however, the transient microbubble still is evident. In the next frame at $t = 11.345$ s, the slow transient is indecipherable. Looking at the following frame confirms microbubble collapse at $t = 11.345$ s. Thus, slow transient response is reported as $t_d = 10.277$ s.

| $t = 1.034$ s | $t = 1.068$ s | $t = 8.342$ s | $t = 9.376$ s |

| $t = 10.611$ s | $t = 11.311$ s | $t = 11.345$ s | $t = 11.378$ s |
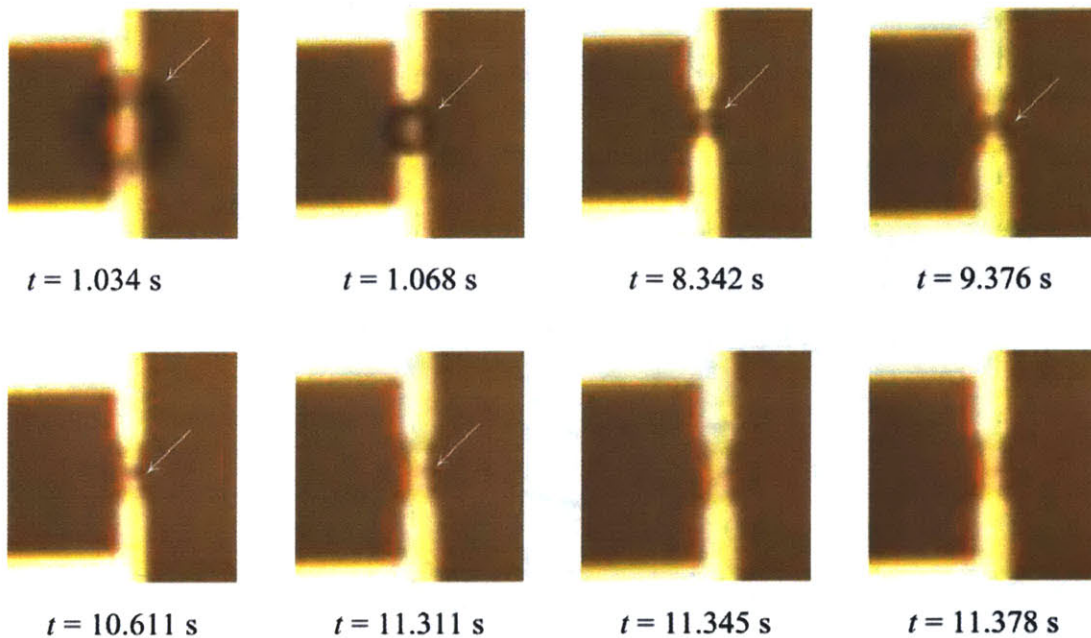
Figure 5-13. *Slow Transient Dissipation Micrographs.*

The confidence interval in the slow transient t_d measurement is due to the limitation of the resolution of the video capture device and the power of the objective. A 25× objective was used throughout the data acquisition process. The confidence interval is ± 0.1 s, as the slow transient may have been visible as much as 32 ms before the frame in which it was evident. However, the data is not available for the time between the frames displaying the event. Similarly, three to four frames at the end of the dissipation are arguably the last frame in which the slow transient is evident. For reference, a sampling of raw data is included in Appendix D.

5.3 Results

5.3.1 Archetypal Curves

For the in-plane (IP) geometries described in Chapter 4, the lowest level of data processing from a single acquisition is the complete system response depicted in terms of average microbubble diameter as a function of time. Figure 5-14 is a plot of such a system response with micrographs depicting the system at critical points along the dissipation curve. For this example, a standard input pulse with $\delta = 30$ ms and $\Delta = \infty$ is applied to a resistor with a 10 μm long by 3 μm wide in-plane nucleation site and total resistance of about 19 Ω.

$$V = 5\ V$$
$$R_{IP} \approx 19\ \Omega$$
$$\delta = 30\ ms$$
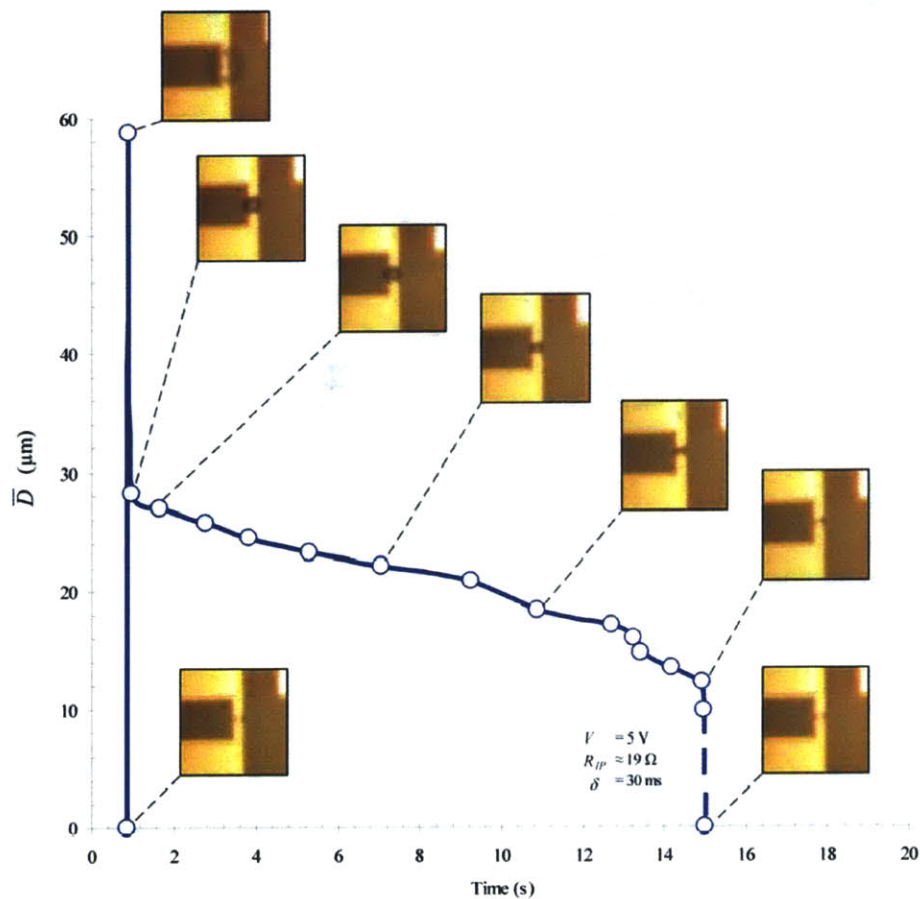
Figure 5-14. *Complete System Response for Resistor with 10 μm Nucleation Site.*

Figure 5-15 illustrates a system response to a standard input pulse width of δ = 30 ms and $\Delta = \infty$ applied to a resistor with a 20 µm long by 3 µm wide nucleation site and total resistance of about 21 Ω. The fast transient response is visible in a single micrograph. The slow transient is evident for > 15 sec before the system returns to steady-state.
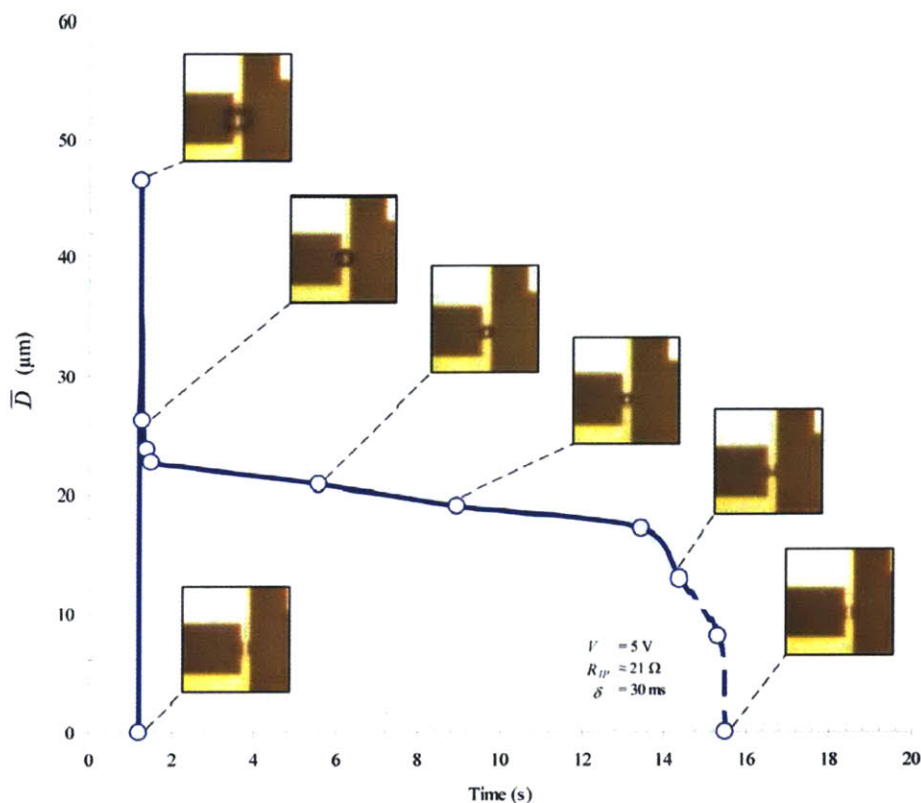
Figure 5-15. *Complete System Response for Resistor with 20 µm Nucleation Site.*

Figure 5-16 is also a system response to a standard input pulse width of δ = 30 ms and $\Delta = \infty$ applied to a resistor. However, this resistor has a 30 µm long by 3 µm wide nucleation site and total resistance of about 35 Ω. The fast transient response is visible in a single micrograph, while the slow transient is evident for < 12 sec.
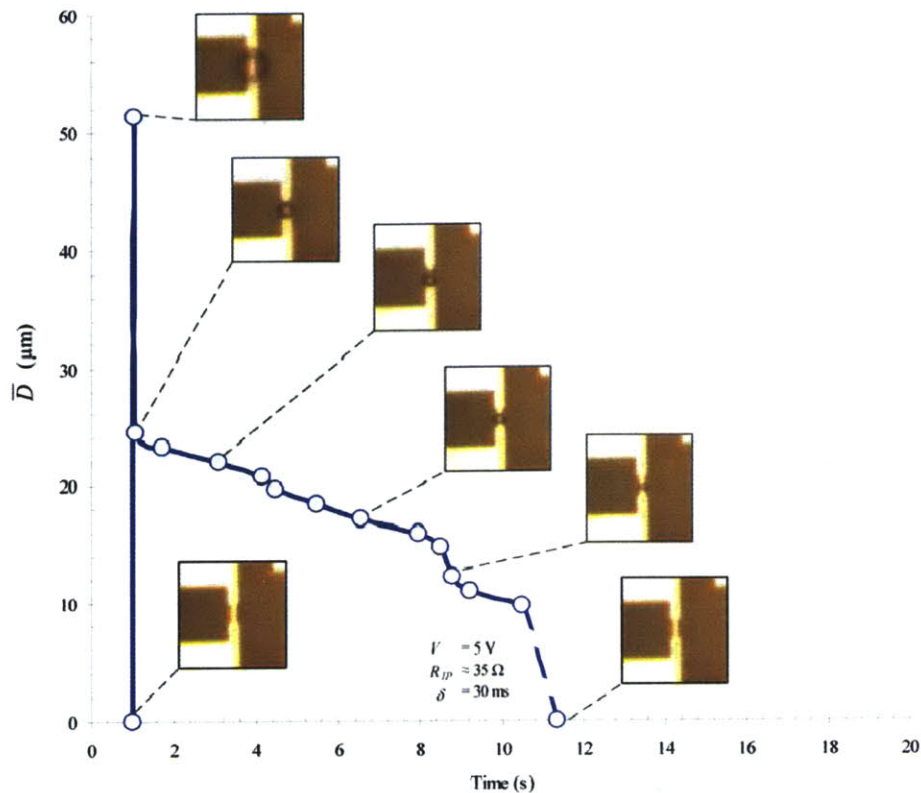
Figure 5-16. *Complete System Response for Resistor with 30 μm Nucleation Site.*

As can be seen from the prototypical complete system response plots, the slow transient $\overline{D}$ decreases as resistor resistance increases for a constant δ and infinite Δ. The fast transient $\overline{D}$ does not appear from the plots to follow a similar trend. For the linear in-plane geometry resistors with patterned nucleation site lengths of 10, 20, and 30 μm and 3 μm in width, microbubbles formed exclusively at the nucleation sites throughout the performance testing. Additionally, only a single microbubble nucleated on the resistor, regardless of the combination of standard and chirped inputs with varying δ and Δ.

The other nucleation site length and width combinations delineated in Chapter 4 did not yield such consistent results. The 3 μm wide nucleation site combinations were successful individual bubble nucleators for total lengths up to 150 μm, inclusively, using standard inputs with $\delta \leq 100$ ms and $\Delta = \infty$. Further results will be presented for the 108

152

in-plane geometries of 10, 20, and 30 μm long by 3 μm wide nucleation sites with total resistor lengths up to 150 μm.

The only system response that is not represented by the typical response curves is for the 10 μm long nucleation site with total resistance of about 7 Ω. This small resistor dependably displayed a fast transient response. However, no slow transient response is evident for $\delta = 5$, 10:10:40 ms. As δ increased, the fast transient maximum $\overline{D}$ increased, while the total system response remained < 10 ms. Figure 5-18 depicts the complete response of the 7 Ω resistor-bubble system to a chirped input with $\delta = 5$, 10:10:50 ms and $\Delta = 2$ min. The micrographs display the response to the fifth input, where $\delta = 40$ ms.
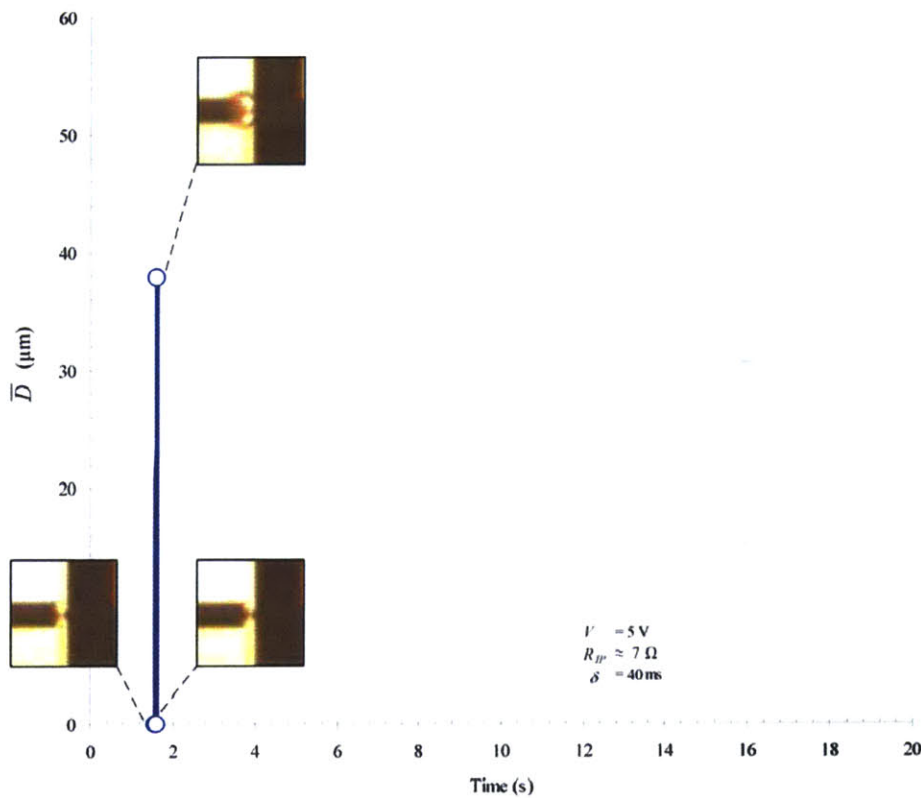
Figure 5-17. *Complete System Response for 7 Ω Resistor.*

For $\delta = 50$ ms, the fast transient response was evident in two frames, and a slow transient response was evident in three frames. Thus, the total system response was < 2 ms.

A typical curve for a chirped input with $\delta = 5$, 10:10:50 ms and $\Delta = 2$ min is shown in Figure 5-18. For each system response to the input pulse, the slow transient maximum $\overline{D}$ is measured and then is plotted as a function of δ or energy. For Figure 5-18, plotting as a function of energy is equivalent to scaling the x-axis as the voltage and resistance are held constant. The main trend evident in Figure 5-18 is that as input δ or energy increases, the slow transient maximum $\overline{D}$ also increases. The shaded and hatched region denotes the confidence interval.
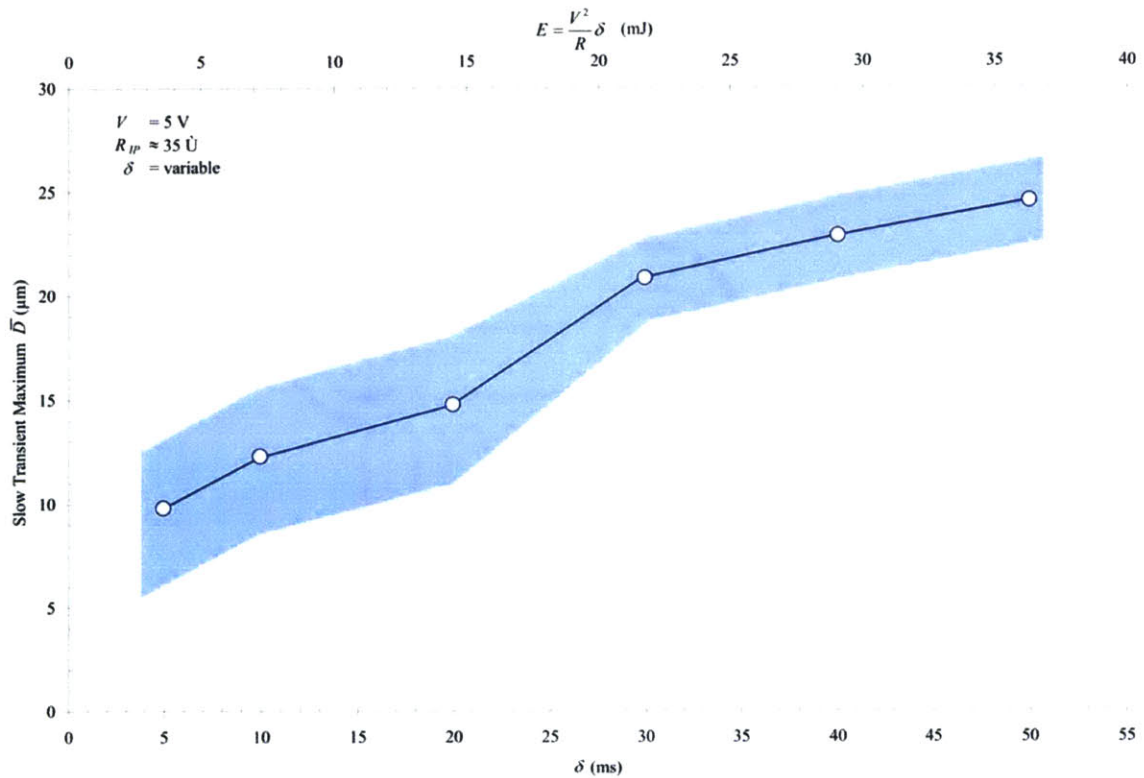
Figure 5-18. *Representative Chirped Input Maximum Diameter Curve.*

154

The slow transient t_d also can be plotted as a function of δ or energy. A prototypical curve for a chirped input with $\delta = 5$, 10:10:50 ms and $\Delta = 2$ min is shown in Figure 5-19. For each system response to the input pulse, the slow transient t_d is measured and plotted as a function of δ or energy. For Figure 5-19, plotting as a function of energy also is equivalent to scaling the x-axis as the voltage and resistance are held constant. From Figure 5-19, the slow transient t_d increases as the input δ or energy increases.
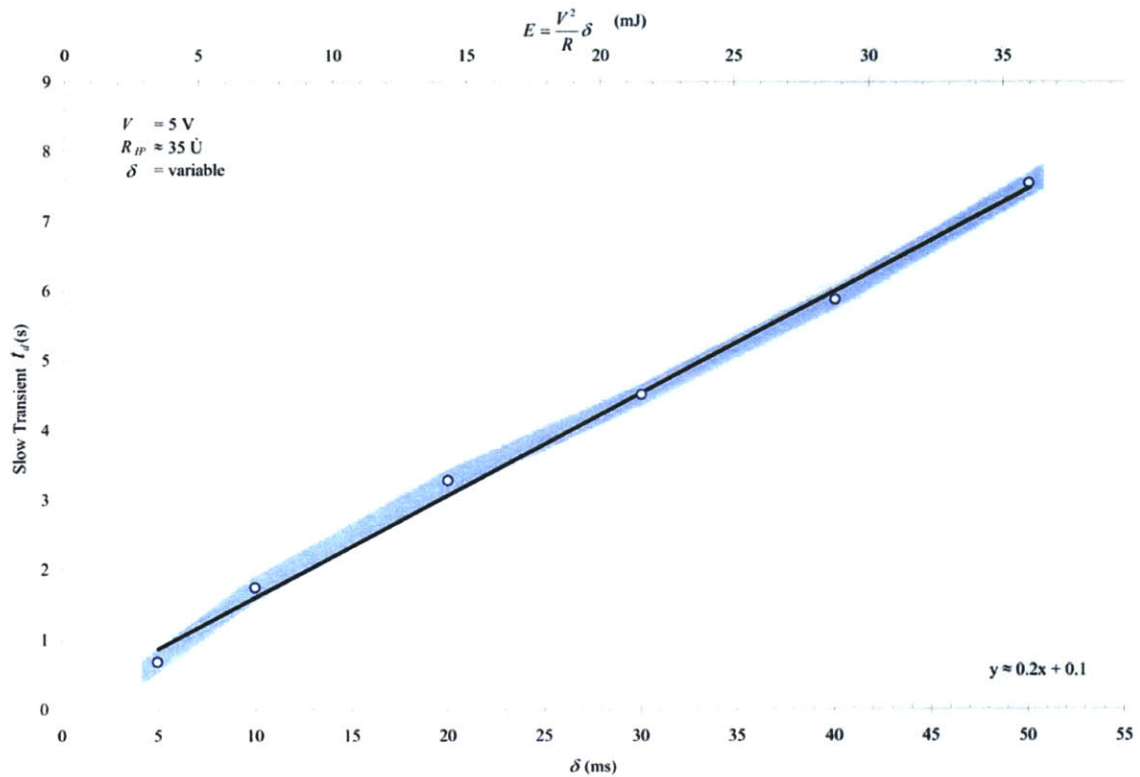
Figure 5-19. *Representative Slow Transient t_d Curve.*

In addition to plotting the slow transient maximum $\overline{D}$ and t_d as functions of δ or energy, the slow transient maximum $\overline{D}$ and t_d can be plotted against each other. A typical curve for a chirped input with $\delta = 5$, 10:10:50 ms and $\Delta = 2$ min is shown in Figure 5-20. For each system response to the input pulse, the slow transient maximum $\overline{D}$ and t_d are measured and plotted as the y- and x-axis, respectively.
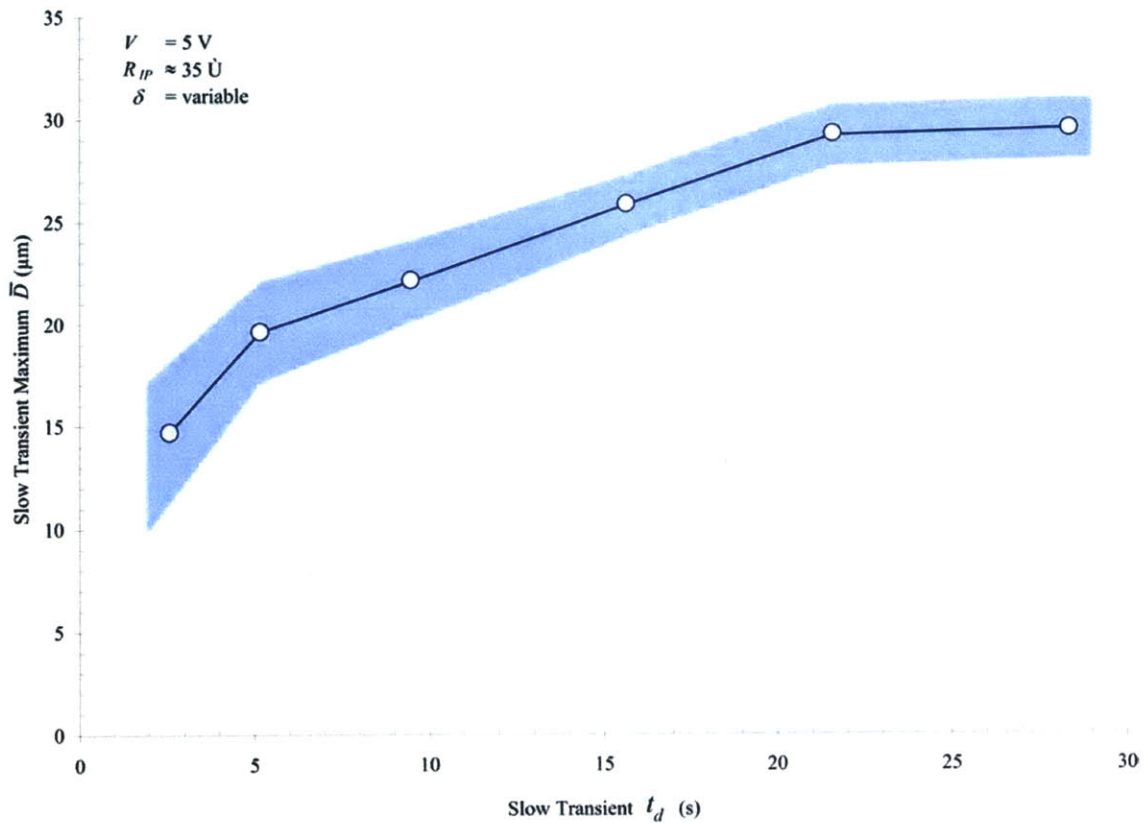
Figure 5-20. *Representative Slow Transient Maximum Average Diameter vs. t_d Curve.*

Figure 5-20 illustrates the third trend: as the slow transient maximum $\overline{D}$ increases in diameter, the dissipation time increases. Thus, Figure 5-18, Figure 5-19, and Figure 5-20 are inexorably linked. Increasing the input δ or energy increases the slow transient maximum $\overline{D}$ that, in turn, increases the t_d.

5.3.2 Microbubble Shape and Location

The compilation of eccentricity and centricity results from chirped inputs on resistors of varying resistance for $\delta = 5$, 10:10:50 ms and $\Delta = 2$ min is shown in Figure 5-21. The data is plotted statistically in box plots.
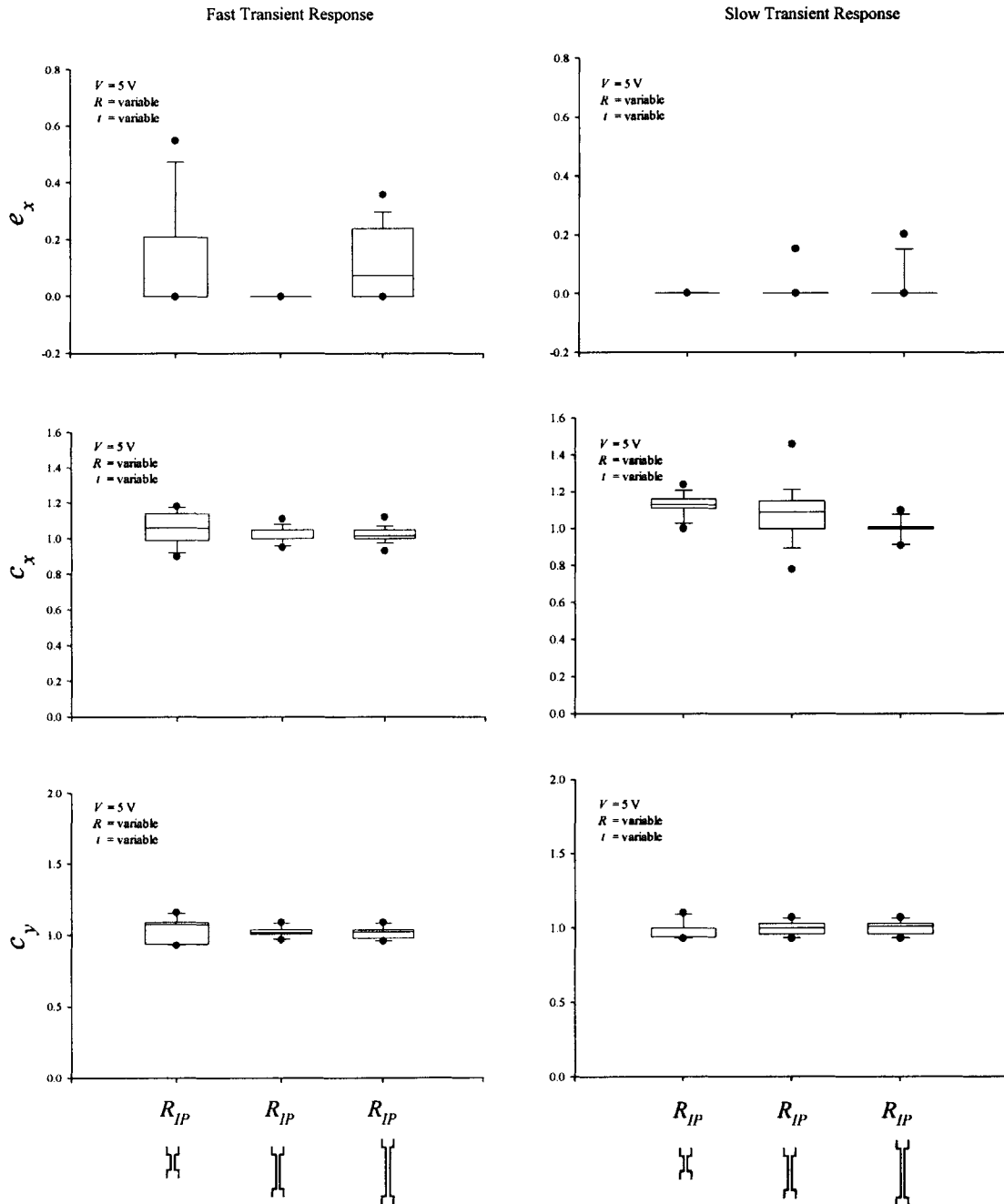
Figure 5-21. *In-Plane Microbubble Shape and Location.*

The line in the middle of each box plot corresponds to the median. The whisker below each box represents the 10th percentile, and the whisker above each box represents the 90th

percentile. The boundary of the box closest to the origin portrays the 25th percentile, and the box boundary away from the origin renders the 75th percentile. The 5th and 95th percentiles are represented as outlining points closest to and farthest from the origin, respectively.

As illustrated at the bottom of the figure, the first column in each set of box plots corresponds to a 10 μm long by 3 μm in-plane nucleation site. Similarly, the second and third columns in each set of box plots depict data from a 20 μm long and 20 μm nucleation site by 3 μm wide, respectively. The fast and slow transient system responses are nearly perfect spheres, where a perfect sphere would have an $e = 0$. Greater ellipticity is present in the fast transient response, while the majority of data points for the slow transient response are at $e = 0$.

The center of the microbubbles in the x-direction nearly is aligned with the center of the 3 μm nucleation site, where $c_x = 1$ represents a perfect alignment. In kind, the center of the microbubbles in the y-direction are aligned at the center point of the length of the nucleation site, where $c_y = 1$ represents an ideal alignment. Thus, the microbubbles are forming at the intersection of the x-direction and y-direction lines of symmetry on the in-plane resistors.

5.3.3 Microbubble Size

A variation of the chirped input slow transient maximum $\overline{D}$ curve shown in Figure 5-18 is depicted in Figure 5-22. Chirped input pulse widths of $\delta = 5$, 10:10:50 ms and $\Delta = 2$ min were used on several resistors of varying resistance. In Figure 5-18, the observed trend is that as input δ or energy increases, the slow transient maximum $\overline{D}$ also increases. With variation in resistance as well as δ, Figure 5-22 more strongly demonstrates that as input energy increases, the slow transient maximum $\overline{D}$ also increases.
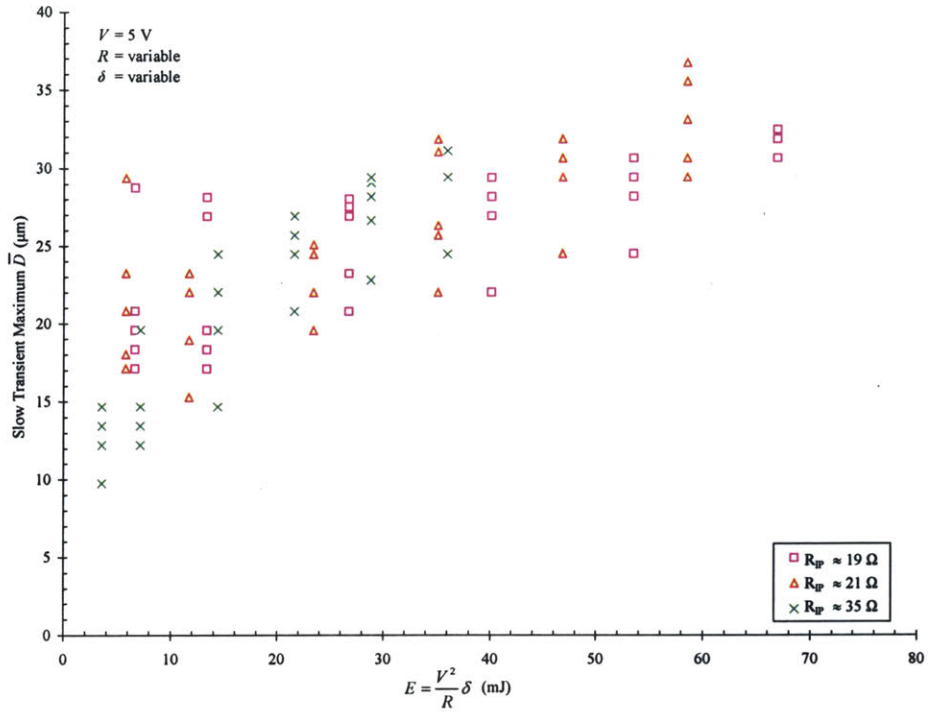
Figure 5-22. *In-Plane Slow Transient Maximum Microbubble Size.*

5.3.4   Microbubble Dissipation

Chirped input pulse widths of δ = 5, 10:10:50 ms and Δ = 2 min were used on resistors of varying resistance to compile a dense representation of the slow transient t_d curve shown in Figure 5-19. In Figure 5-19, the observed trend is that the slow transient t_d increases as the input δ or energy increases. With variation in resistance as well as δ, Figure 5-23 more strongly demonstrates the trend that slow transient t_d increases as input energy increases. A linear fit was applied to the data. The equation of the fit is shown at the bottom of the legend in Figure 5-23.
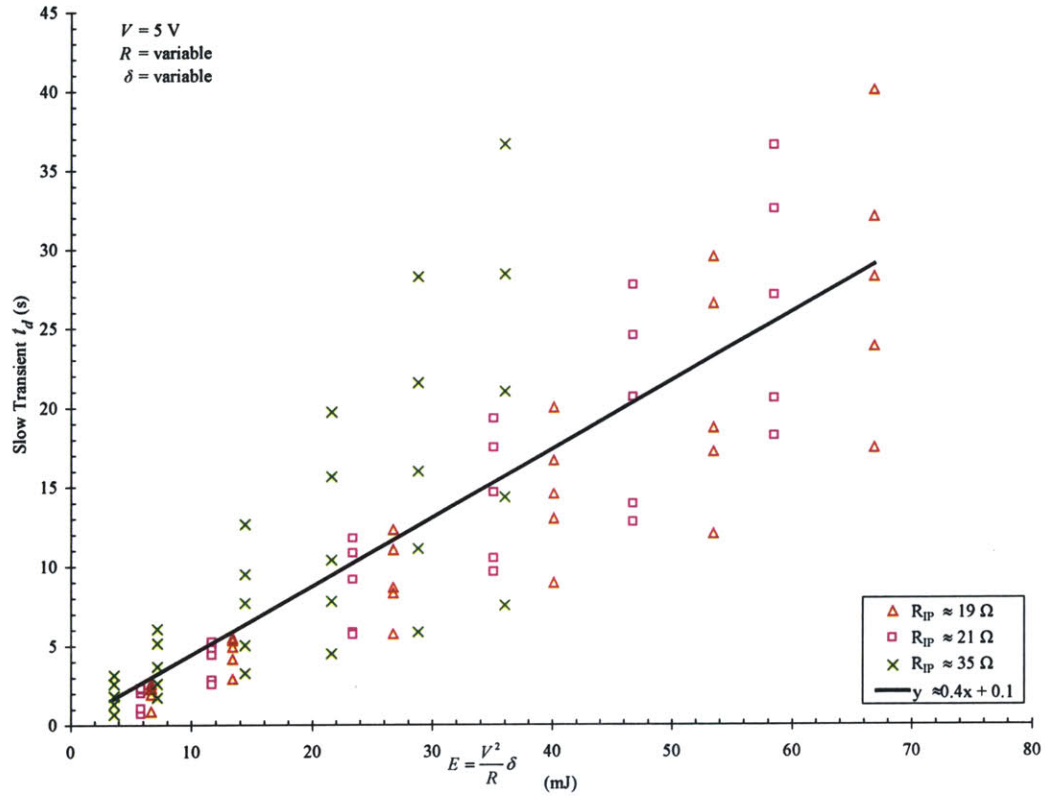
Figure 5-23. *In-Plane Slow Transient t_d.*

In Figure 5-24, the slow transient maximum $\overline{D}$ and the t_d are plotted on the y- and x-axis, respectively. The data represent a chirped input pulse widths of $\delta = 5$, 10:10:50 ms and $\Delta = 2$ min applied to resistors of varying resistance. In the stereotypical plot shown in Figure 5-20, an observed trend is that as the slow transient maximum $\overline{D}$ increases, the slow transient t_d also increases. Figure 5-24 also displays this trend. Thus, the plots of the slow transient t_d exhibit a dependence on both the input energy and the maximum slow transient $\overline{D}$.
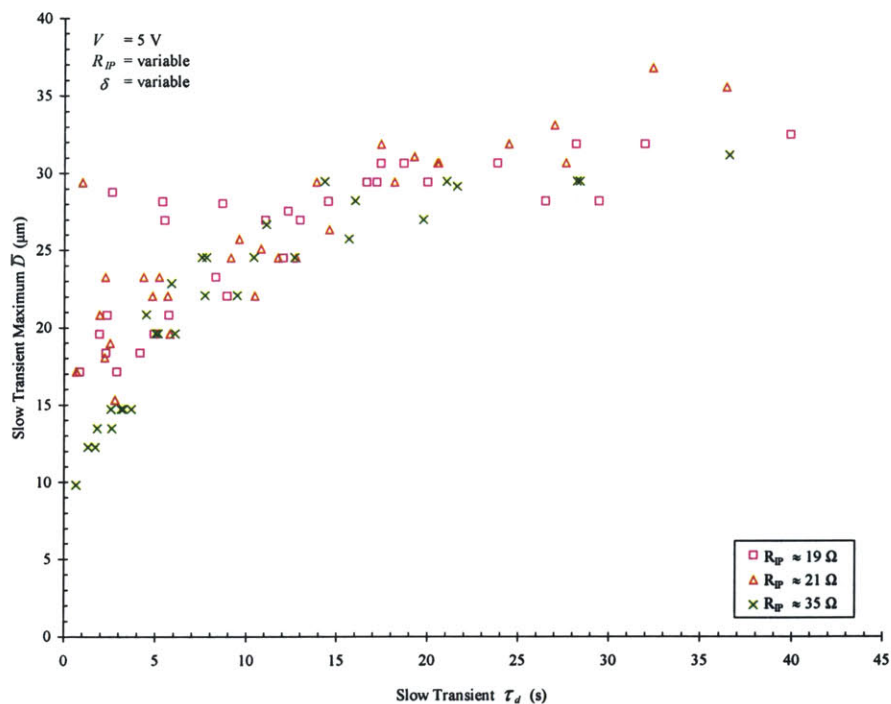
Figure 5-24. *In-Plane Slow Transient Microbubble Size vs. t_d.*

5.3.5 Performance Comparison of Out-of-Plane and In-Plane Geometries

A performance comparison study of out-of-plane and in-plane geometries is used to determine the similarities and differences in the resistor behavior. For the study, an out-of-plane geometry with 6 μm diameter nucleation cavity is used, fabricated as described in Chapter 4 with a hydrophobic surface modification of CYTOP™ and silane to enable repeatable nucleation at the nucleation site. The in-plane geometries for the study include three representative resistors with no surface modifications, nucleation site width of 3 μm, and lengths of 10, 20, and 30 μm, respectively.

A typical complete system response for an out-of-plane (OP) geometry depicted in Figure 5-25. Micrographs illustrate the system at critical points along the dissipation curve. For this example, a standard input pulse with δ = 30 ms and $\Delta = \infty$ is applied to an

out-of-plane resistor with a total resistance of about 16 Ω. The 6 μm diameter nucleation cavity is visible in the first micrograph and final micrograph.
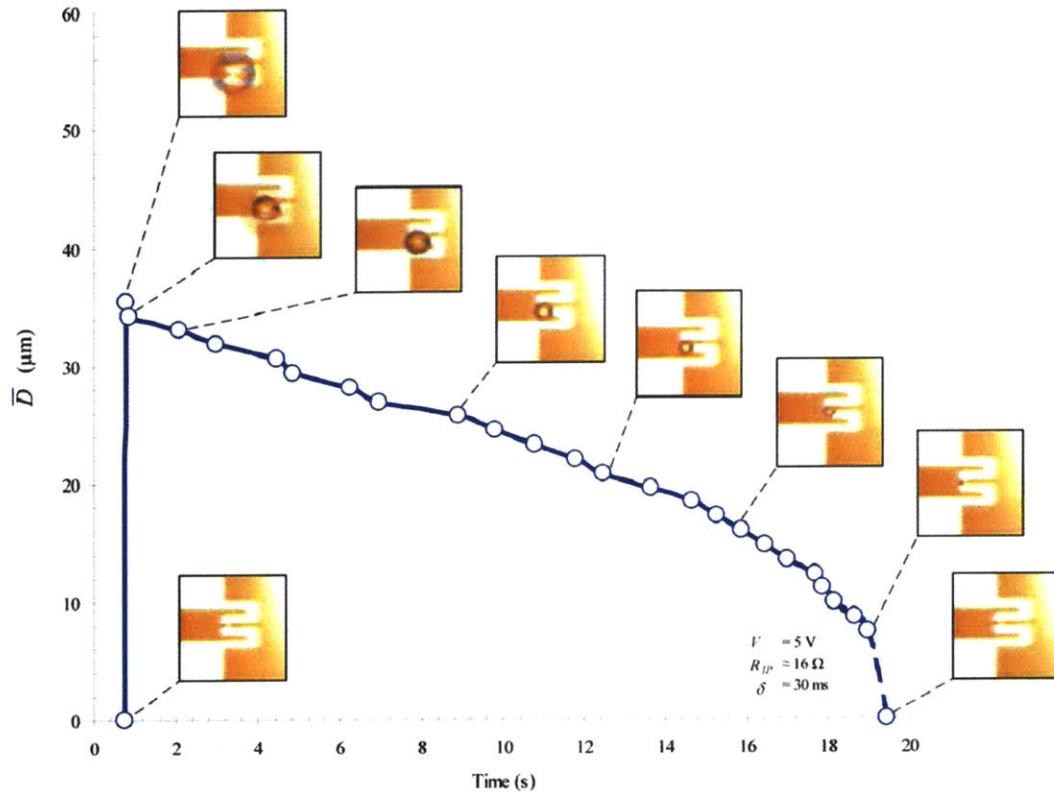
Figure 5-25. *Complete System Response for Out-of-Plane Geometry.*

The shape and location of the out-of-plane and in-plane resistor-bubble system responses are compiled in a set of statistical box plots, Figure 5-26. The first row of box plots details the microbubble eccentricity. The second and third rows of the box plots correspond to centricity in the x- and y-direction, respectively. The first column of plots depicts the fast transient response, while the second column of plots illustrate the slow transient response.
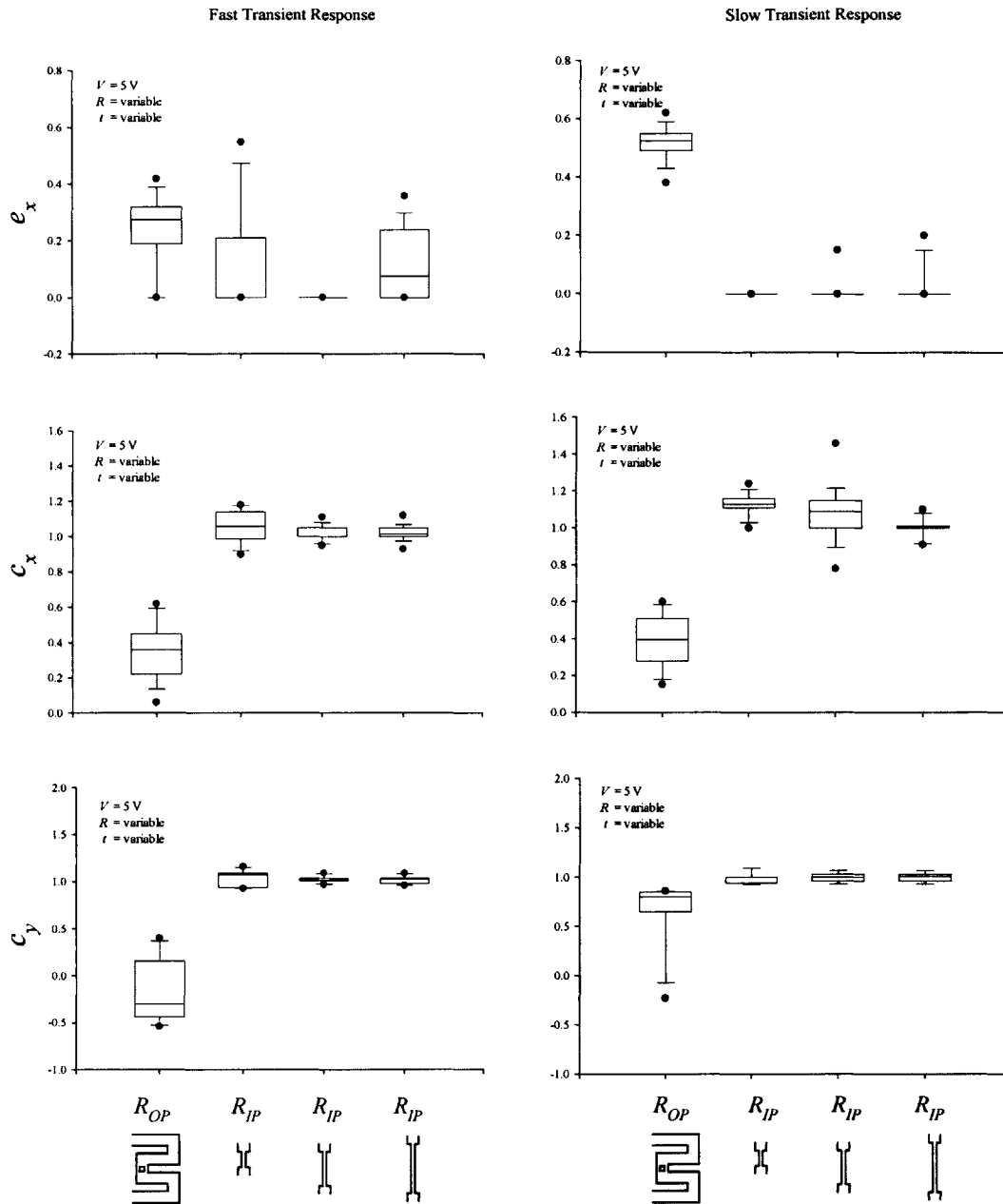
Figure 5-26. *Out-of-Plane and In-Plane Microbubble Shape and Location.*

As illustrated at the bottom of the figure, the first column in each plot is associated with the out-of-plane geometry. The second, third, and fourth columns represent the in-plane nucleation sites of length 10, 20, and 30 μm, respectively. The results are from chirped inputs on the four resistors with δ = 5, 10:10:50 ms and Δ = 2 min, as shown in Figure 5-26.

The fast transient response of the out-of-plane geometry is more elliptical than spherical, as a perfect sphere would have a value e = 0. In contrast, the fast transient responses of the in-plane geometries are more spherical, but the data is not very tight. The slow transient response of the out-of-plane geometry has an eccentricity represented in a much tighter box plot and is much more elliptical than spherical with a mean of $e \approx 0.5$. The slow transient in-plane resistors generate spherical bubbles with means of $e \approx 0$.

Regarding centricity, the fast transient response of the out-of-plane geometry has means of $c_x \approx 0.38$ and $c_y \approx 0.4$, where a centered microbubble would have a mean value of $c_x \approx c_y \approx 1$. The in-plane geometries demonstrate a fast transient response with mean values of $c_x \approx c_y \approx 1$. Similar results are seen for the slow transient responses of the out-of-plane and in-plane geometries.

The out-of-plane geometry exhibits an off-center slow transient response with a greater deviation in c_x than c_y. The slow transient mean c_x and c_y values correspond to microbubble centers located below and to the right of the nucleation site. An example of such a nucleation is shown in Figure 5-26. However, the height of the c_x and c_y box plots also demonstrate that the location of the microbubble center varies as much as a fourth of the radius of the microbubble. In contrast, the in-plane geometry has a c_x and c_y centered slow transient response.

The slow transient maximum $\overline{D}$ for out-of-plane and in-plane resistor-bubble system responses is shown in Figure 5-27. Chirped input pulse widths of δ = 5, 10:10:50 ms and Δ = 2 min were used on the four resistors. The plot illustrates a general trend of increasing slow transient maximum $\overline{D}$ with increasing input energy.
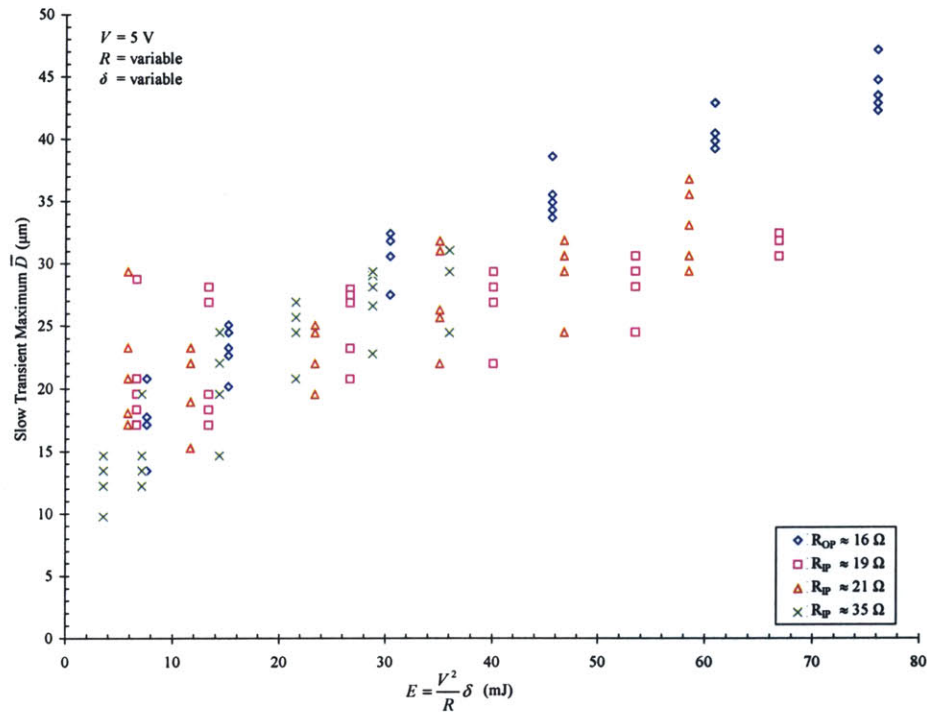
Figure 5-27. *Out-of-Plane and In-Plane Slow Transient Maximum Microbubble Size.*

Figure 5-28 depicts the slow transient maximum t_d for out-of-plane and in-plane resistor-bubble system responses. Chirped input pulse widths applied to the four study resistors are δ = 5, 10:10:50 ms, and Δ = 2 min. The main trend is that the slow transient t_d increases as input energy increases.

A linear fit was applied to the data in the same manner that the linear fit was applied to the in-plane data in Figure 5-23. Both Figure 5-23 and Figure 5-28 illustrate the increase in slow transient maximum t_d with increase in input energy. Comparing the linear fits, both the in-plane plot in Figure 5-23 and the combined out-of-plane and in-plane plot in Figure 5-28 are fit with the same slope line where the slope $m \approx 0.4$.
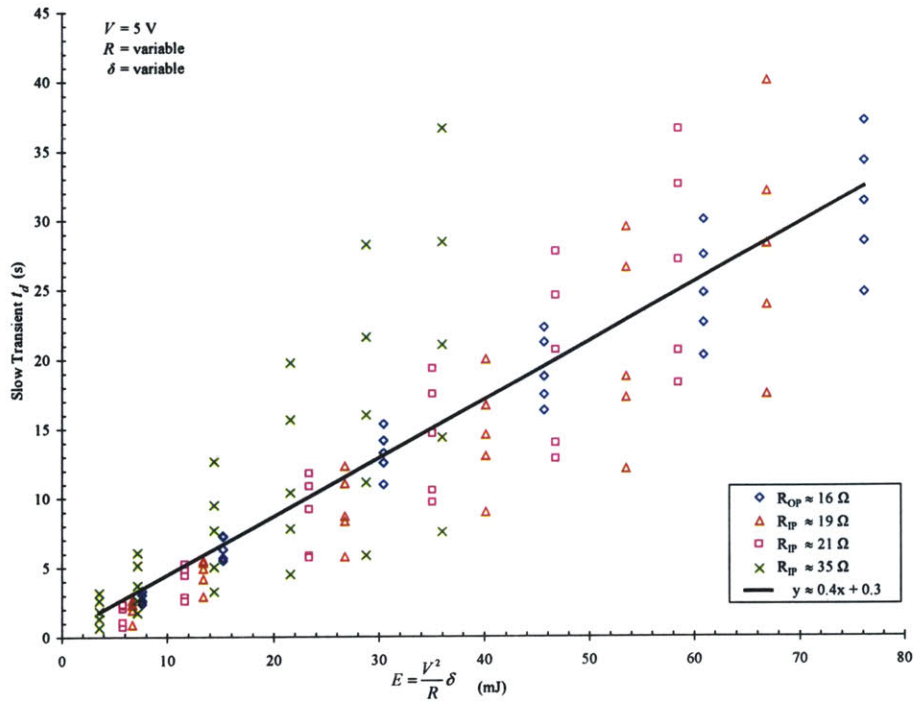
Figure 5-28. *Out-of-Plane and In-Plane Slow Transient t_d.*

A similar relationship between the slow transient maximum $\overline{D}$ and the t_d also is apparent in Figure 5-29. The data represents chirped input pulse widths of $\delta = 5$, 10:10:50 ms and a $\Delta = 2$ min. The general trend, as also was seen in the plot for solely in-plane geometries, is an increase in slow transient t_d for an increase in maximum slow transient $\overline{D}$. Combining the apparent trends in Figure 5-28 and Figure 5-29, the plot of the slow transient t_d exhibits a dependence on both the input energy and the maximum slow transient $\overline{D}$.
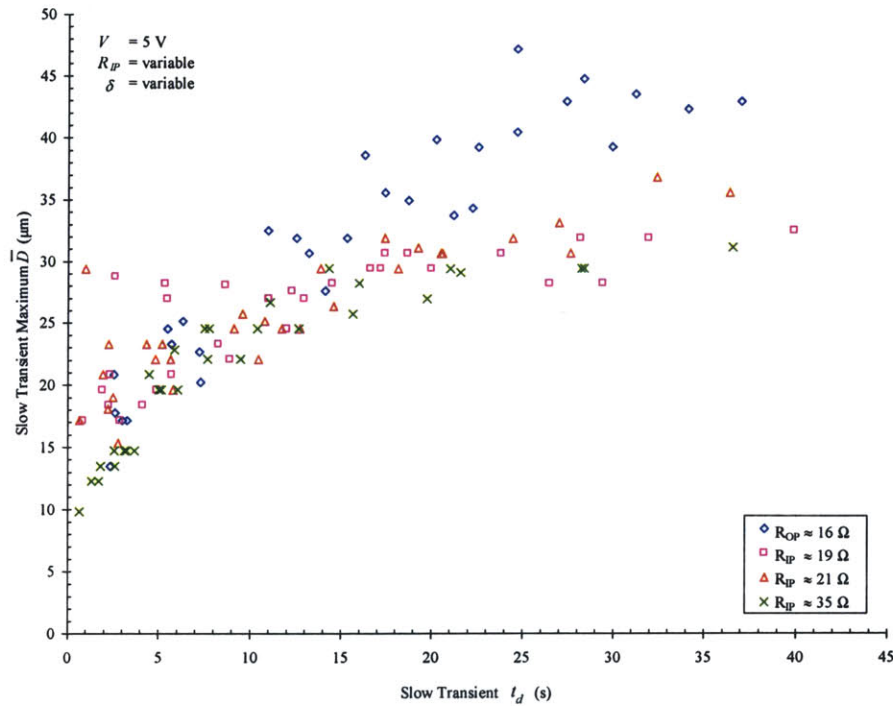
Figure 5-29. *Out-of-Plane and In-Plane Slow Transient Microbubble Size vs. t_d.*

5.3.6 Drift

In the course of data acquisition and early analysis, a drift in the behavior of the system with time is observable. To quantify the system drift, a series of trials on resistors of varying resistance is conducted with chirped input of $\delta = 5$, 10:10:50 ms. For the trials, $\Delta = 2$ or 5 min. Figure 5-30 depicts the results of the drift quantification.

The series of pulses for $\delta = 5$ ms and $\Delta = 2$ min between each pulse results in a fairly repeatable dissipation time for trials 1-5. For $\delta = 5$ ms and $\Delta = 15$ min, the dissipation time begins to drift, requiring longer time periods for dissipation as time increases in increments of 15 minutes. Similarly, the drift also is evident for $\delta = 10:10:50$ ms and $\Delta = 15$ min, where the relative size of the drift increases with an increase in δ.
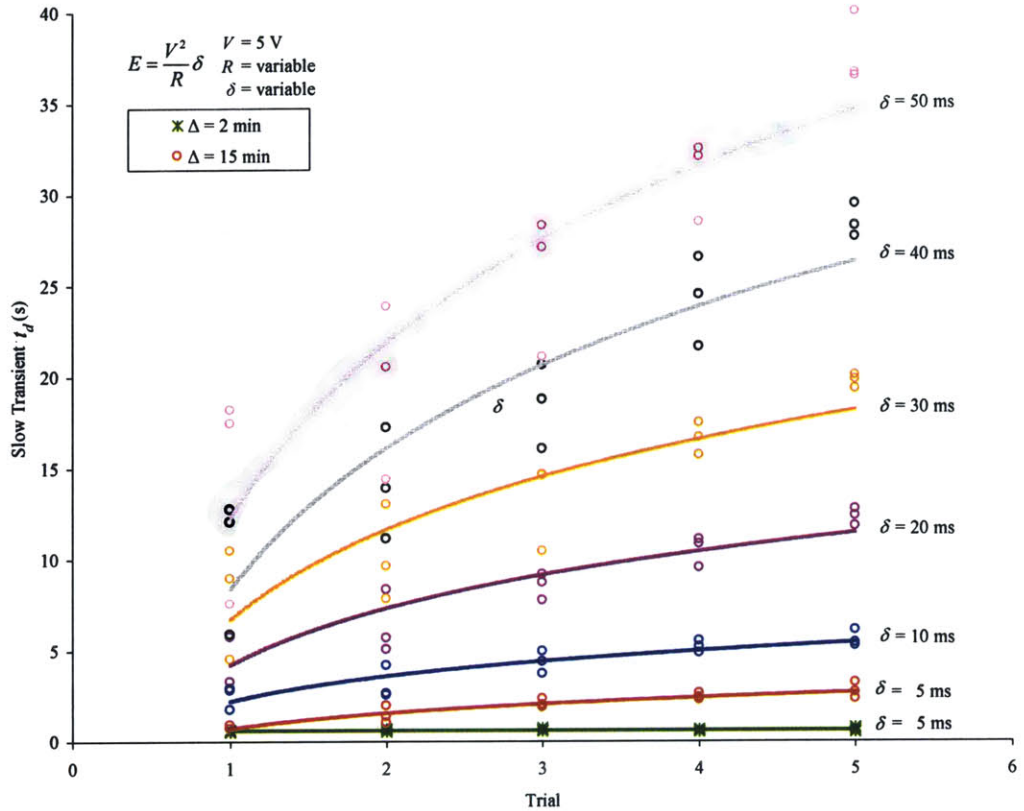
Figure 5-30. *Drift.*

5.3.7 Rapid Cycling

To discern performance of the resistor-bubble system for rapid cycling, a standard input with $\delta = 30$ ms and $f_\Delta = 1$ Hz is applied to the system for four resistor geometries. The first geometry is an out-of-plane geometry with 6 µm diameter nucleation cavity and hydrophobic surface modification of CYTOP™ and silane. The other three geometries are in-plane geometries with no surface preparations, nucleation site width of 3 µm, and lengths of 10, 20, and 30 µm, respectively.

Dissipation for an impulse pulse with $\delta = 30$ ms and $\Delta = \infty$ is on the order of seconds for all four geometries, as shown in Figure 5-25, Figure 5-14, Figure 5-15, and Figure 5-16. For the non-dissipative cycling study, the standard input pulses are applied at a frequency

such that the second pulse is applied before the first slow transient has dissipated. The complete system responses depicted in terms of average microbubble diameter as a function of time are shown in Figure 5-31, Figure 5-32, Figure 5-33, and Figure 5-34.
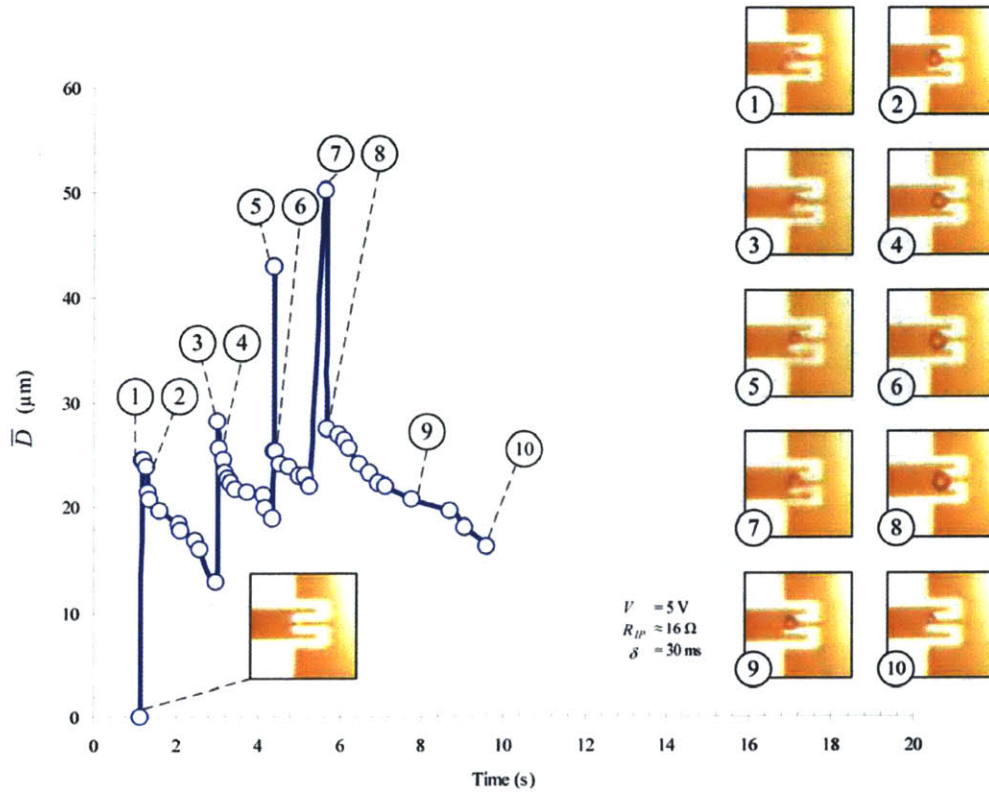
Figure 5-31. *Rapid Cycling Out-of-Plane Geometry Resistor.*

In Figure 5-31, the out-of-plane geometry is pulsed a total of four times. The fast transient from the first pulse is visible as the first peak in the curve and in the corresponding micrograph. The slow transient that appears in the succeeding frame is shown in the second micrograph and also marked on the curve. The responses of the following three pulses are denoted with the numbers 3 – 8. Odd numbers correspond to fast transient responses, and the even numbers correspond to slow transient responses. Micrograph 9 and micrograph 10 illustrate the final slow transient dissipating until it is no longer measurable due to the

presence of the out-of-plane etched nucleation site. For each pulse, the slow transient measured 25, 26, 25, and 28 μm with confidence interval as denoted in Section 5.2.
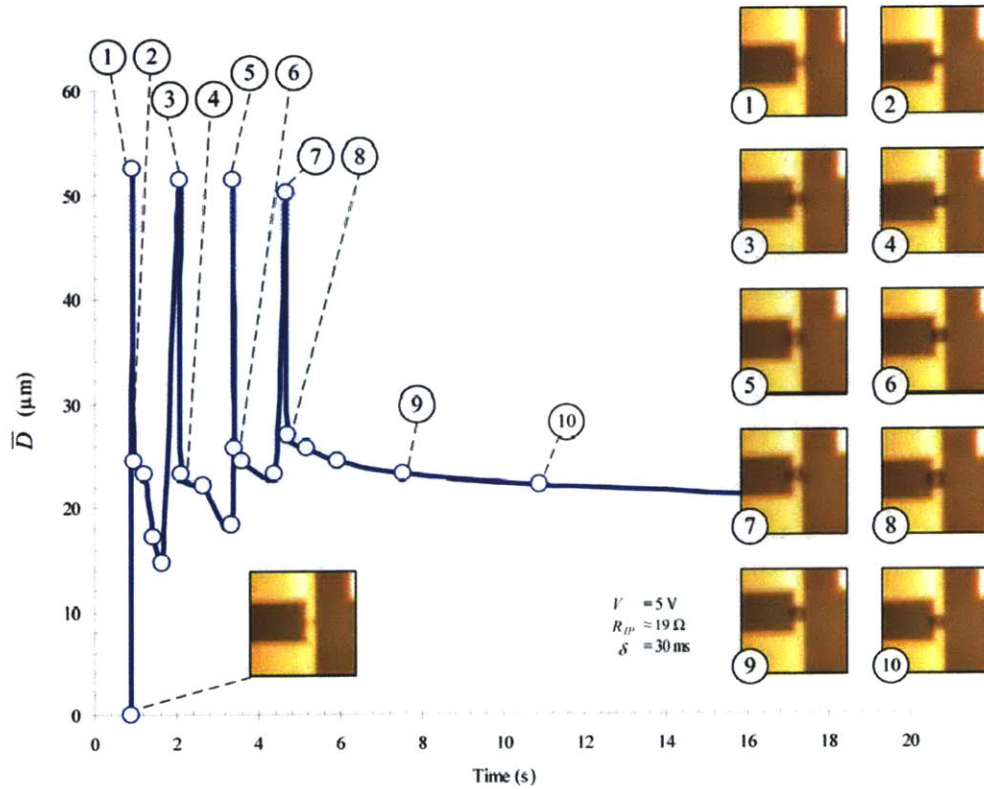
Figure 5-32. *Rapid Cycling In-Plane Geometry Resistor with 10 μm Nucleation Site.*

The results of applying a 1 Hz pulse to the in-plane geometry with 10 μm nucleation site length is shown in Figure 5-32. In kind to the pulse applied to the out-of-plane geometry, the pulse is applied a total of four times before the system is given time to return to steady state. The fast and slow transient responses comprise the numbers 1 – 8 and are shown in the corresponding micrographs. The odd numbers correspond to the fast transient responses, and the even numbers correspond to the slow transient responses. Micrograph 9 and micrograph 10 illustrate time frames in the dissipation of the last slow transient. For

each pulse, the slow transient measured 25, 23, 26, and 27 µm with confidence interval as denoted in Section 5.2.
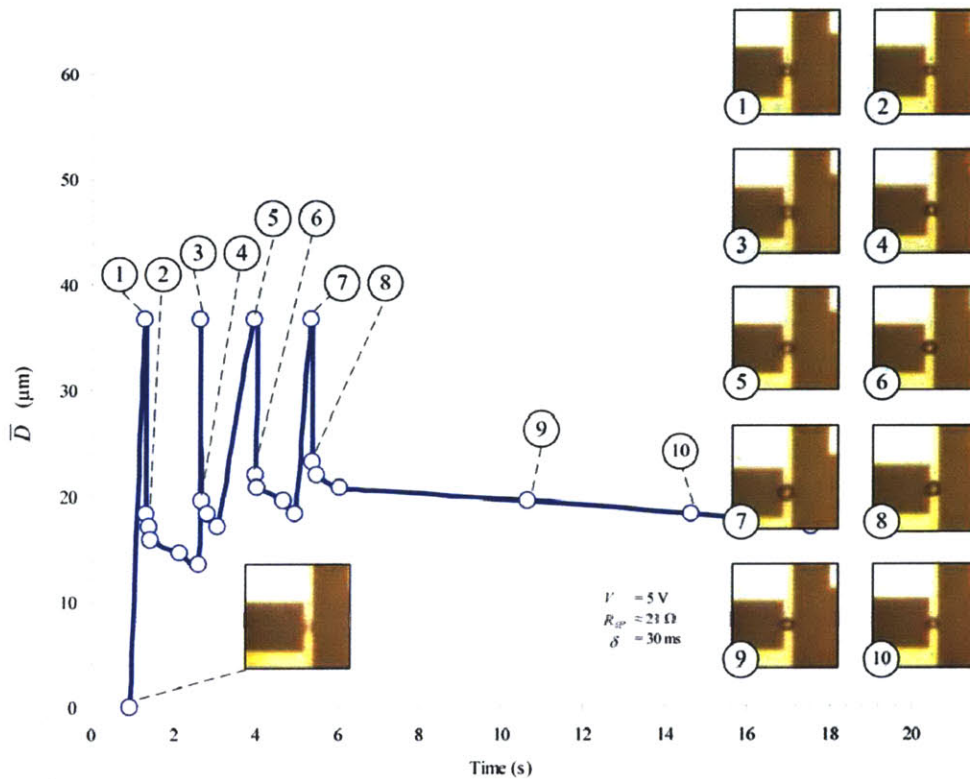
Figure 5-33. *Rapid Cycling In-Plane Geometry Resistor with 20 µm Nucleation Site.*

Figure 5-33 depicts the complete system response of an in-plane geometry resistor with 20 µm nucleation site to a 1 Hz standard pulse. The steady state of the system is shown in the unnumbered micrograph in the figure. The first four odd-numbered micrographs capture the fast transient system response to the four applied pulses. The first four even-numbered micrographs in the second column correspond to the first frame depicting the slow transient response toe ach of the four input pulses. The final two micrographs – micrograph 9 and micrograph 10 – show the system as it returns to steady state. For each pulse, the slow transient measured 37 µm with confidence interval as described in Section 5.2.
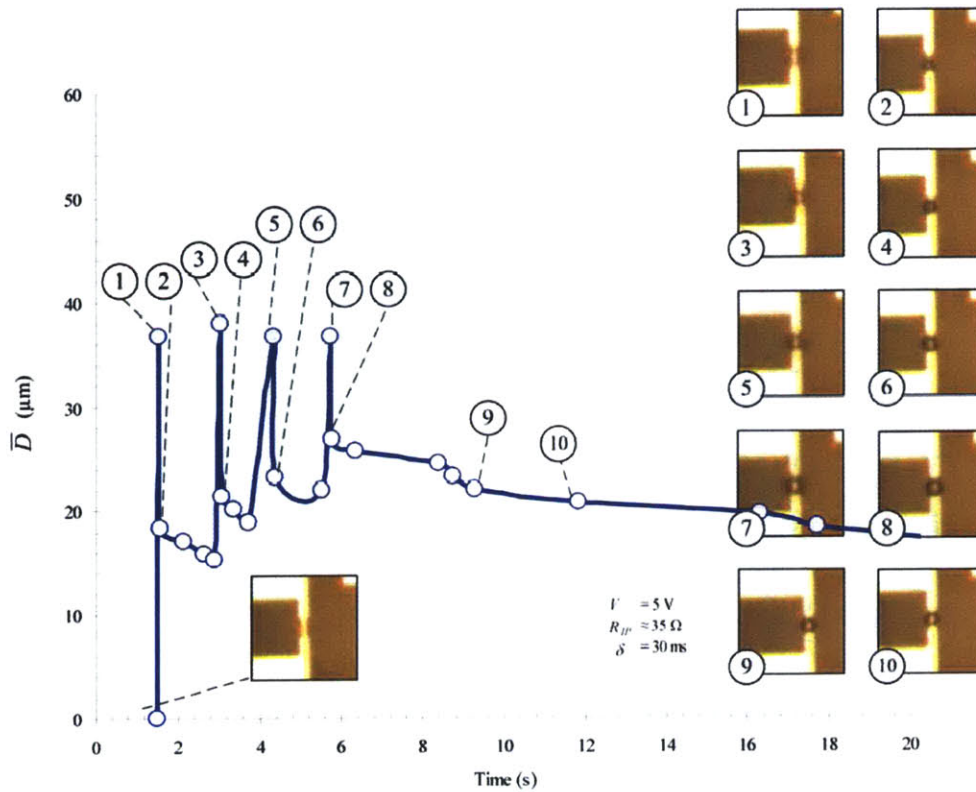
Figure 5-34. *Rapid Cycling In-Plane Geometry Resistor with 30 μm Nucleation Site.*

The results of applying a 1 Hz pulse to the in-plane geometry with 30 μm nucleation site length is shown in Figure 5-34. The pulse is applied a total of four times before the system is left unmodified for a period long-enough to return to steady state. The fast and slow transient responses comprise the numbers 1 – 8 and are shown in the corresponding micrographs. The odd numbers correspond to the fast transient responses, and the even numbers correspond to the slow transient responses. Micrograph 9 and micrograph 10 illustrate time frames in the dissipation of the last slow transient. For each pulse, the slow transient measured 18, 21, 23, and 27 μm with confidence interval as depicted in Section 5.2.

5.4 References

[1]   R. B. Maxwell, A. L. Gerhardt, M. Toner, M. L. Gray, and M. A. Schmidt, "A Microbubble-Powered Bioparticle Actuator," *Journal of Microelectromechanical Systems*, vol. 12, no. 5, pp. 630-640, 2003.

[2]   R. B. Maxwell, "Controllable Vapor Microbubble for Use in Bioparticle Actuation," PhD Dissertation, Cambridge, Massachusetts: Massachusetts Institute of Technology (MIT), 2003.

[3]   R. A. Braff, "Microbubble Cell Actuator," S.M. Thesis, Cambridge, Massachusetts: Massachusetts Institute of Technology (MIT), 1999.

[4]   R. A. Braff, A. L. Gerhardt, M. Toner, M. L. Gray, and M. A. Schmidt, "A Microbubble Bioparticle Actuator," In *Proc. IEEE Conference on Solid State Sensor, Actuator, and Microsystems Workshop*, Hilton Head, South Carolina, 2002, pp. 138-141.

[5]   R. A. Braff, A. L. Gerhardt, M. Toner, M. L. Gray, and M. A. Schmidt, "Controllable Vapor Microbubbles," *Journal of Microelectromechanical Systems*, Submitted for publication, 2003.

Chapter 6 Discussion and Conclusions

The performance evaluation serves to quantify the system response of in-plane geometry μBA-base components. A comparison between out-of-plane and in-plane geometry system responses enables the results depicted in Chapter 5 to be placed in context with past μBA research. A quantification of drift presents one of many remaining challenges in a field of research where new findings often bring more questions than answers. Considering the results of the chip performance study and the process development toward an arrayed, μBA-powered μDAC device introduces some of the achievements and remaining challenges in the development of μBA-powered devices.

6.1 Performance Discussion

Three hypotheses, as described in detail in Section 5.1, directed the focus of the chip performance testing. The first hypothesis is that the shape and location of microbubble formation can be controlled with microfabrication. The second hypothesis is that controlling the energy input to the system — which is dependent on microfabricated geometry, resistor resistance, and input pulse width δ — can regulate the microbubble size, meaning that bubble size is a function of input energy. In the same line of thinking, the final hypothesis is that microbubble dissipation time is a function of bubble size, which, in turn, is a function of input energy.

6.1.1 Control of Microbubble Shape and Location

For symmetrical in-plane resistors, the results show that the fast and slow transient responses are spherical in shape. Additionally, a non-symmetrical out-of-plane resistor exhibits an elliptically-shaped transient response. Two variables are varying in the comparison: (1) the spherical microbubble formed on an in-plane symmetric resistor and (2) the elliptical microbubble formed on an out-of-plane asymmetric resistor. However, an additional piece of data is available. A linear resistor with an out-of-plane nucleation site is shown in [1] generating a spherical microbubble.

In-plane modeling in Chapter 3 demonstrates that the shape of the resistor affects the temperature profile across the plane of the chip. In turn, this temperature profile across the resistor probably affects where hot-adjacent liquid is available to be vaporized at the liquid-vapor interface of the microbubble during its growth phase. Changing the geometry of the resistor then would change the location of the hot-adjacent fluid. The effect would be more rapid bubble growth where hot-adjacent liquid is available. After the liquid cools to ambient temperature, the bubble becomes spherical, as a spherical shape is the most thermodynamically favorable condition. The change from elliptical to spherical was seen repeatedly in out-of-plane geometry testing at a time on the order of 1-2 s after the dissipation of the fast transient.

The potential relationship between geometry and available hot-adjacent liquid during the bubble growth phase further suggests that the symmetry of the microfabricated geometry does have an effect on the resultant shapes of the slow and fast transient responses. By carefully designing the geometry of the resistor, the results show that a dependably spherical microbubble can be nucleated. A potential for engineering the shape of the early slow transient microbubble also may exist.

6.1.2 Regulation of Microbubble Size

For in-plane and out-of-plane resistors, the results show that the slow transient maximum $\overline{D}$ increases as input energy increases. As separately illustrated in the prototypical curves of Section 5.3 and in later figures, the increase in input energy can be attributed to the geometry of the resistor or the use of a lower resistance resistor or larger pulse width δ. The correlation between increased energy input and increased slow transient maximum $\overline{D}$ output may be due to the available hot-adjacent liquid at the liquid-vapor interface.

From the microbubble theory presented in Chapter 2, liquid adjacent to the nucleated bubble serves as a growth factor. The hot adjacent liquid provides thermal energy to vaporize more liquid at the liquid-vapor interface. Thus, the size of the slow transient maximum $\overline{D}$ would be a function of the available energy. Increasing the regional amount of thermal energy available then would make more thermal energy available for the vaporization process. The outcome would be a larger slow transient maximum $\overline{D}$. Thus, the slow transient maximum $\overline{D}$ is a function of the input energy to the system. By engineering the amount of energy available to the microbubble in the growth phase, the slow transient maximum $\overline{D}$ can be regulated to within the confidence interval and to system specifications as long as drift is controlled.

6.1.3 Regulation of Microbubble Dissipation

Results show that for in-plane and out-of-plane resistors the slow transient dissipation time t_d increases as input energy increases. Also, since the slow transient maximum $\overline{D}$ increases as input energy increases, t_d also increases as the slow transient maximum $\overline{D}$ increases. The correlation between increased slow transient maximum $\overline{D}$ and increased t_d again may be due to the available hot liquid at the liquid-vapor interface.

From the microbubble theory presented in Chapter 2, liquid adjacent to the nucleated bubble serves as a growth factor. The adjacent liquid provides thermal energy to vaporize more liquid at the liquid-vapor interface. At the point that the microbubble has extended beyond the layer of superheated liquid, the bubble begins to dissipate through evaporation and convection losses.

A larger microbubble contains more vaporized liquid within its volume. Since the evaporation and convection losses occur over the surface area of the microbubble, a microbubble of larger volume would require longer to dissipate. The results demonstrate that dissipation time is linearly related to the energy input to the system and is a function of the slow transient maximum $\overline{D}$. Regulating the slow transient maximum $\overline{D}$ to within the confidence interval and to system specifications by controlling the input energy enables simultaneous regulation of the dissipation time as long as drift is controlled.

6.2 Comparison of Out-of-Plane and In-Plane Performance

The results of the performance comparison study illustrate the similarities and differences in resistor behavior of out-of-plane and in-plane resistor geometries. Table 6-1 summarizes the compared attributes. Included attributes are from the system behavior results quantified in Chapter 5 as well as from fabrication requirements discussed in Chapter 4 and additional factors observed in the process of testing both geometries.

Table 6-1. *Comparison of Out-of-Plane and In-Plane Resistor Geometries.*

Characteristic	Resistor Geometry	
	Out-of-Plane	**In-Plane**
Number of required masks	(1) Define cavities (2) Define resistors	(1) Define resistors
Required characteristics of substrate for μDAC application	(1) Etchable (2) Optically transparent	(1) Optically transparent
Potential substrates for μDAC application	(1) Fused silica (quartz)	(1) Fused silica (quartz) (2) Pyrex (3) Borofloat
Number of required post-fabrication coatings	(1) CYTOP^{TM} (2) Silane	0
Required chip area per μBA resistor	>	<
Observable microbubble diameter	> than diameter of nucleation site >> minimum microscope resolution	> minimum microscope resolution
Eccentricity (e)	$0 < e < 1$ ⇓ ovoidal microbubbles	$e \approx 0$ ⇓ spherical microbubbles
Centricity (c_x, c_y)	$c_x < 1, c_y < 1$ ⇓ off-center microbubbles	$c_x \approx c_y \approx 1$ ⇓ centered microbubbles
Regulation of Microbubble Size	$\overline{D} = f(E)$	$\overline{D} = f(E)$
Regulation of Microbubble Dissipation	$t_d = f(\overline{D})$	$t_d = f(\overline{D})$
Surface modification required to prevent electrolytic breakdown in ionic solutions	(1) CYTOP^{TM}	future research

The out-of-plane resistor geometry requires a minimum of two masks. The first mask is used to define the nucleation sites and the alignment marks, both of which then are etched. The second mask is used to define the resistors for the metallization process. The in-plane resistor geometry only requires a single mask to define both the resistors and nucleation sites. Eliminating a photolithography step and chrome mask are time and cost saving. Yet, the largest savings is the elimination of the etch step. The etch process can be tedious, inexact, and time intensive, especially for non-commercial fabrication facilities. For this research and previous research, an outside vendor — Surface Technology Systems (STS) — courteously provided proprietary process etching, as in-house etching processes did not yield timely, repeatable results with good uniformity and etch depth [1-4].

As discussed in Chapter 1, the µDAC application of the µBA-powered device is enhanced by an optically transparent substrate, which allows data to be collected from both vertical axes. The second required characteristic of the substrate has been that it must be easily, or relatively easily, etched. However, in-plane geometry does not require etching.

Without the requirement of etching, in-plane geometry can be fabricated on a variety of optically transparent substrates. The µBA-powered µDAC standard is fused silica (quartz), as quartz is an etchable substrate. For in-plane geometries, several less expensive glass substitutes such as Pyrex and Borofloat may be used. The glass wafers are relatively expensive, and Pyrex is commonly used in medical laboratories because it is autoclavable.

Previous research on out-of-plane, cavity-sponsored nucleation demonstrated that a surface modification of either CYTOP™ or silane is required to nucleate bubbles repeatedly at a nucleation site [1-4]. Unmodified out-of-plane resistors were reported to seldom form microbubbles at the nucleation site, while modified resistors nucleated microbubbles at the nucleation site 98% of the time. In contrast, the in-plane geometries require no surface modifications for successful and repeatable microbubble nucleation. With no surface modifications, the in-plane geometries were observed to nucleate single microbubbles at the nucleation site 100% of the time during the course of the testing.

For some applications, maximizing the number of μBA resistors per area can be an issue. By design, the out-of-plane geometry resistor requires a greater surface area. Typical out-of-plane resistors occupy a square area ranging from 4,900 – 32,400 μm^2 [1-4]. Depending on the output transient desired, valid nucleating in-plane resistor designs occupy areas as small as 300 μm^2, for only an evident fast transient response, to 500 μm^2, for a complete response consisting of both fast and slow transients.

For out-of-plane resistor geometry, the slow transient dissipation process can be observed until the diameter of the microbubble is the diameter of the nucleation cavity. At cavity-size, the microbubble becomes optically indecipherable regardless of available microscope magnification. For out-of-plane geometry, the minimum observable resolution is limited by the diameter of the cavity rather than minimum microscope resolution. A microbubble dissipating on an in-plane geometry resistor is observable until the minimum resolution of the microscope is reached. Therefore, in-plane geometry offers a mechanism by which to study the tail of the slow transient dissipation process.

The shape and location of the out-of-plane generated fast and slow transient microbubbles vary over the course of multiple trials. Generated microbubbles range from the most common, elliptical, to occasionally spherical. In addition, elliptical microbubbles often become spherical several seconds into the slow transient dissipation process. The out-of-plane microbubble seems to form almost randomly around the nucleation site, while always maintaining contact with the nucleation site at some point on the microbubble. In comparison, the in-plane generated microbubble is spherical and centered on the nucleation site.

The out-of-plane and in-plane geometries also share some attributes. Both geometries exhibit the same functional maximum slow transient $\overline{D}$ dependence on input energy. The out-of-plane and in-plane geometries also evince the same functional t_d dependence on the maximum slow transient $\overline{D}$ and exhibit a same-sloped linear functional relationship between t_d and the input energy.

6.3   Recommendations, Future Work, and Potential Applications

This work demonstrates that by careful design of in-plane resistor geometry, a dependably spherical microbubble can be nucleated at a designed location. Thus, the shape and location of an in-plane generated microbubble can be controlled with considerable precision. Slow transient maximum $\overline{D}$ is shown to be a function of input energy and can be regulated to within the confidence interval and to system specifications by that dependence, as long as drift is controlled. Similarly, the slow transient t_d is a function of the slow transient maximum $\overline{D}$, which, in turn, is a function of the input energy. Thus, t_d also can be regulated directly to within the confidence interval and to system specifications by controlling the input energy by means of the geometry, resistor resistance, or input pulse δ, as long as drift is controlled.

Future areas of work could be to determine the functional relationship between the slow transient maximum $\overline{D}$ and input energy as well as the functional relationship between t_d and the slow transient maximum $\overline{D}$. Additionally, a drift was quantified, which shows that the slow transient maximum $\overline{D}$ increases as time between trials increases. This drift may be due to operation of the resistor or a change in DI water with time. For high precision fluidic delivery or control systems, the drift may be unacceptable. Future work could study the mechanism behind the drift and discern if such a drift exists with other mediums.

In addition to designing and fabricating an arrayed µBA-based device and testing and characterizing over one hundred in-plane and out-of-plane µBA-based component geometries, many guidelines for future µBA-based devices and systems are presented within the chapters. From the perspective of design, the first decision is whether an in-plane or out-of plane geometry is desired. After choosing the dimensionality of the geometry, a substrate can be selected, and the resistors can be engineered to affect the desired eccentricity and centricity. In terms of fabrication for in-plane geometries, special attention for non-commercial fabrication facilities is required to achieve the 3 µm nucleation site. For out-of-plane geometries, extra time in the fabrication process should be budgeted for nucleation cavity etching.

For out-of-plane geometries, a surface modification was found to be essential for robust operation of the µBA-based component. Previously tested optional coatings include CYTOP™ and silane [1-4]. For robust operation of the in-plane geometry, no surface modification is required. For biological applications, the in-plane geometry surface may need to be modified to prevent electrolytic breakdown with ionic solutions. This, additionally, could be an area of future research to determine if such a surface modification would be necessary.

The results of the chip performance study and the process development toward an arrayed µBA-powered µDAC device introduce some of the achievements and remaining challenges in developing µBA-powered devices. Following the progression of microbubbles from their macro counterpart to their indentured bubbling in ink-jet printers and in the Champagne project demonstrate that µBA has the potential to be used as a low power, input high work output commercial mechanism in fluidic valves and pumps; fuel injection; precise-dose drug delivery; and in a vast array of fluidic actuation applications such as fluid-bed processing in the petrochemical, petroleum, chemical, pharmaceutical, biochemical, environmental, defense, and medical fields.

6.4 References

[1]   R. B. Maxwell, "Controllable Vapor Microbubble for Use in Bioparticle Actuation," PhD Dissertation, Cambridge, Massachusetts: Massachusetts Institute of Technology (MIT), 2003.

[2]   R. A. Braff, A. L. Gerhardt, M. Toner, M. L. Gray, and M. A. Schmidt, "A Microbubble Bioparticle Actuator," In *Proc. IEEE Conference on Solid State Sensor, Actuator, and Microsystems Workshop*, Hilton Head, South Carolina, 2002, pp. 138-141.

[3]   R. A. Braff, A. L. Gerhardt, M. Toner, M. L. Gray, and M. A. Schmidt, "Controllable Vapor Microbubbles," *Journal of Microelectromechanical Systems*, Submitted for publication, 2003.

[4]   R. B. Maxwell, A. L. Gerhardt, M. Toner, M. L. Gray, and M. A. Schmidt, "A Microbubble-Powered Bioparticle Actuator," *Journal of Microelectromechanical Systems*, vol. 12, no. 5, pp. 630-640, 2003.

Appendix A   Fabrication Process Flows

In Chapter 4, the fabrication procedures for the PHE chip, TSC, DI header mold, and IM header mold are described textually and with illustrations. The delineated process flows provide more detailed descriptions of the fabrication procedures involved in creating the nucleation chips and fluidic interface for the device. For each process flow, a general purpose, process overview, starting material, and illustration of the final chip is provided. The final chip picture corresponds to the final picture in each pictorial process flow in Chapter 4 Figure 4-20, 4-22, 4-26, and Figure 4-29, respectively.

In addition, MTL-machine names are listed for each step along with machine-specific detail including exposure and developing times. See Chapter 4 for the corresponding non-MTL specific machines used for each step and the company of machine manufacture. For the DI and IM header molds, the delineated process flows often list only one of several possible SU-8 photoresists that could have been employed to create the structure of specified height. For example, step 4 of the IM process flow uses SU-8 2075. Another SU-8 photoresist that can be spun to achieve heights of 100 μm is SU-8 50.

Variable parameters also are noted. Information regarding the variability and parameters affecting the variability are included in Chapter 4. For example, the SU-8 developing time of the finished multi-layer structure depends on additive bake time in the process. The typical develop time range is noted as 4-6 hours.

Figure A-1 delineates the PHE chip process. As denoted, the overarching purpose of the fabrication procedure is to create resistors with out-of-plane nucleation sites to be used as thermal actuators. A total of seven main steps create the finished product depicted in the labeled schematic. The step numbers in the process flow correspond to the step-numbered illustrations in Figure 4-20.

PHE Chip Process

Purpose:

Fabricate resistors with nucleation cavities to be used as thermal actuators

Process Overview:

Build, layer-by-layer, nucleation cavity and resistor structure

Material:

6" quartz wafers
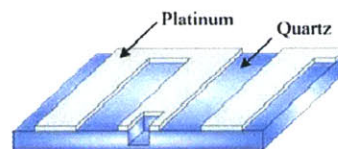
Step		Description	Coral Name	Lab	Notes
1	**Clean wafers**				
	1.1	RCA clean	rca	ICL	
2	**Transfer etch mask**				
	2.1	2 μm polysilicon deposition	6b-npoly	ICL	t = 200 min (rate ~ 100? /min)
	2.2	Photolithography			
		2.21 HMDS	hmds	TRL	recipe = 5 (72? contact angle)
		2.22 Spin photoresist	coater	TRL	resist = OCG 825 20CS (pump 1);
					spin = 9 s @ 0.2 | 6 s @ 0.75 | 30 s @ 3 krpm
		2.23 Prebake	prebake	TRL	t = 30 min; T = 90°C
		2.24 Align, expose *mask1*	ev1	TRL	t = variable (~1.7 s)
		2.25 Develop	photo-wet	TRL	developer = OCG 934 1:1; t = 90 s with 30 s rinse
		2.26 Postbake	postbake	TRL	t = 30 min; T = 120°C
	2.3	Etch polysilicon	sts2	TRL	recipe = stshall_a; t = 8:30 min
3	**Define nucleation cavities**				
	3.1	Etch quartz	external vendor		
4	**Clean wafers**				
	4.1	Pirahna clean	acid-hood/acid-hood2	TRL	t = 10 min (blue dot)
	4.2	Pirahna clean	acid-hood/acid-hood2	TRL	t = 10 min (green dot)
	4.3	Etch polysilicon	lam490	TRL	recipe = nitride; t = 2:30 min
5	**Transfer metal mask**				
	5.1	Photolithography			
		5.11 HMDS	hmds	TRL	recipe = 5 (72? contact angle)
		5.12 Spin photoresist	coater	TRL	resist = AZ® 5124-E (pump 2);
					spin = 9 s @ 0.2 | 6 s @ 0.75 | 30 s @ 4 krpm
		5.13 Prebake	prebake	TRL	t = 30 min; T = 90°C
		5.14 Align, expose *mask2*	ev1	TRL	t = variable (~ 1.3 s)
		5.15 Hardbake	postbake	TRL	t = 30 min; T = 105°C
		5.16 Flood expose	ev1	TRL	t = 1 min
		5.17 Develop	photo-wet	TRL	developer = AZ® 422; t = 90 s with 30 s rinse
6	**Deposit and lift-off metal**				
	6.1	Evaporate 100 Å Ti; 1000 Å Pt	e-beam	TRL	
	6.2	Acetone (metal liftoff, pr strip)	solventhood	TRL	t = variable (~ 3 hours)
	6.3	Anneal (optional)	tubeB1-Au	TRL	t = 60 min; T = 600°C; N_2 flow rate ~ 5 L/min
7	**Develop SU-8 structure**				
	7.1	Diesaw	diesaw	ICL	black blade

(left margin label, vertical: Au contaminated)

Figure A-1. *PHE Chip Delineated Process Flow.*

Figure A-2 portrays the TSC process. The process objective is to fabricate resistors with in-plane nucleation sites to be used as thermal actuators. A total of four main steps create the finished product depicted in the labeled illustration. The step numbers in the process flow correspond to the step-numbered schematics in Figure 4-22.

TSC Process

Purpose:

Fabricate resistors with in-plane nucleation sites to be used as thermal actuators

Process Overview:

Build in-plane nucleation site and resistor structure

Material:

6" quartz wafers
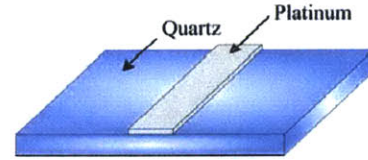
	Step		Description	Coral Name	Lab	Notes
	1		**Clean wafers**			
		1.1	Pirahna clean	acid-hood/acid-hood2	TRL	t = 10 min
	2		**Transfer metal mask**			
		2.1	Photolithography			
			2.11 HMDS	hmds	TRL	recipe = 5 (72? contact angle)
			2.12 Spin photoresist	coater	TRL	resist = AZ® 5124-E (pump 2); spin = 9 s @ 0.2 | 6 s @ 0.75 | 30 s @ 4 krpm
			2.13 Prebake	prebake	TRL	t = 30 min; T = 90°C
			2.14 Align, expose *mask2*	ev1	TRL	t = variable (~ 1.3 s)
			2.15 Hardbake	postbake	TRL	t = 30 min; T = 105°C
			2.16 Flood expose	ev1	TRL	t = 1 min
			2.17 Develop	photo-wet	TRL	developer = AZ® 422; t = 90 s with 30 s rinse
	3		**Deposit and lift-off metal**			
		3.1	Evaporate 100 Å Ti; 1000 Å Pt	e-beam	TRL	
		3.2	Acetone (metal liftoff, pr strip)	solventhood	TRL	t = variable (~ 3 hours)
		3.3	Anneal (optional)	tubeB1-Au	TRL	t = 60 min; T = 600°C; N_2 flow rate ~ 5 L/min
	4		**Develop SU-8 structure**			
		4.1	Diesaw	diesaw	ICL	black blade

(Au contaminated)

Figure A-2. *TSC Chip Delineated Process Flow.*

Figure A-3 renders the DI header mold process. The process is used to fabricate an SU-8 structure to be used as a positive mold for PDMS molding. A total of seven main steps create the finished product depicted in the labeled schematic. The step numbers in the process flow correspond to the step-numbered illustrations in Figure 4-26.

Deionized (DI) Process

Purpose:

Fabricate SU-8 structure to be used as a positive mold for PDMS molding

Process Overview:

Build, layer-by-layer, multi-layer SU-8 structure

Material:

6" silicon wafers
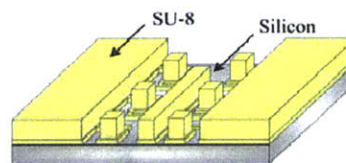
Step			Description	CAFÉ Name	Lab	Notes
1		**Clean wafers**				
	1.1		Piranha clean	acid-hood/acid-hood2	TRL	t = 10 min
2		**Transfer alignment marks**				
	2.1		Photolithography			
		2.11	HMDS	hmds	TRL	recipe = 5 (72? contact angle)
		2.12	Spin photoresist	coater	TRL	resist = OCG 825 20CS (pump 1);
						spin = 9 s @ 0.2	6 s @ 0.75	30 s @ 3 krpm
		2.13	Prebake	prebake	TRL	t = 30 min; T = 90°C
		2.14	Align, expose *mask1*	ev1	TRL	t = variable (~1.7 s)
		2.15	Develop	photo-wet	TRL	developer = OCG 934 1:1; t = 90 s with 30 s rinse
		2.16	Postbake	postbake	TRL	t = 30 min; T = 120°C
	2.2		Etch silicon	sts2	TRL	recipe = stshall_a; t = 3 min
3		**Clean wafers**				
	3.1		Piranha clean	acid-hood/acid-hood2	TRL	t = 10 min
4		**Define patterns on first layer**				
	4.1		Dehydrate	hotplate/oven	TRL	t = 5 min; T = 200 °C / t = 30 min; T = 200 °C
	4.2		Static dispense SU-8	pispinner	TRL	SU-8 = 2005
	4.3		Spin 6 μm	pispinner	TRL	spin = 5 s @ 0.5	30 s @ 2 krpm
	4.4		Soft bake	hotplate	oven	TRL	t = 1 min @ 65 °C	2 min @ 95 °C
	4.5		Align, expose *mask3*	ev1	TRL	t = 60 s
	4.6		Postbake	hotplate	oven	TRL	t = 1 min @ 65 °C	1 min @ 95 °C
5		**Define patterns on second layer**				
	5.1		Static dispense SU-8	pispinner	TRL	SU-8 = 2075
	5.2		Spin 100 μm	pispinner	TRL	spin = 5 s @ 0.5	30 s @ 3 krpm
	5.3		Soft bake	hotplate	oven	TRL	t = 5 min @ 65 °C	var @ 120 °C
	5.4		Static dispense SU-8	pispinner	TRL	SU-8 = 2075
	5.5		Spin 100 μm	pispinner	TRL	spin = 5 s @ 0.5	30 s @ 3 krpm
	5.6		Soft bake	hotplate	oven	TRL	t = 5 min @ 65 °C	var @ 120 °C
	5.7		Static dispense SU-8	pispinner	TRL	SU-8 = 2075
	5.8		Spin 100 μm	pispinner	TRL	spin = 5 s @ 0.5	30 s @ 3 krpm
	5.9		Soft bake	hotplate	oven	TRL	t = 5 min @ 65 °C	var @ 120 °C
	5.10		Align, expose *mask4*	ev1	TRL	t = 60 s
	5.11		Postbake	hotplate	oven	TRL	t = 5 min @ 65 °C	20 min @ 95 °C
7		**Develop SU-8 structure**				
	7.1		Develop SU-8		TRL	developer = SU-8 Developer; t ~ 4-6 hrs
	7.2		Rinse and nitrogen dry	solvent-noAu	TRL	solution = IPA

Figure A-3. *DI Header Mold Delineated Process Flow.*

Figure A-4 displays the IM header mold process, which creates a positive mold for PDMS molding. Seven main steps create the product depicted in the labeled schematic. Step numbers in the process flow correspond to the step-numbered illustrations in Figure 4-29.

Input Medium (IM) Process

Purpose:

Fabricate SU-8 structure to be used as a positive mold for PDMS molding

Process Overview:

Build, layer-by-layer, multi-layer SU-8 structure

Material:

6" silicon wafers
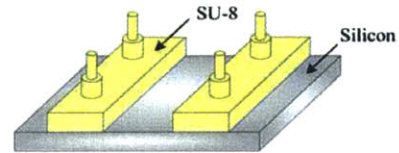
Step		Description	CAFÉ Name	Lab	Notes
1		**Clean wafers**			
	1.1	Piranha clean	acid-hood/acid-hood2	TRL	
2		**Transfer alignment marks**			
	2.1	Photolithography			
		2.11 HMDS	hmds	TRL	recipe = 5 (72? contact angle)
		2.12 Spin photoresist	coater	TRL	resist = OCG 825 20CS (pump 1);
					spin = 9 s @ 0.2 | 6 s @ 0.75 | 30 s @ 3 krpm
		2.13 Prebake	prebake	TRL	t = 30 min; T = 90°C
		2.14 Align, expose *mask1*	ev1	TRL	t = variable (~1.7 s)
		2.15 Develop	photo-wet	TRL	developer = OCG 934 1:1; t = 90 s with 30 s rinse
		2.16 Postbake	postbake	TRL	t = 30 min; T = 120°C
	2.2	Etch silicon	sts2	TRL	recipe = stshall_a; t = 3 min
3		**Clean wafers**			
	3.1	Piranha clean	acid-hood/acid-hood2	TRL	t = 10 min
4		**Define patterns on first layer**			
	4.1	Dehydrate	hotplate/oven	TRL	t = 5 min; T = 200 °C / t = 30 min; T = 200 °C
	4.2	Static dispense SU-8	pispinner	TRL	SU-8 = 2075
	4.3	Spin 100 μm	pispinner	TRL	spin = 5 s @ 0.5 | 30 s @ 3 krpm
	4.4	Soft bake	hotplate | oven	TRL	t = 5 min @ 65 °C | var min @ 120 °C
	4.5	Static dispense SU-8	pispinner	TRL	SU-8 = 2075
	4.6	Spin 100 μm	pispinner	TRL	spin = 5 s @ 0.5 | 30 s @ 3 krpm
	4.7	Soft bake	hotplate | oven	TRL	t = 5 min @ 65 °C | var min @ 120 °C
	4.8	Static dispense SU-8	pispinner	TRL	SU-8 = 2075
	4.9	Spin 100 μm	pispinner	TRL	spin = 5 s @ 0.5 | 30 s @ 3 krpm
	4.10	Soft bake	hotplate | oven	TRL	t = 5 min @ 65 °C | var min @ 120 °C
	4.11	Align, expose *mask7*	ev1	TRL	t = 60 s
	4.12	Postbake	hotplate | oven	TRL	t = 1 min @ 65 °C | 20 min @ 95 °C
5		**Define patterns on second layer**			
	5.1	Static dispense SU-8	pispinner	TRL	SU-8 = 2010
	5.2	Spin 15 μm	pispinner	TRL	spin = 5 s @ 0.5 | 30 s @ 3 krpm
	5.3	Soft bake	hotplate | oven	TRL	t = 1 min @ 65 °C | 2 min @ 95 °C
	5.4	Align, expose *mask6*	ev1	TRL	t = 60 s
	5.5	Postbake	hotplate | oven	TRL	t = 1 min @ 65 °C | 2 min @ 95 °C
6		**Define patterns on third layer**			
	6.1	Static dispense SU-8	pispinner	TRL	SU-8 = 50
	6.2	Spin 40-50 μm	pispinner	TRL	spin = 5 s @ 0.5 | 30 s @ 2 krpm
	6.3	Soft bake	hotplate | oven	TRL	t = 6 min @ 65 °C | var @ 120 °C
	6.4	Align, expose *mask5*	ev1	TRL	t = 60 s
	6.5	Postbake	hotplate | oven	TRL	t = 1 min @ 65 °C | 5 min @ 95 °C
7		**Develop SU-8 structure**			
	7.1	Develop SU-8		TRL	developer = SU-8 Developer; t ~ 4-6 hrs
	7.2	Rinse and nitrogen dry	solvent-noAu	TRL	solution = IPA

Figure A-4. *IM Header Mold Delineated Process Flow.*

Appendix B   Mask Design

Fabrication procedures for the PHE chip, TSC, DI header mold, and IM header mold are described textually and with illustrations in Chapter 4. Appendix A contains more delineated process flows that include the notation of the mask used for each photolithography step within the respective process. A standard nomenclature for the masks is used throughout to ease the photolithography process as multiple iterations developed over the course of the research.

The mask number, denoted at the bottom left of the wafer, provides the stacking order of the mask in the assembly and packaging procedure. For example, mask 1 is the mask used, for the out-of-plane process, to define the nucleation sites and alignment marks that will be etched. Mask 2 defines the metal. In the case of the TSC, no out-of-plane etching procedure is required. Thus, the TSC begins with a metal mask, mask 2. The succeeding fluidic masks that form the layers of the SU-8 mold and the subsequent PDMS casting are numbered in the same fashion. Thus, the lowest layer is mask 3, and the topmost layer is wafer mask 7.

The masks are designed in AutoCAD LT 2002® (Autodesk®, San Rafael, CA). The final mask is either on 178 mm square soda-lime plates of 3 mm thickness with chrome plating (Advanced Reproductions, North Andover, MA) or on a high-resolution precision laser transparency of dimensions 178 mm square and resolution 1/25.4 mil (Photoplot Store, Colorado Springs, CO). The transparency then is transferred to a 178 mm square photomask plate (Nanofilm, WestLake Village, CA) to enable more precise pattern transfer during repeat photolithography processes. The transparency mask transferred to a mask blank is valid for minimum feature sizes on the order of 10 μm. For minimum feature sizes of less than 10 μm, chrome photomasks are used.

B.1 Platinum Heating Electrode Chip

PHE chip fabrication with out-of-plane nucleation sites requires two chrome photomasks. Mask 1 defines the patterns to be etched into the quartz wafer, and mask 2 serves as the metal mask. Figure B-1 is a screen capture of mask 1, which has open polygons. Meaning, the shapes inside the wafer are clear, and the field of the mask is dark. The wafer contains fifteen chips of size 3 cm by 2 cm.
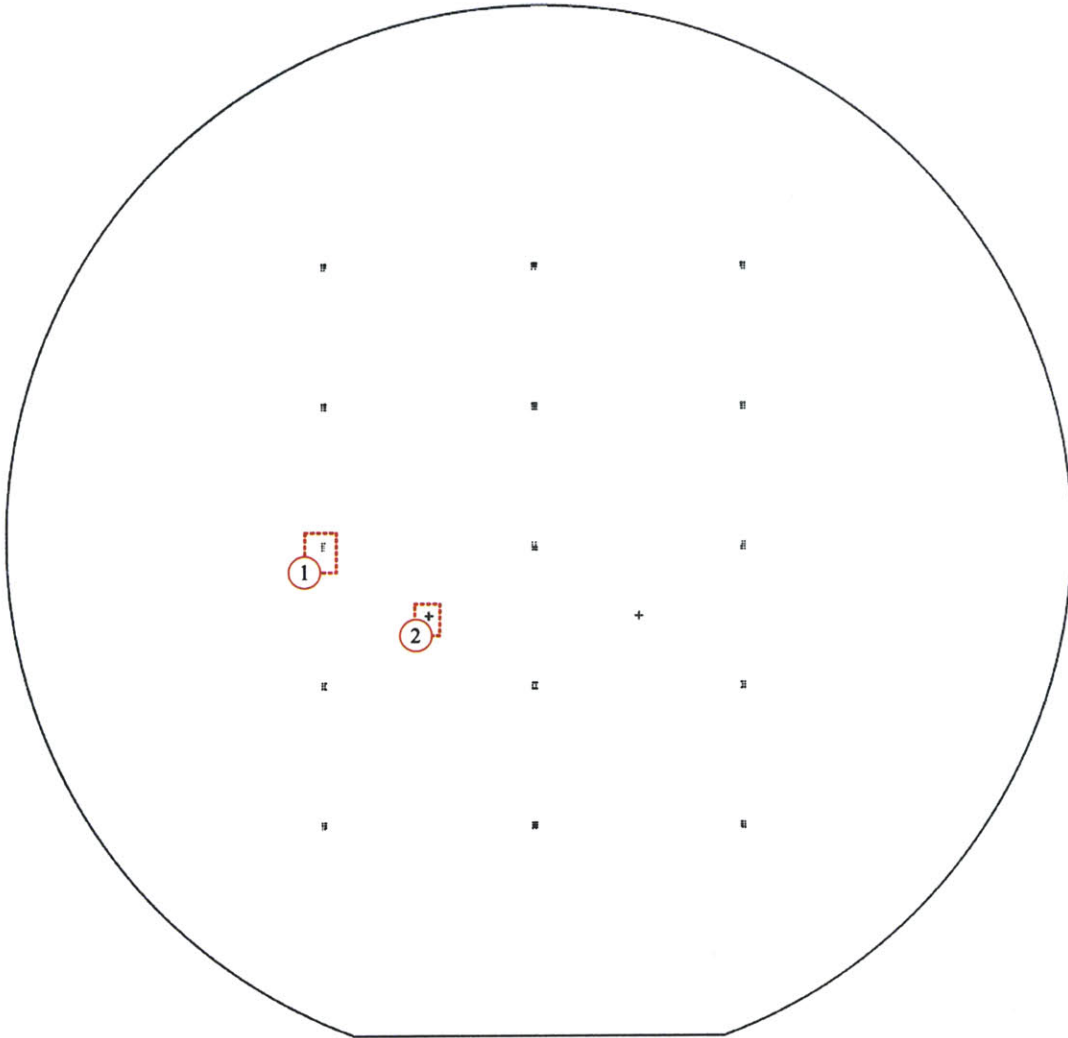
Figure B-1. *PHE Chip Mask 1.*

At the center of each chip are eight nucleation sites arranged in four rows with two columns. Each nucleation site is 6 μm in diameter. The number 1 in Figure B-1 denotes a set of eight nucleation sites. The left alignment mark in Figure B-1 is designated with the number 2 and is shown in magnified detail in Figure B-2. The right alignment mark is vertically aligned with the left alignment mark on the mask. Each of the four compass lines are 300 μm in length by 20 μm in width. The inner feature has outer petals of length 40 μm and width 20 μm. The inner portion is 35 μm long by 10 μm wide.
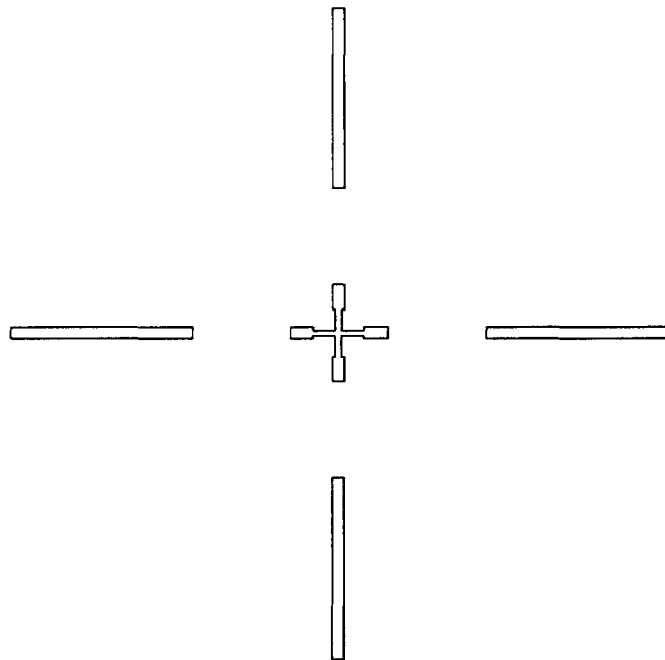
Figure B-2. *PHE Chip Alignment Mark.*

The metal mask, which is the second mask in the process, is shown in Figure B-3. The mask has filled polygons. Meaning, the shapes inside the wafer are dark, and the field of the mask is clear. In this mask, the chip layout of fifteen chips of size 3 cm by 2 cm is discerned more easily. At the center of each chip are the eight resistors depicted in detail in Chapter 4.

The MIT text on either side of each chip serves as an alignment pattern in the assembly process. The MIT text is found on the PHE chip, the DI header cast, and the IM header cast. When the semitransparent DI header cast is placed over the PHE chip during assembly, a moiré pattern becomes visible. Slight motions in the alignment process create large-scale changes in the moiré pattern, and the pattern becomes indistinguishable with a near-perfect alignment.
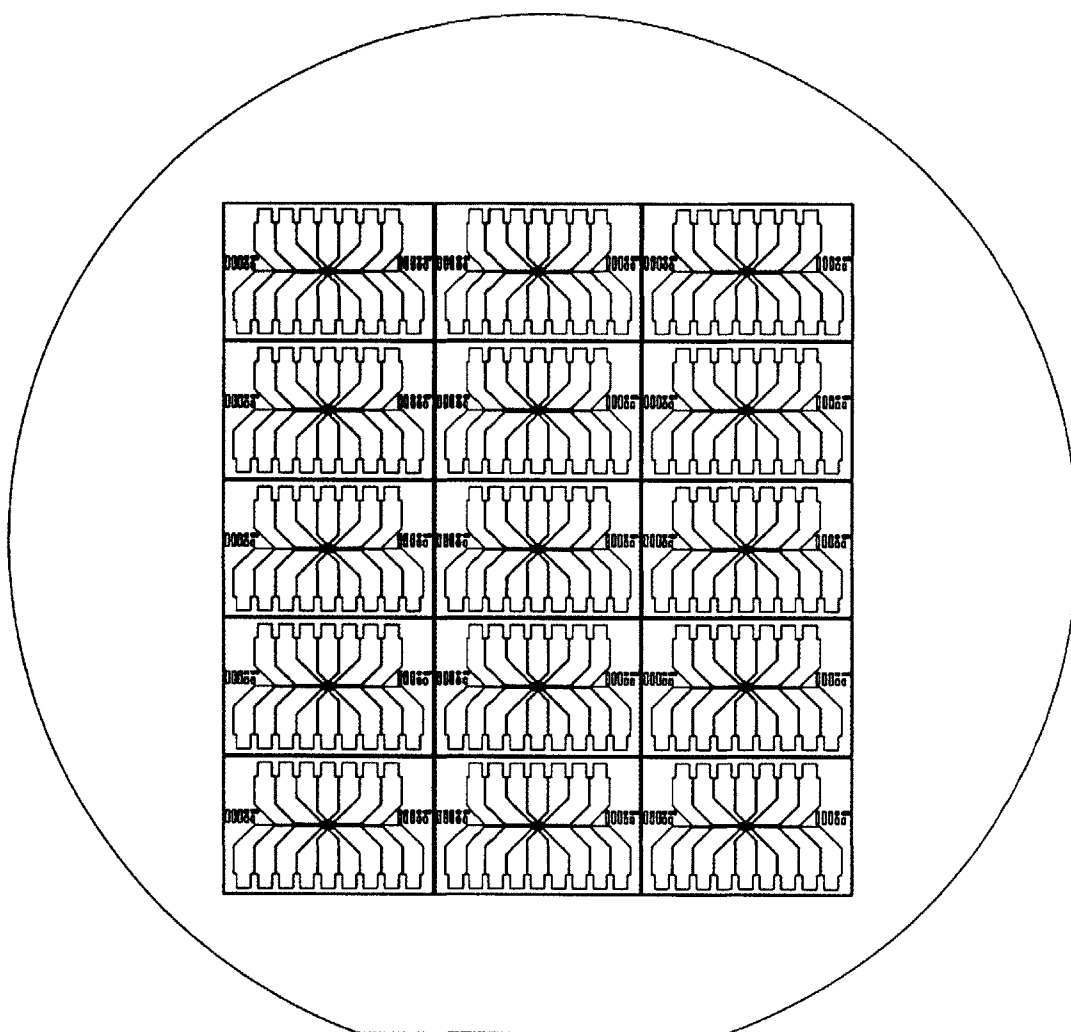
Figure B-3. *PHE Chip Mask 2.*

B.2 Test Structure Chip

One mask is used in the TSC fabrication process. Called mask 2, as no etch mask is required for the in-plane nucleation site process, the mask defines the nucleation sites and resistors. Three iterations of the TSC are described in Chapter 4. The first iteration TSCv3.0 mask is on transparency transferred to a mask blank. Figure B-4 is a screen capture of the TSCv3.0 mask. The mask has filled polygons. At the center of each chip are the eight resistors depicted in detail in Chapter 4.
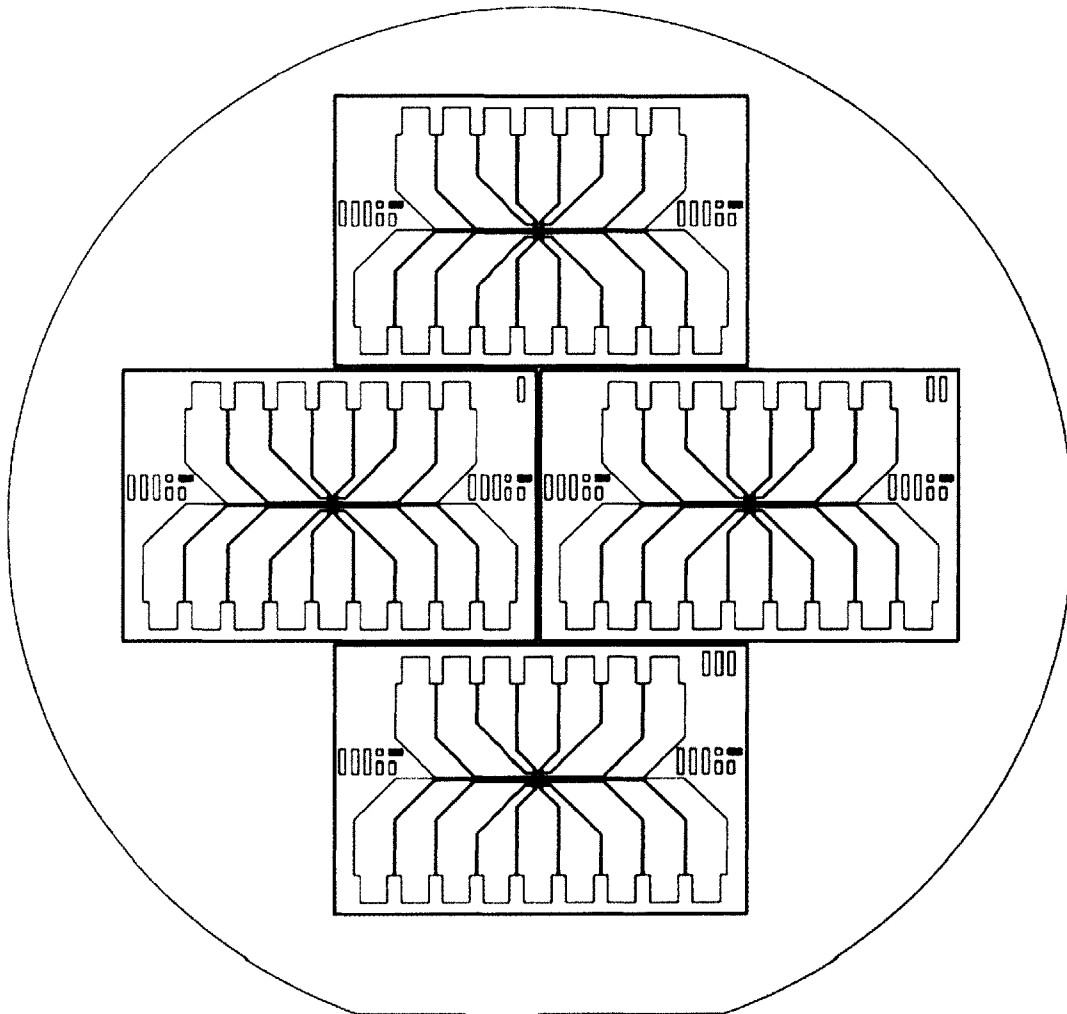
Figure B-4. *TSCv3.0 Mask 2.*

The TSCv3.1 mask also is on a transparency transferred to a blank. Figure B-5 is a screen capture of the TSCv3.1 mask. The mask has filled polygons. In this mask, the chip layout has fifteen chips of size 3 cm by 2 cm. Each chip contains twelve resistors depicted in detail in Chapter 4.
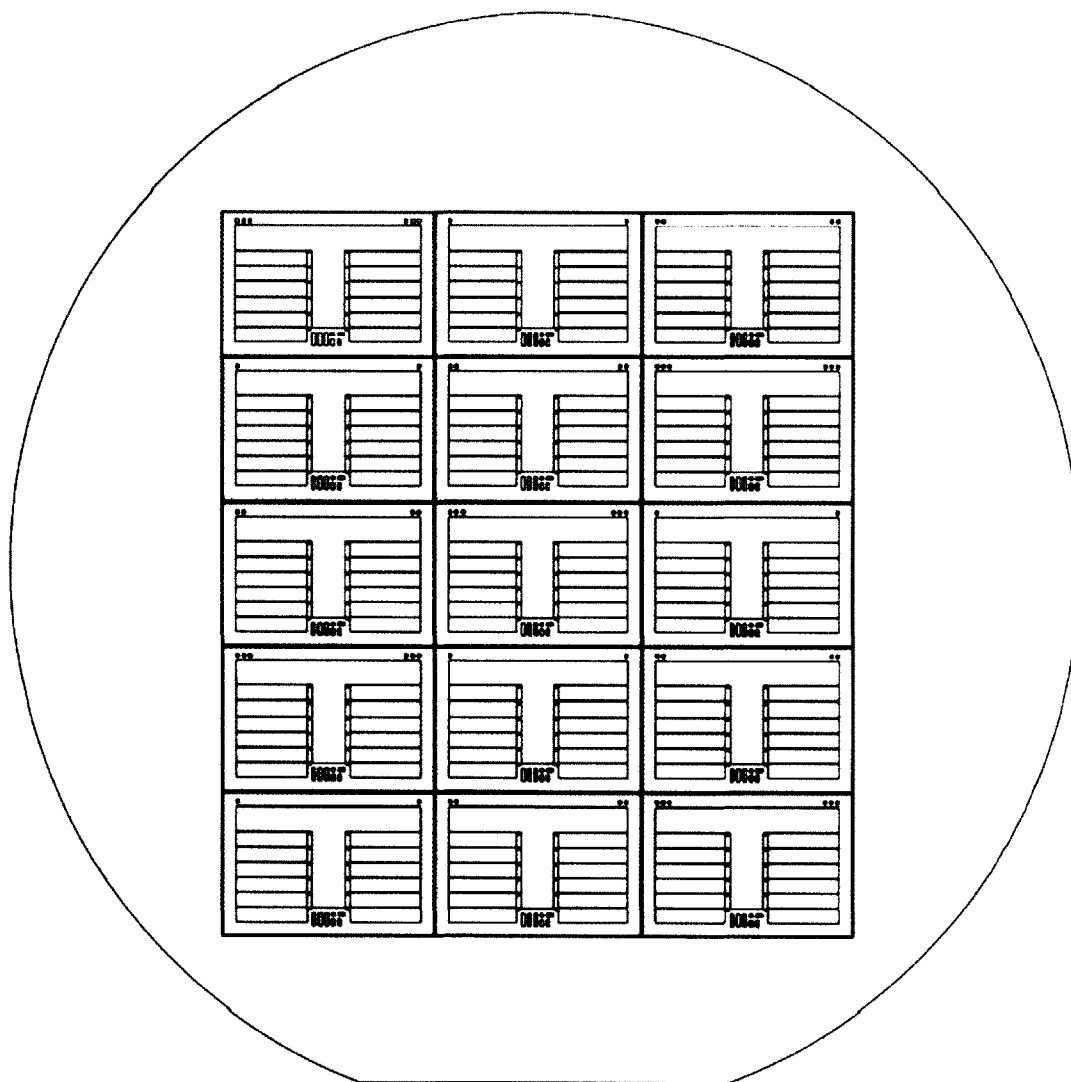
Figure B-5. *TSCv3.1 Mask 2.*

The TSCv3.1 mask is on a chrome mask. Figure B-6 is a screen capture of the TSCv3.1 mask. The mask has filled polygons. In this particular mask, the chip contains layout ten chips. Eight chips are of size 3 cm by 2 cm, and two chips are of size 6 cm by 4 cm. Each chip has multiple resistors, which are described and depicted in Chapter 4.
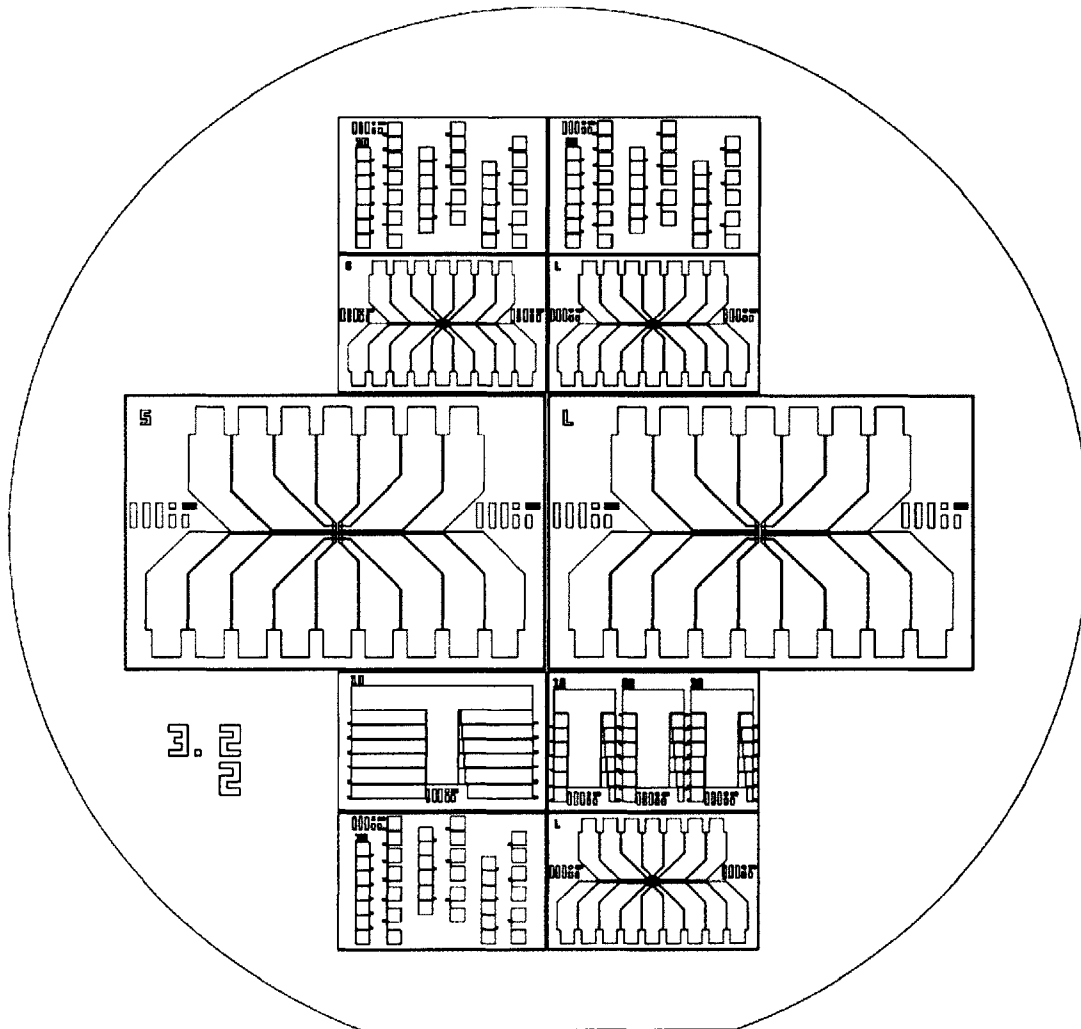
Figure B-6. *TSCv3.2 Mask 2.*

B.3   Deionized Header Mold

The DI header mold process uses three masks. One of the iterations of the DI header mold is described in Chapter 4; the corresponding 2× and 1× masks are presented in Section B.3. Previous iterations use less elaborate alignment marks, which do not facilitate alignment through thick SU-8 layers. Two alignment marks used in previous versions are shown in Figure B-2 and Figure B-7.
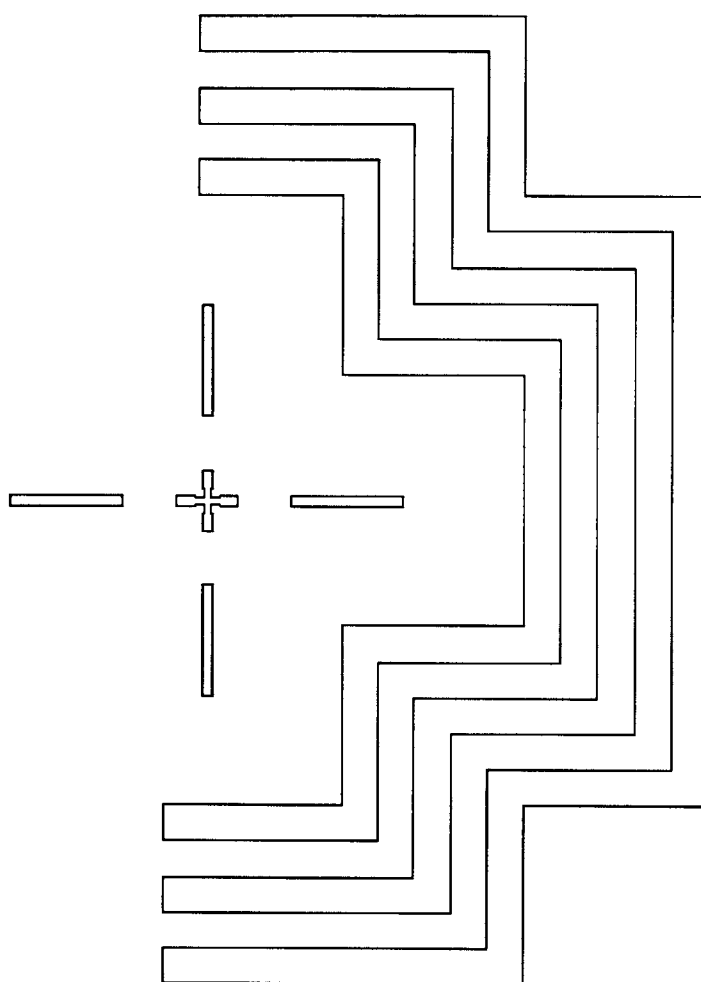
Figure B-7. *DI Header Mold Right Alignment Mark.*

The first 2× mask, denoted mask 1, defines alignment marks for the thick SU-8 photolithography process. Chapter 4 describes the purpose of the specialty alignment marks and provides a figure that depicts the alignment marks used during the alignment process. Mask 1 is a transparency mask with clear polygons that is transferred to a blank. This mask is shown in Figure B-8.
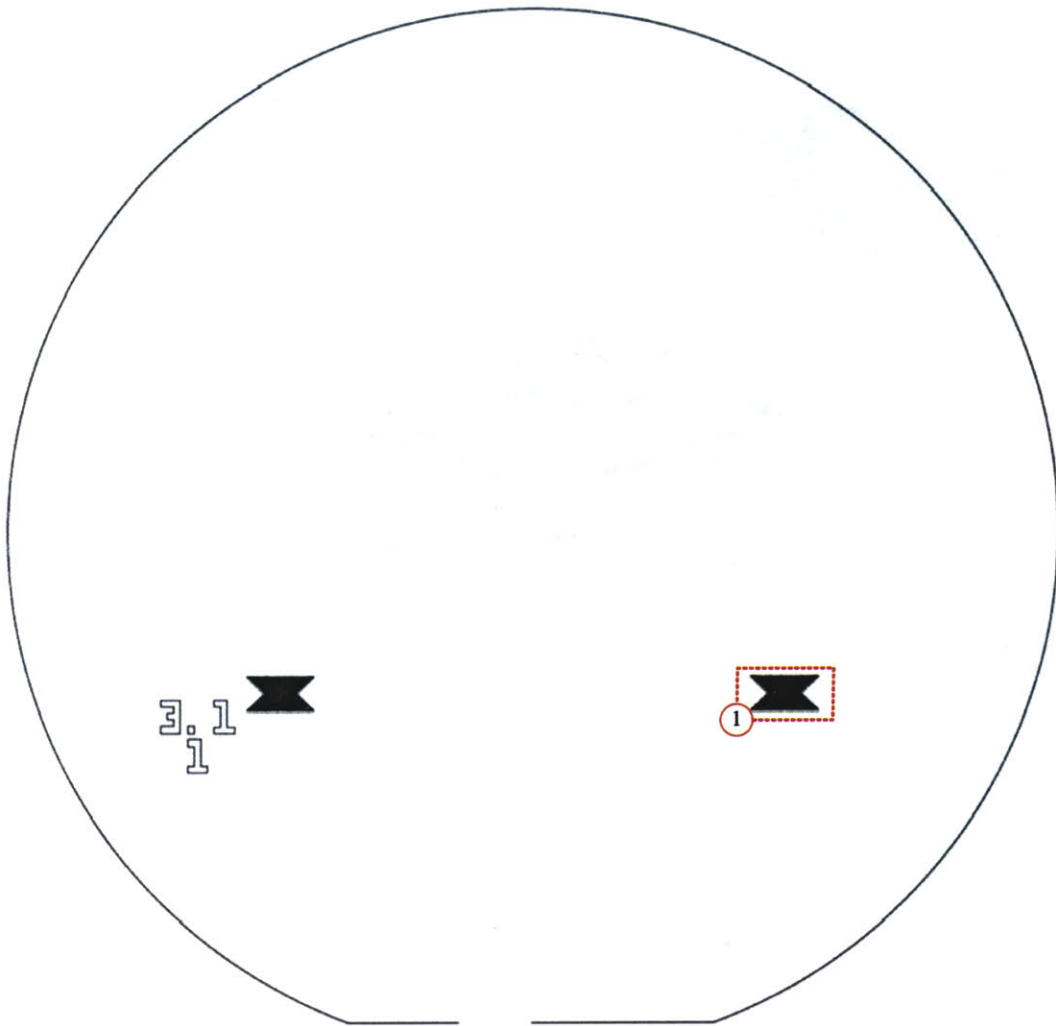
Figure B-8. *Header Mold 2× Mask 1.*

The right alignment mark in Figure B-8 is designated with the number 1 and is shown in detail in Figure B-9. The left alignment mark is vertically aligned with the right alignment mark and also can be seen in Figure B-8. Each alignment mark is composed of thousands of arrows of length 110 μm and width 20 μm that serve to direct photolithography alignment to the central crosshair. For thin SU-8 layers, the alignment mark features in Figure B-2 and Figure B-8 are adequate. However, thicker SU-8 layer photolithography alignment is much easier with the alignment marks illustrated in Figure B-9.
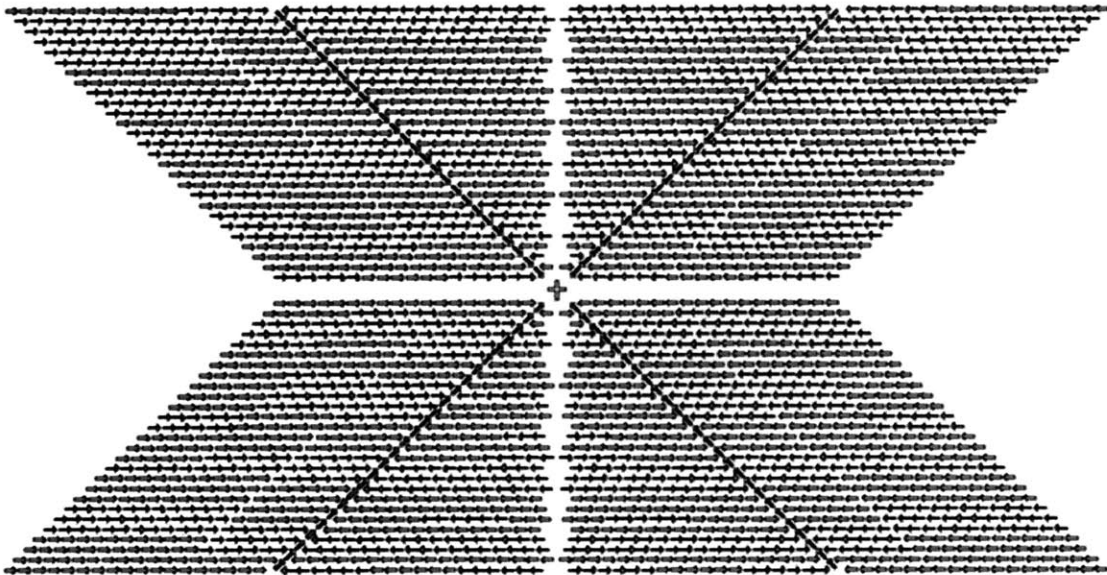
Figure B-9. *Header Mold Alignment Mark.*

The 1× version of mask 1 also has open polygons and contains a pair of the alignment marks featured in Figure B-9. The alignment marks are positioned slightly higher to enable the 3 cm by 2 cm chips to be arrayed in a pattern of five rows with three columns each. The 1× mask is a transparency mask transferred to a blank and is shown in Figure B-10.
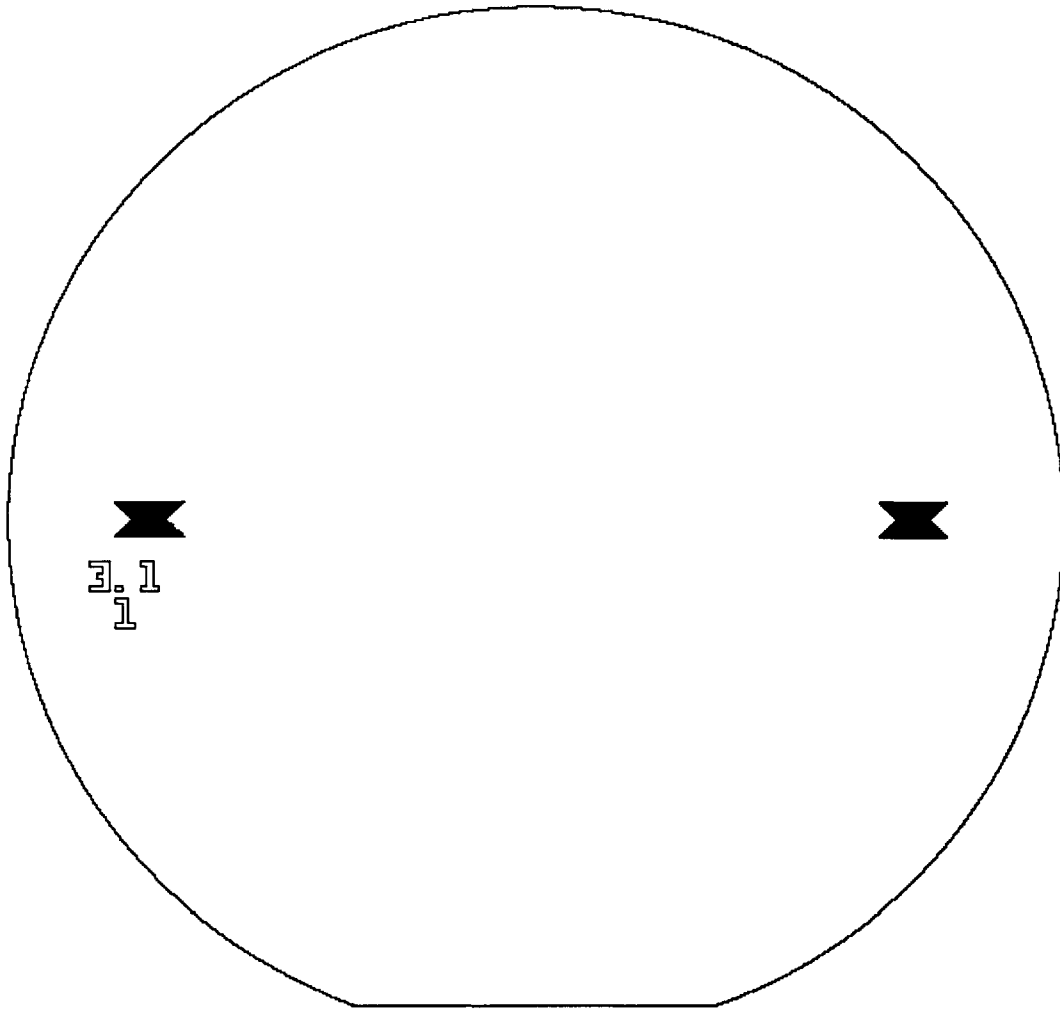
Figure B-10. *Header Mold 1× Mask 1.*

The second 2× mask in the process is mask 3. Mask 3 has open polygons and serves to define the DI header inlet, outlet, and fluidic hub. In kind with the PHE chip, the MIT text on each side of each chip serves as a moiré pattern for alignment in the assembly process. The complete DI moiré pattern will be formed after each of the DI masks is used, and the SU-8 is developed at the end of the fabrication process as described in Appendix A. In this mask, the chip layout is four chips with dimensions 6 cm by 4 cm. The transparency mask is shown in Figure B-11.
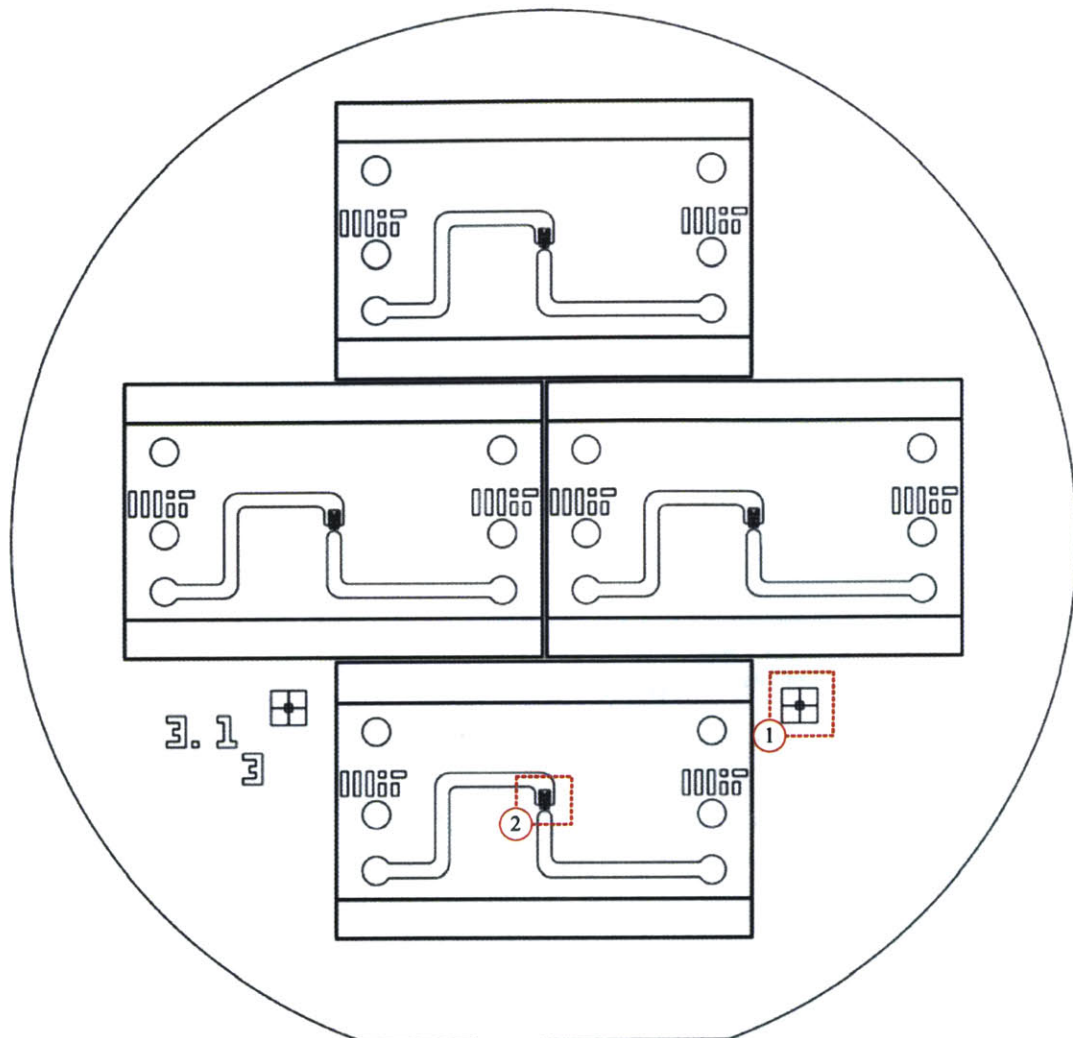
Figure B-11. *DI Header Mold 2× Mask 3.*

The right alignment mark on the mask is designated with the number 1 and is shown in detail in Figure B-12. The right alignment mark is vertically aligned with the left alignment mark. The main feature of the alignment mark is a crosshair surrounded by four clear view-squares, which facilitate alignment. See Chapter 4 for a detailed image of the alignment process.
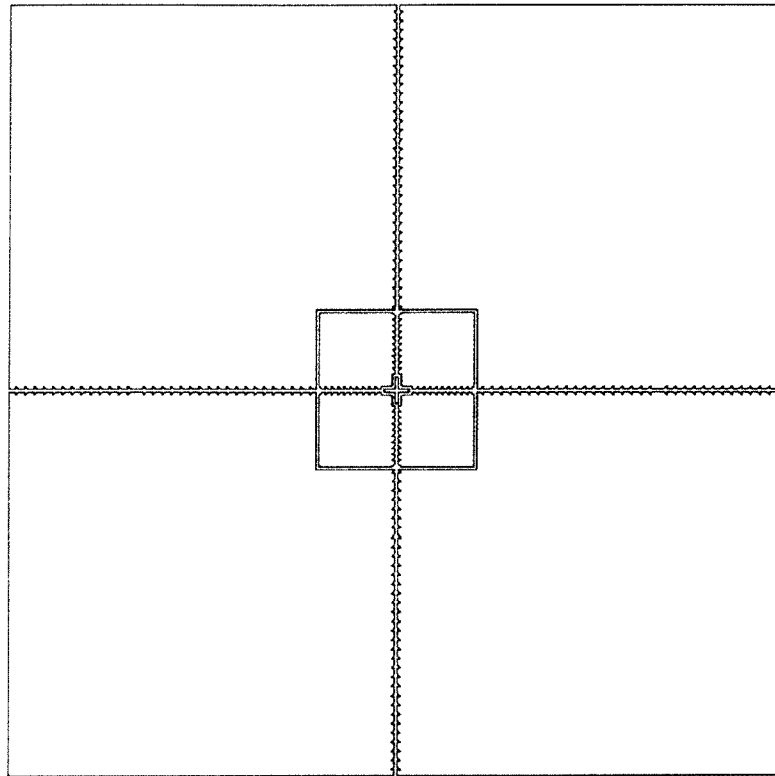
Figure B-12. *Header Mold Upper Alignment Mark.*

The central portion of each chip is the fluidic hub of the DI header mold. In this hub, the fluid flows in through the main inlet and then separates into eight parallel flows through the individual fluidic inlets. From the individual fluidic inlets, the fluid flows through the respective nucleation chamber and then out through the fluidic outlets. Chapter 4 describes the fluidic system, providing images of the particulate-level fluidic system and the lumped element model for the chip-level system. The fluidic hub is designated on mask 3 with the number 2 and is shown in detail in Figure B-13.
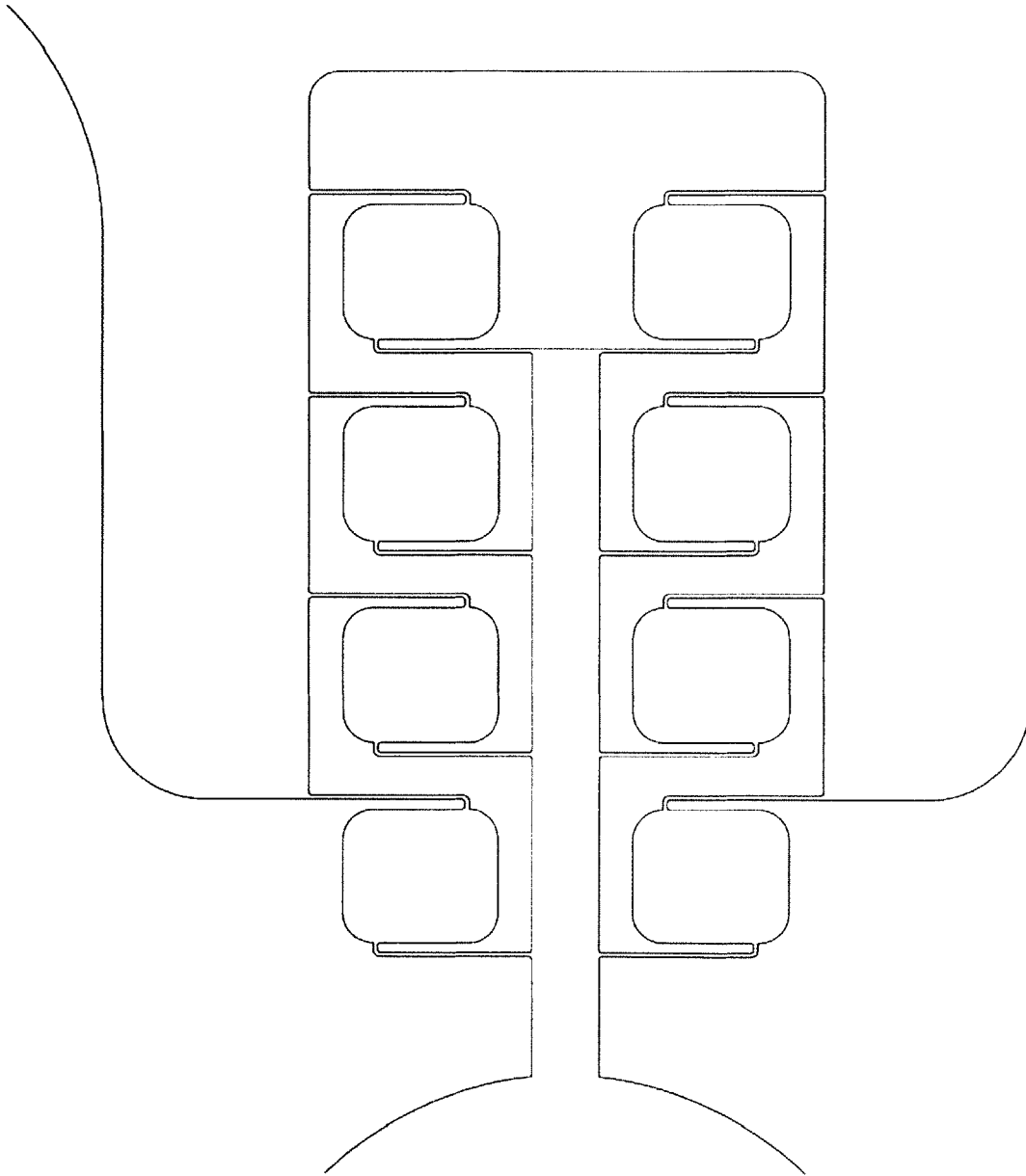
Figure B-13. *DI Header Mold Fluidic Hub.*

The 1× version of mask 3 also has open polygons and contains a pair of the alignment marks featured in Figure B-12. The alignment marks are positioned slightly higher to enable the 3 cm by 2 cm chips to be arrayed in a pattern of five rows with three columns each. The 1× mask is a chrome mask and is shown in Figure B-14.
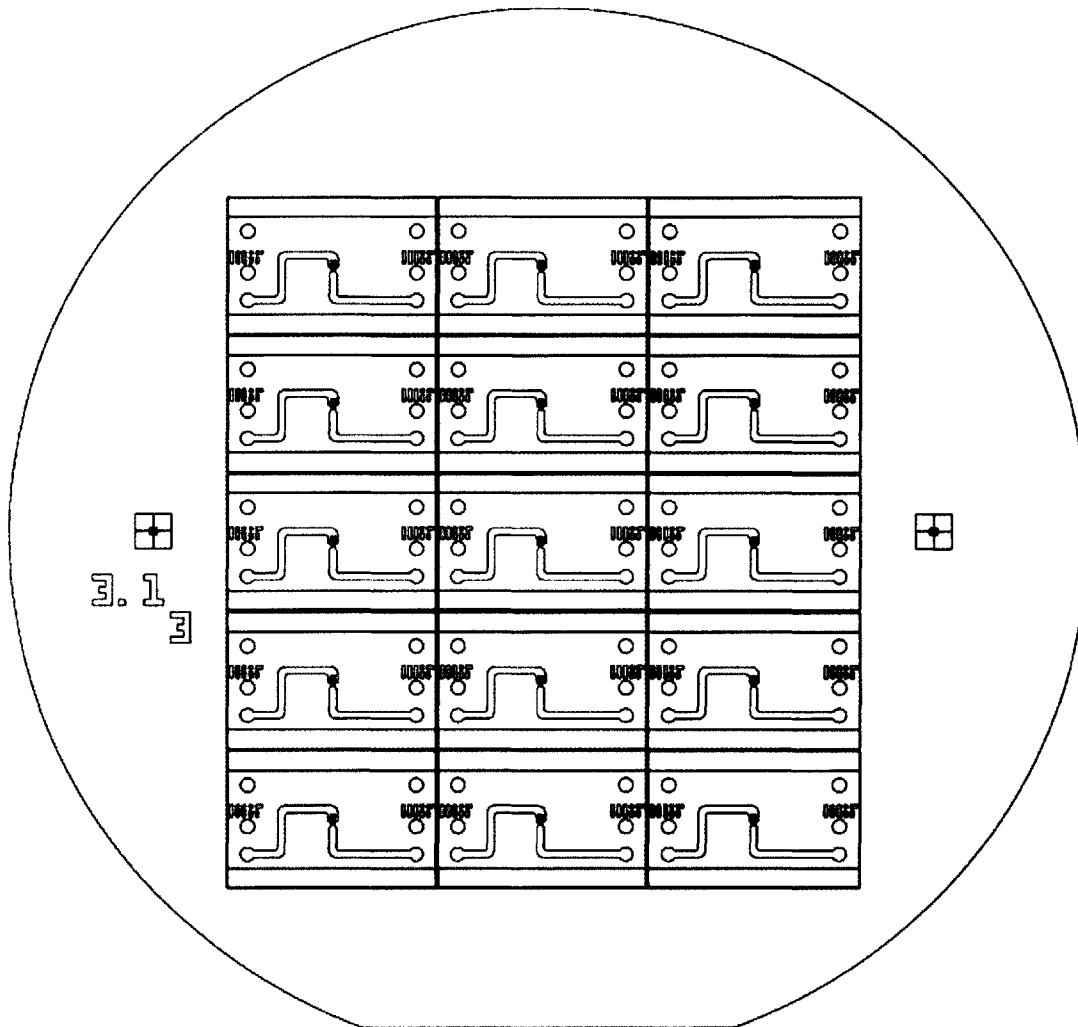
Figure B-14. *DI Header Mold 1×Mask 3.*

The third 2× mask in the process is mask 4. Shown in Figure B-15, the mask has open polygons and is made on a transparency transferred to a blank. Mask 4 defines the main fluidic inlet and outlet headers, which are first thinly defined in mask 3. Mask 4 enables the inlet and outlet headers to be fabricated to have a total thickness of about 300 μm.
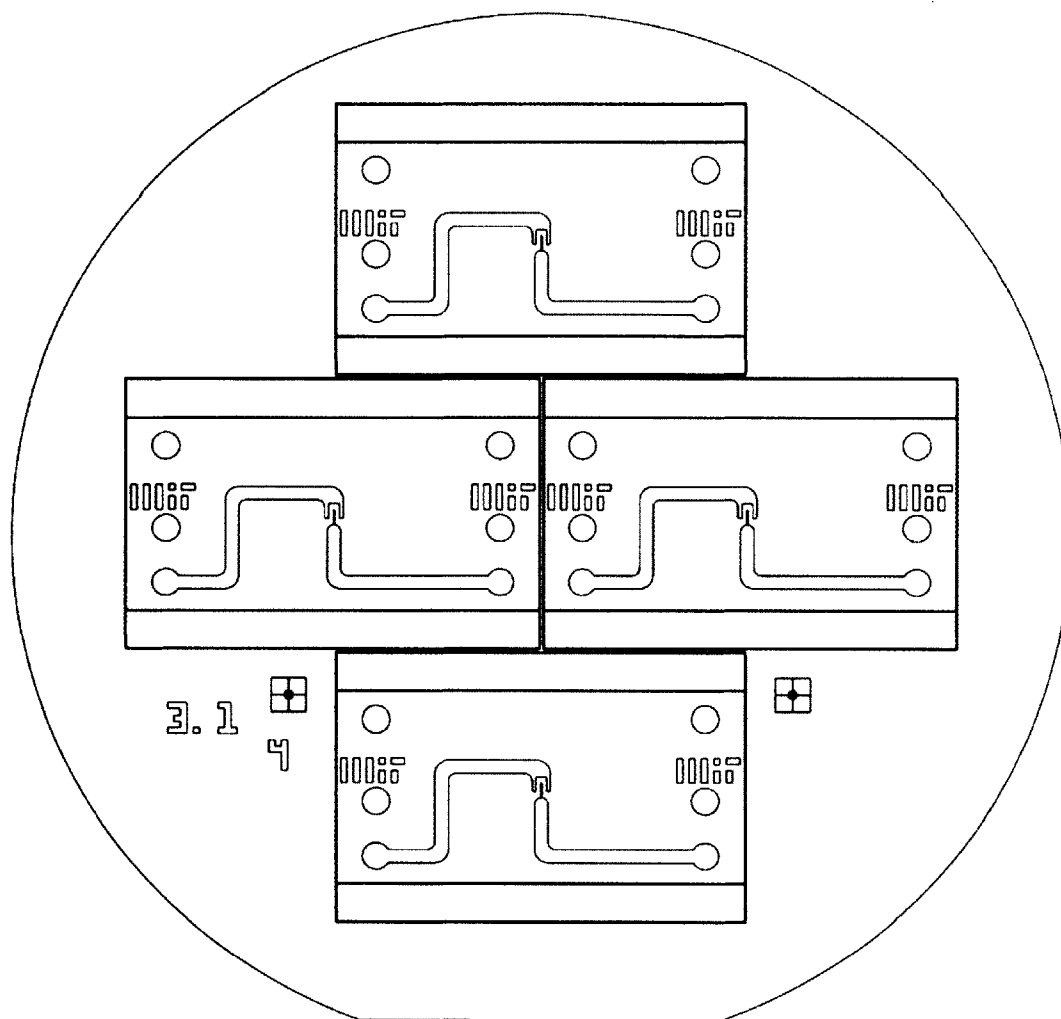
Figure B-15. *DI Header Mold 2× Mask 4.*

The third 1× mask in the process has clear polygons and is a chrome mask. Since the 1× mask is the 1× version of the 2× mask in the process, the mask also is named mask 4. Illustrated in Figure B-16, the mask contains fifteen chips and defines the main fluidic inlet and outlet.
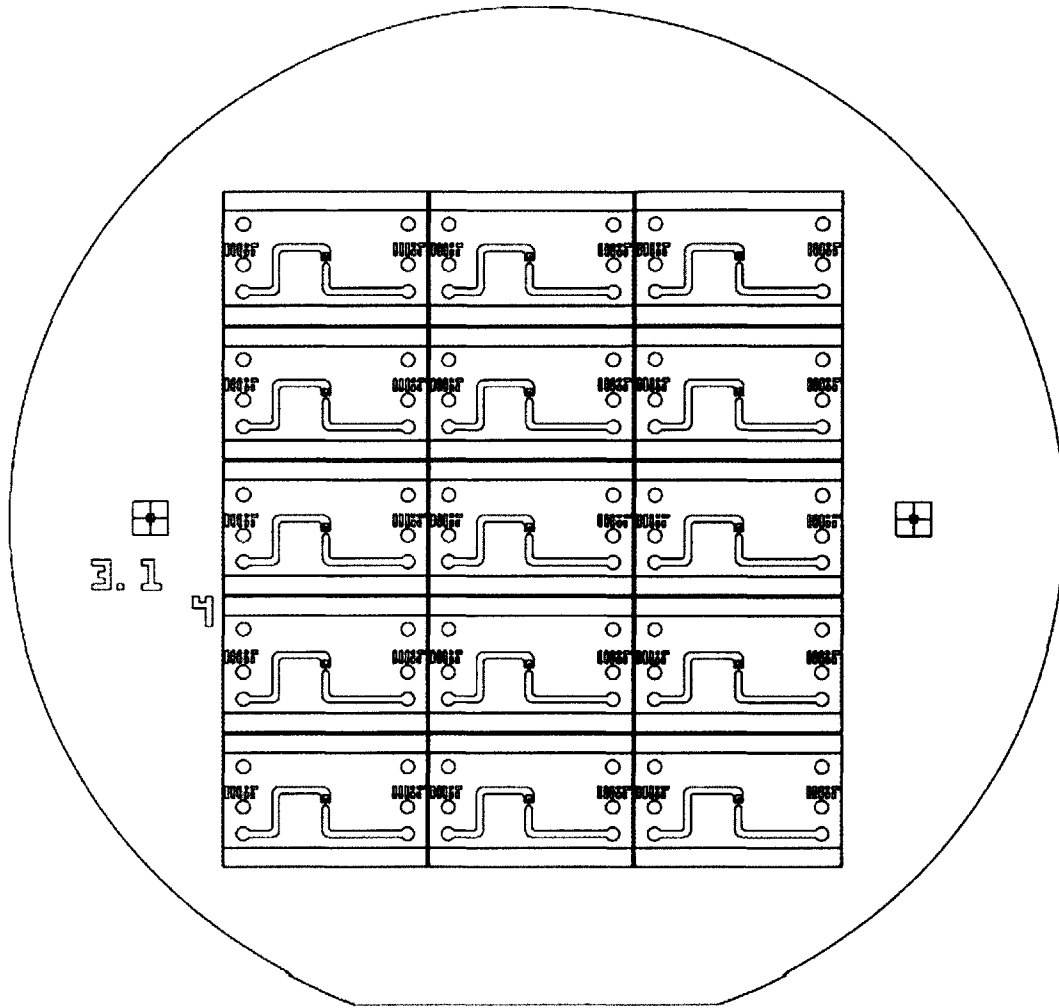
Figure B-16. *DI Header Mold 1× Mask 4.*

B.4   Input Medium Header Mold

The IM header mold process involves four masks. One of the iterations of the IM header mold is described in Chapter 4; the corresponding masks will be presented in this section. Previous iterations use less elaborate alignment marks, which do not facilitate alignment through thick SU-8 layers. The first mask, mask 1, defines alignment marks for the thick SU-8 photolithography process. Mask 1 is used in the IM header mold process shown in 2× in Figure B-8 and in 1× in Figure B-10 with details shown in Figure B-9.

The second mask in the process is mask 7. This transparency mask has open polygons. In this mask, the chip layout is four chips of dimensions 6 cm by 4 cm and defines the main IM input and output headers. The 2× version of mask 7 is shown in Figure B-17.
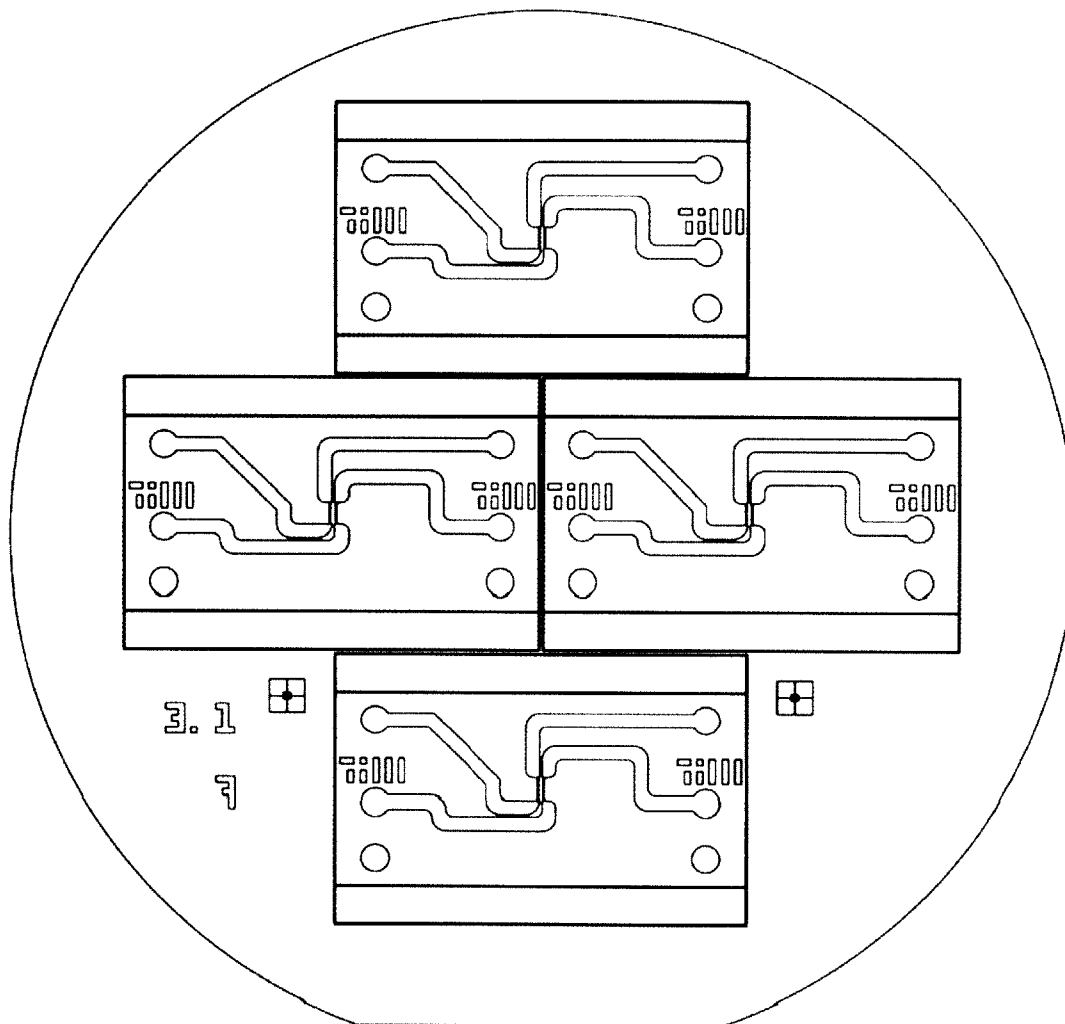
Figure B-17. *IM Header Mold 2×Mask 7.*

The 1× version of the second mask in the process is a chrome mask is denoted as mask 7. The mask also has open polygons. In this mask, the chip layout is fifteen chips of dimensions 3 cm by 2 cm and defines the main IM input and output headers. The 1× version of mask 7 is shown in Figure B-18.
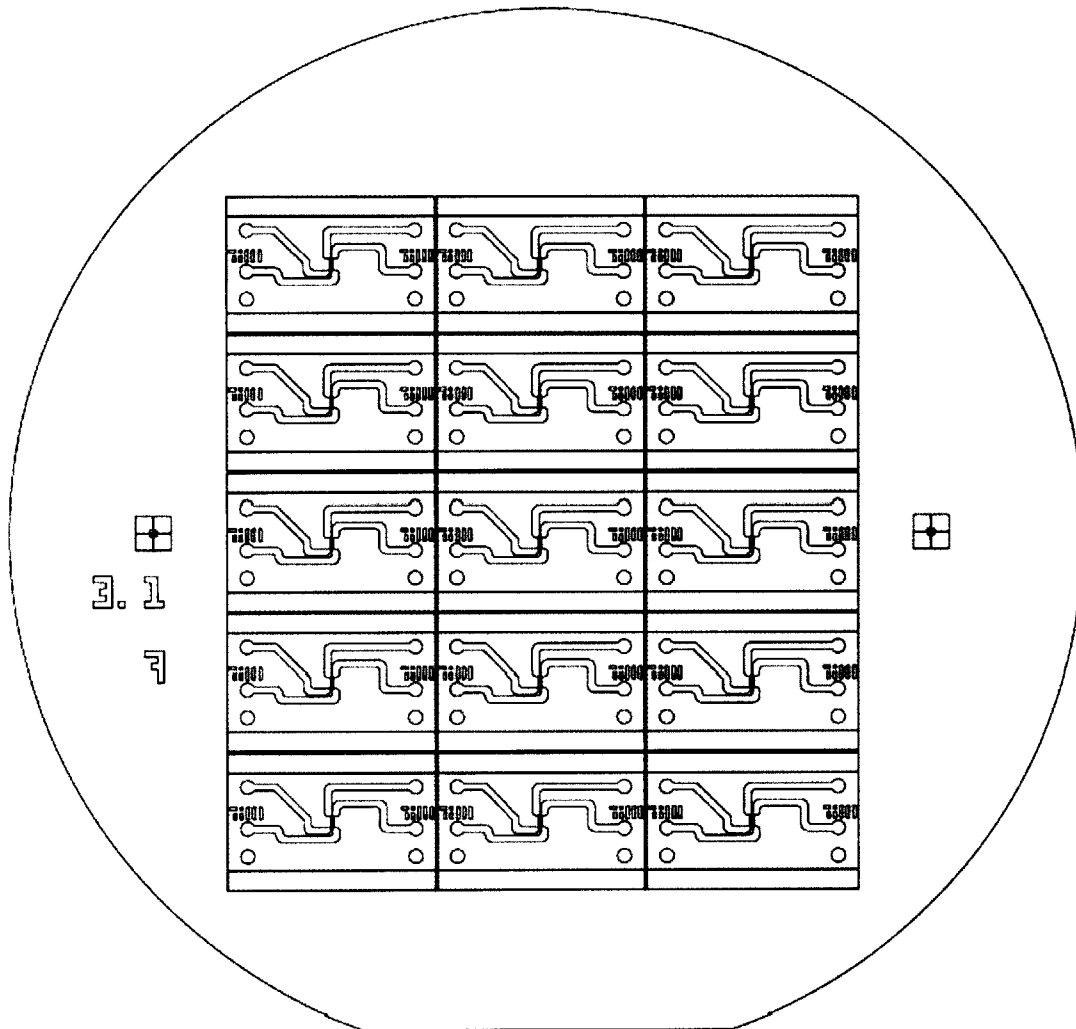
Figure B-18. *IM Header Mold 1×Mask 7.*

A screen capture of the 2× mask 6, the third mask in the IM header mold process, is shown in Figure B-19. The transparency mask has open polygons and serves to define the captures sites. The chip layout is four chips of dimensions 6 cm by 4 cm.
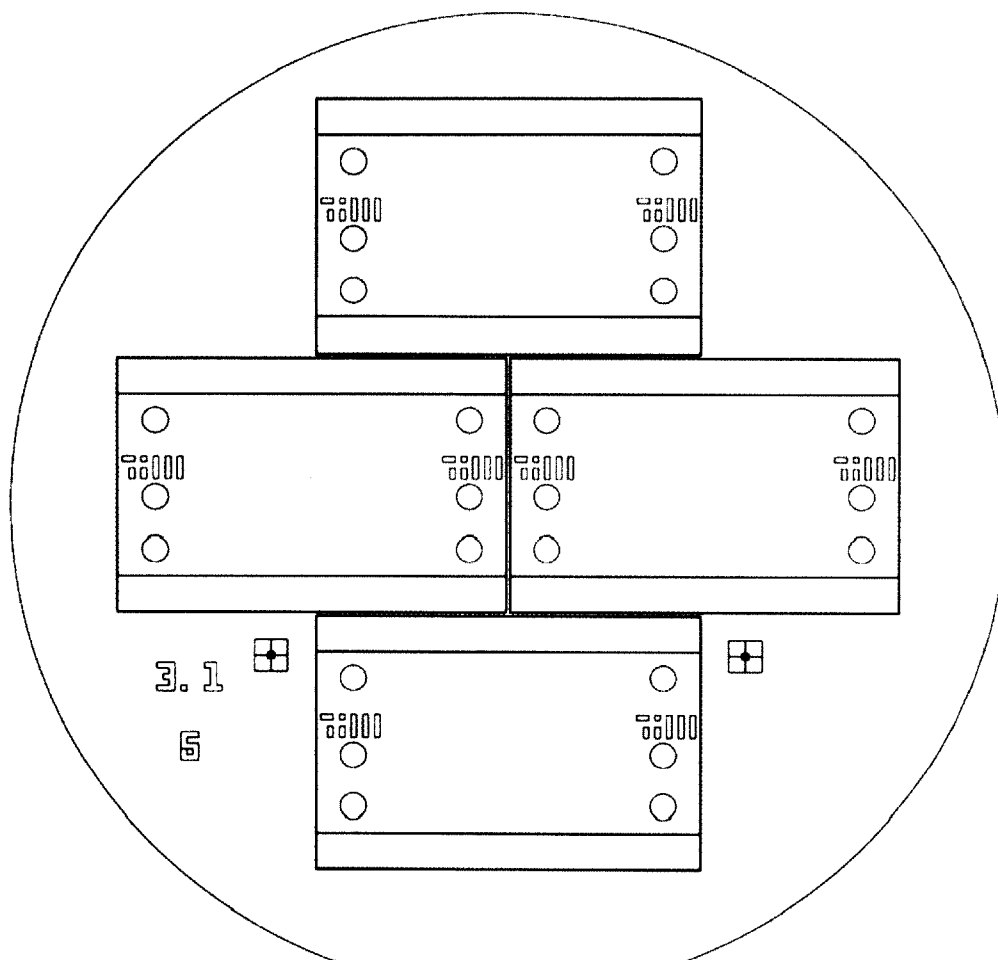
Figure B-19. *IM Header Mold 2×Mask 6.*

The 1× version of mask 6 is shown in Figure B-20. The chrome mask has open polygons and serves to define the captures sites. The chip layout is fifteen chips of dimensions 3 cm by 2 cm.
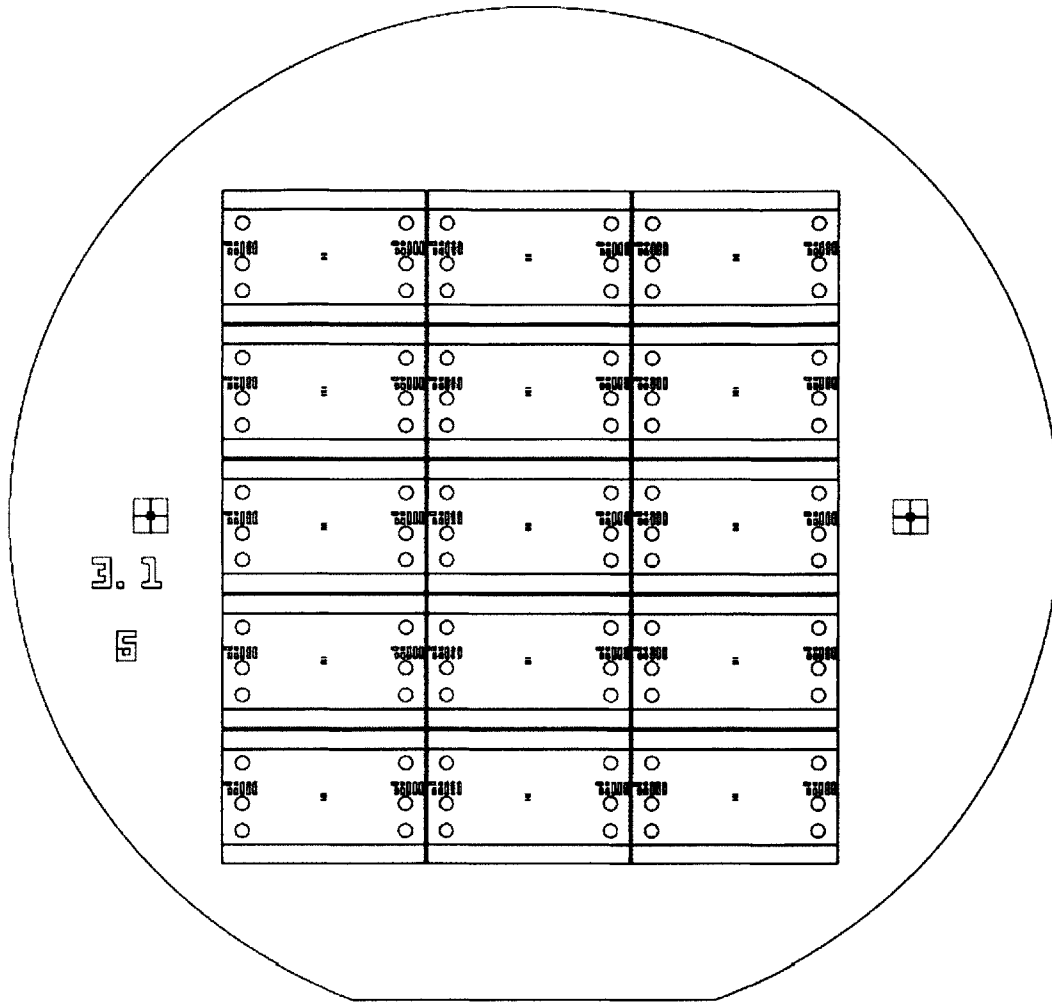
Figure B-20. *IM Header Mold 1× Mask 6.*

Mask 5 is the fourth and final mask in the IM header mold process. A screen capture of the 2× version of the mask is shown in Figure B-21. The chrome mask has open polygons and defines the jet channels.
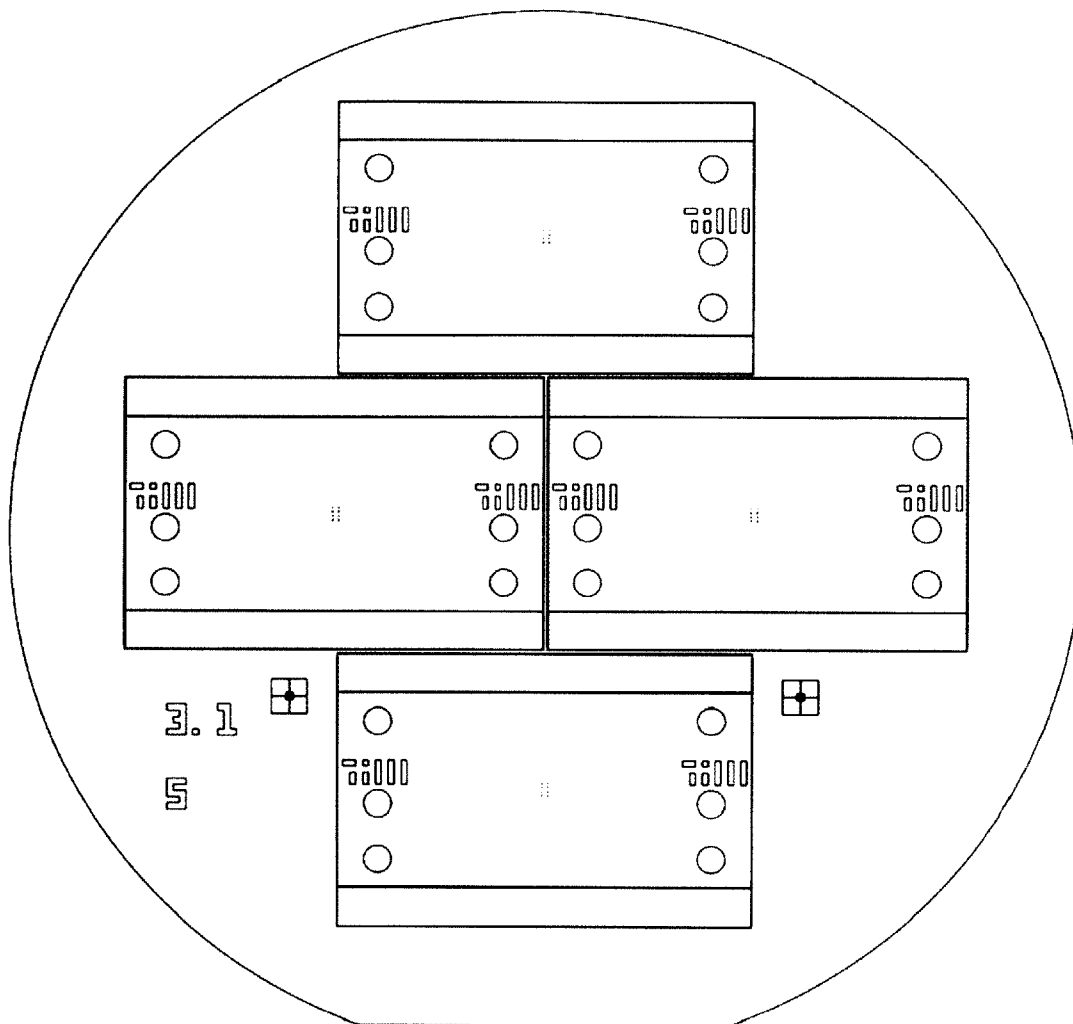
Figure B-21. *IM Header Mold 2x Mask 5.*

The final 1× mask of the IM header mold process is mask 5. With open polygons, the design consists of fifteen chips of dimension 3 cm by 2 cm. A screen capture of the 1× transparency mask 5 is shown in Figure B-22. The mask has open polygons and defines the jet channels.
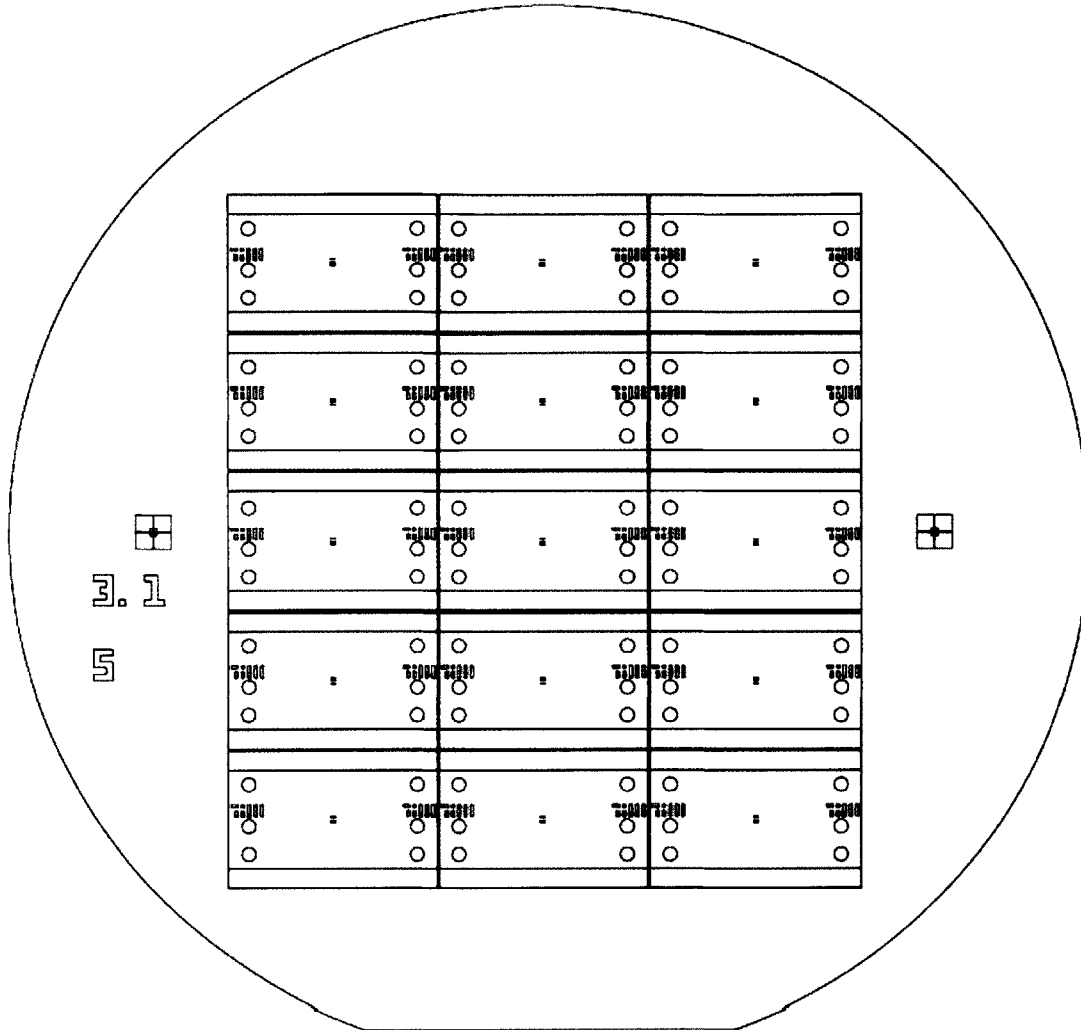
Figure B-22. *IM Header Mold 1× Mask 5.*

Appendix C   Electrical Schematic Diagrams

As discussed in Section 4.2, the system architecture design focus is to maximize the usage of commercially available components without sacrificing the desired performance of the μBA-driven device. The resultant architecture consists of microfabricated components, custom electronics, electronics, and packaging. The microfabricated components and custom electronics specific to the μBA-driven device include a fluidic interface, PHE chip, MMI, and UIM.
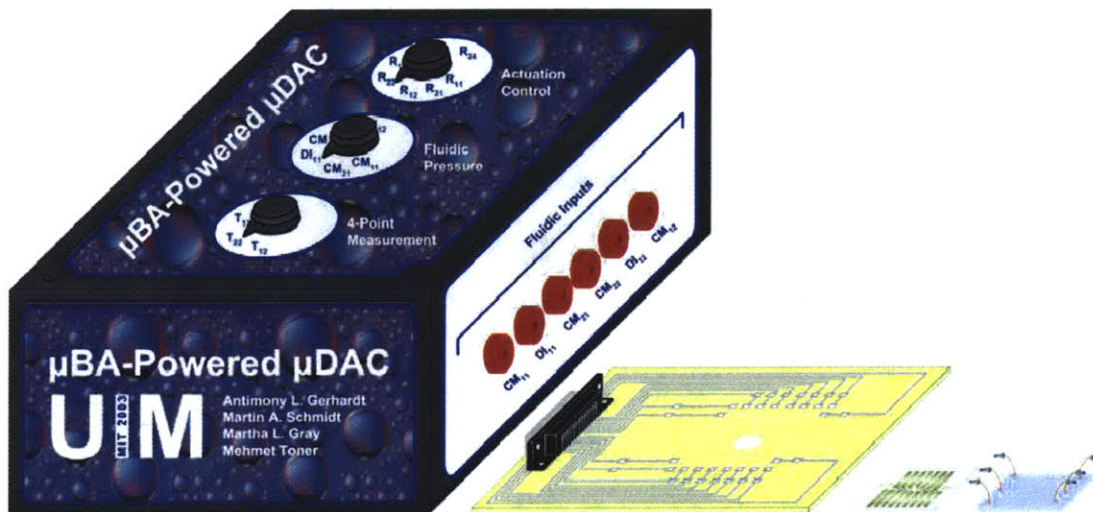
Figure C-1. *PHE Chip Electrical Schematic.*

Figure C-1 illustrates drawings of these four components in reverse order — UIM, MMI, PHE chip, and fluidic interface. The lumped element model of the fluidic system is depicted and described in Section 4.2.3 and shown in Figure C-2. The full electrical schematic diagrams of the PHE chip, MMI, and UIM are shown in Figure C-3, Figure C-4, and Figure C-5. Pin numbers and part values are labeled, and wire crossings are shown with a half-circular jog for ease of viewing and wire tracing.
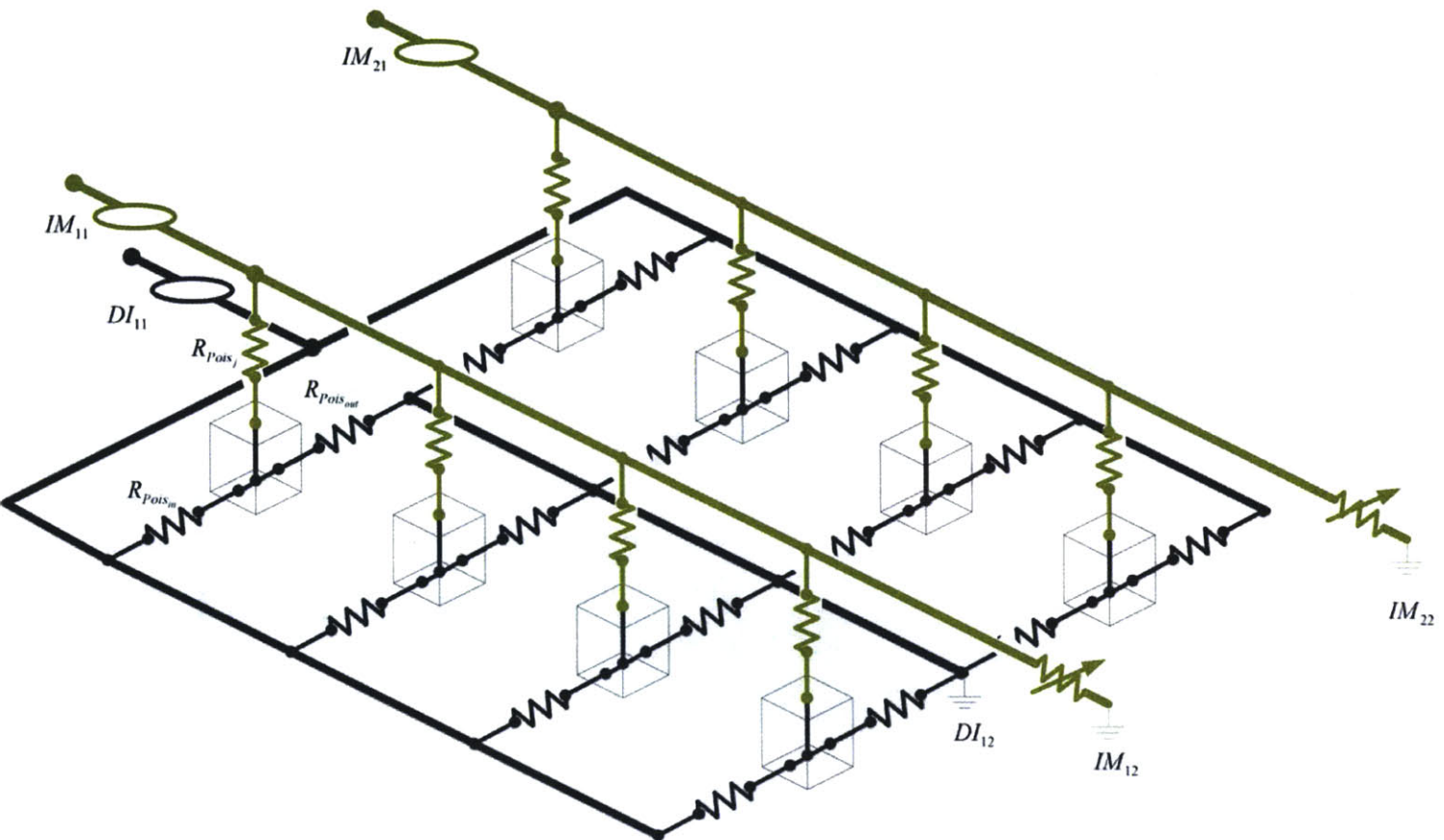
Figure C-2. *Fluidic System Lumped Element Model Electrical Schematic.*

Figure C-3. *PHE Chip Electrical Schematic.*
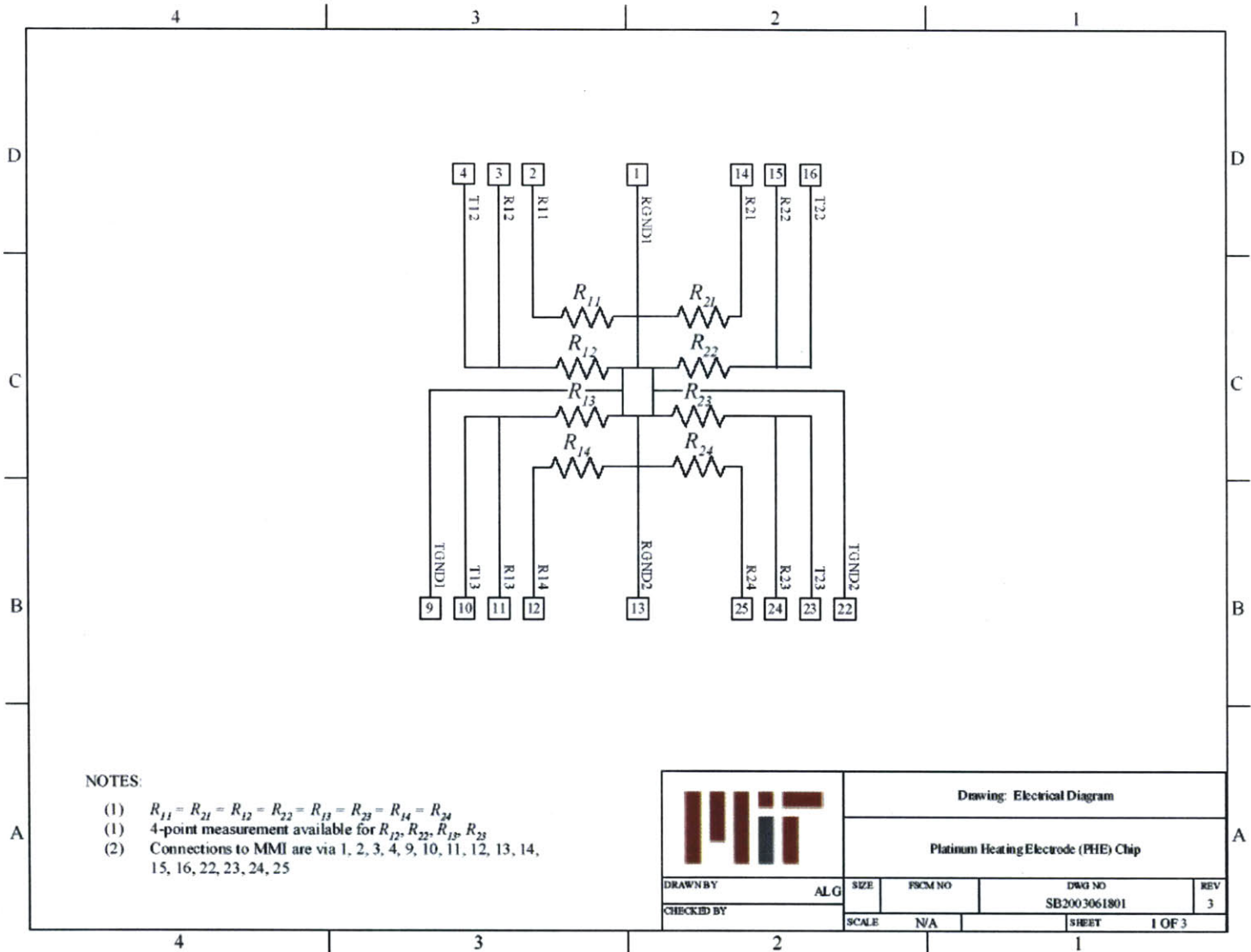
NOTES:

(1) $R_{11} = R_{21} = R_{12} = R_{22} = R_{13} = R_{23} = R_{14} = R_{24}$

(1) 4-point measurement available for R_{12}, R_{22}, R_{13}, R_{23}

(2) Connections to MMI are via 1, 2, 3, 4, 9, 10, 11, 12, 13, 14, 15, 16, 22, 23, 24, 25

Drawing: Electrical Diagram					
Platinum Heating Electrode (PHE) Chip					

DRAWN BY ALG
CHECKED BY
SIZE FSCM NO DWG NO SB2003061801 REV 3
SCALE N/A SHEET 1 OF 3
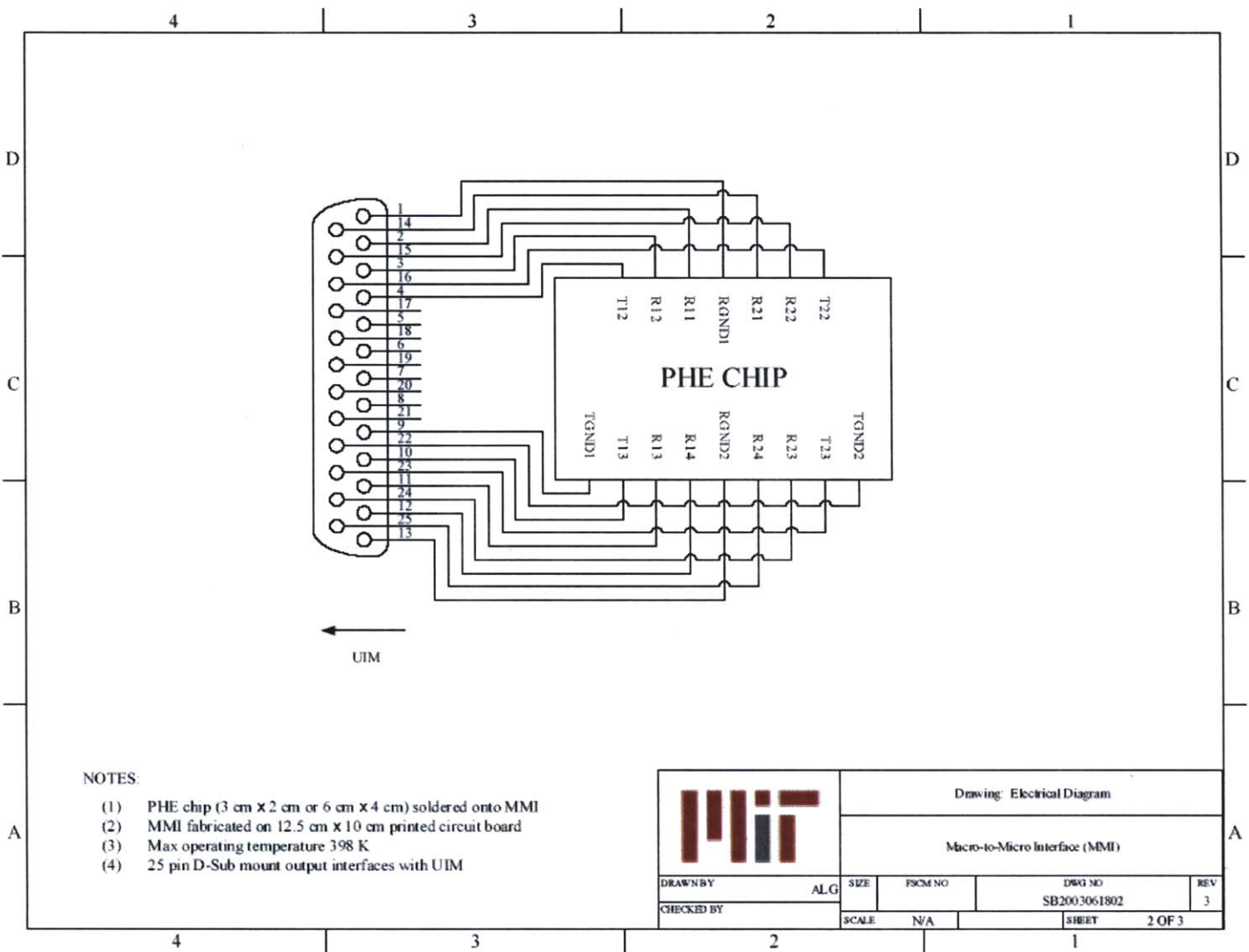
Figure C-4. *MMI Electrical Schematic.*

PHE CHIP

UIM

NOTES:

(1) PHE chip (3 cm x 2 cm or 6 cm x 4 cm) soldered onto MMI
(2) MMI fabricated on 12.5 cm x 10 cm printed circuit board
(3) Max operating temperature 398 K
(4) 25 pin D-Sub mount output interfaces with UIM

Drawing: Electrical Diagram				
Macro-to-Micro Interface (MMI)				

DRAWN BY	ALG	SIZE	FSCM NO	DWG NO	REV
CHECKED BY				SB2003061802	3
		SCALE	N/A	SHEET 2 OF 3	
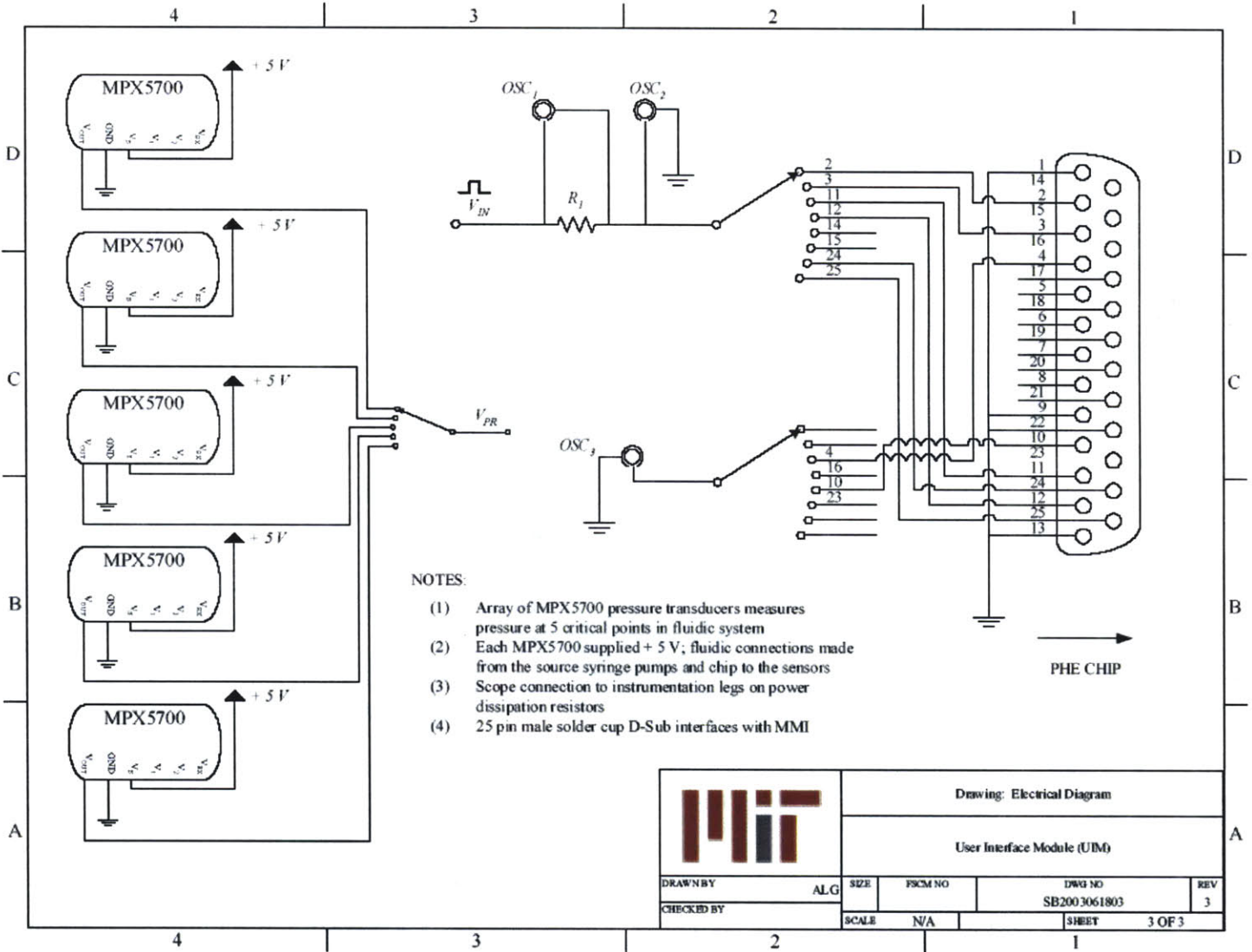
Figure C-5. UIM Electrical Schematic.

NOTES:

(1) Array of MPX5700 pressure transducers measures pressure at 5 critical points in fluidic system

(2) Each MPX5700 supplied + 5 V; fluidic connections made from the source syringe pumps and chip to the sensors

(3) Scope connection to instrumentation legs on power dissipation resistors

(4) 25 pin male solder cup D-Sub interfaces with MMI

			Drawing: Electrical Diagram	
			User Interface Module (UIM)	
DRAWN BY	ALG	SIZE	FSCM NO	DWG NO	REV
CHECKED BY				SB2003061803	3
		SCALE	N/A	SHEET	3 OF 3

PHE CHIP

Appendix D   Sampling of Raw Data

The chip performance hypotheses, methods, and results are presented in Chapter 5. The raw data is collected after a standard input or a chirped input is applied to a selected resistor. Recorded data include: (1) input type, (2) pulse width δ, (3) pulse frequency f_A, (4) resistor resistance, (5) video file of the nucleation through dissipation process, (6) whether a microbubble formed, (7) time at which the maximum fast transient $\overline{D}$ is evident, (8) time at which the maximum slow transient $\overline{D}$ is evident, (9) time at which the slow transient is no longer evident, and (10) experimental observations. The video file then is used to collect: (11) the major and minor maximum fast transient D measurements, (12) major and minor maximum slow transient D measurements, (13) fast transient x-centricity and y-centricity, (14) slow transient x-centricity and y-centricity, (15) fast transient diameters as a function of time, and (16) slow transient diameters as a function of time.

Table D-1, Table D-2, Table D-3, and Table D-4 contain raw data from each of the distinct geometries tested — in-plane with 10 μm long nucleation site, in-plane with 20 μm long nucleation site, in-plane with 30 μm long nucleation site, and out-of-plane with 6 μm cavity. Figure D-1 illustrates the four distinct geometries with the out-of-plane geometry first. The out-of-plane geometry has a 6 μm square nucleation site (a). The in-plane geometries have a 3 μm wide nucleation site by 10 μm long (b), 20 μm long (b), and 30 μm long (c)

(a)   (b)   (c)   (d)
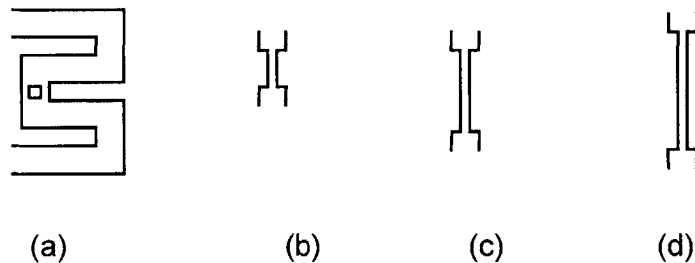
Figure D-1. *Distinct Nucleation Geometries.*

Table D-1 contains a sampling of raw data (1) through (14) from an in-plane resistor of total length 70 µm and nucleation site length of 10 µm. This is a geometry six resistor, as depicted in Chapter 4. The raw data specifies the input parameters, which indicate that a chirped input was applied with input pulse width δ = 5, 10:10:50 ms and Δ = 2 min. Each column corresponds to an input pulse width in increasing width order.

The resistance of the resistor is measured to be about 19 Ω, and video files were created for each of the nucleation and dissipation processes. For this performance test, a microbubble formed for each applied pulse. For the δ = 5 ms input pulse, the fast transient forms at 1.26 s:ff, which means that the fast transient formed at 1 second and 26/30 frames. The slow transient formed at 1.27 s:ff, and the slow transient is no longer evident at 2.23 s:ff.

An experimental observation was made that fresh DI was used for the performance test. The major and minor maximum fast transient D measurements are 24 mm and 20 mm, respectively. The measurements are calibrated as described in Chapter 5. The major and minor maximum slow transient D measurements are 14 mm and 14 mm. The fast transient d_x = 13 mm and d_y = 12 mm. Similarly, the slow transient d_x = 7 mm and d_y = 7 mm. The d_x and d_y raw data then are converted to centricity measurements, as specified in Chapter 5. The fast transient and slow transient diameters as a function of time are collected from the video file as described in Chapter 5, which also illustrates several archetypal transient diameters as a function of dissipation time curves.

Table D-1. *Sampling of Raw Data for In-Plane Resistor with 10 μm Nucleation Site.*

Property	Sample of Data Collected for Chirped Input					
	Input 1	Input 2	Input 3	Input 4	Input 5	Input 6
Input Type	Chirped	Chirped	Chirped	Chirped	Chirped	Chirped
δ (ms)	5	10	20	30	40	50
Δ (min)	2	2	2	2	2	2
R (Ω)	19	19	19	19	19	19
Video File	IP6_R32	IP6_R32	IP6_R32	IP6_R32	IP6_R32	IP6_R32
Bubble?	Yes	Yes	Yes	Yes	Yes	Yes
Max FT $\overline{D}$ (s:ff)	1.26	0.28	0.29	0.28	0.26	1.00
Max ST $\overline{D}$ (s:ff)	1.27	0.29	1.00	0.29	0.27	1.01
No ST (s:ff)	2.23	3.26	6.22	9.27	12.28	18.14
Experimental Observation	Fresh DI	—	—	—	—	—
Max FT Major D (mm)	24	31	39	49	48.5	49
Max FT Minor D (mm)	20	28	39	49	48.5	49
Max ST Major D (mm)	14	14	17	18	20	25
Max ST Minor D (mm)	14	14	17	18	20	25
Max FT d_x (mm)	13	14.5	20	22	22	22
Max FT d_y (mm)	12	16	18	23	28	26
Max ST d_x (mm)	7	8	10.5	10	11	14.5
Max ST d_y (mm)	7	6.5	8	9	11	12.5

Table D-2 contains raw data (1) through (14) from an in-plane resistor of total length 80 μm and nucleation site length of 20 μm. This is a geometry seven resistor, as depicted in Chapter 4. Table D-3 contains raw data (1) through (14) from an in-plane resistor of total length 90 μm and nucleation site length of 30 μm. This is a geometry eight resistor, as depicted in Chapter 4. Table D-4 contains raw data (1) through (14) from an out-of-plane resistor with 6 μm nucleation site.

Table D-2. *Sampling of Raw Data for In-Plane Resistor with 20 μm Nucleation Site.*

Property	Sample of Data Collected for Chirped Input					
	Input 1	Input 2	Input 3	Input 4	Input 5	Input 6
Input Type	Chirped	Chirped	Chirped	Chirped	Chirped	Chirped
δ (ms)	5	10	20	30	40	50
Δ (min)	2	2	2	2	2	2
R (Ω)	21	21	21	21	21	21
Video File	IP7_R32	IP7_R32	IP7_R32	IP7_R32	IP7_R32	IP7_R32
Bubble?	Yes	Yes	Yes	Yes	Yes	Yes
Max FT $\overline{D}$ (s:ff)	1.01	1.01	0.25	1.01	0.25	1.19
Max ST $\overline{D}$ (s:ff)	1.02	1.02	0.26	1.02	0.26	1.20
No ST (s:ff)	1.22	3.26	6.20	11.16	13.18	19.25
Experimental Observation	Fresh DI	—	—	—	—	—
Max FT Major D (mm)	30	33	37	37	37	42
Max FT Minor D (mm)	30	33	37	37	37	42
Max ST Major D (mm)	14	12.5	16	18	20	24
Max ST Minor D (mm)	14	12.5	16	18	20	24
Max FT d_x (mm)	15	17	18.5	20	20	22
Max FT d_y (mm)	19	22	23	22	23	26
Max ST d_x (mm)	7.5	6	6	7	9	13
Max ST d_y (mm)	6.5	6	8	9.25	10	12

Table D-3. *Sampling of Raw Data for In-Plane Resistor with 30 μm Nucleation Site.*

Property	Sample of Data Collected for Chirped Input					
	Input 1	Input 2	Input 3	Input 4	Input 5	Input 6
Input Type	Chirped	Chirped	Chirped	Chirped	Chirped	Chirped
δ (ms)	5	10	20	30	40	50
Δ (min)	2	2	2	2	2	2
R (Ω)	35	35	35	35	35	35
Video File	IP8_R32	IP8_R32	IP8_R32	IP8_R32	IP8_R32	IP8_R32
Bubble?	Yes	Yes	Yes	Yes	Yes	Yes
Max FT $\overline{D}$ (s:ff)	0.02	1.10	0.27	0.23	0.25	1.10
Max ST $\overline{D}$ (s:ff)	0.03	1.11	0.28	0.24	0.26	1.11
No ST (s:ff)	0.23	3.03	4.06	5.09	6.22	8.27
Experimental Observation	Fresh DI	—	—	—	—	—
Max FT Major D (mm)	28	12	35	39	42	45
Max FT Minor D (mm)	27	12	34	36	40	42
Max ST Major D (mm)	8	10	12	17	18.75	20
Max ST Minor D (mm)	8	10	12	17	18.5	20
Max FT d_x (mm)	14	6	16	21	22	22
Max FT d_y (mm)	17	7	22	25	26	26
Max ST d_x (mm)	4.5	5	5.5	8	10	11
Max ST d_y (mm)	3.5	4.5	6	8	9	9.5

Table D-4. *Sampling of Raw Data for Out-of-Plane Resistor with 6 μm Nucleation Site.*

Property	Sample of Data Collected for Chirped Input					
	Input 1	Input 2	Input 3	Input 4	Input 5	Input 6
Input Type	Chirped	Chirped	Chirped	Chirped	Chirped	Chirped
δ (ms)	5	10	20	30	40	50
Δ (min)	2	2	2	2	2	2
R (Ω)	16	16	16	16	16	16
Video File	OP1_R15	OP1_R15	OP1_R15	OP1_R15	OP1_R15	OP1_R15
Bubble?	Yes	Yes	Yes	Yes	Yes	Yes
Max FT $\overline{D}$ (s:ff)	0.16	1.09	1.02	1.07	1.07	11.21
Max ST $\overline{D}$ (s:ff)	0.17	1.08	1.03	1.08	1.08	11.22
No ST (s:ff)	3.04	6.23	12.02	17.17	21.15	36.13
Experimental Observation	Fresh DI	—	—	—	—	—
Max FT Major D (mm)	20	37	42	44	48	46
Max FT Minor D (mm)	20	36	41	40	46	46
Max ST Major D (mm)	18	22	28	33	35	42
Max ST Minor D (mm)	16	18	25	30	30	35
Max FT d_x (mm)	3	9	5	8	14	11
Max FT d_y (mm)	5	22	28	21	28	33
Max ST d_x (mm)	1	8	5	8	11	14
Max ST d_y (mm)	3	8	12	17	26	1

Bibliography

Agilent Technologies, "Tiny bubbles - the secret to tomorrow's broadband networks,"
[Online document], 2000, [cited 2003 October 26], Available HTTP:
http://www.agilent.com.

Agilent Technologies, "Building Australian businesses based on frontier technologies,"
[Online document], 2003, [cited 2003 October 26], Available HTTP:
http://www.agilent.com.

A. G. Alenitsyn, E. I. Butikov, and A. S. Kondratyev, *Concise Handbook of Mathematics
and Physics*. Boca Raton, Florida: CRC Press, LLC, 1997.

C. K. Alexander, *Fundamentals of Electric Circuits*. Boston, Massachusetts: Mc-Graw Hill
Higher Education, 2000.

R. R. Allen, J. D. Meyer, and W. R. Knight, "Thermodynamics and Hydrodynamics of
Thermal Ink Jets," *Hewlett-Packard Journal*, vol. 36, May, pp. 21-27, 1985.

D. Armani and C. Liu, "Re-configurable Fluid Circuits By PDMS Elastomer
Micromachining," In *Proc. 12th International Conference on MEMS (MEMS '99)*,
Orlando, Florida, 1999, pp. 222-227.

V. S. Arpaci, *Conduction Heat Transfer*. Reading, Massachusetts: Addison-Wesley
Publications Company, 1966.

A. Asai, "Application of the Nucleation Theory to the Design of Bubble Jet Printers,"
Japanese Journal of Applied Physics, vol. 28, pp. 909-915, 1989.

S. aus der Wiesche, C. Rembe, C. Maier, and E. P. Hofer, "Dynamics in Microfluidic
Systems with Microheaters," In *Proc. International Conference on Modeling and
Simulation of Microsystems (MSM '99)*, San Juan, Puerto Rico, 1999, pp. 510-513.

G. Barthau, "Active nucleation site density and pool boiling heat transfer - an experimental
study," *International Journal of Heat and Mass Transfer*, vol. 35, no. 2, pp. 271-278,
1992.

G. T. Baxter, L. J. Bousse, T. D. Dawes, J. M. Libby, D. N. Modlin, J. C. Owicki, and W.
Parce, "Microfabrication in Silicon Microphysiometry," *Clinical Chemistry*, vol. 40,
no. 9, pp. 1800-1804, 1994.

C. C. Beatty, "A chronology of thermal ink-jet structures," In *Proc. IEEE Solid-State Sensor,
Actuator, and Microsystems Workshop*, Hilton Head, South Carolina, 1996, pp. 200-
204.

D. J. Bedard, A. L. Gerhardt, T. M. Montalbo, P. R. Russo, M. Shusteff, and L. Theogarajan,
"Integration of Microfluidics and Microelectronics: Enabling High Speed Sample
Switching and pH Detection," Massachusetts Institute of Technology (MIT),
Cambridge, Massachusetts 6.151 Report, May 2002.

D. J. Beebe, G. A. Mensing, and G. M. Walker, "Physics and Applications of Microfluidics
in Biology," *Annual Review of Biomedical Engineering*, vol. 4, no. 1, pp. 261-286,
2002.

M. Blander and J. L. Katz, "Bubble Nucleation in Liquids," *American Institute of Chemical
Engineering Journal*, vol. 21, no. 5, Sept., pp. 833-848, 1975.

L. Bousse, "Whole Cell Biosensors," *Sensors and Actuators B: Chemical*, vol. 34, no. 1-3, pp. 270-275, 1996.

L. Bousse, R. J. McReynolds, G. Kirk, T. Dawes, P. Lam, W. R. Bemiss, and J. W. Parce, "Micromachined Multichannel Systems for the Measurement of Cellular Metabolism," *Sensors and Actuators B: Chemical*, vol. 20, no. 2-3, pp. 145-150, 1994.

L. Bousse and W. Parce, "Applying Silicon Micromachining to Cellular Metabolism," *IEEE Engineering in Medicine and Biology*, vol. 13, no. 3, pp. 396-401, 1994.

L. J. Bousse, J. W. Parce, J. C. Owicki, and K. M. Kercso, "Silicon micromachining in the fabrication of biosensors using living cells," In *Proc. IEEE Solid-State Sensor, Actuator, and Microsystems Workshop*, Hilton Head, South Carolina, 1990, pp. 173.

R. A. Braff, "Microbubble Cell Actuator," S.M. Thesis, Cambridge, Massachusetts: Massachusetts Institute of Technology (MIT), 1999.

R. A. Braff, A. L. Gerhardt, M. Toner, M. L. Gray, and M. A. Schmidt, "A Microbubble Bioparticle Actuator," In *Proc. IEEE Conference on Solid State Sensor, Actuator, and Microsystems Workshop*, Hilton Head, South Carolina, 2002, pp. 138-141.

R. A. Braff, A. L. Gerhardt, M. Toner, M. L. Gray, and M. A. Schmidt, "Controllable Vapor Microbubbles," *Journal of Microelectromechanical Systems*, Submitted for publication, 2003.

J. P. Brody, P. Yager, R. E. Goldstein, and R. H. Austin, "Biotechnology at Low Reynolds Numbers," *Biophysical Journal*, vol. 71, Dec., pp. 3430-3441, 1996.

Y. A. Buyevich and B. W. Webbon, "The isolated bubble regime in pool nucleate boiling," *International Journal of Heat and Mass Transfer*, vol. 40, no. 2, pp. 365-377, 1997.

S. A. Campbell, *The Science and Engineering of Microfabrication*. New York, New York: Oxford University Press, 2001.

H. S. Carslaw and J. C. Jaeger, *Conduction of Heat in Solids*. 2nd ed., Amen House, London: Oxford University Press, 1959.

L.-H. Chien and R. L. Webb, "A nucleate boiling model for structured enhanced surfaces," *International Journal of Heat and Mass Transfer*, vol. 41, no. 14, pp. 2183-2195, 1998.

B. Choi, M. Ma, C. White, and C. Liu, "Electrolytic and thermal bubble generation using AC inductive powering," In *Proc. 10th International Conference of Solid-State Sensors, Actuators, and Microsystems (Transducers '99)*, Sendai, Japan, 1999.

L. L. Chu, K. Takahata, P. Selvaganapathy, J. L. Shohet, and Y. B. Gianchandani, "A Micromachined Kelvin Probe for Surface Potential Measurements in Microfluidic Channels and Solid-State Applications," In *Proc. 12th International Conference on Solid State Sensors, Actuators, and Microsystems (Transducers '03)*, vol. 1, Boston, Massachusetts, 2003, pp. 384-387.

R. Cole, "Boiling Nucleation," in *Advances in Heat Transfer*, J. P. Hartnett and T. F. Irvine, Eds. Chicago, Illinois: Academic Press, 1974.

R. Cole and S. V. Stralen., *Boiling Phenomena*. vol. 1, Washington, D.C.: Hemisphere Publishing Corporation, 1979.

Z. Darzynkiewicz, E. Bedner, X. Li, W. Gorczyca, and M. R. Melamed, "Laser-Scanning Cytometry: A New Instrumentation with Many Applications," *Experimental Cell Research*, vol. 249, no. 1, pp. 1-12, 1999.

S. S. Davis, "Biomedical applications of nanotechnology - implications for drug targeting and gene therapy," *Trends in Biotechnology*, vol. 15, Jun., pp. 217-224, 1997.

[34]   P. Deng, Y.-K. Lee, and P. Cheng, "Design and Characterization of a Micro Single Bubble Actuator," In *Proc. 12th International Conference on Solid State Sensors, Acutuators, and Microsystems (Transducers '03)*, vol. 1, Boston, Massachusetts, 2003, pp. 647-650.

K. Derewnicki, "Vapour Bubble Formation During Fast Transient Boiling on a Wire," *International Journal of Heat and Mass Transfer*, vol. 26, no. 9, pp. 1405-1408, 1983.

M. Deutsch and A. Weinreb, "Apparatus for High-Precision Sequential Optical Measurement of Living Cells," *Cytometry*, vol. 16, pp. 214-226, 1994.

D. C. Duffy, O. J. A. Schueller, S. T. Brittain, and G. M. Whitesides, "Rapid Prototyping of Microfluidic Switches in Poly(dimethyl siloxane) and their Actuation by Electro-osmotic Flow," *Journal of Micromechanics and Microengineering*, vol. 9, no. 3, pp. 211-217, 1999.

P. Dutta, A. Beskok, and T. C. Warburton, "Electroosmotic Flow Control in Complex Microgeometries," *Journal of Microelectromechanical Systems*, vol. 11, no. 1, Feb., pp. 36-44, 2002.

M. Elwenspoek, T. S. J. Lammerink, R. Miyake, and J. H. J. Fluitman, "Towards integrated microliquid handling systems," *Journal of Micromechanics and Microengineering*, vol. 4, pp. 227-245, 1994.

M. R. Emmert-Buck, R. F. Bonner, P. D. Smith, R. Chuaqui, F., Z. Zhuang, S. R. Goldstein, R. A. Weiss, and L. A. Liotta, "Laser Capture Microdissection," *Science*, vol. 274, pp. 998-1001, 1996.

J. Evans, D. Liepmann, and A. P. Pisano, "Planar Laminar Mixer," In *Proc. 10th International Conference of Solid-State Sensors, Actuators, and Microsystems (Transducers '99)*, Sendai, Japan, 1999, pp. 96-101.

J. D. Evans and D. Liepmann, "The Bubble Spring and Channel (BSaC) Valve: An Actuated, Bi-stable Mechanical Valve for In-Plane Fluid Control," In *Proc. 10th International Conference on Solid-State Sensors, Actuators, and Microsystems (Transducers '99)*, Sendai, Japan, 1999, pp. 1122-1125.

J. A. Fay, *Introduction to Fluid Mechanics*. Cambridge, Massachusetts: MIT Press, 1994.

J. S. Fitch, A. K. Henning, E. B. Arkilic, and J. M. Harris, "Pressure-based mass-flow control using thermopneumatically-actuated microvalves," In *Proc. IEEE Solid-State Sensor, Actuator, and Microsystems Workshop*, Cleveland, Ohio: Transducers Research Foundation, 1998, pp. 162-165.

A. E. Fitzgerald, *Basic Electrical Engineering*. New York, New York: McGraw-Hill, 1945.

M. Fogiel, Ed., *The Handbook of Electrical Engineering*. Piscataway, New Jersey: Research & Education Association, 1996.

C. G. Fonstad, *Microelectronic Devices and Circuits*. New York, New York: Mc-Graw Hill, 1994.

A. Fu, C. Spence, A. Scherer, F. H. Arnold, and S. R. Quake, "A Microfabricated Fluorescence-Activated Cell Sorter," *Nature Biotechnology*, vol. 17, pp. 1109-1111, 1999.

G. Fuhr, T. H. Schnelle, R. Hagedorn, and S. G. Shirley, "Dielectrophoretic Field Cages: Technique for Cell, Virus and Macromolecule Handling," *Cellular Engineering*, vol. 1, pp. 44-57, 1995.

G. Fuhr and S. G. Shirley., "Biological application of microstructures," in *Microsystem Technology in Chemistry and Life Science*, A. Manz and H. Becker, Eds. Verlag, Germany: Springer, 1998.

M. Gad-el-Hak, Ed., *The MEMS Handbook*. Boca Raton, Florida: CRC Press, 2001.

S. Gawad, L. Schild, and P. Renaud, "Micromachined impedance spectroscopy flow cytometer for cell analysis and particle sizing," *Lab on a Chip*, vol. 1, no. 1, pp. 76-82, 2001.

X. Geng, H. Yuan, H. N. Oguz, and A. Prosperetti, "Bubble-Based Micropump for Electrically Conducting Liquids," *Journal of Micromechanics and Microengineering*, vol. 11, no. 3, pp. 270-276, 2001.

T. Goldmann and J. S. Gonzalez, "DNA-printing: utilization of a standard inkjet printer for the transfer of nucleic acids to solid supports," *Journal of Biochemical and Biophysical Methods*, vol. 42, no. 3, pp. 105-110, 2000.

P. Gravesen, J. Branebjerg, and O. S. Jensen, "Microfluidics - A Review," *Journal of Micromechanics and Microengineering*, vol. 3, pp. 168-182, 1993.

M. L. Gray, M. A. Schmidt, M. Toner, R. A. Braff, J. Voldman, and A. L. Gerhardt, "Microfabrication-based Dynamic Array Cytometer (μDAC)," Presented at *Proc. Alliance for Cellular Signaling (AfCS) 2nd Annual Meeting*, Dallas, Texas, 2002.

M. L. Gray, M. A. Schmidt, M. Toner, J. Voldman, and R. A. Braff, "Microfabrication-based Dynamic Array Cytometer (μDAC)," Alliance for Cellular Signaling (AfCS), Bridging Project Proposal, 1999.

C. Grosjean and Y. C. Tai, "A Thermopneumatic Peristaltic Micropump," In *Proc. 10th International Conference of Solid-State Sensors, Actuators, and Microsystems (Transducers '99)*, Sendai, Japan, 1999, pp. 1776-1779.

D. Halliday, R. Resnick, and K. S. Krane, *Physics: Part Two*. New York, New York: John Wiley & Sons, Inc., 1992.

D. Halliday, R. Resnick, and J. Walker, *Fundamentals of Physics*. New York, New York: John Wiley & Sons, Inc., 1993.

A. Hatch, A. E. Kamholz, G. Holman, P. Yager, and K. F. Böhringer, "A Ferrofluidic Magnetic Micropump," *Journal of Microelectromechanical Systems*, vol. 10, no. 2, Jun., pp. 215-221, 2001.

A. K. Henning, "Liquid and gas-liquid phase behavior in thermopneumatically actuated microvalves," In *Proc. Microfluidic Devices and Systems*, vol. 3515, Bellingham, Washington: SPIE, 1998, pp. 53-63.

A. K. Henning, "Microfluidic MEMS," In *Proc. IEEE Aerospace Conference*, vol. / paper 4.906, Piscataway, New Jersey: IEEE Press, 1998.

Hewlett-Packard Company, "Myths About Thermal Inkjet Printings," [Online document], 1994, [cited 2003 July 21], Available HTTP: http://www.hp.com.

C. M. Ho and Y. C. Tai, "Micro-Electro-Mechanical-Systems (MEMS) and Fluid Flows," *Annual Review of Fluid Mechanics*, vol. 30, pp. 579-612, 1980.

G. Hong, A. S. Holmes, M. E. Heaton, and K. R. Pullen, "Design, Fabrication, Characterization of an Axial-Flow Turbine for Flow Sensing," In *Proc. 12th International Conference on Solid State Sensors, Actuators, and Microsystems (Transducers '03)*, vol. 1, Boston, Massachusetts, 2003, pp. 702-705.

P. Horowitz and W. Hill, *The Art of Electronics*. Cambridge, Massachusetts: Cambridge University Press, 2001.

R. T. Howe and C. G. Sodini, *Microelectronics: An Integrated Approach*. Upper Saddle River, New Jersey: Prentice Hall, 1997.

S.-S. Hsieh, C.-J. Weng, and J.-J. Chiou, "Nucleate Pool Boiling on Ribbed Surfaces at Low and Moderate Heat Flux," *Journal of Heat Transfer*, vol. 121, May, pp. 376-385, 1999.

Y. Y. Hsu, "On the Size Range of Active Nucleation Cavities on a Heating Surface," *Journal of Heat Transfer*, Aug., pp. 207-216, 1962.

D. Huang and E. S. Kim, "Micromachined Acoustic-Wave Liquid Ejector," *Journal of Microelectromechanical Systems*, vol. 10, no. 3, pp. 442-449, 2001.

R. G. Hudson., *The Engineers' Manual*. New York, New York: Jon Wiley & Sons, Inc., 1917.

Y. Iida, K. Okuyama, and K. Sakurai, "Boiling nucleation on a very small film heater subjected to extremely rapid heating," *International Journal of Heat and Mass Transfer*, vol. 37, no. 17, pp. 2771-2780, 1994.

J. D. Irwin, *Basic Engineering Circuit Analysis*. New York, New York: Jon Wiley & Sons, Inc., 2002.

S. C. Jakeway, A. J. d. Mello, and E. L. Russell, "Miniaturized Total Analysis Systems for Biological Analysis," *Fresenius Journal of Analytical Chemistry*, vol. 366, no. 6-7, pp. 525-539, 2000.

H. Jerman, "Electrically-activated micromachined diaphragm valves," In *Proc. IEEE Solid State Sensors, Actuators, and Microsystems Workshop*, Hilton Head, South Carolina, 1990, pp. 65-69.

H. Jerman, "Electrically-activated, normally closed diaphragm valves," *Journal of Micromechanics and Microengineering*, vol. 4, pp. 210-216, 1994.

L. A. Kamentsky and M. R. Melamed, "Spectrophotometric Cell Sorter," *Science*, vol. 156, pp. 1364-1365, 1967.

S. G. Kandlikar, M. Shoji, and V. K. Dhir, Eds., *Handbook of Phase Change: Boiling and Condensation*. Philadelphia, Pennsylvania: Taylor & Francis, 1999.

T. Kawakatsu, Y. Kikuchi, and M. Nakajima, "Visualization of Microfiltration Phenomena Using Microscope Video System and Silicon Microchannels," *Journal of Chemical Engineering of Japan*, vol. 29, no. 2, pp. 399-401, 1996.

Y. Kikuchi, K. Sato, and Y. Mizuguchi, "Modified Cell-Flow Microchannels in a Single-Crystal Silicon Substrate and Flow Behavior of Blood Cells," *Microvascular Research*, vol. 47, pp. 126-139, 1994.

K. Kim, S. W. Park, H. Monohara, and J.-B. Lee, "Polydimethylsiloxane (PDMS) for High Aspect Ratio Three-dimensional MEMS," In *Proc. 2000 International Symposium on Mechatronic and Intelligent Mechanical Systems for 21 Century (ISIM 2000)*, KyongSangNam-Do, Korea, 2000.

M. Koch, N. Harris, A. G. R. Evans, N. M. White, and A. Brunnschweiler, "A novel micromachined pump based on thick-film piezoelectric actuation.," *Sensors and Actuators A: Physical*, vol. 70, pp. 98-103, 1998.

G. Kotzar, M. Freas, P. Abel, A. Fleischman, S. Roy, C. Zorman, J. M. Moran, and J. Melzak, "Evaluation of MEMS materials of construction for implantable medical devices," *Biomaterials*, vol. 23, pp. 2737-2750, 2002.

F. Kreith and M. S. Bohn, *Principles of Heat Transfer*. 5th ed., Saint Paul, Minnesota: West Publishing Company, 1993.

J. Kruger, K. Singh, A. O'Neill, C. Jackson, A. Morrison, and P. O'Brien, "Development of a Microfluidic Device for Fluorescence Activated Cell Sorting," *Journal of Micromechanics and Microengineering*, vol. 12, no. 4, pp. 486-494, 2002.

L. Latorre, J. Kim, J. Lee, P.-P. de Guzman, H. J. Lee, P. Nouet, and C.-J. Kim, "Electrostatic Actuation of Microscale Liquid-Metal Droplets," *Journal of Microelectromechanical Systems*, vol. 11, no. 4, Aug., pp. 302-308, 2002.

C.-J. Lin and F.-G. Tseng, "A Novel Micro Faby-Perot Sensor Utilizing Refractive Index Matched Medium for High Sensitive Shear Stress Sensing," In *Proc. 12th International Conference on Solid State Sensors, Actuators, and Microsystems (Transducers '03)*, vol. 1, Boston, Massachusetts, 2003, pp. 710-713.

L. Lin, "Microscale Thermal Bubble Formation: Thermophysical Phenomena and Applications," *Microscale Thermophysical Engineering*, vol. 2, no. 2, Apr.-Jun., pp. 71-85, 1998.

L. Lin, "Microscale Thermal Bubble Formation: Thermophysical Phenomena and Applications," *Microscale Thermophysical Engineering*, vol. 2, pp. 71-85, 1998.

L. Lin and A. P. Pisano, "Bubble Forming on a Micro Line Heater," In *Proc. DSC ASME Micromechanical Sensors, Actuators, and Systems - Winter Annual Meeting*, vol. 32, 1991, pp. 147-163.

L. Lin and A. P. Pisano, "Thermal Bubble Powered Microactuators," *Microsystem Technologies Journal*, vol. 1, no. 1, pp. 51-58, 1994.

L. Lin, A. P. Pisano, and V. P. Carey, "Thermal Bubble Formation on Polysilicon Micro Resistors," *Journal of Heat Transfer*, vol. 120, Aug., pp. 735-742, 1998.

L. Lin, A. P. Pisano, and A. P. Lee, "Microbubble Powered Actuator," In *Proc. 6th International Conference on Solid-State Sensors, Actuators, and Microsystems (Transducers '91)*, San Francisco, California, 1991, pp. 1041-1044.

L. Lin, K. S. Udell, and A. P. Pisano, "Phase Change Phenomena on a Heated Polysilicon Micro Heater in Confined and Unconfined Micro Channels," *Thermal Sciences and Engineering*, vol. 2, pp. 52-59, 1994.

M. R. Lindeburg, *Mechanical Engineering Reference Manual*. 8th ed., Belmont, California: Professional Publications, Inc., 1990.

T. Lisec, M. Kreutzer, and B. Wagner, "A bistable pneumatic microswitch for driving fluidic components," *Sensors and Actuators A: Physical*, vol. 54, pp. 746-749, 1996.

C.-C. Liu and Z. Jin, "Applications of microfabrication and micromachining techniques in biotechnology," *Trends in Biotechnology*, vol. 15, Jun., pp. 213-216, 1997.

R. H. Liu, Q. Yu, and D. J. Beebe, "Fabrication and Characterization of Hydrogel -Based Microvalves," *Journal of Microelectromechanical Systems*, vol. 11, no. 1, Feb., pp. 45-53, 2002.

M. Losey, "Novel Multiphase Chemical Reaction Systems Enabled by Microfabrication Technology," Ph.D. Dissertation, Cambridge, Massachusetts: Massachusetts Institute of Technology (MIT), 2001.

M. S. Lou, J. C. Chen, and C. M. Li, "Surface Roughness Prediction Technique for CNC End-Milling," *Journal of Industrial Technology*, vol. 15, no. 1, Nov. - Jan., pp. 2-6, 1998.

H. Lu, M. A. Schmidt, and K. F. Jensen, "Photochemical reactions and on-line UV detection in microfabricated reactors," *Lab on a Chip*, vol. 1, no. 1, pp. 22-28, 2001.

P. Luginbuhl, P.-F. Indermuhle, M.-A. Grétillat, F. Willemin, N. F. de Rooij, D. Gerber, G. Gervasio, J.-L. Vuilleumier, D. Twerenbold, M. Düggelin, D. Mathys, and R. Guggenheim, "Femtoliter injector for DNA mass spectrometry," *Sensors and Actuators B: Chemical*, vol. 63, pp. 167-177, 2000.

A. Manz, C. S. Effenhauser, N. Burggraf, D. J. Harrison, K. Seiler, and K. Fluri, "Electroosmotic pumping and electrophoretic separations for miniaturized chemical analysis systems," *Journal of Micromechanics and Microengineering*, vol. 4, pp. 257-265, 1994.

J. C. Martin and D. E. Swartzendruber, "Time: A New Parameter for Kinetic Measurements in Flow Cytometry," *Science*, vol. 207, pp. 199-201, 1980.

Y. Matsumoto, K. Yoshida, and M. Ishida, "A novel deposition technique for fluorocarbon films and its applications for bulk- and surface-micromachined devices," *Sensors and Actuators A: Physical*, vol. 66, no. 1-3, pp. 308-314, 1998.

R. B. Maxwell, "Controllable Vapor Microbubble for Use in Bioparticle Actuation," PhD Dissertation, Cambridge, Massachusetts: Massachusetts Institute of Technology (MIT), 2003.

R. B. Maxwell, A. L. Gerhardt, M. Toner, M. L. Gray, and M. A. Schmidt, "A Microbubble-Powered Bioparticle Actuator," *Journal of Microelectromechanical Systems*, vol. 12, no. 5, pp. 630-640, 2003.

E. Meng and Y.-C. Tai, "A Parylene MEMS Flow Sensing Array," In *Proc. 12th International Conference on Solid State Sensors, Actuators, and Microsystems (Transducers '03)*, vol. 1, Boston, United States, 2003, pp. 686-689.

H. Merte, Jr. and H. S. Lee, "Quasi-Homogeneous Nucleation in Microgravity at Low Heat Flux: Experiments and Theory," *Journal of Heat Transfer.*, vol. 119, May, pp. 305-312, 1997.

B. B. Mikic and W. M. Rohsenow, "Bubble Growth Rates in Non-uniform Temperature Field," in *Progress in Heat and Mass Transfer*, vol. 2, T. F. Irvine, W. E. Ibele, J. P. Hartnett, and R. J. Goldstein, Eds. Oxford, England: Pergamon Press, 1969, pp. 283-294.

A. F. Mills, *Heat Transfer*. Concord, Massachusetts: Irwin, 1992.

A. F. Mills, *Basic Heat and Mass Transfer*. Concord, Massachusetts: Irwin, 1995.

A. F. Mills, *Heat and Mass Transfer*. Concord, Massachusetts: Irwin, 1995.

J. Monahan, A. A. Gewirth, and R. G. Nuzzo, "A Method for Filling Complex Polymeric Microfluidic Devices and Arrays," *Analytical Chemistry*, vol. 73, pp. 3193-3197, 2001.

G. Murphy, *Mechanics of Materials*. New York, New York: Ronald Press Company, 1948.

A. D. Myškiv, *Advanced Mathematics for Engineers*. Moscow, Russia: Mir Publishers, 1975.

N. J. Nielsen, "History of Thinkjet Printhead Development," *Hewlett-Packard Journal*, vol. 36, May, pp. 4-10, 1985.

T. Okamoto, T. Suzuki, and N. Yamamoto, "Microarray Fabrication with Covalent Attachment of DNA Using Bubble Jet Technology," *Nature Biotechnology*, vol. 18, Apr., pp. 438-441, 2000.

P. V. O'Neil, *Advanced Engineering Mathematics*. Pacific Grove, California: Brooks/Cole Publishing Company, 1995.

A. V. Oppenheim and A. S. Willsky, *Signals & Systems*. Upper Saddle River, New Jersey: Prentice Hall, 1997.

A. P. Papavasiliou, D. Liepmann, and A. P. Pisano, "Electrolysis-Bubble Actuated Gate Valve," In *Proc. IEEE Solid-State Sensors, Actuators, and Microsystems Workshop*, Hilton Head, South Carolina, 2000, pp. 200-204.

J. W. Parce, J. C. Owicki, K. M. Kercso, G. B. Sigal, H. G. Wada, V. C. Muir, L. J. Bousse, K. L. Ross, B. I. Sikir, and H. M. McConnell, "Detection of Cell-Affecting Agents with a Silicon Biosensor," *Science*, vol. 246, Oct., pp. 243-247, 1989.

R. Pethig, "Application of A.C. electrical fields to the manipulation and characterization of cells," in *Automation in Biotechnology*, I. Karube, Ed. Amsterdam, Netherlands: Elsevier Science, 1991, pp. 159-185.

R. Pethig, "Dielectrophoresis: Using inhomogeneous AC electrical fields to separate and manipulate cells," *Critical Reviews in Biotechnology*, vol. 16, no. 4, pp. 331-348, 1996.

R. Rammig and R. Weiss, "Growth of vapor bubbles from artificial nucleation sites," *Cryogenics*, vol. 31, Jan., pp. 64-69, 1991.

E. Ross, Private communication. Alliance for Cellular Signaling (AfCS) 3rd Annual Meeting, Pasadena, CA, 2003.

C. Saint and J. Saint, *IC Layout Basics*. New York, New York: McGraw-Hill, 2001.

A. Sakurai and M. Shiotsu, "Transient Pool Boiling Heat Transfer, Part 1: Incipience Boiling Superheat," *Journal of Heat Transfer.*, vol. 99, no. 547-553, 1997.

K. Sato, Y. Kawamura, S. Tanaka, K. Uchida, and H. Kohida, "Individual and Mass Operation of Biological Cells using Micromechanical Silicon Devices," *Sensors and Actuators A: Physical*, vol. 23, no. A21-A23, pp. 948-953, 1990.

M. G. Say, Ed., *Newnes Concise Encyclopedia of Electrical Engineering*. London, England: George Newnes, Ltd., 1962.

S. D. Senturia, *Microsystem Design*. Norwell, Massachusetts: Kluwer Academic Publishers, 2001.

L. J. Shadle, E. R. Monazam, and J. S. Mei, "Circulating Fluid Bed Operating Regimes," In *Proc. 7th International CFB Conference*, Niagra Falls, New York, 2001, pp. 255-262.

J. Shih, J. Xie, and Y. C. Tai, "Surface Micromachined and Integrated Capacitive Sensors for Microfluidic Applications," In *Proc. 12th International Conference on Solid State Sensors, Acuators, and Microsystems (Transducers '03)*, vol. 1, Boston, Massachusetts, 2003, pp. 388-395.

S. Shoji and M. Esashi, "Microflow Devices and Systems," *Journal of Micromechanics and Microengineering*, vol. 4, pp. 157-171, 1994.

C. F. Shoop and G. L. Tuve, *Mechanical Engineering Practice*. New York, New York: McGraw-Hill Book Company, Inc., 1949.

W. M. Siebert, *Circuits, Signals, and Systems*. Cambridge, Massachusetts: MIT Press, 1986.

T. Stanczyk, B. Ilic, P. J. Hesketh, and J. G. B. IV, "A Microfabricated Electrochemical Actuator for Large Displacements," *Journal of Microelectromechanical Systems*, vol. 9, no. 3, pp. 314-320, 2000.

Y. Su, L. Lin, and A. P. Pisano, "A Water-Powered Osmotic Actuator," *Journal of Microelectromechanical Systems*, vol. 11, no. 6, Dec., pp. 736-742, 2002.

K. Takahashi, J. Weng, and C.Tien, "Marangoni Effect in Microbubble Systems," *Microscale Thermophysical Engineering*, vol. 3, pp. 169-182, 1999.

L. S. Tong and Y. S. Tang, *Boiling Heat Transfer and Two-Phase Flow*. 2nd ed., Washington, D.C.: Taylor and Francis, Incorporated, 1997.

J. Tsai and L. Lin, "Nozzle-Diffuser Based Micro Bubble Pump," In *Proc. Late News Poster Session Supplemental Digest of IEEE Solid-State Sensors, Actuators, and Microsystems Workshop*, Hilton Head, South Carolina, 2000, pp. 13-14.

J. Tsai and L. Lin, "Transient Bubble Formation On A Polysilicon Micro Resister," In *Proc. 2000 ASME International Mechanical Engineering Congress and Exposition, ASME Heat Transfer Division*, vol. 2, Orlando, Florida, 2000, pp. 251-258.

J. Tsai and L. Lin, "Transient Thermal Bubble Formation on Polysilicon Micro-Resistors," *Journal of Heat Transfer.*, vol. 124, Apr., pp. 375-382, 2002.

J. Tsai and L. Lin, "Active Microfluidic Mixer and Gas Bubble Filter Driven by Thermal Bubble Micropump," *Sensors and Actuators A: Physical*, vol. 97-98, pp. 665-671, 2002.

J. Tsai and L. Lin, "A Thermal-Bubble-Actuated Micronozzle-Diffuser Pump," *Journal of Microelectromechanical Systems*, vol. 11, no. 6, Dec., pp. 665-671, 2002.

J. Tsai and L. Lin, "Transient Thermal Bubble Formation on Polysilicon Micro-Resistors," *Journal of Heat Transfer.*, vol. 124, Apr., pp. 375-382, 2002.

F. Tseng, C. Kim, and C. Ho, "A High-Resolution High-Frequency Monolithic Top-Shooting Microinjector Free of Satellite Drops - Part I: Concept, Design, and Model," *Journal of Microelectromechanical Systems*, vol. 11, no. 5, Oct., pp. 427-436, 2002.

F. Tseng, C. Kim, and C. Ho, "A High-Resolution High-Frequency Monolithic Top-Shooting Microinjector Free of Satellite Drops - Part II: Fabrication, Implementation, and Characterization," *Journal of Microelectromechanical Systems*, vol. 11, no. 5, pp. 437-447, 2002.

N. Vandelli, D. Wroblewski, M. Velonis, and T.Bifano, "Development of a MEMS Microvalve Array for Fluid Flow Control," *Journal of Microelectromechanical Systems*, vol. 7, no. 4, Dec., pp. 395-403, 1998.

J. Voldman, "A Microfabricated dielectrophoretic trapping array for cell-based biological assays," PhD Dissertation, Cambridge, Massachusetts: Massachusetts Institute of Technology (MIT), 2001.

J. Voldman, R. A. Braff, M. Toner, M. L. Gray, and M. A. Schmidt, "Quantitative design and analysis of single-particle dielectrophoretic traps," In *Proc. Micro Total Analysis Systems (µTAS '00)*, Twente, Netherlands: Kluwer Academic Publishers, 2000, pp. 431-434.

J. Voldman, R. A. Braff, M. Toner, M. L. Gray, and M. A. Schmidt, "Holding Forces of Single-Particle Dielectrophoretic Traps," *Biophysical Journal*, vol. 80, no. 1, pp. 531-541, 2001.

J. Voldman, M. L. Gray, and M. A. Schmidt, "Liquid mixing studies using an integrated mixer/valve," In *Proc. Micro Total Analysis Systems (µTAS '98)*, Netherlands: Kluwer Academic Publishers, 1998, pp. 181-184.

J. Voldman, M. L. Gray, and M. A. Schmidt, "Microfabrication in Biology and Medicine," *Annual Review of Biomedical Engineering*, vol. 1, pp. 401-425, 1999.

J. Voldman, M. L. Gray, and M. A. Schmidt, "An integrated liquid mixer/valve," *Journal of Microelectromechanical Systems*, vol. 9, pp. 295-302, 2000.

J. Voldman, M. L. Gray, M. Toner, and M. A. Schmidt, "A Microfabrication-Based Dynamic Array Cytometer," *Analytical Chemistry*, vol. 74, no. 16, pp. 3984-3990, 2002.

J. Voldman, M. Toner, M. L. Gray, and M. A. Schmidt, "A dielectrophoresis-based array cytometer," In *Proc. 11th International Conference of Solid-State Sensors, Actuators, and Microsystems (Transducers '01)*, Munich, Germany, 2001, pp. 322-325.

J. Voldman, M. Toner, M. L. Gray, and M. A. Schmidt, "A Microfabrication-Based Dynamic Array Cytometer," *Analytical Chemistry*, vol. 74, pp. 3984-3990, 2002.

J. Voldman, M. Toner, M. L. Gray, and M. A. Schmidt, "Design and analysis of extruded quadrupolar dielectrophoretic traps," *Journal of Electrostatics*, vol. 57, pp. 69-90, 2003.

C. H. Wang and V. K. Dhir, "Effect of Surface Wettability on Active Nucleation Site Density During Pool Boiling of Water on a Vertical Surface," *Journal of Heat Transfer*, vol. 115, Aug., pp. 659-669, 1993.

C. H. Wang and V. K. Dhir, "On the Gas Entrapment and Nucleation Site Density During Pool Boiling of Saturated Water," *Journal of Heat Transfer*, vol. 115, Aug., pp. 670-679, 1993.

X.-Q. Wang, A. Desai, Y.-C. Tai, and T. D. Lee, "Polymer-based electrospray chips for mass spectrometry," In *Proc. 12th International Conference on Microelectromechanical Systems (MEMS '99)*, Orlando, Florida, 1999.

R. C. Weast, Ed., *Handbook of Chemistry and Physics*. 52nd ed., Cleveland, Ohio: The Chemical Rubber Company, 1971.

R. B. White and A. Zakhari, "Internal Structures in Fluid Beds of Different Scales: An Application of Electrical Capacitance Tomography," In *Proc. 1st World Congress on Industrial Process Tomography*, Burdon, Greater Manchester, England, 1999, pp. 39-46.

S. a. d. Wiesche, C. Rembe, C. Maier, and E. P. Hofer, "Dynamics in Microfluidic Systems with Microheaters," In *Proc. Technical Proceedings of the 1999 International Conference on Modeling and Simulation of Microsystems (MSM '99)*, San Juan, Puerto Rico, 1999, pp. 510 - 513.

K. Yanagisawa, H. Kuwano, and A. Tago, "An Electromagnetically Driven Microvalve," In *Proc. 7th International Conference of Solid-State Sensors, Actuators, and Microsystems (Transducers '93)*, 1993, pp. 102-105.

M. Yang, C. Li, and J. Yang, "Cell Docking and On-Chip Monitoring of Cellular Reactions with a Controlled Concentration Gradient on a Microfluidic Device," *Analytical Chemistry*, vol. 74, pp. 3991-4001, 2002.

R. B. Yarborough, *Electrical Engineering Reference Manual for the PE Exam*. 5th ed., Belmont California: Professional Publications, Inc., 1997.

M. J. Zdeblick, J. J. R. Anderson, B. Kline-Schoder, R. M. L. Christel, and W.Weber., "Thermopneumatically actuated microvalves and integrated electrofluidic circuits," In *Proc. IEEE Solid-State Sensors, Actuators, and Microsystems Workshop*, 1994, pp. 251-255.

R. Zengerle, M. Richter, F. Brosinger, A. Richter, and H. Sandmaier, "Performance simulation of microminiaturized membrane pumps," In *Proc. 7th International Conference of Solid-State Sensors, Actuators, and Microsystems (Transducers '93)*, Yokohama, Japan, 1993, pp. 106-109.

R. Zengerle, J. Ulrich, S. Kluge, M. Richter, and A. Richter, "A bidirectional silicon micropump," *Sensors and Actuators A: Physical*, vol. 50, no. 1-2, pp. 81-86, 1995.

Q. Zou, U. Sridhar, and R. Lin, "A study on micromachined bimetallic actuation," *Sensors and Actuators A: Physical*, vol. 78, pp. 212-219, 1999.